STRUCTURES, BONDING AND TRANSPORT PROPERTIES OF HIGH PRESSURE SOLIDS

A Thesis Submitted to the College of
Graduate Studies and Research
In Partial Fulfillment of the Requirements
For the Degree of Doctor of Philosophy
In the Department of Physics and
Engineering Physics
University of Saskatchewan
Saskatoon

By
Yansun Yao

© Copyright Yansun Yao, September, 2008. All rights reserved.

PERMISSION TO USE

In presenting this thesis in partial fulfilment of the requirements for a Postgraduate degree from the University of Saskatchewan, I agree that the Libraries of this University may make it freely available for inspection. I further agree that permission for copying of this thesis in any manner, in whole or in part, for scholarly purposes may be granted by the professor or professors who supervised my thesis work or, in their absence, by the Head of the Department or the Dean of the College in which my thesis work was done. It is understood that any copying or publication or use of this thesis or parts thereof for financial gain shall not be allowed without my written permission. It is also understood that due recognition shall be given to me and to the University of Saskatchewan in any scholarly use which may be made of any material in my thesis.

Requests for permission to copy or to make other use of material in the thesis in whole or part should be addressed to:

Head of the Department of Physics and Engineering Physics
116 Science Place
University of Saskatchewan
Saskatoon, Saskatchewan
Canada
S7N 5E2

ABSTRACT

The objective of this investigation is to study the distinct physical and electronic properties of high-pressure solids, through state-of-the-art first-principles numerical computations. This thesis is composed of four distinct research topics.

The superconducting properties of several high-pressure solids were investigated based on the Migdal-Eliashberg theory within the framework of the BCS model. The possibility of pressure-induced superconductivity was investigated for selected materials, including dense Li, Xe, and Group IV hydrides. The pressure-induced phase transition FCC → *cI*16 in Li and the superconducting properties in the FCC and *cI*16 phases were investigated. Noble gas Xe is predicted being a superconductor under pressure with a comparatively low T_c. Two Group IV hydrides, SiH_4 and SnH_4, were predicted to be good superconductors under high pressure.

The Bader's AIM analysis, IR and Raman spectroscopes were used as diagnostic tools to differentiate among candidate structural models for solid H_2, O_2, and SiH_4. For solid H_2, IR and Raman spectra are used to examine two recently proposed competing structures of the high-pressure phase III; the *Cmcm* and *C*2/*c* structures. For solid O_2, the experiment observed structure, IR and Raman spectra of the recently solved *C*2/*m* structure of the high-pressure ε phase were well produced. Using Bader's AIM method and from the analysis of the electron charge density, the preference on the formation of $(O_2)_4$ clusters in the *C*2/*m* structure and the nature of the interactions between O_2 molecules is explained. For SiH_4, IR and Raman spectra were calculated for our predicted $P4_2/nmc$ structure and the agreement with available experiment results is very good.

Typical theoretical approaches for predicting/determining unknown high-pressure crystal structures usually involve dynamical processes. An alternative approach based on a recently proposed genetic algorithm was explored in this thesis. The focus is to predict stable and meta-stable structures at high pressure without any assumption on initial structures. The high-pressure structures of Ca were investigated and two new stable structures that might explain the diffraction pattern of the Ca-IV and Ca-V phases were predicted. The high-pressure phase II and phase III of AlH_3 were also investigated, and structures were successfully predicted for each phase. Another example presented is the prediction of a metastable single-bonded phase of nitrogen.

A first-principles approach was developed for the calculation of XAS within the framework of the DFT. The PAW method was used to reconstruct the core orbitals. These orbitals are essential for the calculation of the transition matrix elements. This approach provides a straightforward framework for the investigation of single particle core hole and electron screening effects, which have been demonstrated to be significant for all investigated materials. To test the implementation, the C, Si, and O *K*-edge XAS were calculated for diamond, fullerene C_{60}, α-quartz and water molecule. In all cases, the calculated XAS agree very well with experiments. For the water molecule, the quality of the calculated XAS sensitively depends on the delicate theoretical treatment of core hole potential and electron screening. The overall agreement between the calculated XAS and experiment is reasonable.

Much of the work presented in this thesis has now been accepted for publication in journals. The references are as follows:

1. M. I. Eremets, I. A. Trojan, S. A. Medvedev, J. S. Tse and Y. Yao, 'Superconductivity in hydrogen dominant materials: silane', *Science* **319** 1506 (2008).

2. J. S. Tse, Y. Yao and K. Tanaka, 'Novel superconductivity in metallic SnH_4 under high

pressure', *Phys. Rev. Lett.* **98**, 117004 (2007).

3. I. N. Goncharenko, M. I. Eremets, M. Hanfland, J. S. Tse, M. Amboage, Y. Yao and I. A. Trojan, 'Pressure-induced hydrogen-dominant metallic state in aluminum hydride', *Phys. Rev. Lett.* **100**, 045504 (2008).

4. Y. Yao, J. S. Tse, Y. Ma and K. Tanaka, 'Superconductivity in high-pressure SiH_4', *Europhys. Lett.* **78**, 37003 (2007).

5. Y. Yao, J. S. Tse, Z. Song, D. D. Klug, J. Sun and Y. Le Page, 'Structures and superconducting properties of the high-pressure IV and V phases of calcium from first principles', *Phys. Rev. B* **78** 054506 (2008).

6. Y. Yao, J. S. Tse and K. Tanaka, 'High-pressure single-bonded metastable phases of nitrogen predicted via genetic algorithm', *Phys. Rev. B* **77** 052103 (2008).

7. Y. Yao and J. S. Tse, 'Electron-phonon coupling in the high-pressure hcp phase of xenon: A first-principles study', *Phys. Rev. B* **75**, 134104 (2007).

8. J. S. Tse, Y. Yao, D. D. Klug and S. Desgreniers, 'Bonding in the epsilon-phase of oxygen at high pressure', *J. Phys.: Conf. Series* **121** 012006 (2008).

9. J. S. Tse, Y. Yao and Y. Ma, 'Superconductivity in high-pressure solids', *J. Phys.: Condens. Matter* **19,** 425208 (2007).

10. J. S. Tse, D. D. Klug, Y. Yao, Y. Le Page and J. R. Rodgers, 'Structure and spectroscopic properties of dense solid hydrogen at 160 GPa', *Solid State Comm.* **145**, 5 (2007).

Other work has been performed, but not included in this thesis for reasons of continuity. The references are as follows:

1. J. Yang, J. S. Tse, Y. Yao and T. Iitaka, 'Structural and electronic properties of pristine and Ba-doped clathrate-like carbon fullerenes', *Angew. Chem. Int. Ed.* **46**, 2675 (2007) .

2. H. Shimizu, N. Wada, T. Kume, S. Sasaki, Y. Yao and J. S. Tse,

‘Pressure-induced structural transformation in solid xenon studied by Raman spectroscopy’, *Phys. Rev. B* **77** 052101 (2008).

3. J. S. Tse, D. D. Klug, Y. Yao and S. Desgreniers, ‘Electronic structure of epsilon-oxygen at high pressure’, *Phys. Rev. B* (in press).

ACKNOWLEDGEMENT

Many wonderful people have helped me during the five years of my study at the University of Saskatchewan. Firstly I would take the opportunity to thank my supervisor Dr. John Tse who gave me the chance to work as I felt with total support and encouragement. I was very fortunate to work with him and his appeal for insightful knowledge helped me move on and develop me as a researcher. Particularly I appreciate the great efforts he has taken to introduce me into the high-pressure research community. I would like to thank my supervisor Dr. Kaori Tanaka for her constant and invaluable guidance and help during my research work. I am also indebted to the care she has taken in the reading and revision of this thesis. I would also like to acknowledge Dr. Stefano Fabris, my supervisor at DEMOCRITOS, for his careful guidance and fully support during my trip to Trieste.

I owe big thanks to Michelle Shaw who was always so nice and patient in answering my questions on computer clusters and in giving me the latest news about the Chinese restaurants in town. Drs. Tom Steele, Rainer Dick and Akira Hirose made it possible for me to accumulate the knowledge on Quantum Mechanics and Electromagnetic Theory. Their wonderful classes I took in the first year have left marks on me. I would also like to thank my colleague graduate student and post-docs, Jianjun Yang, Victor Song, and Yunfeng Liang. I have taken great advantages from many scientific and non-scientific conversations with them. I would also like to acknowledge Dr. Dennis Klug for his valuable discussions and encouragement.

During my stay in Saskatoon, I had the opportunity to meet many new friends. I am very much in debt to my friends who supported my family and me. My friends Mr. Clint Cory, Mrs. Sylvia Cory, Mrs. Ruth Eremko and their families, each of them in their

own particular and unforgettable way made these years more than a good memory. Special thanks to Mr. Clint Cory for helping me expand my English during weekly coffee meeting and also for his instruction on how to make cowboy coffee.

On a more personal note, I would like to thank my wife and son, Hongbin and Edison, for their unending support and love. This work took away a lot of my time and care they deserved. My thanks are also devoted to my parents who continuously offer their love and care over many miles from China. An ocean between us, made me realize how much I love them.

致知力行

To my family and the memory of my beloved grandmother

CONTENTS

LIST OF TABLES

LIST OF FIGURES

LIST OF ABBREVIATIONS

DFT	Density Functional Theory
PSPW	Pseudopotential Planewave
KS	Kohn-Sham
LDA	Local Density Approximation
GGA	Generalized Gradient Approximation
PBE	Perdew-Burke-Ernzerhof
BZ	Brillouin zone
PW	Planewave
DFPT	Density Functional Perturbation Theory
EM	Electromagnetic
IR	Infrared
XES	X-ray Emission Spectroscopy
XAS	X-ray absorption spectroscopy
EELS	Electron Energy Loss Spectroscopy
PAW	Projector Augmented Wave
Quantum-ESPRESSO	Open Source Package for Research in Electronic Structure, Simulation, and Optimization.
VASP	Vienna Ab-initio Simulation Package
SIESTA	Spanish Initiative for Electronic Simulations with Thousands of Atoms
MD	Molecular Dynamics
DOS	Density of States
PHDOS	Phonon Density of States
AIM	Atoms in Molecules
ASAP	Advanced Structure seArching Package
DEMOCRITOS	National Simulation Center of the Italian Istituto Nazionale per la Fisica della Materia
EPC	Electron-Phonon Coupling
FCC	Face Centered Cubic
SC	Simple Cubic
BCC	Body Centered Cubic
HCP	Hexagonal Close Packed
FS	Fermi surface
BCS	Bardeen, Cooper and Schrieffer
TA	Transverse Acoustic
LO	Longitudinal Optical
TO	Transverse Optical

ELF	Electron Localization Function
ETT	Electron Topological Transition
2D	Two Dimensional
3D	Three Dimensional
CP	Critical Point
BCP	Bond Critical Point
RCP	Ring Critical Point
CCP	Cage Critical Point
MP	Monkhorst-Park
GA	Genetic Algorithm
RDF	Radial Distribution Functions
BP	Black Phosphorus
CG	Cubic Gauche
SB	Single-Bonded
EOS	Equation of States
LENEXAFS	Low-Energy Near-Edge X-ray Absorption Fine Structure
NEXAFS	Near-Edge X-ray Absorption Fine Structure
EXAFS	Extended X-ray Absorption Fine Structure
GIPAW	Gauge-Including Projector Augmented Waves
C-G	Clebsch-Gordan

CHAPTER 1

Introduction

Many interesting questions in geophysics and planetary physics, as well as in applied science, concern the physical properties of solids at high pressure. At high pressure, most ambient-pressure materials become unstable and transform into new phases with higher densities. In recent years, many solids with new structure types have been found at high pressure through experiments and numerical simulations [1]. These structures are often novel and sometimes not seen in any solids at ambient pressure. It has been found that these new structures can possess a variety of electronic states, *i.e.*, metallic, superconducting, super-hard, or super-ionic states. These discoveries are of high interests both for their potential technological applications and contribute to the understanding of the fundamental aspects of electronic processes in solids such as chemical bonding. The study of physical properties of high-pressure solids is one research area that have greatly benefited from numerical simulations. In experiments, high pressure is not easy to reach and control in diamond anvil cells. On the contrary, adjusting pressure in numerical simulations can be accomplished straightforwardly by varying the size of unit cell. With the rapid developments of computational power and advanced software, theoretical studies of solids at high pressure have had a blossom over the past two decades. The complexities of the materials that can be studied and the accuracy in which physical properties can be predicted have increased rapidly over the years. Numerical simulations with well-established first-principles methods have played a very important role in exploring and guiding experiments at high pressure. Numerical simulations have now been established as a very important tool in cooperation with experiments at high pressure. On the other hand, new experiments at high pressure continue to provide challenging tests for both theory and numerical methods, and help to

further develop more sophisticated principles and algorithms.

Solid materials are constructed by atomic nuclei and electrons whose behavior is governed by the laws of quantum mechanics. In principle, physical properties in a solid can be calculated by solving the many-body Schrödinger equation. In practice, however, a full quantum mechanical treatment is intractable for all but the simplest systems. The total number of particles in a solid, including both nuclei and electrons, is on the scale of 10^{23}. As one particle moves in the lattice, the other particles feel its Coulomb potential, experience a force, and move in response. Hence, the motion of each particle in the system is correlated with the motions of all other particles. The complexity of the total correlations increases exponentially with the degree of freedom of the system. Therefore, only the simplest systems such as isolated atoms or simple polyatomic molecules can be completely solved. Over the years, many approximations have been developed to reduce the burdens of solving such many-body problems. For example, the Born-Oppenheimer approximation [2] separates the motion of electrons from that of massive nuclei assuming that the velocity of the nuclei is much slower than that of electrons. In this way, the positions of nuclei can be considered as fixed and the electronic degree of freedom can be separated. The periodic boundary conditions, based on the Bloch theorem, allows the treatment of very large number of electrons in a crystal by reducing the problem to that of a perfect periodic unit cells and confining all the physics within a single cell. The density functional theory (DFT) [3-5] transforms a many-body electronic problem into multiple one-particle electronic problems by treating the ground-state electron density as a basic variable instead of the coordinate of each electron. Pseudopotential methods [6-8] treat the overall effects of the core electrons into an ionic potential, and overcome the convergence problems associated with rapidly oscillating electronic wavefunctions within the core regions of the atoms. Planewave basis sets are used to replace the complicated form of the electronic wavefunctions with simple and adjustable mathematical representations. The pseudopotential planewave (PSPW) method within the DFT framework is a quantum mechanical approach incorporating all of these approximations [9, 10]. The PSPW method has evolved over recent years, and now it is possible to perform calculations for real materials entirely based on first-principles (without any

experimental input) with results allowing quantitative comparison with experimental measurements. This method is now a well-established tool for studying solids. In this thesis, all the first-principles calculations were performed using this method.

1. 1 Density functional theory

Within the DFT framework, the ground state of a crystal lattice is described by its ground-state electron density. The electrons move in an effective potential that includes the static external ionic potential, Coulomb repulsion, and the exchange-correlation potential between the electrons. The motion of each electron resembles that of a non-interacting single electron, and is described by a single-particle Schrödinger-like equation, Kohn-Sham (KS) equation [5]. The many-body system is then mapped into a system of non-interacting single electrons. The solutions to the KS equations of each electron in the system, often referred to as KS orbitals, are used to build the electron density. As stated in the Hohenberg-Kohn theorem [3], all ground-state observables are functional of the electron density. The total energy of the system can be derived from minimization in terms of the ground-state electron density. The effective potential is a functional of electron density determined by the KS orbitals, which in turns depend on the effective potential. Thus, the problem of solving a Kohn-Sham equation is iterative with the effective potential and the resulting charge density must be self-consistent. The calculation starts with an initial guess of electron density, from which the corresponding effective potential is calculated. The KS equation is solved with this effective potential, and resulting KS orbitals are used to produce a new electron density. If this new electron density differs from the previous one by more than a given tolerance, one replaces the previous electron density with the new one and repeats the calculation again. This procedure is repeated until convergence within the tolerance is achieved. It should be noticed that the KS orbitals of non-interacting electrons are used to mimic the electron density of the original many-body system. The total energy is obtained by minimizing the energy functional. The KS orbitals and corresponding eigenvalues do not have well-

defined physical interpretations. The only physical observable of the DFT is the ground-state electron density.

1. 1. 1 Kohn-Sham formulation of DFT

The microscopic description of a crystal is a system constructed from nuclei and electrons that interact with each other through Coulomb interactions. An approximation to decouple the electronic degrees of freedom from those of the nuclei is the Born-Oppenheimer approximation [2]. This is based on the fact that electrons have much smaller masses compared with the nuclei. Within this approximation, the nuclei are regarded as fixed ions acting as an external potential. The behavior of the interacting electrons in this nuclear potential is described by the Schrödinger equation,

$$\hat{H}\psi(\vec{r}_1,...,\vec{r}_n) = E\psi(\vec{r}_1,...,\vec{r}_n)\,, \tag{1.1}$$

with Hamiltonian $\hat{H}$

$$\hat{H} = -\frac{1}{2}\sum_{i=1}^{N}\vec{\nabla}_i^2 + \sum_{i=1}^{N}V_{ext}(\vec{r}_i) + \frac{1}{2}\sum_{i\neq j}\frac{1}{\left|\vec{r}_i - \vec{r}_j\right|}. \tag{1.2}$$

In this equation, as well as in the following discussion, the atomic units are used throughout with $\hbar$=1, e=1, and m_e=1. Here $\vec{r}_i$ is the position of the *i-th* electron. The N is the number of electrons in the system. The $V_{ext}(\vec{r})$ is the external potential describing the Coulomb interaction between the electrons and a given configuration of the nuclei. In a solid, imposed by the periodic boundary condition, $V_{ext}(\vec{r})$ is explicitly determined by the Bravais lattice vectors and internal atomic coordinates. The last term in Eq. (1.2) represents the electron-electron Coulomb interactions. This term involves all electronic degrees of freedom, and therefore makes the numerical solution of Eq. (1.1) intractable. An approximation to solve this problem was made by Hohenberg and Kohn, known as the Hohenberg-Kohn theorems [3]. The Hohenberg-Kohn theorems state that for any

system of interacting electrons in an external potential, the ground-state energy is a unique functional of the electron density. Moreover, the true ground-state electron density minimizes the energy functional, and the resulting minimum energy is the correct ground-state energy. However, the energy functional of an interacting many-body system is not known. Kohn and Sham [5] proposed a practical scheme for DFT. In this approach, the many-body model of *interacting* electrons in the external potential is reproduced by a simpler model of *non-interacting* electrons moving in an effective potential, and by construction the electron densities in these two systems are identical.

The ground-state total energy of a solid, including both electrons and nuclei, can be written as,

$$E_{total}[n] = E_{electron}[n] + E_{ion}\,. \tag{1.3}$$

Here E_{ion} is the Coulomb energy between nuclei and is explicitly determined by the atomic configurations. The electronic energy functional $E_{electron}[n]$ is written as,

$$E_{electron}[n] = \int_V d\vec{r}\, V_{ext}(\vec{r}) \cdot n(\vec{r}) + F[n]\,, \tag{1.4}$$

where the functional $F[n]$ includes all the kinetic energy and electron-electron interaction terms. It is convenient to separate the Coulomb energy term arising from the electron distribution out of the functional $F[n]$,

$$F[n] = \frac{1}{2}\int_V\int_V d\vec{r}\,d\vec{r}\,' \frac{n(\vec{r})n(\vec{r}\,')}{|\vec{r}-\vec{r}\,'|} + G[n]\,. \tag{1.5}$$

This new functional $G[n]$ contains the kinetic energy functional $T[n]$ and the exchange-correlation energy functional $E_{xc}[n]$,

$$G[n] = T[n] + E_{xc}[n]\,. \tag{1.6}$$

The ground-state total energy is obtained by minimizing the electronic energy functional $E_{electron}[n]$ subject to the constraint that the electron number is conserved:

$$\int_V d\vec{r} n(\vec{r}) = N . \tag{1.7}$$

This minimization leads to

$$V_{ext}(\vec{r}) + \int_V d\vec{r}' \frac{n(\vec{r}')}{|\vec{r} - \vec{r}'|} + \frac{\delta E_{xc}[n]}{\delta\, n(\vec{r})} + \frac{\delta T[n]}{\delta\, n(\vec{r})} = \mu , \tag{1.8}$$

where μ is a Lagrange multiplier. Since the form of the kinetic energy functional $T[n]$ is unknown, one has to find an alternative way of finding $n(\vec{r})$. Considering a system constituted by *non-interacting* electrons in an external potential $V_{ext}(\vec{r})$, the many-body wavefunction is simply a product of all one-electron wavefunctions. The electron density for this non-interacting system can be written readily as

$$n(\vec{r}) = \sum_{i=1}^{N} \left|\phi_i(\vec{r})\right|^2 . \tag{1.9}$$

Here $\phi_i(\vec{r})$ is the single-particle wavefunction in the non-interacting system. Each wavefunction $\phi_i(\vec{r})$ obeys the Schrödinger equation

$$\left\{-\frac{1}{2}\nabla^2 + V_{ext}(\vec{r})\right\}\phi_i(\vec{r}) = \varepsilon_i \phi_i(\vec{r}) . \tag{1.10}$$

Kohn and Sham generalized this formulation to the case of *interacting* electrons. They defined an effective potential to include all the potential terms in Eq. (1.8),

$$V_{eff}(\vec{r}) = V_{ext}(\vec{r}) + \int_V d\vec{r}' \frac{n(\vec{r}')}{|\vec{r} - \vec{r}'|} + \frac{\delta E_{xc}[n]}{\delta\, n(\vec{r})} . \tag{1.11}$$

Therefore, analogously to the *non-interacting* electron system, each electron in the *interacting* electron system is described by

$$\left\{-\frac{1}{2}\nabla^2 + V_{eff}[n]\right\}\psi_i(\vec{r}) = \varepsilon_i\psi_i(\vec{r}), \tag{1.12}$$

with the electron density

$$n(\vec{r}) = \sum_{i=1}^{N}\left|\psi_i(\vec{r})\right|^2 . \tag{1.13}$$

Eq. (1.12) is known as the KS equation and it clearly resembles non-interacting single-electron Schrödinger equation. The eigenstates and eigenvalues of the KS equation are often referred to as the KS orbitals and KS energies, respectively. The KS orbitals are used to build up the ground-state electron density via Eq. (1.13). The correct ground-state total energy should be obtained from the minimization in terms of the ground-state electron density.

1. 1. 2 Forms of exchange correlations

The KS DFT provides a practical procedure to solve the many-body problem by breaking the problem into a set of single-particle problems. This formalism is exact but practically still unsolvable since the many-body wavefunctions are still included in the exchange-correlation term $E_{xc}[n]$, whose exact form is not known. To make the formalism useful, it is necessary to make some approximations for the exchange-correlation term $E_{xc}[n]$. The most common and straightforward approximation to $E_{xc}[n]$ is the Local Density Approximation (LDA) [3]. The idea of the LDA is assuming that the exchange-correlation energy per electron of a *non-uniform* system at any point in space is equal to the exchange-correlation energy per electron in a *uniform* electron gas having the same density at this point. Thus

$$E_{xc}^{LDA}[n] = \int_V d\vec{r}\,\varepsilon_{xc}[n]n(\vec{r}) \tag{1.14}$$

with

$$\varepsilon_{xc}[n] = \varepsilon_{xc}^{uniform}[n]. \tag{1.15}$$

By definition, the LDA is local because the exchange correlation energy $\varepsilon_{xc}[n]$ at each point in space only depends on the electron density at the same point. The $\varepsilon_{xc}[n]$ has been calculated and parameterized through Monte Carlo total energy calculation for a uniform electron gas with a variety of electron densities [11, 12]. Since the LDA is based on uniform electron gas, it is expected to be accurate only for systems in which the electron density varies slowly. It is clearly not suitable for the situations where the electron density undergoes rapid changes, as in the case of covalent bounded solids. To overcome this deficiency of the LDA, another form of exchanged-correlation functional has been developed, that is the Generalized Gradient Approximation (GGA) [13-17]. The GGA functional depends on the local electron density as well as the spatial variation of the electron density that is represented by the density gradient. The GGA functional can be written as

$$E_{xc}^{GGA}[n] = \int_V d\vec{r}\,\varepsilon_{xc}[n]F_{xc}[n,\vec{\nabla}n]n(\vec{r}). \tag{1.16}$$

The analytic function F_{xc} is known as the enhancement factor that includes the correlation term E_c and exchange term F_x. The enhancement factor are usually represented by a dimensionless reduced density gradient,

$$s(\vec{r}) = \frac{\left|\vec{\nabla}n(\vec{r})\right|}{2k_F n(\vec{r})}, \tag{1.17}$$

where k_F is the Fermi wavevector. Unlike the unique form of LDA, GGA can have many different forms, each corresponding to a different enhancement factor. Among them, the

Perdew-Burke-Ernzerhof (PBE) functional [18] is the most commonly used. The exchange enhancement factor of the PBE functional is

$$F_x^{PBE}(s) = 1 + \kappa - \frac{\kappa}{1 + \mu s^2 / \kappa}, \tag{1.18}$$

where $\mu \sim 0.2195$ and $\kappa \sim 0.804$. The exchange energy is written as

$$E_c^{PBE} = \int_V d\vec{r} n(\vec{r}) \cdot \{\varepsilon_c[n] + H(t, r_s, \varsigma)\}. \tag{1.19}$$

Here r_s is the Seitz radius and ς is the spin polarization. The parameter t is another dimensionless gradient term given by

$$t(\vec{r}) = \frac{\left|\vec{\nabla} n(\vec{r})\right|}{2 g k_s n(\vec{r})}, \tag{1.20}$$

where $k_s = (4k_F / \pi)^{1/2}$ and $g = [(1+\varsigma)^{1/3} + (1+\varsigma)^{2/3}]/2$. The term $\varepsilon_c[n]$ is the correlation energy per electron of a uniform electron gas. The correction term $H(t, r_s, \varsigma)$ is written as

$$H(t, r_s, \varsigma) = \gamma g^3 \log\left(1 + \frac{\gamma}{\beta} t^2 \frac{1 + At^2}{1 + At^2 + A^2 t^4}\right). \tag{1.21}$$

Here $\beta \sim 0.0667$, $\gamma \sim 0.031$ and

$$A = \frac{\beta}{\gamma}\left[\exp\left(\frac{-\varepsilon_c(r_s, \varsigma)}{\gamma g^3}\right) - 1\right]^{-1}. \tag{1.22}$$

The implementation of PBE functional has led to a simplified version of exchange-correlation term that is parameterized entirely from fundamental constants. Computationally, the inclusion of simple gradients in the exchange-correlation term only result in minor cost of computer workload. The PBE functional has gained considerable success. Significant improvement has been observed using PBE functional compared with LDA functional in predicting the structural geometries, bulk modulus, atomic total energies, and vibrational properties. For example, the lattice constants of ferromagnetic body centered cubic (BCC) phase for iron [19, 20], and the energy difference between α-quartz and stishovite in the SiO_2 system were correctly predicted by PBE functional [21].

1. 1. 3 Periodic boundary condition, *k*-point sampling

Even with a reasonable approximation for the exchange-correlation term, the KS equations of a solid are still intractable due to the infinite number of non-interacting electrons. For each electron, the electronic wavefunction extends in the entire lattice, and thus the basis set required to expand the KS orbital is infinite too. Fortunately, perfect crystallized solids can be described as spatially repeated unit cells that only contain a small number of electrons and nuclei. This leads to the use of periodic boundary conditions through the Bloch theorem, which confines the study of a very large number of electrons into a single unit cell. The Bloch theorem states that the solution of the single-particle Schrödinger equation (*i.e.*, KS equation) in the presence of a periodic potential must have the form

$$\psi_i(\vec{k},\vec{r}) = e^{i\vec{k}\cdot\vec{r}} u_i(\vec{k},\vec{r}), \tag{1.23}$$

where $u_i(\vec{k},\vec{r})$ is the cell-periodic part of the wavefunction such that $u_i(\vec{k},\vec{r}) = u_i(\vec{k},\vec{r}+\vec{R})$ for all lattice vectors $\vec{R}$. The variable $\vec{k}$ is the wave vector of the electron in the first Brillouin zone (BZ). Thus,

$$\psi_i(\vec{k},\vec{r}+\vec{R}) = e^{i\vec{k}\cdot\vec{R}}\psi_i(\vec{k},\vec{r})\,. \tag{1.24}$$

Substituting Eq. (1.24) into the KS equation Eq. (1.12), a new set of eigen-equations is found, each for a given $\vec{k}$. Each electron occupies an electronic state of definite wave vector $\vec{k}$. Therefore, the problem of solving for an infinite number (~10^{23}) of electrons within the extended system is converted to solving for a finite number of electronic bands at an infinite number of *k*-points within the single (reciprocal) unit cell. Changing from one infinite number to another, however, does not directly make the problem simpler. Nevertheless, the electronic wavefunctions at the *k*-points that are very close to each other will be almost identical, and therefore in practice one can represent the wavefunctions over a small region of reciprocal space around one *k*-point by the wavefunction at this *k*-point. In this case, only a finite number of *k*-points are needed to determine the ground state of solids. The density of allowed *k*-points is proportional to the volume of the solid.

Many efficient schemes have been developed for the *k*-point sampling in the first BZ. Using these schemes, one can obtain very good approximation for the electron potential and total energy of a solid. The idea is to represent any integral over almost continuous *k*-points in the first BZ by the summation over a *k*-points mesh,

$$\frac{\Omega}{(2\pi)^3}\int_V d\vec{k} f(\vec{k}) \sim \sum_i f(\vec{k}_i) w_i\,, \tag{1.25}$$

where w_i is the weight of the point $\vec{k}_i$. The most widely used scheme for the *k*-point sampling was developed by Monkhorst and Park [22], the so-called MP mesh. The MP mesh utilizes the space group symmetries of the lattice and confines the sampling only in the irreducible wedge of the first BZ. The *k*-points are also selected according to their point group symmetries, which in turn decide the weight w_i. In this way, a sufficient sampling can be achieved in a very small number of *k*-points. The magnitude of error in

the calculated total energy due to insufficient *k*-point sampling can always be reduced by using a denser *k*-point mesh. With sufficient *k*-points, the computed total energy will converge and the error due to the *k*-point sampling approaches zero.

1. 1. 4 The planewave basis set

With the approximation of exchange-correlation term and using the periodic boundary conditions, it is possible to solve the KS equation Eq. (1.12). In order to solve the KS equation numerically, the KS orbitals need to be expanded by some well-defined basis sets. Although there are many choices of basis sets available [23-25], the planewave (PW) basis set is probably the most straightforward. The planewaves are not centered at atoms. Moreover, it forms a complete basis set with very simple mathematical functions. The completeness of the basis set is easy to adjust, essentially through only one parameter, *i.e.*, the kinetic energy cutoff E_{cut}.

The KS orbital $\psi_i(\vec{k},\vec{r})$ can be expanded using the PW basis set as,

$$\psi_i(\vec{k},\vec{r}) = e^{i\vec{k}\cdot\vec{r}} u_i(\vec{k},\vec{r}) = \frac{1}{\sqrt{V}} \sum_{\vec{G}} c_{i,\vec{k}+\vec{G}} \cdot e^{i\vec{G}\cdot\vec{r}} \cdot e^{i\vec{k}\cdot\vec{r}}, \tag{1.26}$$

where $\vec{G}$ is the reciprocal lattice vector. In principle, an infinite basis set of $\vec{G}$ should be used to expand the KS orbital $u_i(\vec{k},\vec{r})$. In practice, it is possible to truncate the infinite basis set to include only PW's that have kinetic energies less than a defined cutoff energy,

$$\frac{1}{2}\left|\vec{k}+\vec{G}\right|^2 < E_{cut}. \tag{1.27}$$

Clearly, the truncation of the PW basis set will introduce some error in the calculated total energy. However, the computed total energy to a given tolerance should converge by gradually increasing the kinetic energy cutoff.

1. 1. 5 The pseudopotential approximation

It has been shown above that using the periodic boundary conditions the KS orbitals can be expanded with a discrete PW basis set of finite size truncated at the kinetic energy cutoff E_{cut}. Unfortunately, it is still not straightforward to solve the KS equation numerically. The core electrons are tightly bounded to the nuclei, and thus their wavefunctions are much localized in the regions near the nuclei (Fig. 1.1). To expand localized wavefunctions a very high energy cutoff E_{cut}, and hence a very large set of PW's are needed. Since the wavefunctions of the valence electrons are orthogonal to the core wavefunctions, they must oscillate in the regions where the core wavefunctions exist (Fig. 1.1). Expanding oscillating wavefunctions requires a very large number of PW's. However, the energies of the core electrons are usually much negative than those of the valence electrons, therefore the chemical properties of a solid depends almost solely on the valence electrons. Furthermore, the oscillations of valence wavefunctions in the core regions have very little influence to the electronic structure, since they interact very little with the neighboring atoms. These facts lead to the use of the pseudopotential approximation [6-8, 26] in which the core electrons and ionic potential are removed and replaced by a pseudopotential that acts on a set of pseudo wavefunctions instead of the true valence wavefunctions. In this approximation only the valence electrons outside the core regions are explicitly considered; therefore the pseudo wavefunctions need not be orthogonal to the core wavefunctions and can be represented by a node less function inside the core regions. Hence, much fewer PW's are required in the expansion of pseudo wavefunctions. The pseudo wavefunction and pseudopotential are identical to the all-electron valence wavefunction and potential outside a cutoff radius r_c (Fig. 1.2). The cutoff radius r_c is decided by the criteria that the core regions of neighboring atoms should not overlap. Choosing smaller core cutoff radius usually means improving the transferability of the pseudopotential, *i.e.,* making it suitable for more diversity of chemical environments. However, small core cutoff radius also makes the pseudo wavefunctions tighter and therefore more PW's are needed in the expansion.

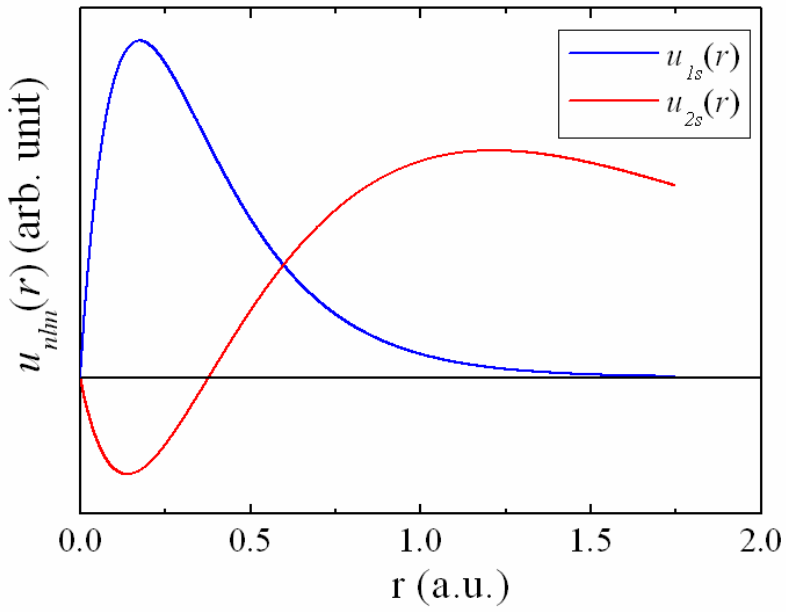

Figure 1.1. The calculated all-electron 1s and 2s wavefunctions of an isolated carbon atom. Due to the orthogonal rule, the number of nodes in each wavefunction is *n*-*l*-1. Therefore the 1s wavefunction is node less and the 2s wavefunction has one node.

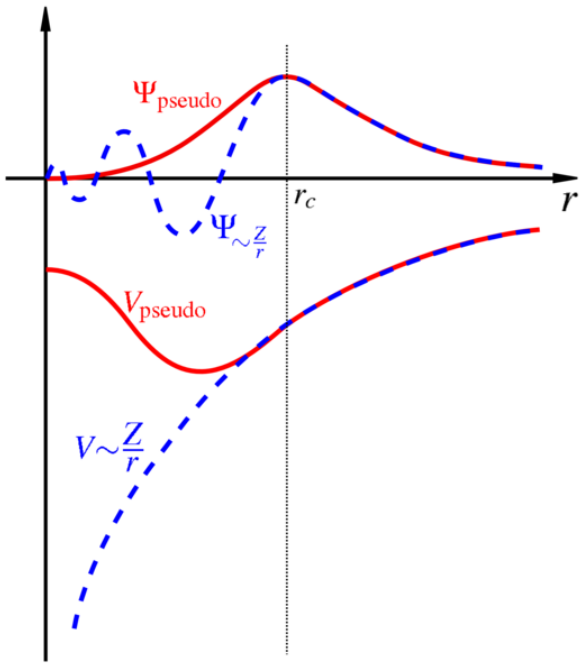

Figure 1.2. Comparison of a valence wavefunction in the Coulomb potential of the nucleus (dashed curves) to that of pseudopotential (solid curves). Outside the cutoff

radius r_c, the pseudo wavefunction and pseudopotential are identical to the all-electron valence wavefunction and potential. This figure is taken from Z. Song's M. Sc. thesis (Department of Physics and Engineering Physics, University of Saskatchewan, 2007).

1. 1. 6 Self-consistency and ground-state total energy

The ingredients needed to solve the KS equations are now complete. The KS energies, KS orbitals, as well as the ground-state electron density and ground-state total energy, can be solved self-consistently through the pseudopotential planewave method [9, 10]. Fig. 1.3 shows a flow chart diagram of this procedure. The self-consistent calculation starts with an initial guess of electron density that is usually constructed by superimposing the electron densities of non-interacting atoms. With this electron density, the effective potential $V_{eff}[n]$ and therefore the set of KS equations can be constructed. The KS orbitals are represented by pseudo wavefunctions that are expanded with a finite set of PW's truncated at the kinetic energy cutoff E_{cut}. The KS equations need to be solved for each k-point, and the resulting KS orbitals are used to build a new electron density via Eq. (1.13). If the new electron density differs from its initial guess beyond a tolerance, it means that the calculation is not converged. One must construct a new set of potentials using the new electron density and repeat the calculations again. The calculation is repeated until the solutions are self-consistent. Once the convergence is achieved, the resulting electron density is used to calculate the ground-state total energy.

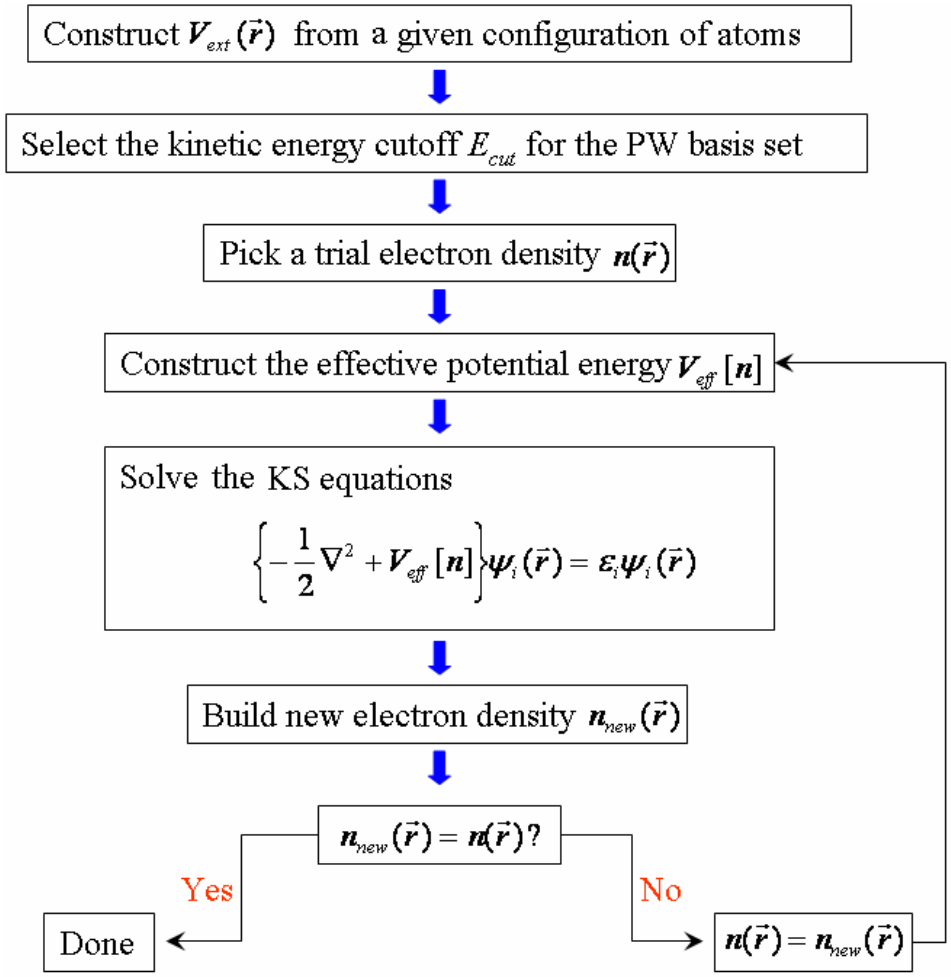

Figure 1.3. The flow chart describing the self-consistent calculation using DFT with PW basis set.

1. 2 Physics at high pressure using DFT

The KS DFT presented in section 1.1 provides a theoretical scheme for the study of the properties of materials at high pressure. This method is fully *ab initio* using very efficient PW basis set and pseudopotential approximations. The quantities that are well defined and can be directly calculated in the DFT scheme are the ground-state total energy and the electron density. However, many bulk physical observables of the solid

are derivatives of the total energy, taken with respect to some structural parameters or various external perturbations. Examples include dielectric constants, Born effective charges, internal strains, and phonon dispersions. The first derivatives can usually be calculated straightforwardly through the Hellmann-Feynman theorem [27, 28], which states that the first derivative of the eigenvalues of a Hamiltonian respect to parameter λ, can be determined by the expectation value of the first derivative of the Hamiltonian in the unperturbed eigenstates,

$$\frac{\partial E_\lambda}{\partial \lambda} = \langle \psi_\lambda | \frac{\partial H_\lambda}{\partial \lambda} | \psi_\lambda \rangle , \tag{1.28}$$

where ψ_λ is the eigenstate of Hamiltonian H_λ corresponding to the eigenvalue E_λ. Clearly, the first derivative of the total energy does not need any expansion of the wavefunctions, and therefore it can readily be calculated in the DFT scheme. The second derivative is more complicated, which requires calculation of both the ground-state electron density $n_\lambda(\vec{r})$ and its linear response to the perturbation, $\partial n_\lambda(\vec{r})/\partial\lambda$. The calculation of higher-order derivatives of the total energy was made possible by the work of Baroni, Giannozzi, and Testa [29-31]. They introduced a perturbation theory into DFT and made an important extension, often referred to as the density functional perturbation theory (DFPT). The DFPT provides an efficient scheme to calculate first-order corrections to the wavefunctions and therefore second-order corrections to the total energy. In fact, it has been demonstrated that the first-order correction to the wavefunction calculated in DFPT can also be used to evaluate the correction to the total energy up to third order. This is a special case of a more general theorem, the so called 2*n*+1 theorem [32-35], which states that the (2*n*+1)-*th* derivative of the eigenvalue of a Hamiltonian can be determined with only a knowledge of the change in the eigenstates up to *n-th* order. One of the main advantages of DFPT is that it allows the study of a perturbed system with computational workload comparable to that of a self-consistent calculation in the unperturbed system. On the other hand, to perform a similar study via numerical differentiation, much more expensive supercell calculations would be needed.

With the application of DFT and its extension DFPT, many properties can be explored for solids at high pressure. Some of them that are related to this thesis are listed below.

1. High-pressure phase diagrams.

At high pressure, most ambient-pressure structures of solids become unstable and transform into new structures of higher densities. The phase diagram provides information on the energetically favorable candidate structures of solids at various pressures. Theoretically, a phase diagram can be constructed from comparison of the energies of candidate structures with pressure. For each candidate structure, the total energy E_{total} needs to be computed at a number of unit cell volumes. At each volume, lattice shape and internal atomic coordinates that minimize E_{total} need to be determined. An example phase diagram for three high-pressure phases of Si is presented in Fig. 1.4. The first phase transition happens at around 40 GPa where the Si-V (primitive hexagonal) structure [36, 37] transforms to the Si-VI (orthorhombic) structure [38]. The Si-VI structure is stable up to about 47 GPa, at which pressure it further transforms to the Si-VII (hexagonal close packed) structure [36]. Several theoretical approaches have been utilized for the prediction of candidate structures, such as simulated annealing, meta-dynamics, and genetic algorithm. An essential step of all these methods is the determination of equilibrium geometry and total energy of candidate structures. To optimize a crystal structure in the presence of a non-vanishing external pressure, both the forces acting on each atom and the stress tensor present in the unit cell need to be calculated. In practice, these tasks essentially are performed using the Hellmann-Feynman theorem [39, 40]. The atomic forces are the first derivatives of the total energy with respect to atomic displacements, while the stress tensor is the first derivative of the total energy with respect to the strain. A solid is in equilibrium if all the atomic forces vanish. A non-zero force acting on an atom means that the total energy of the solid can be lowered by displacing this atom in the direction of the force. The external pressure subject on the solid is represented by non-zero stress tensors, which can be achieved by changing the size or shape of the unit cell.

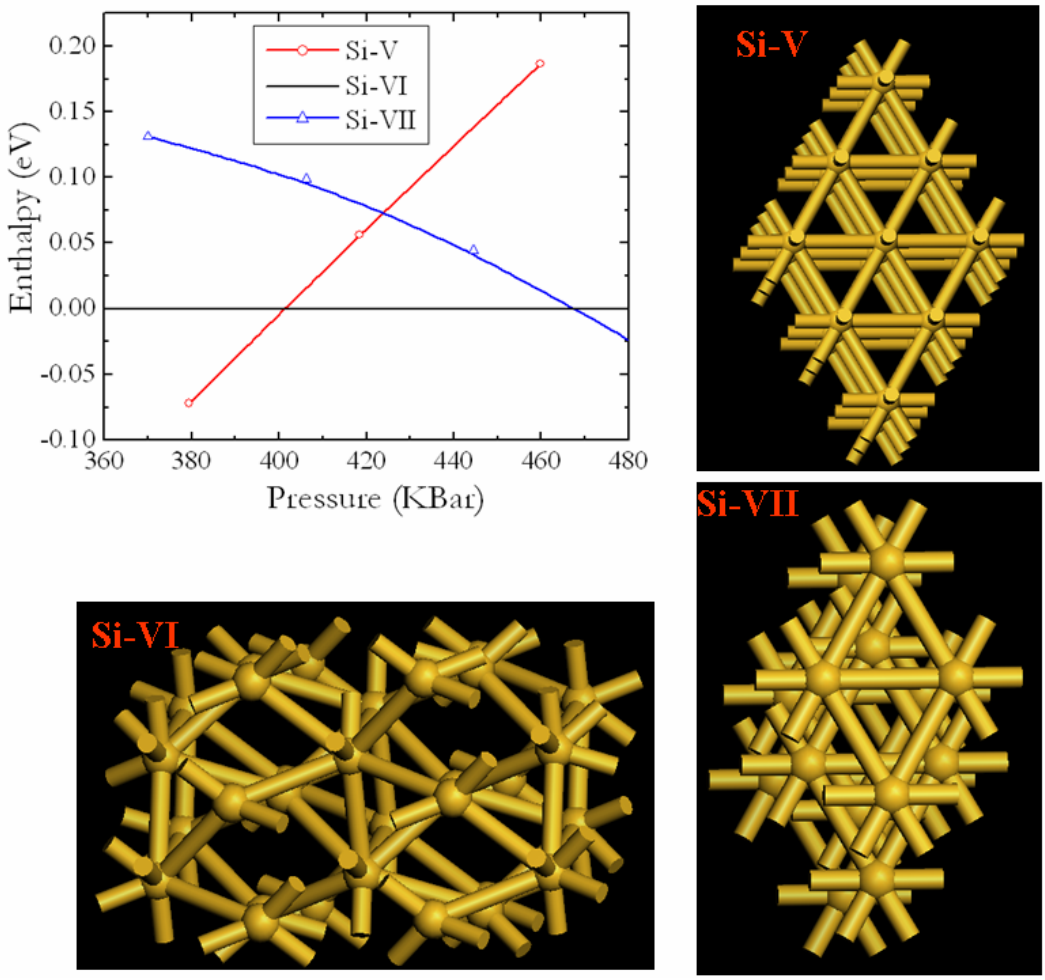

Figure 1.4. The enthalpies per atom as functions of pressure for three high-pressure phases of Si. The enthalpy of the Si-VI phase is used as the zero-energy reference level.

2. Vibrational properties and structural stability of high-pressure solids.

A necessary condition for a stable phase at high pressure is that the structure is mechanically stable. A rigorous verification of structural stability of a crystal structure is that its phonon band structure should not possess imaginary frequency. The phonon band structure, which is a representation of the vibrational frequency at arbitrary wavevector $\vec{q}$ in the first BZ, can be calculated through interpolation of the inter-atomic force constants

that were computed from the second derivatives of the total energy with respect to atomic displacements [40, 41]. These inter-atomic force constants can be efficiently calculated using DFPT. Consider an extended crystal lattice constructed by unit cells with *n* atoms in each cell. The coordinates of each atom in this system is

$$\vec{R}_{L,i} = \vec{R}_L + \vec{\tau}_i , \qquad i = 1,2,\ldots n , \tag{1.29}$$

where $\vec{R}_L$ is the lattice vector of the *L*-th unit cell and $\vec{\tau}_i$ is the fractional coordinates of the *i*-th atom inside the unit cell. A displacement of the atomic coordinates on the equilibrium geometry is defined by

$$\vec{R}_{L,i} \to \vec{R}_{L,i} + \vec{u}_i(\vec{R}_L) . \tag{1.30}$$

The atomic displacements are usually small, and therefore the total potential energy of the system can be expressed within harmonic approximations [43] in terms of the displacements as a Taylor expression,

$$E_{pot} = E^o_{pot} + \frac{1}{2}\sum_{L,L'}\sum_{i,j} \vec{u}_i(\vec{R}_L)\cdot C_{i,j}(\vec{R}_L,\vec{R}_{L'})\cdot \vec{u}_j(\vec{R}_{L'}) + \mathrm{O}(u^3) . \tag{1.31}$$

Here the potential energy E_{pot} includes the clamped-ion energy and electron-ion interaction energy,

$$E_{pot} = E_{ion} + \int_V d\vec{r}\, V_{ext}(\vec{r})\cdot n(\vec{r}) . \tag{1.32}$$

Since the average atomic positions are assumed constant, the first term in the expansion vanishes. The coefficient $C_{i,j}(\vec{R}_L,\vec{R}_{L'})$ is the inter-atomic force constant that is the second derivative of total the potential energy calculated at equilibrium,

$$C_{i,j}(\vec{R}_L,\vec{R}_{L'})=\left.\frac{\partial^2 E_{pot}}{\partial\vec{u}_i(\vec{R}_L)\partial\vec{u}_j(\vec{R}_{L'})}\right|_0 . \tag{1.33}$$

The force acting on the *i*-th atom at site $\vec{R}_L$ can be calculated by differentiating the total potential energy respect to the atomic displacement,

$$\vec{F}_i(\vec{R}_L)=-\frac{\partial E_{pot}}{\partial\vec{u}_i(\vec{R}_L)}=-\sum_{\vec{R}_{L'},j}C_{i,j}(\vec{R}_L,\vec{R}_{L'})\cdot\vec{u}_j(\vec{R}_{L'}) . \tag{1.34}$$

Inserting Eq. (1.34) into the classical equation of motion $\vec{F}=m\vec{a}$ one has

$$M_i\ddot{\vec{u}}_i(\vec{R}_L)=-\sum_{\vec{R}_{L'},j}C_{i,j}(\vec{R}_L,\vec{R}_{L'})\cdot\vec{u}_j(\vec{R}_{L'}), \tag{1.35}$$

with the atomic displacement

$$\vec{u}_i(\vec{R}_L)=\frac{1}{\sqrt{M_i}}\vec{u}_i\cdot e^{i\vec{q}\cdot\vec{R}_L-i\omega t} . \tag{1.36}$$

Here $\vec{q}$ is the wavevector in the first BZ that is decided by the periodic boundary conditions. The frequency ω describing lattice vibrations at phonon $\vec{q}$, is known as the phonon frequency. Combining Eqs. (1.24) and (1.35) the phonon frequency is

$$\omega^2\vec{u}_i(\vec{R}_L)=\sum_j\widetilde{D}_{i,j}(\vec{q})\cdot u_i(\vec{R}_L) , \tag{1.37}$$

with

$$\widetilde{D}_{i,j}(\vec{q})=\frac{1}{\sqrt{M_iM_j}}\sum_{\vec{R}_{L'}}C_{i,j}(\vec{R}_L,\vec{R}_{L'})\cdot e^{-i\vec{q}\cdot\vec{R}_L} . \tag{1.38}$$

Using calculated inter-atomic force constants by DFPT, the phonon frequency at

arbitrary wavevector $\vec{q}$ in the first BZ can be obtained (Fig 1.5). With recent rapid development of computational power, it is now possible to calculate accurate phonon band structures of solids containing several tens of atoms in a unit cell with very fine meshes of wavevectors $\vec{q}$ (phonon q-points). Fig. 1.5 shows a calculated phonon band structure of the candidate *Cmcm* structure of high-pressure III H_2 with each unit cell containing 24 atoms [44]. From calculated phonon band structures, several other properties of the system, such as vibrational energies, heat capacities, and electron-phonon couplings can be calculated.

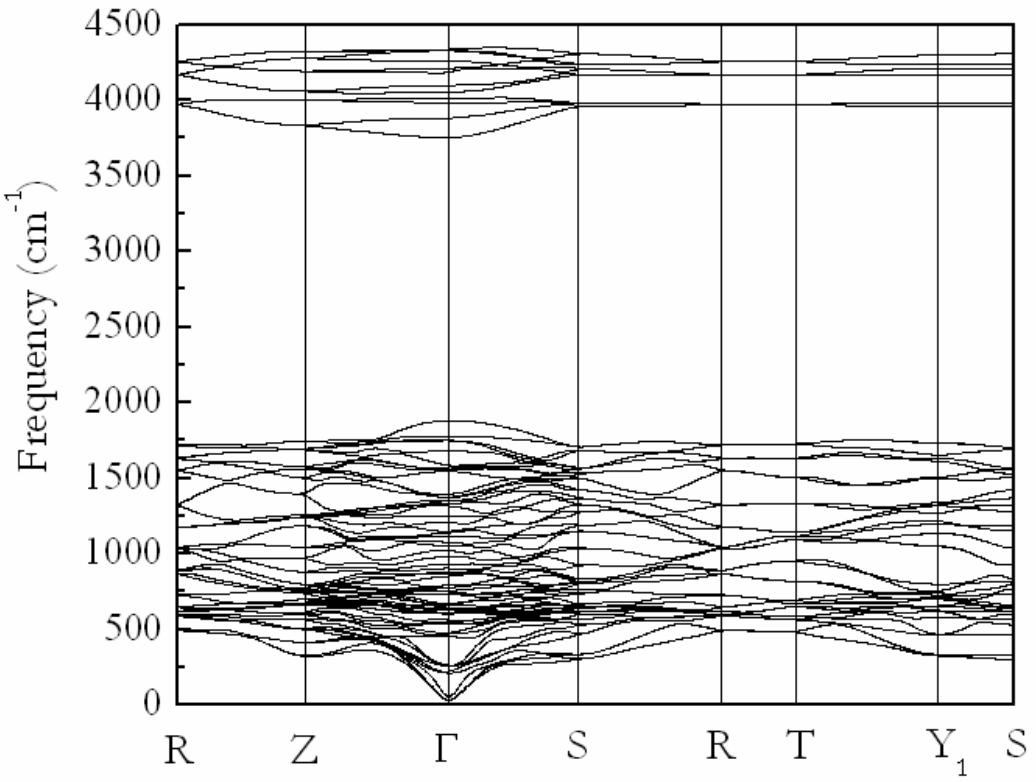

Figure 1.5. The phonon band structure of the *Cmcm* structure of H_2 along several high-symmetry lines in the first BZ calculated at 150 GPa [44].

3. Optical properties for high-pressure solids.

Electromagnetic (EM) radiation interacts in several ways with the crystal solids. For an insulating solid, and considering frequencies of incident EM fields in the vibrational range, phonons are the predominant cause of features in absorption or reflection spectra. Two experimental techniques are commonly used for phonon spectroscopy with the EM fields, infrared (IR) and Raman spectra [45, 46]. Both these two spectra can be modeled within the framework of DFPT. The phonon frequencies only need to be calculated at the center of the first BZ. For IR spectrum, the crystal lattice absorbs radiation by virtue of changes in its electric dipole moment. The frequency of the dipole oscillations must be equal to the frequency of the incident EM radiation for the absorption to occur. Essentially only two physical parameters need to be calculated, the normal-mode eigenvectors and Born effective charges. A normal-mode eigenvector describe the polarization of a vibrational mode, which can be calculated though the linear response method described above. Born effective charge is the second derivative of the electric enthalpy subjected to the macroscopic electric field,

$$Z^*_{i,\alpha,\beta} = -\frac{\partial^2 \widetilde{F}(\vec{\varepsilon})}{\partial \varepsilon_\beta \partial \vec{u}_{i,\beta}}, \tag{1.39}$$

where $\widetilde{F}(\vec{\varepsilon})$ is the electric enthalpy in the present of macroscopic electric field $\vec{\varepsilon}$. The $\vec{u}_{i,\beta}$ is the atomic displacement of the *i*-th atom along Cartesian direction β. The second derivatives can be calculated straightforwardly from the DFPT. For Raman spectra, the incident photos interact with the zone center phonons through the change of polarizability of the system. To model Raman spectra, instead of Born effective charges, the Raman tensors need to be calculated. Raman tensor is the first derivative of the polarizability tensor and hence the third derivative of the electric enthalpy, *i.e.*,

$$T^m_{\alpha,\beta} = \frac{\partial \alpha_{\alpha,\beta}}{\partial q^m}, \tag{1.40}$$

where q^m is the normal coordinates associated with the m-th vibrational mode. The polarizability tensor $\alpha_{\alpha,\beta}$ is the second derivative of the electric enthalpy subjected to the macroscopic electric field,

$$\alpha_{\alpha,\beta} = -\frac{\partial^2 \widetilde{F}(\varepsilon)}{\partial \varepsilon_\alpha \partial \varepsilon_\beta}. \tag{1.41}$$

The DFPT can be extended to handle this third derivative of the total energy through the 2n+1 theorem. A detailed description of modeling IR and Raman spectra will be presented in Chapter 3.

For EM radiation with higher energy, such as X-ray and high energy electrons, core electrons in the crystal lattice are able to gain enough energy to be excited to unoccupied electronic states in the conduction band. The corresponding techniques, namely X-ray emission spectroscopy (XES), X-ray absorption spectroscopy (XAS), and electron energy loss spectroscopy (EELS), are widely used crystallographic techniques to probe electronic states of materials [47-49]. These spectra can be modeled numerically by the DFT as well. For example, XAS describe the transition of an electron from core states into empty lower unoccupied states. The absorption cross section is given by the Fermi golden rule as a sum of probabilities per unit of time of making a transition from an initial state to an unoccupied final state through an interaction Hamiltonian:

$$\sigma(\omega) = 4\pi^2 \alpha_0 \hbar\omega \sum_f |< \psi_f \mid \hat{O} \mid \psi_{core} >|^2 \delta(E_f - E_{core} - \hbar\omega), \tag{1.42}$$

where α_0 is the fine structure constant. The $\hbar\omega$ is the energy of the incident photon, which should match the energy difference E_f-E_{core} between the initial and final electronic states $|\Psi_{core}>$ and $|\Psi_f>$. The $<\Psi_f \mid \hat{O} \mid \Psi_{core}>$ is the matrix element of the transition between the initial and final states. The band energy E_f can be directly calculated from the DFT. The all-electron eigenstates of $|\Psi_{core}>$ and $|\Psi_f>$ can also be accurately evaluated from the extension of the DFT method using the projector augmented wave

(PAW) approach [50, 51]. A detailed description of modeling XAS will be presented in Chapter 5.

1. 3 Description of this thesis

The objective of this thesis is to investigate the distinct physical and electronic properties of high-pressure solids, through state-of-the-art first-principles numerical computations. In this aspect, various properties such as crystal structures, phase transitions, electronic structures, vibrational properties, lattice dynamics, IR spectrum, Raman spectrum, XAS, electron-phonon coupling, and superconducting properties of selected high-pressure materials were investigated. To explore and design new materials, a method combining recently proposed genetic algorithm for crystal structure prediction and first-principles structural optimizations was used to determine/predict candidate structures of materials at high pressure [52-56]. A first-principles computer code [57] was developed for calculation of XAS within the framework of DFT, employing the PAW method. The theoretical tools used are mainly density functional theory, density functional perturbation theory, PSPW methods, projector augmented wave method, and Migdal-Eliashberg theory [58-61]. The DFT and DFPT calculations were mainly performed using the first-principles software including Quantum-ESPRESSO [62], VASP [63], and SIESTA [64]. The following gives a brief description of Quantum-ESPRESSO and VASP packages.

1. Quantum-ESPRESSO package

Quantum-ESPRESSO stands for *Open Source Package for Research in Electronic Structure, Simulation, and Optimization*. It is an integrated suite of first-principles codes for electronic structure calculations and material modeling based on PSPW DFT and DFPT. A distinct advantage of Quantum-ESPRESSO package is that it is implemented for both norm-conserving [65] and ultrasoft [66] pseudopotentials and more recently, the PAW potential [51]. The availability of ultrasoft pseudopotential

makes the treatment of complicated crystal structures feasible. The DFT component of Quantum-ESPRESSO, along with the VASP package (see below), has been used to perform structural optimizations, calculate band energies, and construct phase diagrams of candidate structures. The DFPT component of Quantum-ESPRESSO has been used to calculate phonon band structures, acoustic sum rules, effective changes, Raman tensors, and electron-phonon coupling.

2. VASP package

VASP stands for *Vienna Ab-initio Simulation Package*. It is a first-principles package to perform electronic calculations through quantum mechanical molecular dynamics (MD) using PSPW DFT. The MD approach implemented in VASP is based on a finite-temperature LDA and an exact evaluation of the instantaneous electronic ground state at each MD step using efficient matrix diagonalization schemes and an efficient Pulay mixing. The advantage of the VASP package is that the Blöchl's PAW electronic method has been implemented [50, 51]. The PAW potential, in principle, is an all–electron potential and therefore allows the calculation all-electron properties from pseudopotential-based schemes by reconstructing all-electron wavefunctions from the pseudo wavefunctions. The PAW potential also allows the core orbitals to adjust under extreme pressure.

This thesis is composed of five chapters. For Chapters 2 to 5, each chapter describes research on a distinct topic and contains the motivation, theoretical formulations, computational methods and applications for selected high-pressure materials. Chapter 6 presents a summary and perspectives. A synopsis of Chapters 2 to 5 is given below.

Chapter 2. Superconductivity in simple high-pressure solids.

The superconducting properties of several high-pressure solids were investigated based on the Migdal-Eliashberg theory [58-61] within the framework of the BCS model

[67]. The selected materials, Li, Xe, and Group IV hydrides, each represents a group of chemically distinct system. Alkali metal Li, at ambient conditions behaving like a nearly free-electron gas, has been found to be superconducting with T_c up to 17 K under pressure [68-71]. In this chapter, the pressure-induced phase transition face centered cubic (FCC) → *cI*16 in Li and the superconducting properties in the FCC and *cI*16 phases are investigated. It is found that both phases are superconducting. The estimated T_c for the FCC phase increases with pressure until it reaches the transition to the *cI*16 phase where T_c decreases abruptly. Noble gas Xe is well known for being chemically inert at ambient pressure. However, under pressure, it is predicted that solid Xe can be a superconductor albeit with a comparatively low T_c of ~ 0.04 K [72]. Two Group IV hydrides, SiH_4 and SnH_4, were predicted to be good superconductors under high pressure [73-77]. This is because that the hydrogen atoms are pre-compressed by heavier Group IV atoms and possess high-frequency vibrations. This prediction is supported by the recent experiment on SiH_4, in which the pressure-induced superconducting state was found and a T_c up to at least 17 K was observed [78]. To assist calculations and analyze results on phonons, we have developed a computer program on calculation of projected phonon density of states (DOS) on each atom (Appendix 1).

Chapter 3. Vibrational spectra and electronic structures of high-pressure materials.

The IR and Raman spectra for several new resolved/proposed structures of three materials at high pressure, dense H_2, O_2, and SiH_4, were investigated using the first-principles PSPW calculations within the framework of DFPT. The Bader's atoms in molecules (AIM) method [79-81] was used to characterize electron topology and bonding of $(O_2)_4$ clusters in the newly discovered *C*2/*m* structure of the high-pressure ε phase [82, 83] of solid O_2. For solid H_2, the objective was to examine the two candidate structures of the high-pressure phase III, the *Cmcm* structure and the *C*2/*c* structure proposed very recently [84-86]. Both structures have similar structural features. The Raman and IR spectra as well as the detailed phonon stability of both structures were examined. Comparison of the calculated Raman spectra and the pressure dependence of the IR intensity the structure of phase III of solid hydrogen can be unambiguously assigned to

the *C*2/*c* structure. For O_2, the experimental structure and vibrational spectra (IR and Raman) of the new resolved *C*2/*m* structure of the high-pressure ε phase were well reproduced via DFT using GGA [87]. The interactions in two competing structures, the theoretically proposed *Cmcm* chain structure and observed cluster *C*2/*m* structure were analyzed with the AIM method. A candidate structure for the metallic and superconducting ζ phase is proposed and discussed [88]. For SiH_4, the Raman spectrum of the theoretically predicted $P4_2/nmc$ structure of the high-pressure insulating phase was calculated and compared with experimental data. The good agreement between the calculated spectrum and experiment indicates that the *P*42/*nmc* structure can be a candidate structural model for the high-pressure insulating phase of SiH_4.

Chapter 4. High-pressure crystal structure prediction via genetic algorithm.

Theoretical methods for the prediction of unknown high-pressure crystal structures usually involve dynamical processes that depend strongly on the initial guesses of atomic configurations [10]. In this chapter, we employed an alternate approach based on a recently proposed genetic algorithm [52-56]. The focus is to predict stable and meta-stable structures at high pressure without any preference on initial structures. In the evolutionary procedures, randomly generated structures evolve gradually into lower energy phases after a few generations. The high-pressure structures of calcium were investigated and two new stable structures that might explain the diffraction pattern of the Ca-IV and Ca-V phases were predicted [89]. The high-pressure phase II and phase III of AlH_3 were also investigated, and structures were successfully predicted for each phase [90]. Another example presented in this chapter is the prediction of a metastable single-bonded phase of nitrogen [52]. All the calculations reported in this chapter were performed with a software package ASAP (Advanced Structure seArching Package) developed by the author. A user's guide for ASAP is presented in Appendix B.

Chapter 5. Ab initio X-ray adsorption spectroscopy.

A numerical algorithm is developed for the calculation of XAS within the

framework of DFT, employing the PAW method. The dipole approximation is used, but higher-order multipoles can be easily accounted for and included in the calculation. Validation tests were performed on the carbon, silicon, and oxygen *K*-edge XAS of diamond, fullerene C_{60}, α-quartz and water molecules [57]. The new results are compared with experiments and other calculations already available in the literature. The present approach provides a straightforward framework for the investigation of single particle core hole and electron screening effects, which have been demonstrated to be significant for all investigated materials [91-93]. Significant improvements have been observed in the spectra by simulating the excitation process using both the Z+1 and core hole approaches. In collaboration with the National Simulation Center of the Italian Istituto Nazionale per la Fisica della Materia (DEMOCRITOS), we have coded this method and implemented it into the Quantum-ESPRESSO package [62].

In Chapter 6, the research projects and major conclusions are summarized, with discussions on perspectives and possible directions for future work.

CHAPTER 2

Superconductivity in simple high-pressure materials

In the words of Edward Teller [94], "Under special circumstances, it may be possible to observe an unusual phenomenon: a superconducting state which exists only at high temperatures." These words although remain largely unfulfilled; however, as highlighted by recent experimental studies, superconductivity is ubiquitous in high-pressure materials [95]. At high pressure, most materials become unstable and transform into new structures of higher densities. Many of these new structures are superconducting; despite the fact that sometimes, the materials are not even metallic at ambient pressure. The theoretical prediction and subsequent experimental confirmation of elemental Si (a semiconductor under ambient condition) with a fairly high superconducting critical temperature T_c of 9 K at 15 GPa (Si-V) over 20 years ago was a remarkable feat [96, 97]. Over the years, more solids have been found to be superconducting under high pressure. This list includes insulating and metallic elements and even ionic solids. Elemental Li has a T_c up to 17 K at 37 GPa [69-71]. Recently, the value of T_c of Ca at 160 GPa was found to be surprisingly high at 25 K [98-101]. The superconducting behavior has been found even in the ionic compound CsI [102].

The observation of superconductivity in simple solids at high pressure possesses a challenge to conventional understanding such as the Matthias rule [103], which states that the occurrence of superconductivity is most favorable in systems having (1) *d*-electrons, (2) high symmetries, and (3) high valence electron density. Li, having only one valence electron and in many circumstances behaving like a nearly free-electron gas, is the 'simplest' metal but becomes superconductive below 0.04 mK under ambient pressure

[104, 105]. Recent experiments show that under high pressure, however, this free-electron like character changes radically in Li and leads to superconducting states with T_c up to 17 K [69-71]. What can possibly lead to more than a five order of magnitude increase in T_c when Li is still in a simple, monatomic phase? Are the existing superconducting theories able to explain the mechanism of this startling observation? With recent advancement in computational power and the reliability of first-principles calculations based on the DFT, it is now possible to evaluate the electron-phonon coupling (EPC) strength and to estimate T_c with a fair degree of accuracy [62]. In this chapter, numerical simulations were employed to study the pressure-induced FCC→*cI*16 transition and superconductivity in both phases.

Pressure-induced superconductivity was observed in compressed compound CsI, which has a T_c of 2K at 180 GPa [102]. Considering that both pure iodine and cesium are also superconducting under high pressure, it leads to an interesting question: can solid Xe be superconducting as well, as the Xe atom is isoelectronic with Cs+ and I− ? In fact, solid Xe can be a promising candidate since it is the heaviest noble gas atom with the lowest metallization pressure and possesses low-frequency lattice vibrations that may help promote phonon-mediated superconductivity [106-110]. In this chapter, the possibility of superconductivity of solid Xe under high pressure has been studied by first-principles calculations. It was found that solid Xe could be superconducting at pressure above 150 GPa albeit with a comparatively low T_c of ~ 0.04 K.

The most fascinating pursue is searching for superconductivity in pure hydrogen, which has been predicted to become superconducting at high pressure with an extraordinary high T_c [73, 111]. However, the goal of producing metallic hydrogen in solid phase remains elusive, despite enormous experimental efforts up to 342 GPa [112-114]. The superconductivity found in dense Li brings new hopes to this topic since it is the superconducting element closest to hydrogen. In this chapter, it will be demonstrated that the metallization of hydrogen can be achieved in an alternative approach. This work has been motivated by the recently reported proposals that instead of pure hydrogen, highly compressed hydrogen-rich molecules (hydrides) can be used to reach the

necessary hydrogen density for superconductivity at much lower pressure than with pure hydrogen [73, 74]. Considerably high T_c has been predicted in SiH_4 and SnH_4 compounds at high pressure [75, 76]. This prediction is supported by the recent experiment on SiH_4, in which the pressure-induced superconducting state was found successfully [78].

The research presented in this chapter provides a glimpse of the relevant properties that affect superconductivity in high-pressure materials. It was found that superconductivity is likely to occur in low-dimensional structures close to structural and dynamic instabilities, *i.e.*, with Fermi surface (FS) nesting and Kohn anomaly [76]. It was also shown that the simultaneous existence of flat and steep electronic bands close to the Fermi level together with soft phonon modes help promote EPC. These characteristic features have been observed in a large number of superconductors, for example, the solid Li, Xe, SnH_4, and even C_{60} fullerene [115]. It is hoped that this understanding of superconducting mechanism in high-pressure solids can be extended to other chemical systems, thus providing a practical guide for design of better superconducting materials.

2. 1 The pairing theory of superconductivity—The BCS theory

Superconductivity represents a remarkable many-body phenomenon where quantum coherence effects are manifest at the macroscopic scale. The first successful theoretical understanding of superconducting states was proposed by Bardeen, Cooper and Schrieffer (BCS) from variational principle [67]. The theory provides a theoretical framework to explain other novel features of superconductivity, such as the Meissner or isotope effects. The key concept of the BCS theory is that electrons with opposite momenta and spins close to the Fermi level form a pair (Cooper pair) [116]. All these pairs move in a single coherent motion, leading to the formation of a superconducting state. The pairing of electrons is caused by small attractive interactions resulting from coupling with lattice vibrations. This attractive interaction, usually called the EPC, may

be viewed as two electrons coupled by a virtual exchange of phonons (Fig. 2.1). If the strength of EPC overcomes that of electron-screened Coulomb repulsion, the net interaction is attractive and superconductivity occurs. In the presence of attractive interactions, the FS shows the instability towards formation of bound-pairs of electrons, and stabilizes the system by a second order transition to superconducting states. There are three key ingredients in the BCS theory; EPC, Coulomb repulsion, and the instability at the Fermi surface.

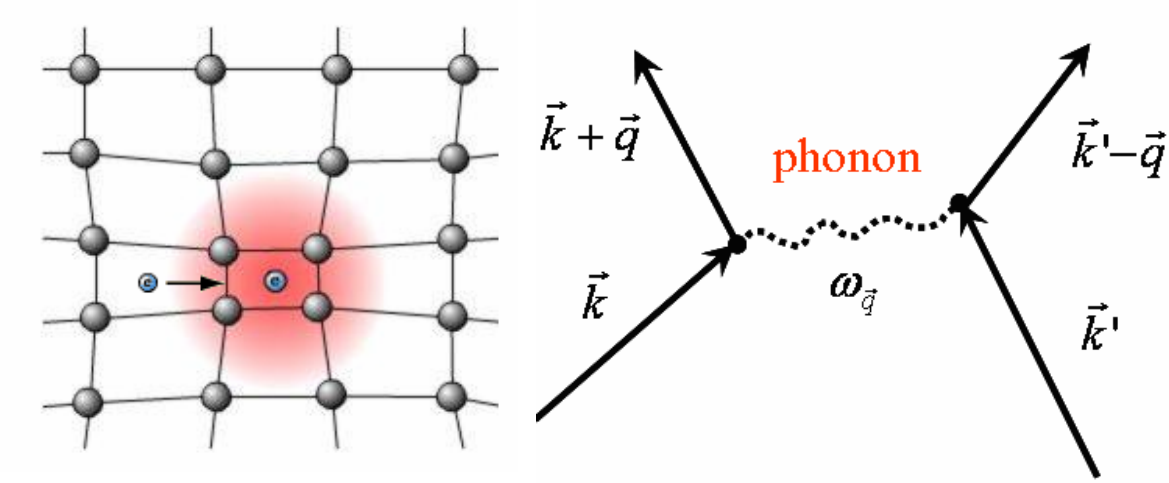

Figure 2.1. (Left) The model of attractive interaction between two electrons in a Cooper pair. A passing electron attracts the ions, causing a slight lattice deformation and locally accumulated positive charges, which attracts another electron. (Right) The Cooper pair interaction. Lattice vibration is described by a phonon with wavevector $\vec{q}$ and frequency $\omega_{\vec{q}}$. The two electrons with momentum $\vec{k}$ and $\vec{k}'$ are coupled via exchange of this phonon.

To describe the ground state of a superconductor, the variational wavefunction in the BCS theory is written as a superposition of the Cooper pair states with all possible number of pairs [67],

$$\left|\Psi_{BCS}\right\rangle = \prod_{\vec{k}} (u_{\vec{k}} + v_{\vec{k}} a^{+}_{\vec{k}\uparrow} a^{+}_{-\vec{k}\downarrow})\left|0\right\rangle . \tag{2.1}$$

The operator $a^{+}_{\vec{k}\uparrow} a^{+}_{-\vec{k}\downarrow}$ creates a pair of electrons with opposite momenta and spins. The parameters $v_{\vec{k}}$ and $u_{\vec{k}}$ are the probability amplitudes of a pair created or annihilated in this state, which are chosen to minimize the expectation energy of the Hamiltonian,

$$\hat{H}_{BCS} = \sum_{\vec{k},\sigma} \varepsilon_{\vec{k}} c^{+}_{\vec{k},\sigma} c_{\vec{k},\sigma} + \sum_{\vec{k},\vec{k}'} V(\vec{k},\vec{k}') \cdot c^{+}_{\vec{k},\uparrow} c^{+}_{-\vec{k},\downarrow} c_{-\vec{k}',\downarrow} c_{\vec{k}',\uparrow} , \tag{2.2}$$

subject to the condition that the average number of electrons is fixed. Here $V(\vec{k},\vec{k}')$ is the interaction leading to the transition of a pair of electron from the state $(\vec{k}\uparrow, -\vec{k}\downarrow)$ to $(\vec{k}'\uparrow, -\vec{k}'\downarrow)$. The $\varepsilon_{\vec{k}}$ is the kinetic energy of an electron in state $\vec{k}$. The wavefunction $\left|\Psi_{BCS}\right\rangle$ is normalized by the requirement that $v_{\vec{k}}^2 + u_{\vec{k}}^2 = 1$. One can represent these two parameters in terms of a single phase,

$$u_{\vec{k}} = \sin\theta_{\vec{k}} , \tag{2.3}$$

$$v_{\vec{k}} = \cos\theta_{\vec{k}} . \tag{2.4}$$

The angle $\theta_{\vec{k}}$ represents the probability that the state $\vec{k}$ is occupied by a Cooper pair. Minimizing the total energy yields the following relations:

$$2u_{\vec{k}} v_{\vec{k}} = \sin 2\theta_{\vec{k}} = \frac{\Delta_{\vec{k}}}{\sqrt{\Delta_{\vec{k}}^2 + \xi_{\vec{k}}^2}} , \tag{2.5}$$

$$v_{\vec{k}}^2 - u_{\vec{k}}^2 = \cos 2\theta_{\vec{k}} = -\frac{\xi}{\sqrt{\Delta_{\vec{k}}^2 + \xi_{\vec{k}}^2}} , \tag{2.6}$$

with $\xi_{\vec{k}} = \varepsilon_{\vec{k}} - \mu$. The μ is the chemical potential. The $\Delta_{\vec{k}}$ is the order parameter. The $\Delta_{\vec{k}}$ and μ are determined self-consistently from the BCS gap equation,

$$\Delta_{\vec{k}} = -\frac{1}{\Omega}\sum_{\vec{k}'} V(\vec{k},\vec{k}')\sin 2\theta_{\vec{k}} \,. \tag{2.7}$$

Here Ω is the volume of the system. The total energy of the ground state is therefore,

$$E^0_{BCS} = -2\sum_{\vec{k}} v^4_{\vec{k}} \sqrt{(\Delta^2_{\vec{k}} + \xi^2_{\vec{k}})} \,. \tag{2.8}$$

BCS made a simplifying assumption that the $V(\vec{k},\vec{k}')$ is isotropic and exists only for the electrons in a narrow shell around the Fermi level [116],

$$V(\vec{k},\vec{k}') = V \quad \text{for } \left|\varepsilon_{\vec{k}}\right|, \left|\varepsilon_{\vec{k}'}\right| \le \hbar\omega_D \,, \tag{2.9}$$

$$V(\vec{k},\vec{k}') = 0 \quad \text{elsewhere,} \tag{2. 10}$$

where ω_D is the Debye frequency. Thus, the order parameter $\Delta_{\vec{k}}$ becomes a constant as well,

$$\Delta_{\vec{k}} = \Delta \,. \tag{2.11}$$

The energy required to break up a Cooper pair and excite an electron from state $\vec{k}'$ to an unoccupied state is

$$\Delta E = 2\sqrt{\Delta^2 + \xi^2_{\vec{k}'}} \,. \tag{2.12}$$

Since the $\varepsilon_{\vec{k}'}$ can be arbitrarily close to the Fermi level, the minimum energy required to break up a Cooper pair is 2Δ, and Δ is the superconducting energy gap.

The materials studied in this chapter can have quite high T_c even comparable to that of the so-called high-T_c superconductors [117, 118]. Unlike unconventional high-T_c superconductors, the superconductivity investigated in this thesis is driven by electron-phonon interactions. Thus, it is appropriate to employ the conventional BCS theory to study these materials.

2. 2 Superconducting critical temperature T_c from first-principles

The Migdal-Eliashberg theory is an extension of the BCS theory to the strong coupling regime [58-61]. It is a formalism relating the microscopic superconducting theory to the observed superconducting critical temperature T_c. In the Migdal-Eliashberg theory, the strength of attractive electron-phonon interactions is characterized by the EPC parameter λ. The repulsive electron-screened Coulomb interaction is represented by the Coulomb pseudopotential μ^*. The conventional BCS theory assumes the simplest form of the attractive interaction among electrons, where the strength of interaction is a constant and exists only within the Debye energy of the Fermi level (Eqs. (2.9) and (2.10)) [116]. On the other hand, the Migdal-Eliashberg theory incorporates all existing modes of electron-phonon interactions at all frequencies. The EPC is characterized for each phonon branch and every phonon frequency, which are solely determined by the lattice dynamics of the material.

The full description of the superconducting state can be derived from the Eliashberg spectral function $\alpha^2F(\omega)$ [119],

$$\alpha^2F(\omega) = \frac{1}{2\pi N(\varepsilon_F)} \sum_{\vec{q}j} \frac{\gamma_{\vec{q}j}}{\omega_{\vec{q}j}} \delta(\omega - \omega_{\vec{q}j}) w(\vec{q}) . \tag{2.13}$$

Here $\omega_{\vec{q}j}$ is the phonon frequency of mode ($\vec{q}j$) (detailed description is presented in section 1. 2), and $w(\vec{q})$ is the weight of phonon point $\vec{q}$ in the first BZ. The $N(\varepsilon_F)$ is the DOS at the Fermi level ε_F. The sum is taken over the complete q-point mesh in the first BZ and all phonon branch j. The $\gamma_{\vec{q}j}$ is the phonon linewidth of mode ($\vec{q}j$), which is defined as

$$\gamma_{\vec{q}j} = 2\pi\omega_{\vec{q}j} \sum_{nm} \int \frac{d^3\vec{k}}{\Omega_{BZ}} | g^{j}_{\vec{k}n,\vec{k}+\vec{q}m} |^2 \delta(\varepsilon_{\vec{k}n} - \varepsilon_F)\delta(\varepsilon_{\vec{k}+\vec{q}m} - \varepsilon_F), \qquad (2.14)$$

where the volume integral is taken over the first BZ. The $\varepsilon_{\vec{k}n}$ and $\varepsilon_{\vec{k}+\vec{q}m}$ are the Kohn-Sham eigenvalues with wavevectors $\vec{k}$ and $\vec{k}+\vec{q}$ in the n-th and m-th band. The $g^{j}_{\vec{k}n,\vec{k}+\vec{q}m}$ is the electron-phonon matrix element determined from the linearized self-consistent potential.

The Eliashberg spectral function $\alpha^2F(\omega)$ describes the contributions to the total EPC of the system from various regimes of vibrational frequencies. It is an observable that can be measured by tunneling experiments. In theory, $\gamma_{\vec{q}j}$ and hence $\alpha^2F(\omega)$ can be calculated from the EPC strength $\lambda_{\vec{q}j}$ of each phonon mode ($\vec{q}j$):

$$\lambda_{\vec{q}j} = \gamma_{\vec{q}j} / \pi\hbar N(\varepsilon_F)\omega^2_{\vec{q}j}. \qquad (2.15)$$

With rapid development of computational power and numerical methods, it is now possible to calculate $\alpha^2F(\omega)$ from first-principles. In simple metals, first-principles calculations of $\alpha^2F(\omega)$ have been performed for Al, Pb, and Li [120]; for Al, Cu, Mo, Nb, Pb, Pd, Ta, and V [121, 122]; and for Al, Au, Na, and Nb [123]. As an example, Fig. 2.2 shows the calculated results of $\alpha^2F(\omega)$ for eight simple metals [121, 122] compared with experimental data. The average effect of attractive interaction in the system is

represented by the EPC parameter λ, which is a weighted average of $\alpha^2 F(\omega)$ over entire vibrational regime,

$$\lambda = 2\int_0^\infty \frac{\alpha^2 F(\omega)}{\omega} d\omega = \sum_{\vec{q}j} \lambda_{\vec{q}j} w(\vec{q}) . \tag{2.16}$$

Namely in terms of the EPC strength $\lambda_{\vec{q}j}$ projected on each mode ($\vec{q}j$), λ is approximated by a weighted average of $\lambda_{\vec{q}j}$ for all vibrational modes ($\vec{q}j$) in the first BZ.

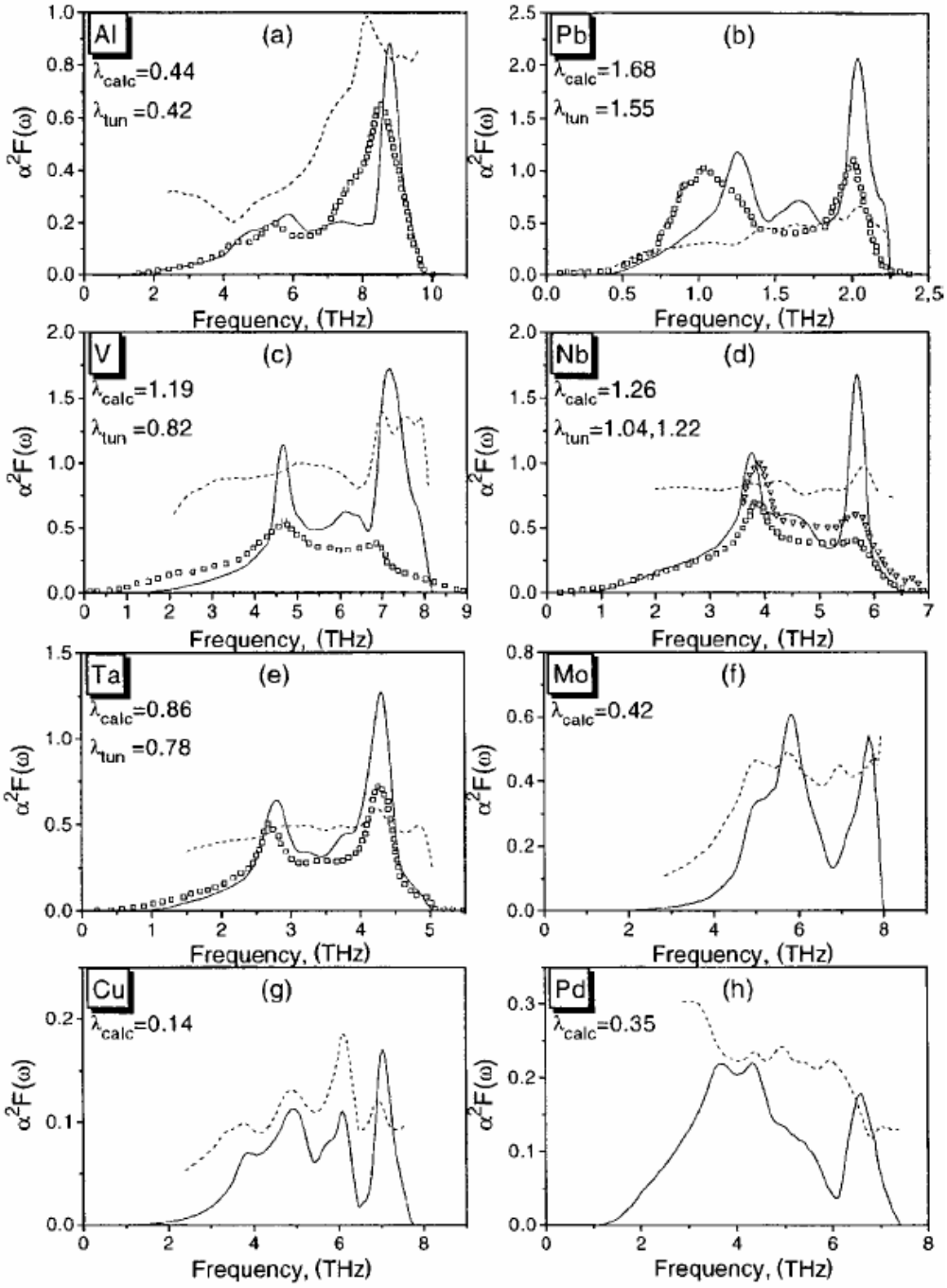

Figure 2.2. Eliashberg spectral functions $\alpha^2 F(\omega)$ for eight elemental metals [121, 122]. Solid curves, calculated data; dashed curves, behavior of the electron-phonon pre-factor $\alpha^2(\omega)$ [defined simply as the ratio $\alpha^2 F(\omega)/F(\omega)$]. Symbol plots are the results of available tunneling experiments.

Once $\alpha^2F(\omega)$ is obtained, superconducting critical temperature T_c can be calculated by solving the Eliashberg gap equations with the knowledge of Coulomb pseudopotential μ^*. General reviews of solving the Eliashberg gap equations can be found in the works of Eliashberg, [58]; Schrieffer, [116]; Scalapino, [124]; McMillan and Rowell, [125]; and the more recent review of Carbotte, [119]. Solving the Eliashberg gap equations is a complicated task. For a qualitative understanding, McMillan constructed a simplified equation relating T_c and $\alpha^2F(\omega)$, often referred to as the McMillan equation [103]. The original form of the McMillan equation is

$$T_c = \frac{\omega_D}{1.45}\exp\left[-\frac{1.04(1+\lambda)}{\lambda-\mu^*(1+0.62\lambda)}\right]. \tag{2.17}$$

The original McMillan equation was found to be accurate for materials with $\lambda < 1.0$ but not appropriate for larger value of λ. The most successful modification of the McMillan equation was made by Allen and Dynes [126, 127], who extended the equation to the large λ regime:

$$T_c = \frac{\omega_{\log}}{1.2}\exp\left[-\frac{1.04(1+\lambda)}{\lambda-\mu^*(1+0.62\lambda)}\right], \tag{2.18}$$

where $\omega_{\log}$ is the logarithmic average of phonon frequency,

$$\omega_{\log} = \exp\left[\frac{2}{\lambda}\int_0^\infty \frac{d\omega}{\omega}\alpha^2F(\omega)\ln\omega\right]. \tag{2.19}$$

The Allen-Dynes modification of the McMillan equation Eq. (2.18) is a successful and widely used equation for the estimation of T_c.

Two of the three ingredients in the Allen-Dynes modification of the McMillan equation, λ and $\omega_{\log,}$ can be derived readily from the knowledge of $\alpha^2F(\omega)$ (Eqs. (2.16)

and (2.19)). The other ingredient, the Coulomb pseudopotential μ^*, is approximated by rescaling the normal Coulomb repulsion parameter μ to include retardation effects [128]:

$$\mu^* = \mu/[1+\mu\ln(T_F/\Theta_D)], \tag{2.20}$$

where T_F and Θ_D are the Fermi and Debye temperatures. The Coulomb repulsion parameter μ depends on the configuration of nuclei and is difficult to evaluate from first-principles [129]. Thus in practice, the empirical value of μ^* between 0.10-0.13 are widely used [73]. Without knowing μ, an approximate upper limit on μ^* can be calculated by setting μ to infinity [130, 131],

$$\mu^*_{\max} = 1/\ln(T_F/\Theta_D). \tag{2.21}$$

The Debye temperature Θ_D can be estimated from the semi-empirical equation [131]

$$\Theta_D = 1.4\frac{\hbar}{k_B}\sqrt{<\omega^2>}, \tag{2.22}$$

where $<\omega^2>$ is defined as

$$<\omega^2> = \frac{2}{\lambda}\int_0^\infty d\omega\omega\alpha^2F(\omega). \tag{2.23}$$

In this chapter, the superconducting properties of selected high-pressure materials will be investigated using the Migdal-Eliashberg theory briefly introduced above. The T_c of these materials was estimated using the Allen-Dynes modification of the McMillan equation Eq. (2.18). The vibrational frequency ω_{qj}, EPC strength λ_{qj}, and Eliashberg spectral function $\alpha^2F(\omega)$ were calculated with PSPW method within the framework of DFPT using the electronic structure package Quantum-ESPRESSO [62] (The description is presented in section 1. 3).

2. 3 Superconductivity in high-pressure Li

Contrary to the nearly free-electron behavior under ambient conditions, high-pressure phases of Li are expected to possess very different physical and electronic properties. X-ray diffraction experiments observed that Li transforms from ambient BCC structure to FCC structure around 7.5 GPa [132-133]. Further compression leads to a mixture of two structures, *hR*1 and *cI*16, at 39.8 GPa [68]. Initially, the *hR*1 structure is the dominant component, but gradually transforms to *cI*16 with increasing pressure and disappears at 42.5 GPa. There are evidences found in recent ac susceptibility and Raman spectroscopic studies that *cI*16 phase might further transform into a new phase around 50 GPa and stabilizes into another high-pressure polymorph above 62 GPa [71, 134]. A recent theoretical study, however, predicts that the *cI*16 phase is stable and until it transforms to an orthorhombic structure (*Cmca*-24) at pressure higher than 88 GPa [135]. Significantly, recent experiments have found that the high-pressure phases of Li are superconducting [69-71]. AC susceptibility measurement in nearly hydrostatic pressure cell uncovered several superconducting phase transitions [69]. It was found that the superconductivity first appears at 20.3 GPa with T_c increases rapidly from 5.4K to 14K at 30 GPa. Then T_c decreases with pressure until 50 GPa. At pressure higher than 50 GPa, T_c increases again and disappears abruptly at 62 GPa. A maximum in T_c has also been observed in early experiments under non-hydrostatic conditions but at a slightly higher pressure of 35 GPa [70, 71]. The observed changes in T_c have been attributed to structural transitions. At 30 GPa, it is understood as the FCC→*cI*16/*hR*1 transition. It is possible that at 50 GPa and 62 GPa, there were two successive phase transitions to new but unknown structures. Theoretical investigations of the pressure-induced superconductivity, however, have been focused on the FCC phase only [136-146]. The variation of T_c near the FCC → *cI*16 phase transition and in the *cI*16 phase has not been studied. In this section, the pressure-induced FCC→*cI*16 phase transition and superconductivity are investigated.

The enthalpies of Li in the FCC, *hR*1, *cI*16 and *Cmca*-24 phases have been calculated at different pressures. Total energy calculations were performed with the

program VASP [63] (The description of this program is presented in section 1. 3) using the PAW pseudopotential [147] (The description of the PAW method is presented in Chapter 5.) employing 1s2*s* as valence states. The LDA exchange-correlation functional is used. For the FCC and *cI*16 phases, a 24×24×24 *k*-point mesh was used. For the *hR*1 and *Cmca*-24 phases, a smaller 16×16×16 mesh was found to be sufficient. The calculated enthalpies as a function of pressure of the four polymorphs are compared in Fig. 2.3.

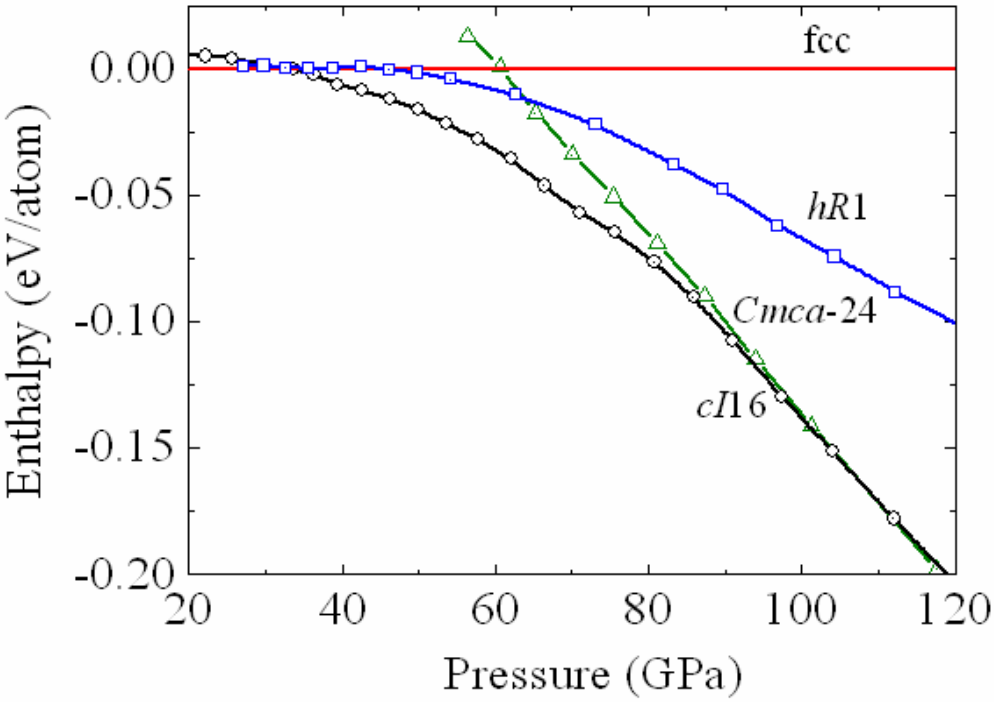

Figure 2.3. The enthalpies per atom for FCC Li, *hR*1 Li, *cI*16 Li and *Cmca*-24 Li as a function of pressure. The enthalpy for FCC Li is taken as a reference.

The enthalpy difference between *hR*1 and FCC phases is almost indistinguishable below 46 GPa. According to X-ray experiments at T=180K [68], the *hR*1 phase was found to co-exist with the *cI*16 phase in a narrow pressure range near the FCC→*cI*16 phase transition. However, the calculation of the phonon band structure of the *hR*1 structure at 33 GPa shows that it is unstable with a very large imaginary frequency. This

discrepancy suggests the possibility that the *hR*1 structure may be entropically stabilized and may not exist at low temperature. A piece of supporting evidence is that accurate ac susceptibility measurements at low temperature failed to observe any notable change in T_c within the pressure range where the FCC/*hR*1/*cI*16 are expected to co-exist [69]. Therefore, the *hR*1 structure was not considered further in this investigation. The *cI*16 phase becomes more stable than the FCC phase at around 33 GPa and up to 110 GPa, where the *Cmca*-24 phase becomes more stable. The calculated transition pressure of 33 GPa for the FCC→*cI*16 transition is close to a feature near 30 GPa observed in susceptibility experiment [69], indicating that the peak in T_c may be related to a structural change. On the other hand, the transition pressure predicted for *cI*16 →*Cmca*-24 at 110 GPa indicates that *Cmca*-24 phase is not a viable candidate for the unknown superconducting phase suggested to exist from 50 GPa to 60 GPa [134].

Phonons of the FCC phase have been obtained from linear-response theory [62]. Individual phonons were calculated on a 8×8×8 *q*-point mesh with a 16×16×16 *k*-point mesh used for the first BZ integrations. The phonon dispersions for FCC Li have been calculated within the pressure range 25-40 GPa. In agreement with previous studies [140, 141], a notable feature in the phonon band structure of the FCC phase is the gradual development of a soft transverse acoustic (TA) mode along the $\Gamma \rightarrow K$ direction with increasing pressure (Fig. 2.4 (a)). The soft mode was found to vanish at *ca*. 33 GPa. When the pressure is increased slightly to 34 GPa, an imaginary frequency of $50i$ cm^{-1} starts to appear, indicating that the FCC phase is now mechanically unstable. The calculated instability at 33 GPa is close to the predicted pressure for the FCC → *cI*16 phase transition from enthalpy calculations (Fig. 2.3). Quite obviously, the soft phonons are responsible for initiating the structural transition. It has also been shown to induce strong FS nesting and the significant enhancement of the EPC.

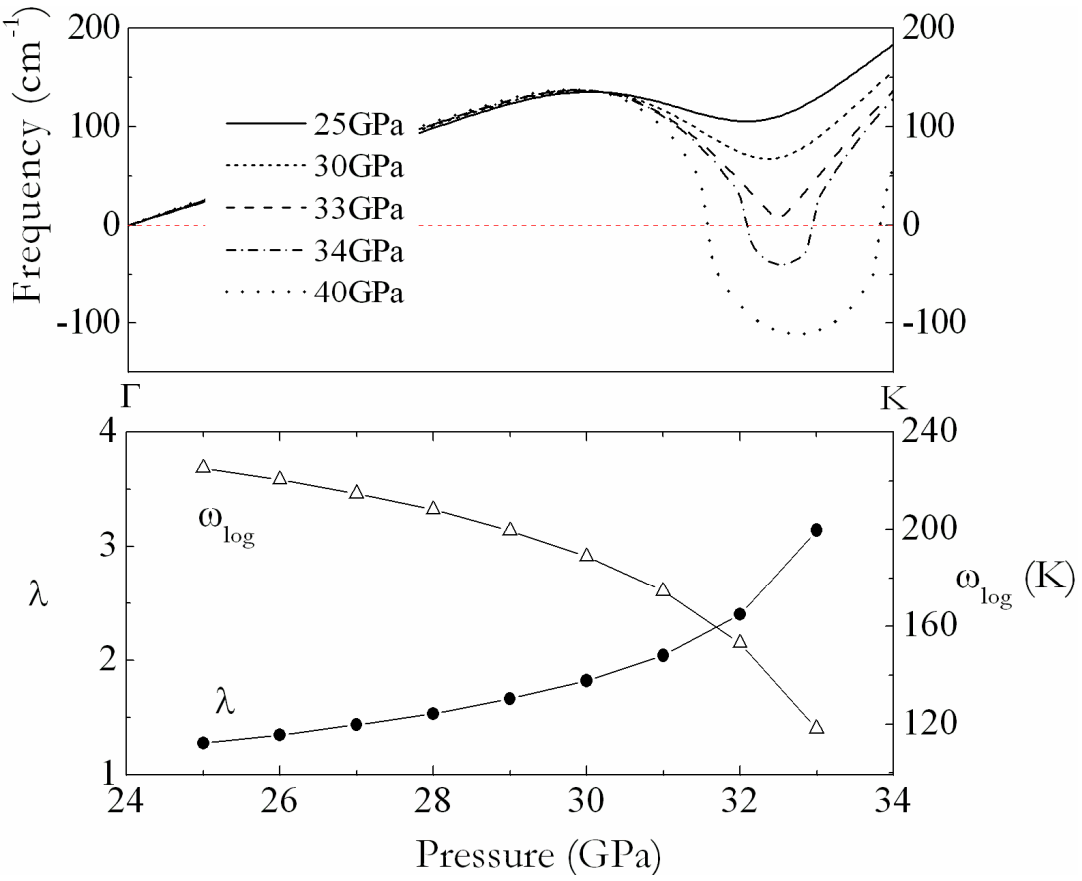

Figure 2.4. (a) The evolution of TA phonon branch for the FCC phase along the $\Gamma \rightarrow K$ direction, within the pressure range 25 GPa to 40 GPa. (b) The calculated λ and ω_{log} for the FCC phase as functions of pressure up to the critical point 33 GPa for the transition to *cI*16 phase.

An objective of this investigation is to rationalize the observed maximum T_c near the FCC $\rightarrow$ *cI*16 phase transition. In the experiment, T_c reaches a maximum and starts to decrease before transforming to the *cI*16 phase. The EPC of the FCC phase were analyzed in the pressure range 25 GPa to 33 GPa. The partial EPC parameters λ_{qj} have been computed in the first BZ on a 12×12×12 *q*-point mesh. Individual λ_{qj} at each *q*-point was calculated with a 32×32×32 *k*-point mesh. Before embarking on the discussion of T_c, the upper limit of μ^* at different pressures have been estimated from the Fermi and

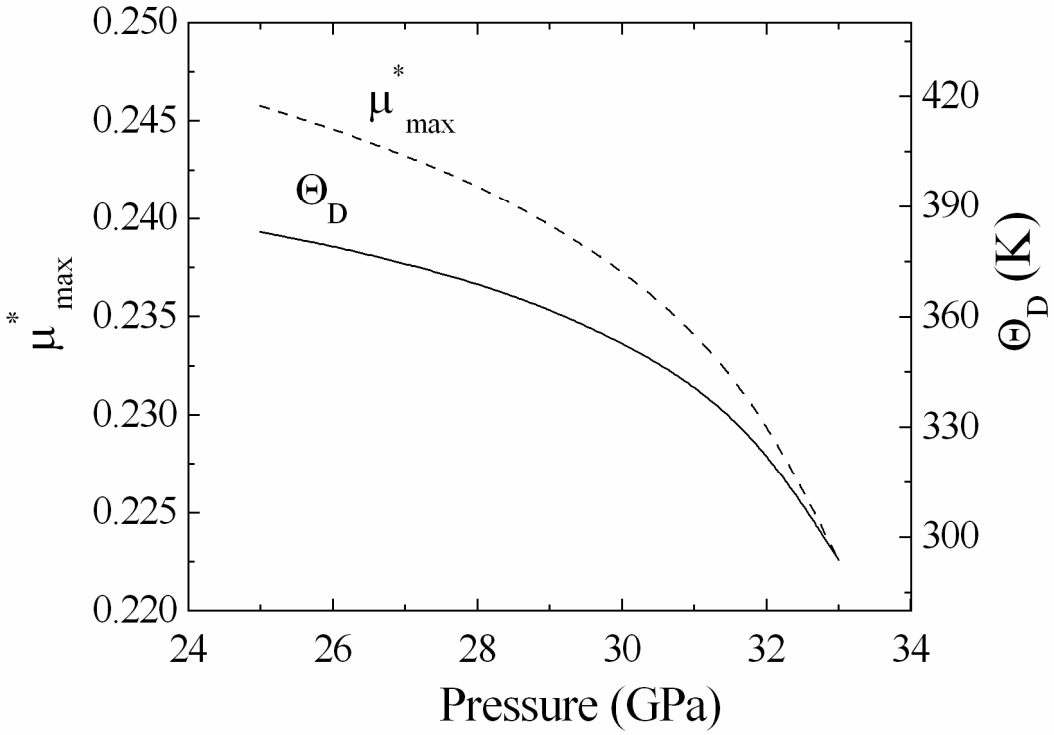

Figure 2.5. The estimated Debye temperature Θ_D and maximum possible value of μ^* for FCC Li as a function of pressure.

Debye temperatures, T_F and Θ_D using Eq. (2.21). It is found that T_F increases with pressure and Θ_D decreases with pressure (Fig. 2.5). As a result, μ^*_{max} decreases with pressure and reaches ~0.223 at the phase transition pressure of 33 GPa. The calculated EPC parameter λ and the logarithmic average of phonon frequencies ω_{log} for the FCC phase are shown as a function of pressure in Fig. 2.4 (b). The λ and ω_{log} increases (decreases) slowly at lower pressure but experiences larger changes as the pressure approaches 33 GPa. These large changes are the consequence of the softening of the TA phonon near the *K* point. As a result, the partial EPC parameter λ_{qj} of these modes are enhanced dramatically and results in notable increasing of the total λ but decreasing ω_{log}. Employing the calculated λ and ω_{log}, T_c for the FCC phase was estimated using the Allen-Dynes modification of the McMillan equation Eq. (2.18) with the nominal value of μ^* = 0.22. The results are compared with experimental data in Fig. 2.6. Despite larger estimated magnitudes, the behavior of calculated T_c with varying pressure agrees very

well with experiments. In view of the substantial phonon softening in FCC Li, it is reasonable to attribute the difference between the predicted and observed T_c to the neglect of anharmonic effects. A significant result is that the calculated T_c also shows a maximum at 32 GPa. This feature has not been reported in previous theoretical investigations [141, 142], which instead found T_c increase monotonously with pressure over a wide pressure range. The present results provide an explanation of superconducting behavior of FCC Li near the FCC → *cI*16 phase transition.

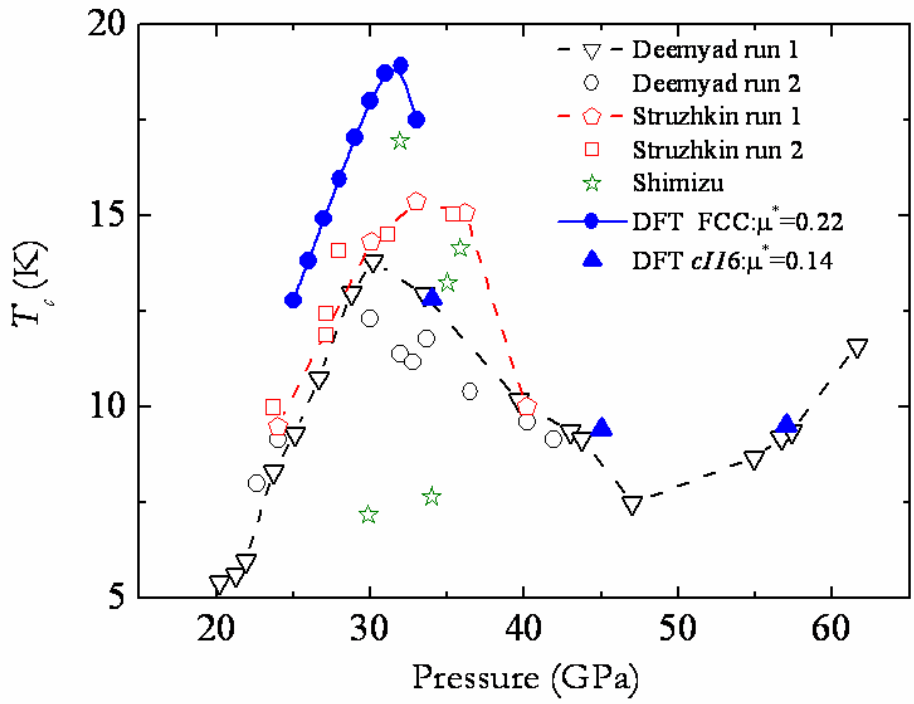

Figure 2.6. Comparison between calculated and experimental T_c obtained at different pressures. The calculated data are represented in solid symbols. The experimental results are taken from Refs 69-71.

The electronic band structures, phonons, and EPC for the *cI*16 phase have been studied at three selected pressures. A pressure of 34 GPa was chosen to investigate the superconducting mechanism close to the phase transition. A second pressure point at 45 GPa was selected to investigate the pressure dependence of T_c in *cI*16 Li. A higher pressure at 57 GPa was chosen to investigate the structural stability of *cI*16 Li since a

structural phase transition was suggested from Raman spectroscopy near 50 GPa. The electronic band structure and DOS were computed with a 32×32×32 *k*-point mesh. Individual phonon calculations were performed on a 8×8×8 *q*-point mesh with a 16×16×16 *k*–point mesh. The EPC parameter λ_{qj} has been computed in the first BZ on a 8×8×8 *q*-point mesh using individual EPC matrices obtained with a 32×32×32 *k*–point mesh. The electronic band structure and DOS of the *cI*16 phase at 34 GPa are shown in Fig. 2.7. The electronic bands crossing the Fermi level are very dispersive except around *Γ*. This feature is contrary to the FCC phase, in which the electronic bands are flat and almost parallel to the Fermi level near the *L* point. In this way, the spherical FS in the FCC phase is distorted anisotropically and develops parallel necks at the boundary of the first BZ. The FS nesting between these necks has been shown to be the origin of strong EPC in the FCC phase [141, 142]. The phonon band structures of the *cI*16 phase at 34 GPa, 45 GPa and 57 GPa are depicted in Fig. 2.8. The phonon band structures show no imaginary modes, thus indicating that the *cI*16 phase is dynamically stable up to at least 57 GPa.

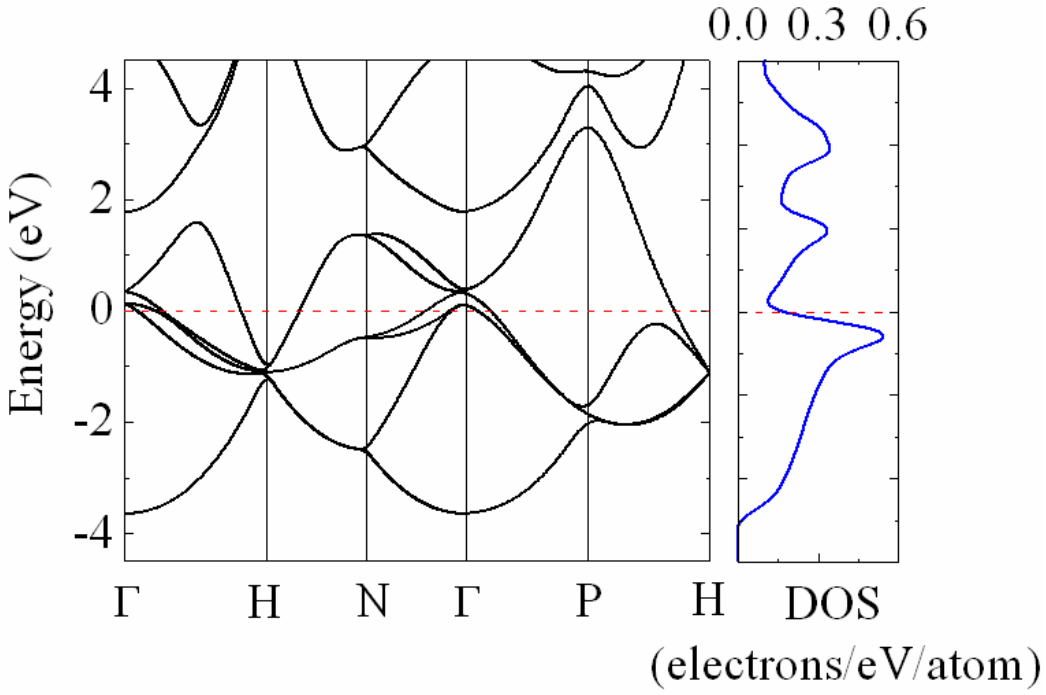

Figure 2.7. The electronic band structure and DOS for the *cI*16 phase calculated at 34 GPa.

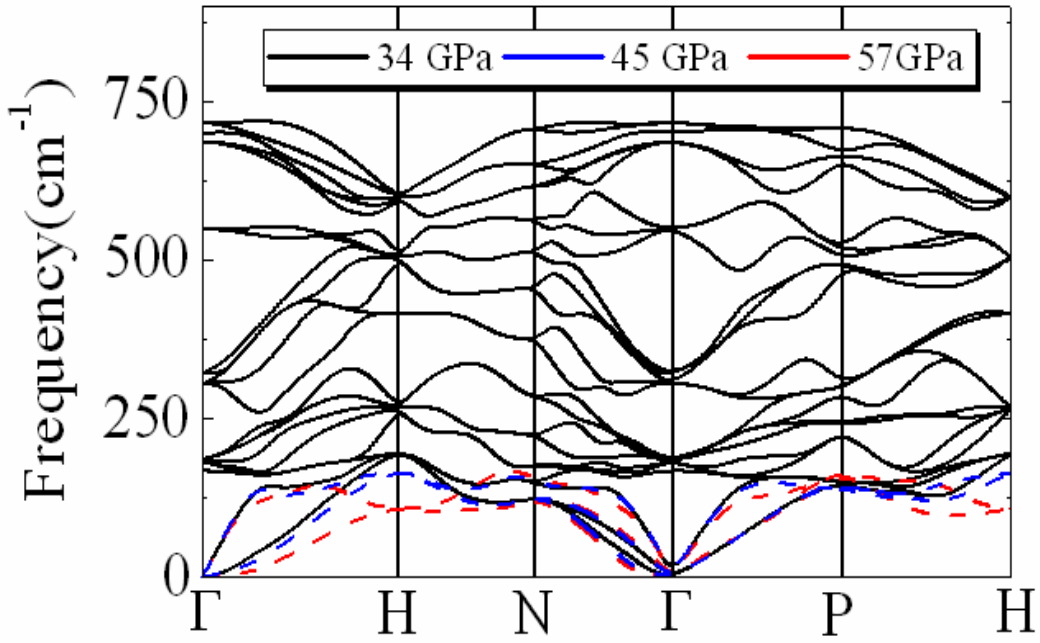

Figure 2.8. The phonon band structures for *cI*16 Li calculated at 34 GPa, 45 GPa and 57 GPa. Only acoustic modes are shown in the phonon band structures for the latter two pressures. The most significant feature of the phonon band structure is that the vibrational modes near *H* softened as pressure increases.

The estimated μ^*_{max} for the *cI*16 phase at three different pressures are almost constant at ~0.225. The calculated λ and ω_{log} at 34 GPa are 0.98 and 233 K, respectively. These values are to be compared with the very large λ of 3.14 for the FCC phase at 33 GPa. The substantially reduced λ is particular interesting. The calculated spectral function $\alpha^2F(\omega)$ for *cI*16 Li at 34 GPa and the integrated EPC parameter, λ, as a function of frequency are shown in Fig. 2.9. As observed from the integrated λ, major contributions to EPC are from the broad peak below 250 cm^{-1}. Incidentally, the maximum in the spectral function coincides with the calculated ω_{log}. The λ and ω_{log} both decrease slowly with pressure and reach 0.92 and 211 K at 45 GPa. At 57 GPa, λ increases to 0.96 and ω_{log} continues to decrease to 180 K. Using calculated λ and ω_{log}, the estimated T_c using the Allen-Dynes modification of the McMillan equation [126, 127] at the three different pressures reproduces the corresponding experimental data very well,

if a μ^* of 0.14 was used (Fig. 2.6). It is interesting that the *cI*16 phase returns to a more 'normal' phonon-mediated superconductor having a nominal value of μ^* between 0.1 and 0.13. The slight drop in T_c between 34 GPa and 45 GPa can be traced to the simultaneous decrease of the Debye temperature Θ_D and density of electrons at the Fermi level.

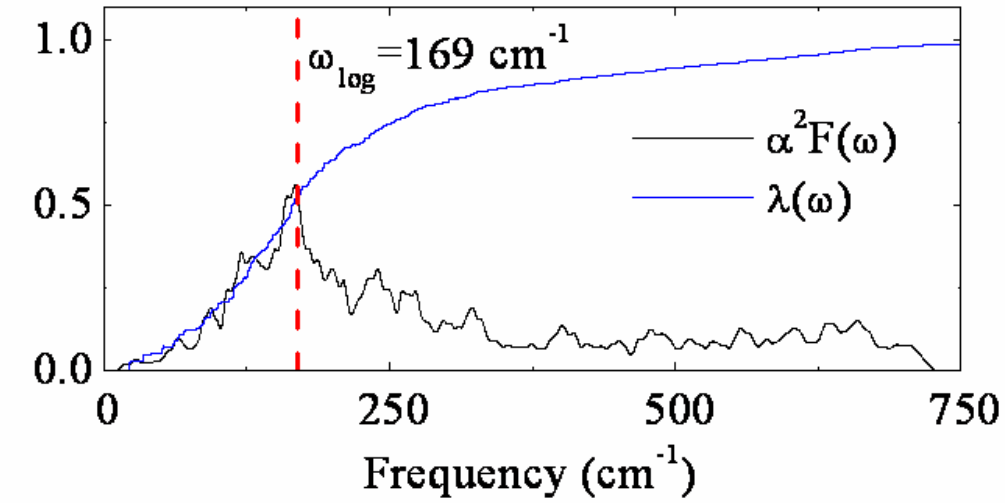

Figure 2.9. The electron-phonon spectral function $\alpha^2F(\omega)$ in *cI*16 Li at 34 GPa.

In summary, the pressure-induced phase transition FCC → *cI*16 in Li has been investigated. The calculated transition pressure 33 GPa is close to the pressure where phonon softening is observed [69-71]. The estimated T_c for the FCC phase increases with pressure until it reaches the transition to the *cI*16 phase where T_c decreases abruptly. This predicted behavior of T_c is in good agreement with experiments [69-71]. The *cI*16 phase was studied at three pressures, 34 GPa, 45 GPa and 57 GPa. It is found that the *cI*16 phase is stable within this pressure range. Using a μ^* of 0.14, the T_c estimated at these three pressures are in very good agreement with the experimental values.

2. 4 Superconductivity in high-pressure phase of SiH_4

Dense hydrogen has been predicted to become superconducting at high pressure

with an extraordinary high T_c [73, 111]. Electronic calculations at an electron density r_s = 1.0 demonstrated that a T_c of 600 K may be possible [111]. However, the task of producing metallic hydrogen in solid state lies outside the possibilities of current experimental techniques, since it requires pressure in excess of 400 GPa [112-114]. To circumvent this problem, another approach has been proposed recently [73, 74]. It is suggested that the strongly compressed hydrogen-dominated alloys of Group IV hydrides can be considered as alternatives for dense hydrogen. The hydrogen atoms are expected to be 'pre-compressed' by the heavy Group IV atoms and reach the density necessary for superconductivity at much lower pressure than with pure hydrogen. This proposal is based on the BCS theory and argued that the lattice dynamics of these systems will comprise of high-frequency proton vibrations and low-frequency vibrations of the massive ions. The combination of overlapping electron bands, which provide high density of states and large electron-ion interactions, yields the essential features of superconductivity. However, the structures of the high-pressure metallic phase of Group IV hydrides remain unknown. A recent theoretical report proposed an **O3** structure having a puckered Si square net involving a distorted local octahedral arrangement of H atoms, which was found to be metallic at 91 GPa (Fig. 2.10) [148]. In another theoretical investigation, a different three-dimensionally connected $I4_1/a$ structure (Fig. 2.10) was predicted [149]. It was shown that the $I4_1/a$ structure is an insulator up to 200 GPa and more energetically stable than the **O3** structure. This prediction apparently agrees with the optical measurement [150], which suggested that the metallization of SiH_4 might not be achievable below 210 GPa. Recent high-pressure X-ray diffraction and infrared studies, however, dispute this finding [151]. It was found that at pressure above 60 GPa, a Drude-like feature was observed in the infrared spectrum indicating the possibility of indirect band gap closure. The electronic state of the high-pressure phase of SiH_4 is still under debate.

In this section, an alternate approach was used to predict the high-pressure phase of SiH_4 by combining a finite-temperature constant pressure molecular dynamic simulation and *ab initio* optimization [62, 64]. The results revealed a high-pressure metallic phase with $C2/c$ symmetry [152]. This $C2/c$ structure has higher enthalpy than

the $I4_1/a$ structure. Therefore, it is a meta-stable phase. The important characteristic of the $C2/c$ structure is that it is metallic and superconducting with a T_c close to 50 K at 125 GPa. Moreover, in subsequent experiments, the metallization and superconductivity of SiH_4 were indeed observed at high pressure. It was found that insulating molecular SiH_4 transforms to a metal and becomes superconducting above 50 GPa.

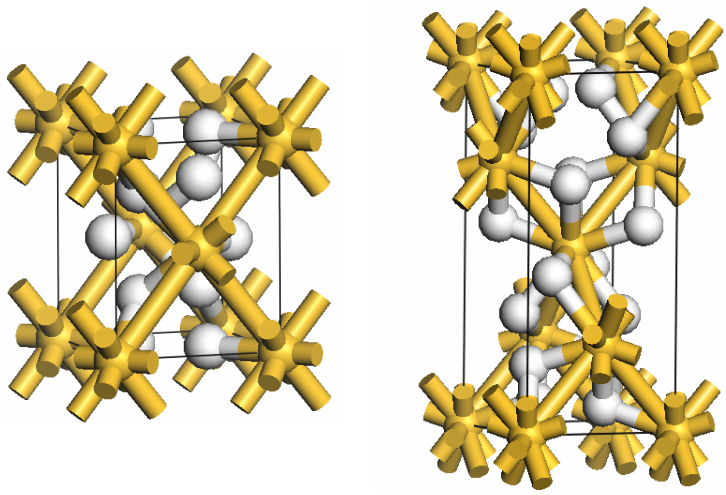

Figure 2.10. (Left) The predicted **O3** structure of high-pressure SiH_4 in Ref. 148. (Right) The predicted $I4_1/a$ structure of high-pressure SiH_4 in Ref. 149. The golden spheres are silicon atoms and white are hydrogen atoms.

The present investigation started from a cubic structure where the Si atoms are placed in the face-centered positions with a tetrahedral arrangement of H atoms around each Si atom. This is the structure adopted by the low-pressure phase of CH_4. The H positions between the closest SiH_4 were chosen such that the H atoms on different molecules are eclipsed. This conformation reduces unfavorable repulsive interactions between H atoms on neighboring molecules. A complete structure-prediction procedure included exploratory simulated annealing and refined structural optimizations on selected candidate structures. A series of simulated annealing at different pressures were performed using a 2×2×2 supercell consisting of 16 SiH_4 units with the linear scaling SIESTA code [64], using Troullier-Martin pseudopotentials [153] and double-zeta valence basis sets and

a 4×4×4 *k*-point mesh. Candidate structures obtained after simulated annealing at each pressure were selected from the trajectory and then fully optimized with more stringent criteria using the VASP code [63] employing the PAW pseudopotentials [147] and a larger 8×8×8 *k*-point mesh.

The low-energy crystal structures obtained are shown in Fig. 2.11. At low pressure, SiH_4 adopts a tetragonal $P4_2/nmc$ structure with two molecules per unit cell. The calculated electronic DOS shows that this molecular phase is insulating. The stability of this structure at 35 GPa is confirmed by phonon band structure calculations. At 60 GPa, the band gap closes and this structure becomes metallic. The predicted transition pressure is supported by the subsequent Raman and electrical resistance measurement that showed the metallization pressure of SiH_4 is between 50 and 65 GPa [78]. This tetragonal structure transforms to an orthorhombic *Ccca* structure. The *Ccca* is a subgroup of $P4_2/nmc$ and most likely an intermediate phase. As pressure increases further, SiH_4 transforms to a monoclinic structure with *C*2/*c* symmetry. The structures of the *Ccca* and *C*2/*c* phases are similar with subtle differences. At high pressure, as expected from the chemical characteristics of elemental Si, Si atoms expand the coordination shell and utilize the 3*d* orbitals to bond with the H atoms of neighboring SiH_4. This bonding picture is confirmed by the projected Si *d*-orbital DOS (Fig. 2.12). The result is the formation of a layer structure with H connecting the SiH_4 units. However, the interactions between bridging H atoms of adjacent layers in the *Ccca* structure are in close contact, to alleviate this unfavorable repulsive interaction, and the two layers "slide" away from each other, resulting in the more stable monoclinic *C2/c* phase. At 125 GPa, the calculated Si-H bond length of 1.58 Å is comparable to the distance between the bridging H-atom in molecular di-silane of 1.58 -1.68 Å. There are two distinct in-plane Si…Si distances of 2.386 and 2.443 Å, which are close to the inter-atomic distance of 2.362 Å in the high-pressure FCC Si-X phase. It is noteworthy that the previously proposed **O3** structure and the present *C*2/*c* structure share one important structural feature - both structures are composed of distinct 2D layers where the Si atoms form a square net bridged by hydrogen atoms.

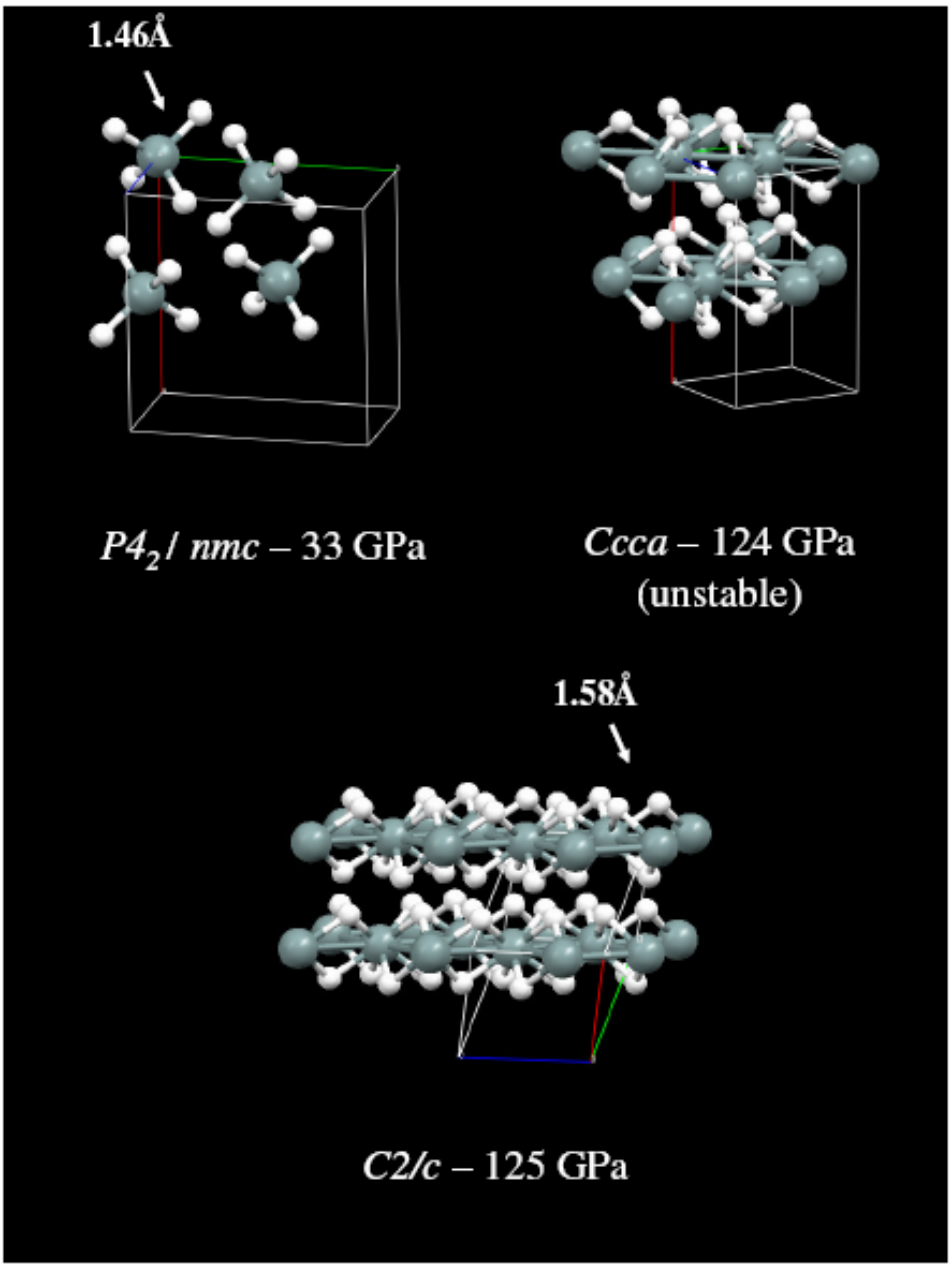

Figure 2.11. Crystal structures of SiH_4 polymorphs at low pressure and high pressure. At 33 GPa the $P4_2/nmc$ structure is stable. The *Ccca* structure is likely an intermediate phase with a small stability range and transforms to the *C*2/*c* structure at ~ 60 GPa.

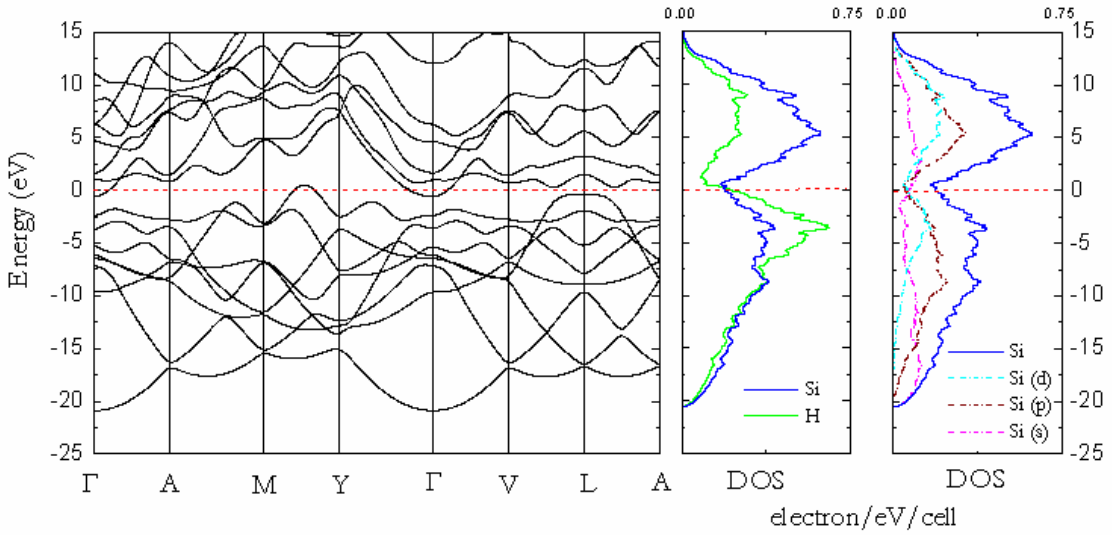

Figure 2.12. The electronic band structure (left panel), and the DOS projected on Si and H atoms (middle panel) and on selected wavefunctions of Si atoms (right panel) of *C*2/*c* SiH_4 at 125 GPa.

It was shown previously that the **O3** structure has a higher enthalpy than the $I4_1/a$ structure [149]. In Fig. 2.13, the enthalpies of the three structures are presented for comparison. The enthalpy of the *C*2/*c* phase is lower than the **O3** phase but higher than the $I4_1/a$ phase. The enthalpy difference between the *C*2/*c* and $I4_1/a$ phase decreases slowly with pressure and reduces to 0.12 eV or 2.76 kcal/SiH_4 unit at 150 GPa. This energy difference is within the limit of absolute accuracy of *ca.* < 6 kcal/mol of the DFT methods [154]. Furthermore, inclusion of the zero-point energy reduces the energy difference to 0.068 eV at 150 GPa. The *C*2/*c* structure was obtained by simulated annealing from a reasonable low-pressure structure. The activation barrier is expected to be in the order of kT ($T = 1000K$), and therefore the transformation to the *C*2/*c* structure may be kinetically driven, even though it is thermodynamically meta-stable with respect to the *I*41/*a* phase. For the **O3** structure, the phonon band structures calculated at the predicted metallization pressure of 91 GPa and 125 GPa show substantial imaginary frequencies, indicating that it is unstable [152]. Therefore, it cannot be a viable candidate metallic structure at high pressure above 91 GPa. Similar phonon calculations on the

*C*2/*c* phase (see later) and $I4_1/a$ phase (not shown) show that both structures are stable between 90 GPa and 150 GPa. Furthermore, from a comparison of the calculated *C*2/*c* with the experimental equations of states for Si IX and solid H_2, it is found that the *C*2/*c* structure is stable against the dissociation into Si and H_2 at 125 GPa. Therefore, the *C*2/*c* structure is a competitive and stable structural model for the high-pressure phase of SiH_4.

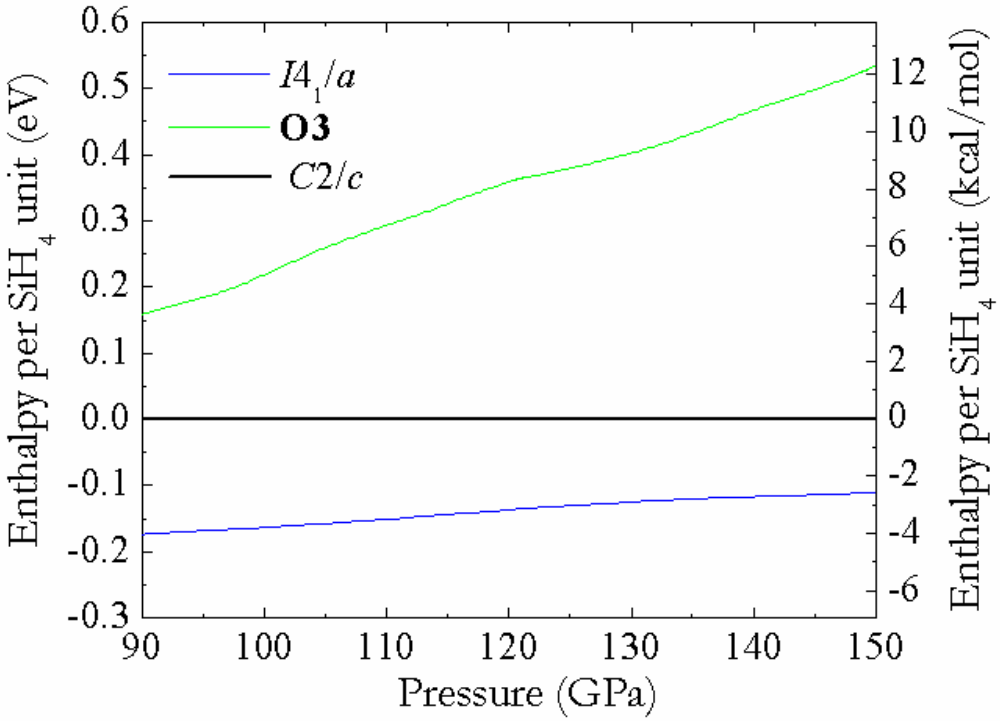

Figure 2.13. Enthalpies per SiH_4 unit of the **O3** and $I4_1/a$ structures relative to the *C*2/*c* phase as functions of pressure.

The electronic band structure of the *C*2/*c* phase at 125 GPa is shown in Fig. 2.12. The valence and conduction bands near the Fermi level are rather flat and not strongly dispersive. Only a few electronic bands along the Γ→A, Γ→Y, Γ→V and M → Y directions cross the Fermi level. The FS is composed of several bands with a significant Si and H character. The projected DOS shown in Fig. 2.12 clearly indicates strong hybridization between the Si and H orbitals resulting in a broad valence band with a width of *ca.* 22 eV. Close to the Fermi surface, the projected DOS on Si atoms shows large contribution from Si *d*-orbitals.

The phonon band structure and density of states (PHDOS) projected on Si and H atoms at 125 GPa are shown in Fig. 2.14. Lattice dynamics calculations confirmed that the *C2/c* structure of SiH_4 is dynamically stable from 65 to 150 GPa. The H and Si vibrations are found to couple strongly in the entire frequency range. As expected, the Si atoms dominate the low-frequency vibrations below 650 cm^{-1}. The lighter H atoms participate strongly in the high-frequency modes. The PHDOS shows a significant mixing of Si and H characters for the vibrations in the 1500-2200 cm^{-1} region. The bands around 1500 cm^{-1} are characteristic of vibrations associated with Si-H-Si, bending and the higher frequency bands at 2200 cm^{-1} can be assigned to Si-H bond stretching. It is noteworthy that the calculated vibrations of superconducting high-pressure Si-V and Si-VI also cover a similar frequency range as the Si-dominant vibrations in SiH_4. Significantly, the flat dispersion of the acoustic branches at *ca*. 180 cm^{-1} throughout most of the BZ also shows some resemblance to that observed in Si-V and Si-VI.

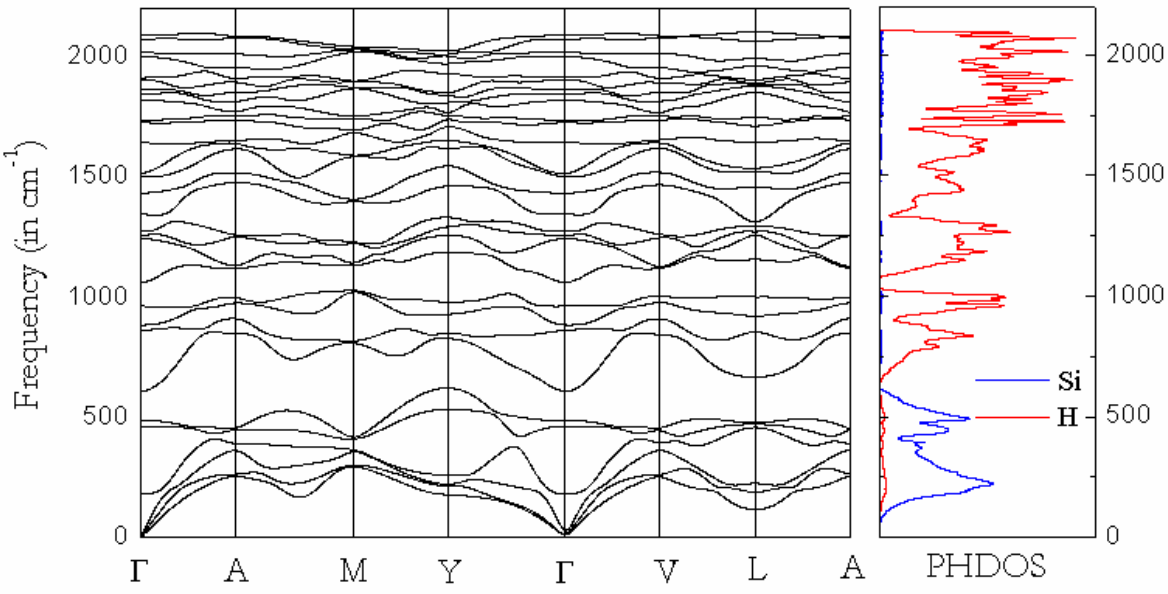

Figure 2.14. The phonon band structure and DOS projected on Si and H atoms in *C*2/*c* SiH_4 at 125 GPa.

In the EPC calculation, a 16×32×32 *k*-point mesh was found to converge to the zero-width limit. The EPC matrices were calculated on a 3×5×5 *q*-point mesh. A very careful convergence check was performed for the *k*-point and *q*-point meshes used here. The procedure of this convergence check has two steps. First, to obtain accurate EPC parameter very accurate phonon results are required. The convergence of the *k*-point mesh in the phonon calculations was checked by systematically increasing the kinetic energy cutoffs and employing denser *k*-point meshes. A maximum deviation of less than 0.05 THz in the calculated phonon frequencies is achieved with a 16×32×32 *k*-point mesh. The second step is to determine the zero limit (taken numerically as 0.03 Ry.) of the EPC parameter, λ, at a given *k*-point mesh. A reasonable *k*-point mesh should yield a converged λ when the Gaussian broadening parameter σ approaches zero. The procedure is as follows: the λ was calculated at several phonon *q*-points with a given set of *k*-point mesh. Then calculations were repeated with a denser *k*-point mesh. In principle, if the process is repeated one should approach a lower limit of σ. Several *q*-points were checked and the results show that a *k*-point mesh 16×32×32 is sufficient to simulate the zero limit. A 8×16×16 *k*-point mesh converged to a value of σ larger than 0.04. This value is not very accurate but is already acceptable for qualitative investigation. On the other hand, a 16×32×32 *k*-point mesh converges to a value of σ smaller than 0.025. Increasing the *k*-points even more may slightly alter the value of λ. However, the difference is expected to be very little. To validate this point, we compared the results obtained using 16×32×32 and 24×48×48 meshes and found the change in the computed λ is less than 10^{-2}.

The calculated Eliashberg spectral function $\alpha^2F(\omega)$ for SiH_4 at 125 GPa and the integrated EPC parameter, λ, as a function of phonon frequency are shown in Fig. 2.15. Low-frequency Si translational vibrations make a significant contribution to the overall EPC parameter. The integrated λ up to 200 cm^{-1} is 0.3 and constitutes almost 30% of the total coupling parameter. The Si-H-Si torsional and bending vibrations from 650 cm^{-1} to 1500 cm^{-1} contribute another 30%, with the remaining 40% derived from the Si-H stretching vibrations. The calculated λ is 0.89 indicating that the EPC is fairly strong.

The T_c was estimated from Eq. (2.18). At 125 GPa, the calculated ω_{log} is 959 K. Using μ^* of 0.1, 0.12 and 0.13 the estimated T_c for the *C2/c* high-pressure phase of SiH_4 are 55, 49 and 46 K, respectively. The pressure dependence of T_c has also been studied. At 90 GPa, the EPC constant λ reduces to 0.81 but ω_{log} increases slightly to 987 K. The estimated T_c are 48, 42 and 39 K with μ^* of 0.1, 0.12 and 0.13, respectively. The pressure coefficient (dT_c/dP) is about 0.2 K/GPa.

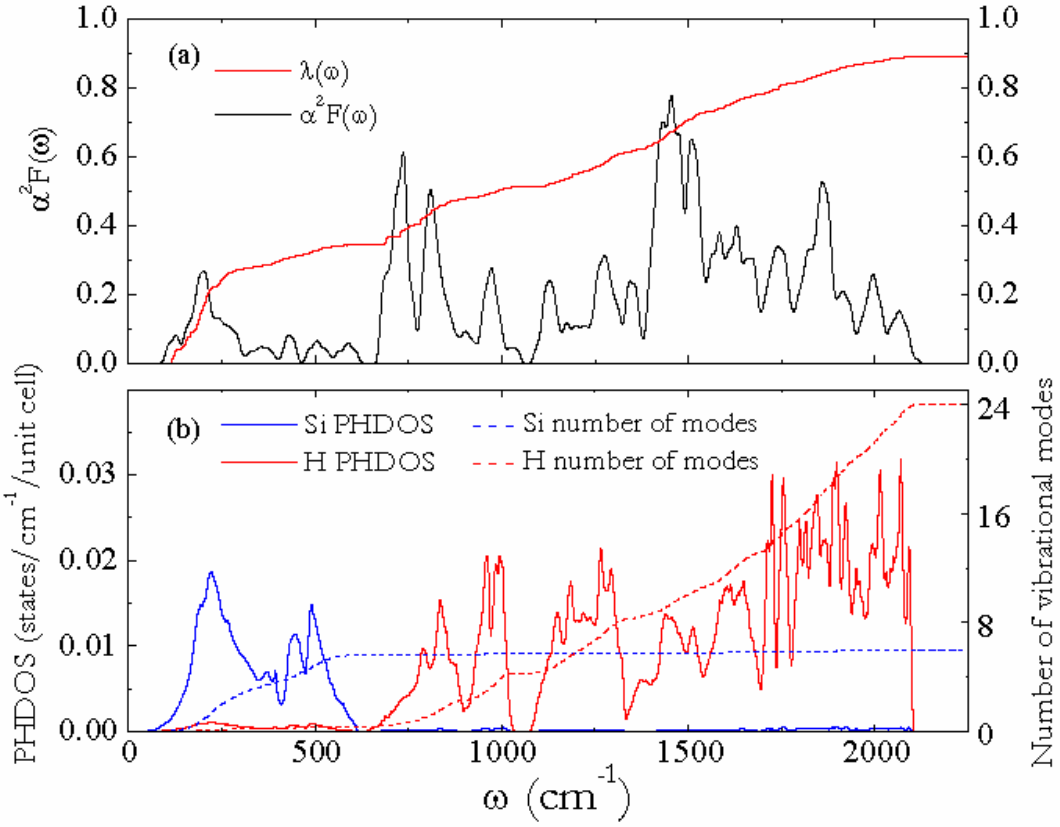

Figure 2.15. The Eliashberg phonon spectral function $\alpha^2F(\omega)$ and electron-phonon integral λ(ω) (top) are compared to the PHDOS projected on Si and H atoms (bottom) in *C*2/*c* SiH_4 at 125 GPa.

The numerical results reported here support the theoretical analysis presented previously [73, 74]. High pressure enhances electronic interactions between SiH_4 molecules, leading to a metallic state with a broad valence band. The combination of

these two effects helps to increase the attractive EPC over the repulsive Coulomb interaction among electrons. The calculated EPC constant of 0.89 at 125 GPa is close to the predicted strong coupling value of 1.0. The integral $\lambda(\omega)$ shows that the maxima of the translational acoustic phonon modes at 200 cm^{-1} are very effective in enhancing the EPC. The Si-H torsional and bending vibrations also contribute significantly, while the highest energy and localized Si-H bond stretch modes above 2000 cm^{-1} seem to have little effect on the superconducting behavior.

Recently, the experimental search for superconductivity in SiH_4 has been performed at pressures up to 200 GPa [78]. It was found that SiH_4 transforms successively to several insulating phase transitions below 50 GPa. Between 50 and 65 GPa, SiH_4 transforms to a metallic and superconducting phase with $T_c \sim 7$ K. Upon further compression, T_c increases and reaches 17.5 K at 96 GPa. From 96 GPa up to 120 GPa, T_c cannot be measured due to experimental difficulties. At 120 GPa, the measured T_c is ~ 17 K. At higher pressure, SiH_4 gradually transforms to an insulator phase. The metallic phase and the insulating phase were observed to co-exist for a broaden range of pressure, with T_c decreasing and reaching down 8.8 K at 165 GPa. The measured metallization pressure and T_c are in good agreement with the theoretical prediction above. However, the observed structure of the superconducting phase is different. The experimental structure was indexed from the X-ray diffraction pattern as a primitive hexagonal cell with lattice parameters a = b = 2.67 Å and c = 4.49 Å at 113 GPa. The positions of hydrogen atoms cannot be determined directly from the diffraction patterns. However, for the close-packed arrangement of Si framework, the only way to place eight hydrogen atoms in the interstices of the unit cell is to have four hydrogen atoms occupy all tetrahedral interstices, with the other four H atoms located in pairs in the large octahedral cages. The resulting structure has a space group of $P6_3$ [78].

The proposed $P6_3$ structure has been examined using the DFT calculations. The structure was fully optimized with constant volume of unit cell. It was surprising that for the same $P6_3$ structure, the unit cell observed in experiments is much denser than the one optimized by theory. The difference is very large and far exceeds any anticipated error in

the calculations. To search for a plausible explanation, a structural search using the genetic algorithm (This method is presented in Chapter 4) was performed. Geometry search was started with a fixed hexagonal close packed (HCP) framework of Si atoms. The positions of H atoms were initially chosen randomly and improved in the evolutionary procedure. Several energetically favorable candidate structures were found including a $P6_3$ structure, but none of the structures reproduce the volume of unit cell determined from experiment. These results shown that given the HCP framework of Si atom there are no satisfactory ways to place H atoms that satisfy the experimental observation. However, the high resolution of X-ray diffraction pattern is not likely to have other assignments other than the HCP Si framework. In view of the discrepancy, a structural model that can bring agreement between experiment and theory is still missing.

2. 5 Superconductivity in high-pressure phase of SnH_4

The successful theoretical prediction [152] and experimental confirmation [78] of superconductivity of SiH_4 at high pressure have motivated the search on the hydrides of heavier group IV elements such as SnH_4. SnH_4 offers several potential advantages over SiH_4. The heavier Sn atom will yield lower-energy vibrations that help mediate EPC. A weaker Sn-H bond enthalpy may facilitate complete dissociation of the Sn-H bonds at lower pressure. To investigate these possibilities, first-principles calculations have been performed to characterize the high-pressure structure and potential superconducting properties of SnH_4. A high-pressure superconducting phase of SnH_4 is revealed [75], which is stable between 70 GPa and 160 GPa with a predicted T_c close to 80 K at 120 GPa. More significantly, the predicted high T_c was characterized by two signatures, (i) the occurrence of low vibrational frequencies, and (ii) simultaneous occurrence of dynamical (phonons) and electronic (Fermi surface) instabilities.

In the absence of knowledge of high-pressure SnH_4 structure, the starting point of this investigation was initiated with the *Ccca* structure [152] (Fig. 2.11), the high-pressure phase of SiH_4. A series of simulated annealing and geometry optimization revealed a metallic *P6/mmm* structure (Fig. 2.16 (a)). The Sn atom occupies the

crystallographic 1*a* site and the H atoms are on the 4*h* sites. The Sn atoms are arranged in 2-D close-packed hexagonal layers. The in-plane Sn-Sn bond length varies from 3.189 Å to 2.961 Å from 70 GPa to 160 GPa. In this pressure range, adjacent Sn layers are bridged by a pair of H atoms with a Sn-H bond length from 2.129 Å to 1.962 Å. The most striking feature of this structure is the exceptionally short H-H contact from 0.845 Å to 0.841 Å from 70 GPa to 160 GPa. The analysis of the electron localization function (ELF) [155] (Fig. 2.16 (a)) shows a very high value (close to 1) in regions between the two H atoms. The strong electron localization between the two H atoms indicates pairing of electrons from the H atoms. As will be described later, interactions of these novel 'H_2' units with the Sn framework contribute significantly to the EPC mechanism. The ELF values in the region connecting the adjacent Sn layers are close to 0.6, suggesting weak covalent bonding.

The electronic band structure and DOS at 120 GPa are shown in Fig. 2.16 (b). The DOS shows significant overlap between the orbitals of Sn and H atoms. The band structure reveals metallic character with large dispersion bands crossing the Fermi level (E_F) and a flat band near E_F close to the M point. The simultaneous occurrence of flat and steep bands near the Fermi level has been suggested as favorable conditions for enhancing electron pairing, which is essential to superconducting behavior [156]. The phonon band structure and the projected DOS at 120 GPa are shown in Fig. 2.17. The absence of imaginary frequency modes indicates that the structure is stable. Additional phonon calculations establish the stability range to be between 70 and 160 GPa. A direct result of this unique H_2 'intercalated layered' structure is that the vibrational modes can be divided into three major regions. Weak interactions between the Sn framework and H atoms are found in the low-energy translational region below 260 cm^{-1}. As will be discussed later, these low-frequency vibrations contribute significantly to the EPC parameter λ. Molecular-like H-H vibrations are observed at high frequencies (2200-2600 cm^{-1}). These almost localized vibrations are the consequence of strong H-H interactions as revealed from the ELF analysis (Fig. 2.16 (a)). The H...Sn...H bending vibrations dominate the intermediate frequency region (500-1400 cm^{-1}).

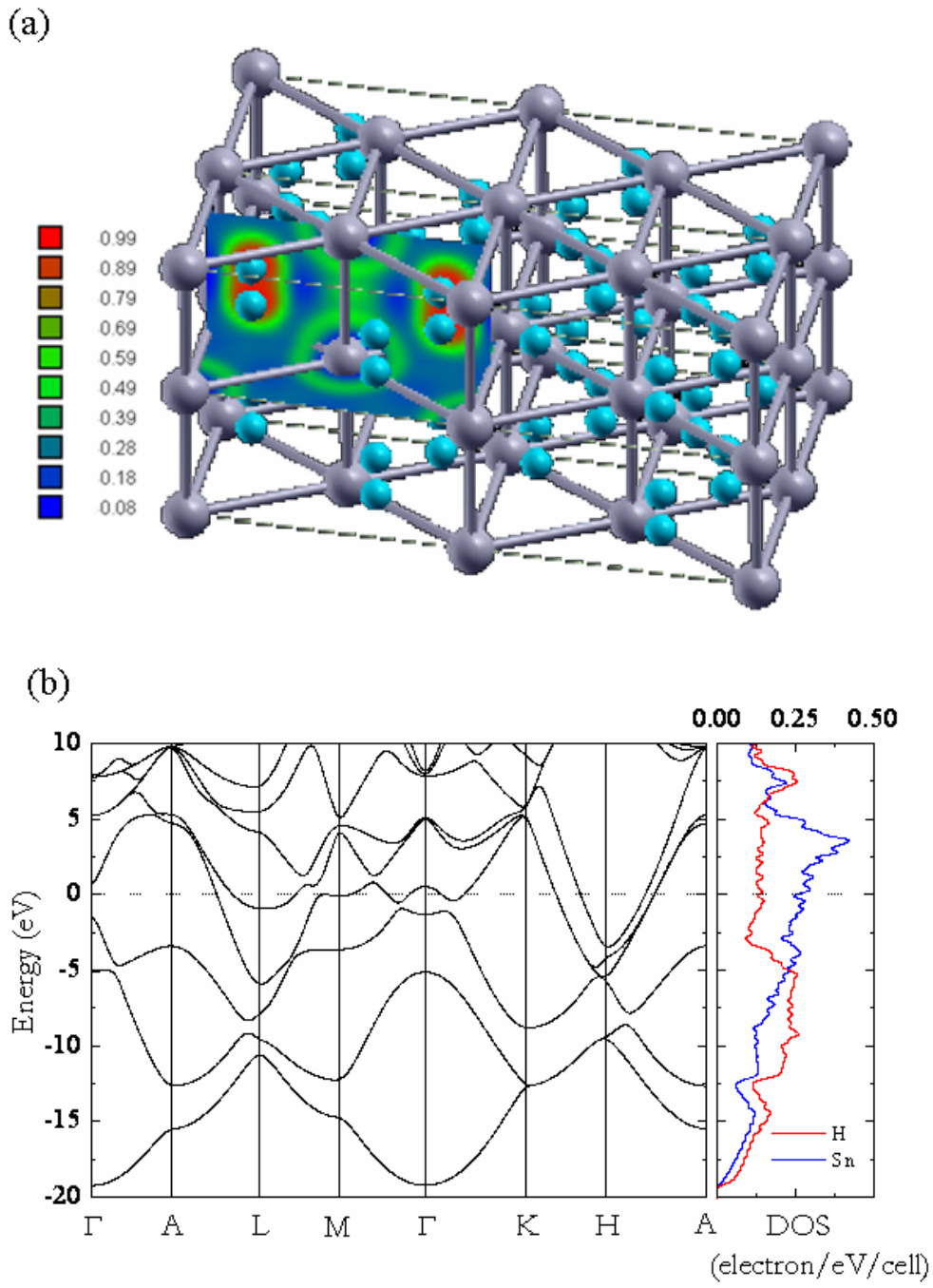

Figure 2.16. (a) The crystal structure of *P*6/*mmm* SnH_4 calculated at 120 GPa with the ELF shown in the (100) plane. (b) The electronic band structure and projected DOS of *P*6/*mmm* SnH_4 calculated at 120 GPa.

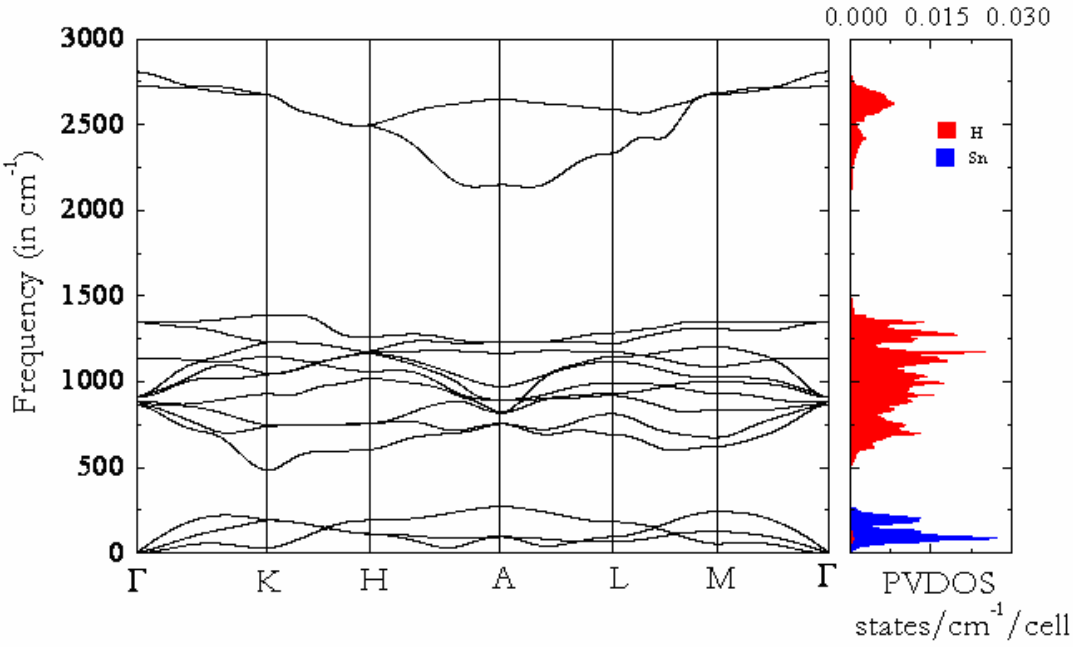

Figure 2.17. The phonon band structure and projected DOS of *P*6/*mmm* SnH_4 calculated at 120 GPa.

A striking feature of the phonon band structure is the presence of soft phonon modes, which can be classified into two groups: those induced by FS nesting and by Kohn anomalies. The former includes the decrease in the phonon frequency of the lowest acoustic branch (branch 1) observed at the K and M points, as well as the dip in the lowest optical branch (branch 4) at the K point. The second group consists of the two dips in phonon branch 1 along the H→A and A→L directions (Fig. 2.17). Details of the nesting of FS can be analyzed in terms of the nesting function [140, 157]

$$\xi(\vec{q}) = \frac{1}{N}\sum_{\vec{k}} \delta(\varepsilon_{\vec{k}} - \varepsilon_F)\delta(\varepsilon_{\vec{k}+\vec{q}} - \varepsilon_F) \propto \oint \frac{d\ell_{\vec{k}}}{\left|\vec{v}_{\vec{k}} \times \vec{v}_{\vec{k}+\vec{q}}\right|}, \qquad (2.24)$$

where the line integral is along the intersection of FS and its image displaced by vector $\vec{q}$, $\vec{v}_{\vec{k}}$ is the Fermi velocity, and N the number of k-points. The $\xi(\vec{q})$ becomes large when

$\vec{v}_{\vec{k}}$ and $\vec{v}_{\vec{k}+\vec{q}}$ are small and/or collinear. This concept helps to determine possible nesting vectors from the FS shown in Fig. 2.18. In the FS of the lowest-energy band crossing the Fermi level (Fig. 2.18(b)), the electron velocities of the opposite faces of the 'hexagonal (sake) cup' shaped portions are parallel to each other. Therefore, FS nesting is expected to occur. Moving downward from the top to the zone center, corresponding nesting vectors span *q*-points along the Γ→M and Γ→K directions. This qualitative description is confirmed by the quantitative calculations presented in Fig. 2.19(a), where $\xi(\vec{q})$ is shown to be strongest along the Γ→M and Γ→K directions. The strong peak at the K point is also facilitated by nesting between two opposite faces of the FS of the middle energy band (Fig. 2.18(c)). This band has smaller Fermi velocities that are collinear in the top portion of the FS. The two peaks in $\xi(\vec{q})$ along the Γ→A direction are related to nesting vectors along the z-axis. Along the A→L and H→A directions, $\xi(\vec{q})$ features several broad but weak peaks that can be attributed to Kohn anomalies. Kohn anomaly is a special case of FS nesting with a nesting vector of $2\vec{k}_F$ (inset of Fig. 2.20), and it induces distinct phonon softening in branch 1 along the H→A and A→L directions. Finally, the decrease in the vibrational frequency of the second highest phonon branch along the H→A→L direction (Fig. 2.17) is likely to be a result of phonon renormalization caused by Kohn anomalies [158]. To explore the dependence of the EPC on soft phonon modes, the partial EPC parameter λ for the two softened branches (branch 1 and 4) along several high-symmetry directions are depicted in Fig. 2.20. As results of phonon softening and FS nesting/Kohn anomalies, broad peaks are observed at the K point and along the H→A and A→L directions. As seen in $\xi(\vec{q})$ (Fig. 2.19(a)), although FS nesting vectors span *q*-points along the Γ→M direction, there is no peak at the M point in the partial EPC parameter λ shown in Fig. 2.20. This feature is a result of smaller magnitudes of the relevant electron-phonon matrix elements [159]. This is substantiated by the fact that in branch 1, the phonon softening at the M point is not as distinct as that at the K point.

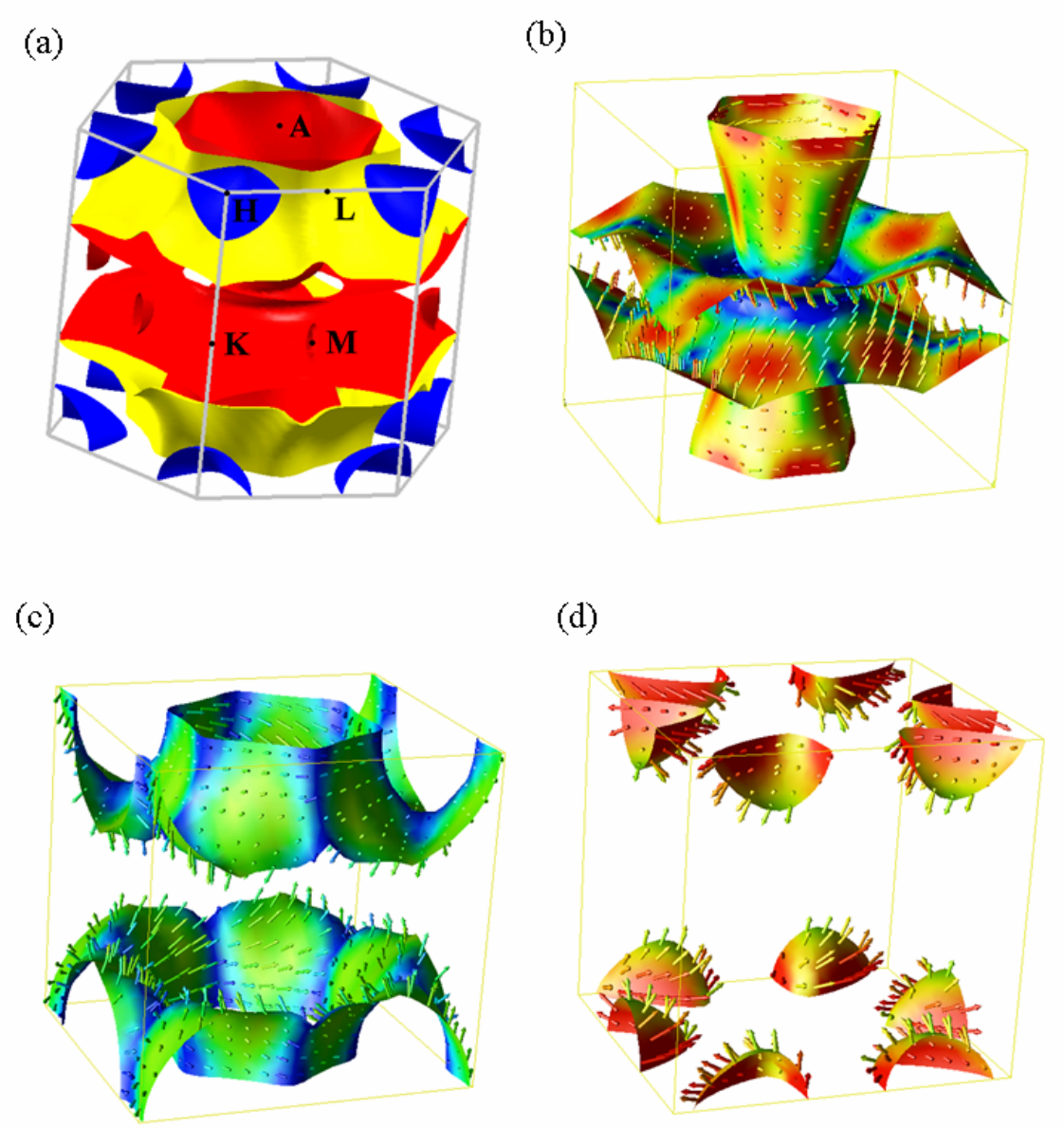

Figure 2.18. The FS of *P*6/*mmm* SnH_4 calculated at 120 GPa. (a) The 3D view of the Fermi surface including all bands. (b), (c), (d) The FS of each band colored by the value of the Fermi velocity, with arrows representing the velocity directions. Red color indicates high velocity; blue color represents low velocity. The FS is sampled with a 24x24x30 *k*-mesh.

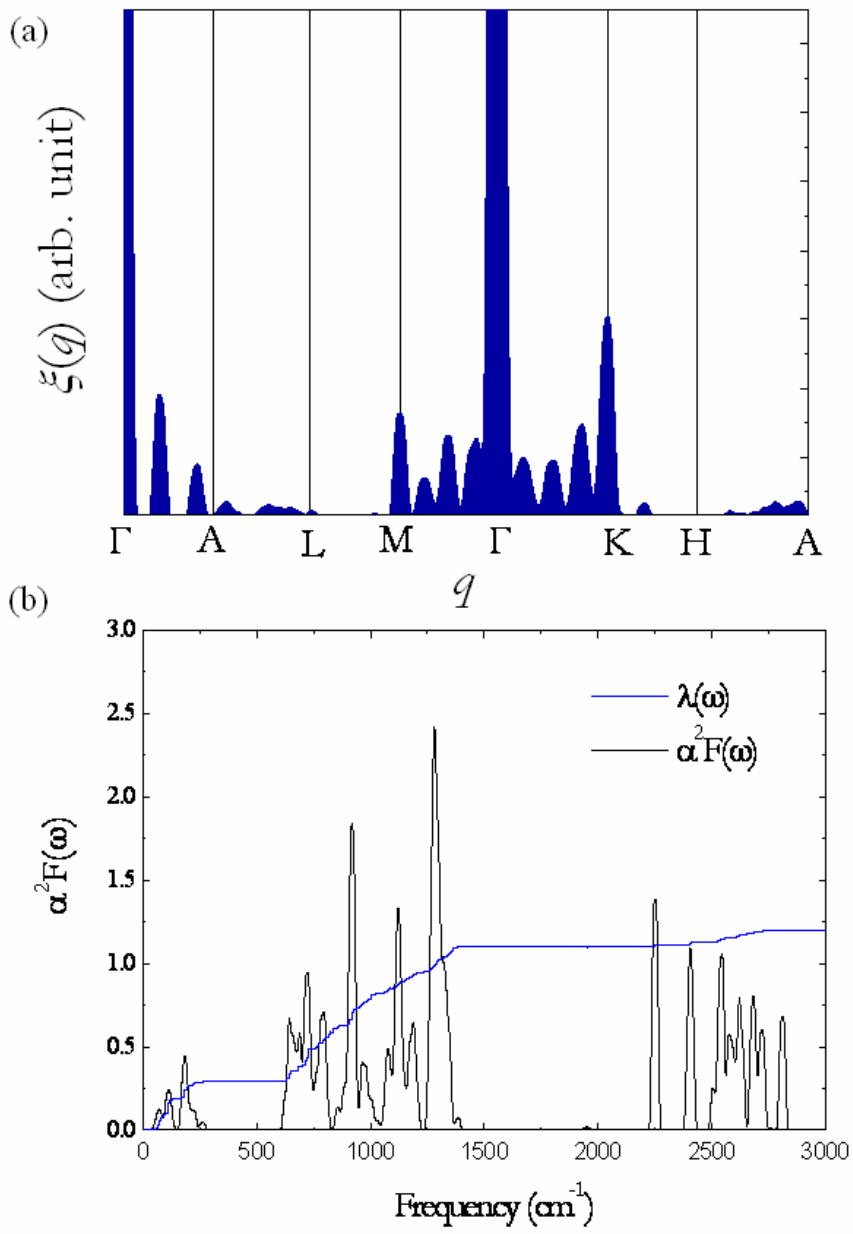

Figure 2.19. (a) The nesting function $\xi(\vec{q})$ of *P*6/*mmm* SnH_4 along several high symmetry lines of $\vec{q}$ calculated at 120 GPa. (b) The Eliashberg phonon spectral function $\alpha^2 F(\omega)$ and the electron-phonon integral $\lambda(\omega)$ of *P*6/*mmm* SnH_4 calculated at 120 GPa.

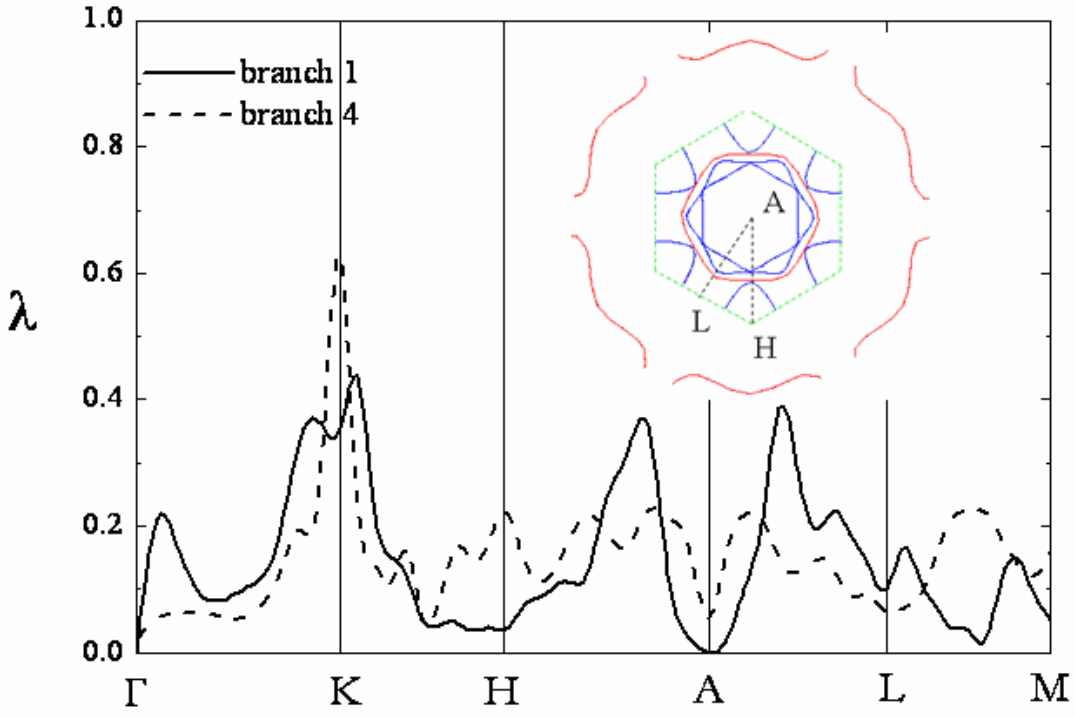

Figure 2.20. The partial EPC parameter λ in two soft phonon branches (branch 1 and 4). Inset is the (001) cross section of the first B. Z. with the boundary represented by green dotted lines. The FS is resented by blue curves. Red curves correspond to the Kohn anomaly surface.

To investigate possible superconductivity, phonon linewidths, the EPC parameter λ and the Eliashberg spectral function $\alpha^2F(\omega)$ have been calculated. The calculated λ is 1.20 at 120 GPa. The spectral function $\alpha^2F(\omega)$ obtained at 120 GPa and the integrated EPC parameter λ as a function of frequency are shown in Fig. 2.19 (b). The integrated λ from acoustic modes below 260 cm^{-1} constitutes 25% of the total EPC parameter. The intermediate-frequency vibrational modes between 500 cm^{-1} and 1400 cm^{-1} contribute 68% to the total EPC parameter. The remaining 7% of the total EPC parameter is derived from the vibrational modes above 2200 cm^{-1}. The superconducting critical temperature can be estimated from the Allen-Dynes modified McMillan equation Eq. (2.18). At 120

GPa, the calculated ω_{log} is 921K. Using μ^* of 0.1, 0.12 and 0.13, the estimated T_c are 83, 77 and 73 K, respectively.

In conclusion, first-principles calculations reveal a novel structure of SnH_4 at high pressure. This structure exhibits a *P6*/mmm symmetry and is stable between 70 and 160 GPa. Due to the exceptionally strong EPC, very high superconducting temperatures are estimated. Low-frequency vibrations of massive Sn atoms and high-frequency vibrations of H_2 units are essential for the EPC. Soft phonon modes have been observed and found to be very effective to enhance the EPC. The soft phonon modes are induced by the FS nesting and Kohn anomalies.

2. 6 Superconductivity in the high-pressure HCP phase of xenon

Noble gas solids have long been regarded not to be superconducting. In one sense, they are against the conventional understanding of superconductivity, which states that the occurrence of superconductivity is most favorable in systems rich in valence electrons [103]. However, it is known that the inert characteristics of noble gas solids will change at high pressure. At lower pressure, noble gases crystallize in the FCC structure. Upon compression, they undergo a phase transition to the HCP structure and become metallic [106-110]. The pressure-induced metallization leads to an interesting question, can solid noble elements be superconducting as well at high pressure? This question, however, has never been investigated.

In this section, the possibility of superconducting behavior in the metallic HCP phase of Xe is explored. Xe is the most promising noble gas solid. It has the lowest metallization pressure (140 GPa). Since it is also the heaviest noble gas atom, therefore it is expect Xe solid to possess low frequency vibrations that may help to promote phonon-mediated superconductivity [106]. Moreover, Xe atom is isoelectronic with Cs^+ and I^- and CsI has been found to be superconducting under high pressure [102]. In this

investigation, HCP Xe has been studied from 150 to 315 GPa. The results show that the EPC of HCP Xe is strongly spatially anisotropic and localized along a few high-symmetry directions in the first BZ. It is also shown that the EPC of HCP Xe is closely related to the topology of FS and enhanced by nesting. The EPC is found to be largest at 215 GPa with a predicted T_c of 0.04 K.

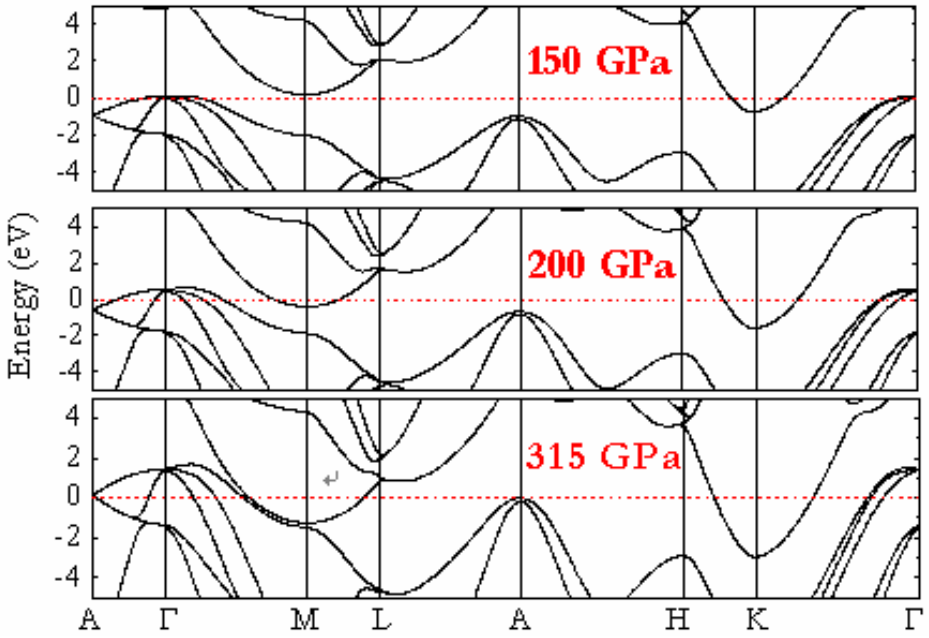

Figure 2.21. The evolution of the electronic band structure of HCP Xe near the Fermi level at selected pressures.

The electronic band structure calculated at 150 GPa (Fig. 2.21), which is close to the observed metallization pressure [109], shows clearly that the metallization in HCP Xe occurs via the closure of the indirect band gap between the Γ and *K* points. This is supported by the experimental observation of a sudden appearance of an absorption peak arising from inter-band transition [109, 110]. When the pressure is increased, more conduction bands cross the Fermi level along the $A \rightarrow \Gamma \rightarrow M$ direction and the dispersion of these bands becomes steeper. Starting from 150 GPa, with increasing pressure the energy of the lowest conduction band at the *M* symmetry point decreases and eventually crosses the Fermi level around 200 GPa. The crossing develops an electron pocket

("hole") at the *M* symmetry point and this has a noticeable effect on the crystal structure. Although the computed hexagonal lattice parameters, ***a*** and ***c***, apparently decrease monotonously with increasing pressure, on closer inspection, a subtle change of slope in the ***c***/***a*** ratio was detected at around 200 GPa (Fig. 2.22). This structural change is undoubtedly associated with a change in the FS electron topology due to the crossing of the conduction band at the *M* symmetry point. This phenomenon is known as electron topological transition (ETT) and is very common in high-pressure metals. A well-known example is the ETT transition in HCP Zn where a similar change in the ***c***/***a*** was also reported at 9 GPa [160, 161].

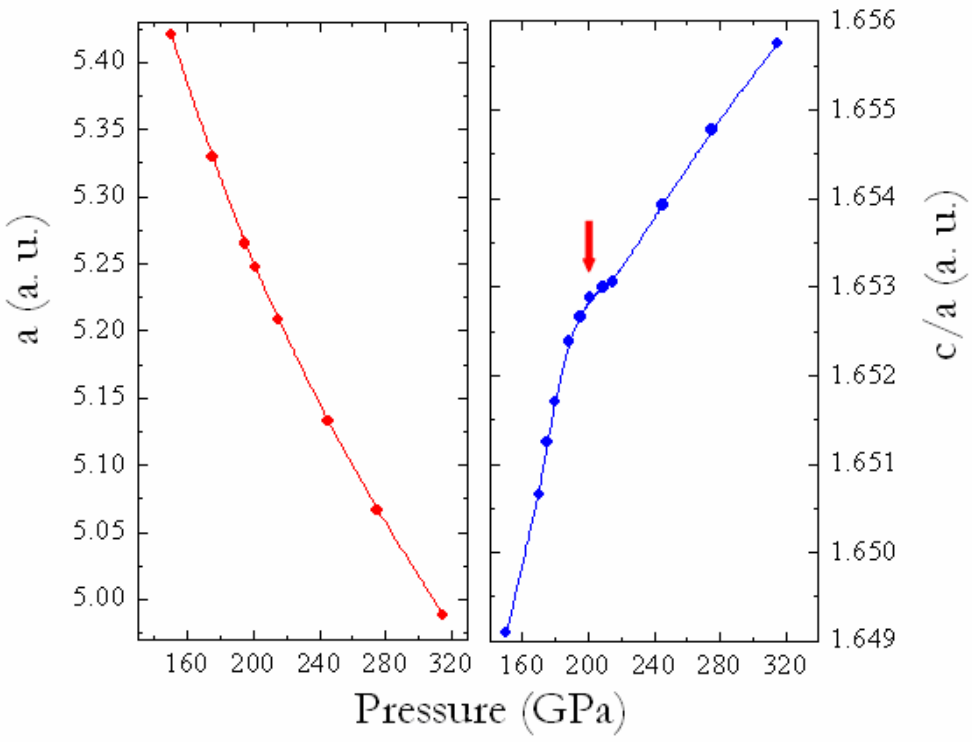

Figure 2.22. The computed unit cell lattice parameters (***a*** and ***c/a***) of HCP Xe as a function of pressure. The position of the electron topological transition is indicated by arrow.

Examination of the electronic bands along the Γ→*M* direction reveals two almost parallel bands crossing the Fermi level and becoming more prominent when the pressure

approaches 200 GPa. Similar parallel bands cutting the Fermi level are also found along the $K \rightarrow \Gamma$ direction. The occurrence of parallel bands in the electron band structure is a sign of possible nesting of the two FS. Another noteworthy feature in Fig. 2.21 is the simultaneous occurrence of 'flat band and steep band' near the Fermi level in the vicinity of the *M* symmetry point. This feature has been suggested as a favorable condition for enhancing electron pairing essential to superconductivity [162].

Two- (2D) and three- dimensional (3D) FS of HCP Xe at selected pressures are depicted in Fig. 2.23. From the plots of the 2D FS, it is observed that the lowest-energy valence band crossing the Fermi level develops into an almost regular hexagon from 150 GPa to 200 GPa. At pressure lower than 200 GPa, the hexagonal FS shrinks and distorts significantly. On the other hand, the hexagonal FS expands and the sides become more concave towards the center of the BZ with increasing pressure. At 200 GPa, the opposite faces of the hexagonal FS are nearly parallel, suggesting possible nesting of the two pieces of the FS. For example, one possible vector is shown as the red arrow in Fig. 2.23. Moreover, other sets of possible nesting vectors can be identified and shown as blue and green arrows, connecting the FS of the second highest energy band to the highest energy band along the $\Gamma \rightarrow K$ and $\Gamma \rightarrow M$ directions, respectively. These two sets of nesting vectors connect the parallel bands crossing the Fermi level along the $\Gamma \rightarrow K$ and $\Gamma \rightarrow M$ directions in the electronic band (Fig. 2.21). The computed nesting function $\xi(\vec{q})$ of HCP Xe at 200 GPa along several high-symmetry directions of $\vec{q}$ in the first BZ is shown in Fig. 2.24. The peaks along the $\Gamma \rightarrow A$ direction show nesting along the *z*-axis. Along the $\Gamma \rightarrow M$ and $\Gamma \rightarrow K$ directions, $\xi(\vec{q})$ exhibits several peaks corresponding to nesting located in the (001) plane. Specifically, the strong sharp peak between the Γ and *M* symmetry points is related to the nesting vector connecting the opposite side faces of the hexagonal FS (red arrow), and several weaker peaks due to nesting vectors on the upper and lower surfaces of the hexagonal FS. The sharp peak between the Γ and *K* symmetry points is attributed to the other set of nesting vectors (blue arrow). The weak peaks around the *K* symmetry point are due to nestings within the highest energy band. Although it is not feasible to visualize all the possible nesting vectors of a 3D FS, the nesting function $\xi(\vec{q})$ clearly shows that nestings are more favorable in the (001) plane. In general, the

occurrence of a FS nesting indicates that the structure is at the proximity of electronic instability. As a result, a nested FS is often strongly correlated to EPC, and enhances the value of λ.

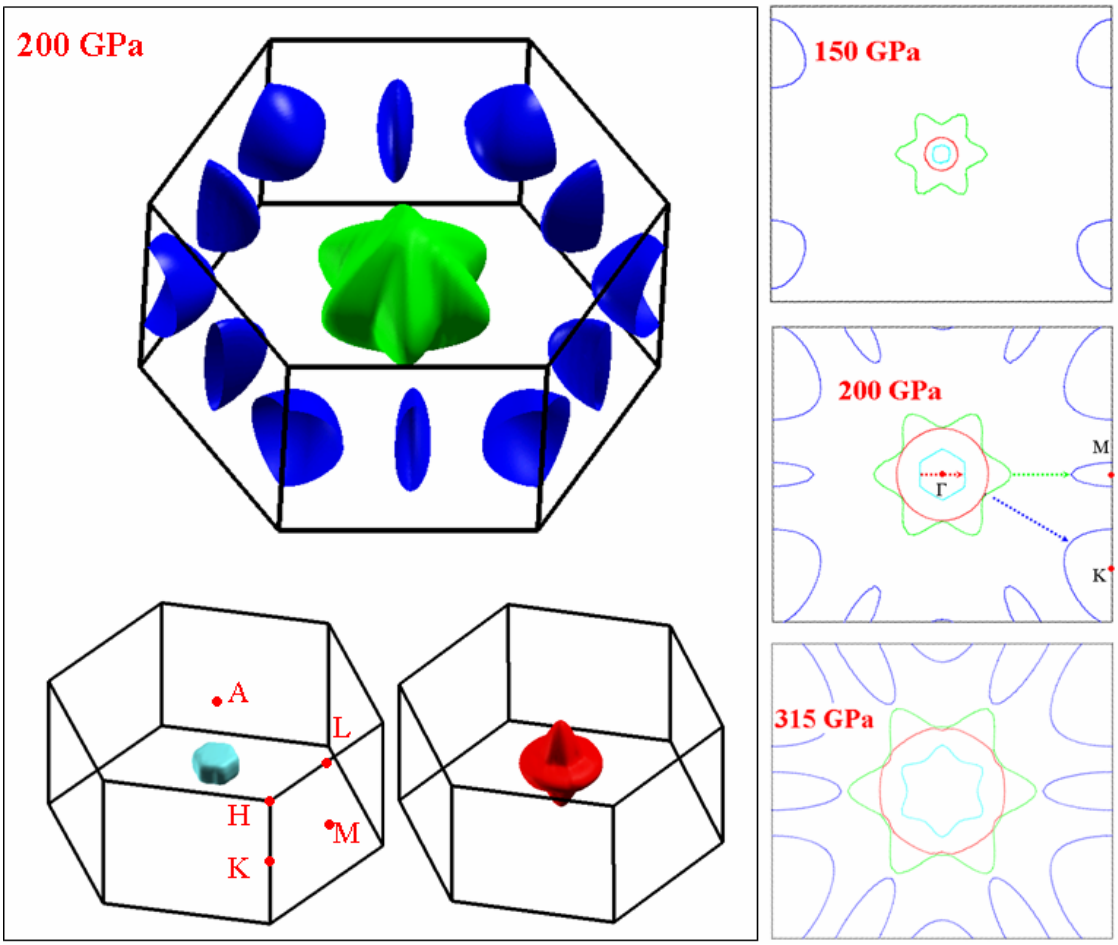

Figure 2.23. The FS of HCP Xe computed at selected pressures. (Left) Three-dimensional FS of HCP Xe at 200 GPa. The FS of the four valence bands crossing the Fermi level, in order of decreasing energy, is colored in blue, green, red and cyan. (Right) 2D FS cross sections parallel to the (001) plane through Γ in the first BZ at three pressures. Possible nesting vectors are indicated by arrows.

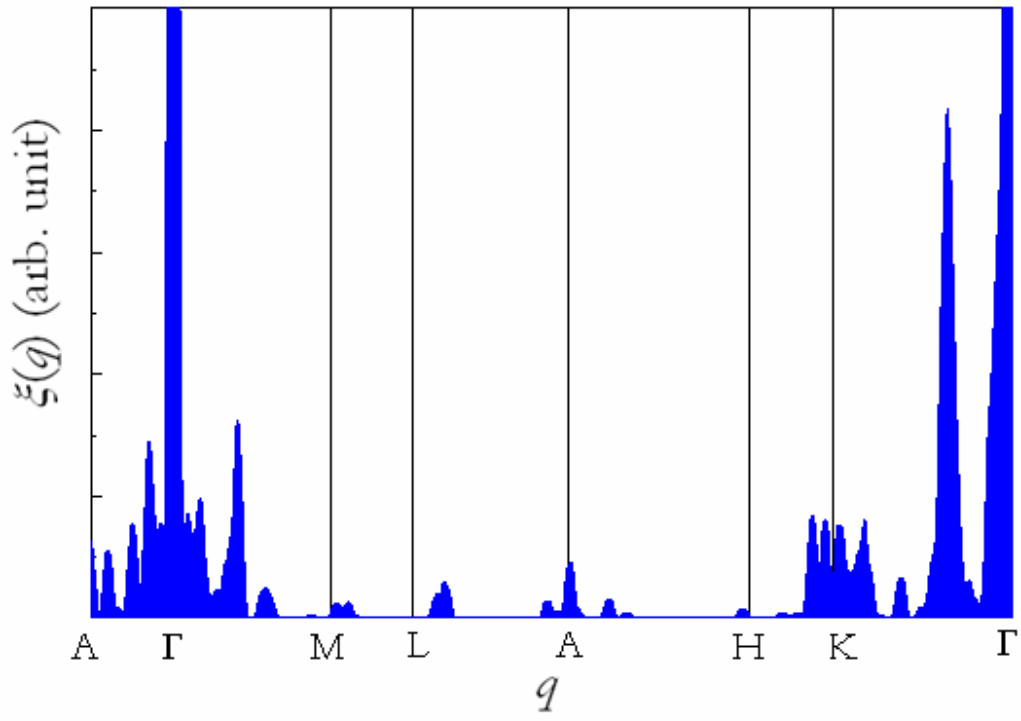

Figure 2.24. The nesting function $\xi(\vec{q})$ along several high-symmetry lines of $\vec{q}$ for HCP Xe at 200 GPa.

The calculated EPC parameter λ was found to increase from 150 GPa reaching a maximum value of 0.27 at 215 GPa. Then it decreases gradually at higher pressures (inset of Fig. 2.25). The two main factors governing λ are FS nestings, which have been quantified by the analysis of the nesting function (*vide supra*), and the electron-phonon matrix elements $g^{j}_{\vec{k}n,\vec{k}+\vec{q}m}$. The FS nesting is most significant at 200 GPa; therefore, the maximum value of λ is expected to be in the proximity provided that $g^{j}_{\vec{k}n,\vec{k}+\vec{q}m}$ does not vary drastically with pressure. In HCP Xe, as a result of a balance between FS nesting and electron-phonon matrix elements, a maximum value of $\lambda = 0.274$ is predicted at 215 GPa.

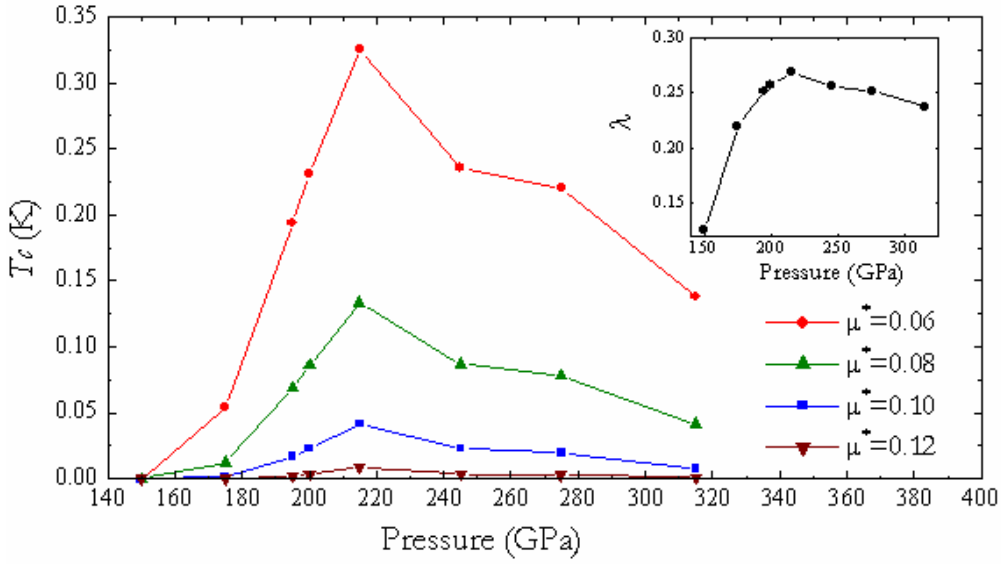

Figure 2.25. The estimated superconducting critical temperature T_c with several Coulomb pseudopotential μ^* computed at selected pressures. (Inset) The EPC parameter λ as a function of pressure.

Fig. 2.26 (a) shows the Eliashberg spectral function $\alpha^2F(\omega)$ at three different pressures. At 150 GPa, a relatively narrow band (indicated by arrow) between 160 and 210 cm^{-1} and centered at 190 cm^{-1} contributes most to the EPC. The integrated λ over this frequency range is 0.54, which constitutes 43% of the total coupling parameter. As pressure increases, the peak shifts to higher frequency and becomes broader. At 215 GPa, the peak is located at *ca*. 220 cm^{-1}. As λ is inversely proportional to the vibrational frequency, lower frequency modes are expected to contribute more effectively to the total EPC. In principle, the shift of the vibrational bands to higher frequency with increasing pressure should reduce the EPC parameter. However, from 150 GPa to 215 GPa, the height of the peak in $\alpha^2F(\omega)$ increases with pressure and this height increase overcomes the increase in frequency, *i.e.*, decrease in $1/\omega$. The net effect is that the EPC parameter λ increases within this pressure range. When the pressure is increased beyond 215 GPa, the height of the "peak" in the spectral function decreases rapidly and the peak becomes very broad. At 315 GPa, EPC is no longer localized within a narrow vibrational region. The distribution of the spectral function now covers almost the entire vibrational range. This

observation suggests that at pressure below 215 GPa, vibrational frequencies between 180 to 220 cm^{-1} contribute most significantly to the EPC. When pressure is increased further, these contributions are reduced, resulting in a net decrease of the EPC parameter. Fig. 2.26 (b) shows $\alpha^2F(\omega)$ and the integrated λ at 215 GPa projected onto individual vibrational modes. The peak centered at 210 cm^{-1} in the $\alpha^2F(\omega)$ (Fig. 2.26 (a)) is found to derive mostly from the longitudinal acoustic (LA) mode. The integrated value of λ of the LA mode between 200 and 214 cm^{-1} is 0.067 that is almost 25% of the total λ . Two transverse acoustic modes (TA1 and TA2) also contribute to this band. The transverse acoustic mode TA1 makes noticeable contribution to the total EPC parameter λ between 115 and 160 cm^{-1}. On the other hand, the TA2 mode contributes more strongly between 225 and 248 cm^{-1}. Several weaker peaks found in the optical region above 290 cm^{-1} do not contribute to the total λ as much as the acoustic modes. Among the optical modes, the transverse mode TO1 contributes most, with an integrated λ of 0.019 which is only about 18 % of the LA mode.

To fully characterize the distribution of EPC in the first BZ, the phonon linewidth of HCP Xe at 215 GPa along several high-symmetry directions are shown in Fig. 2.27 (a). Regions with large phonon linewidth are circled in red in the corresponding phonon band structure shown in Fig. 2.27 (b). The phonon linewidth of the acoustic modes shows a strong spatial anisotropy. The TA1 branch shows three broad peaks near the *M*, *L* and *K* symmetry points. From the phonon band structure, it is found that the peaks in the phonon linewidth at *M* and *L* are associated with vibrational frequencies between 120 and 200 cm^{-1}. This corresponds to the two weak low-frequency peaks in the $\alpha^2F(\omega)$ function (Fig. 2.26 (b)). The peak belonging to the TA1 mode at point *K* has vibrational frequencies between 210 and 230 cm^{-1} and also appears in the electron-phonon spectral function $\alpha^2F(\omega)$. The TA2 mode has a broadly similar distribution of phonon linewidth as the TA1 mode, with the higher energy vibrations having a larger phonon linewidth. The LA mode shows two sharp peaks along the $\Gamma \rightarrow M \rightarrow L$ direction corresponding to vibrations spanning from 180 to 220 cm^{-1}. Evidently, these are the dominant phonons giving the large integrated λ for the LA mode near the 210 cm^{-1} band in $\alpha^2F(\omega)$ as

discussed earlier. Other LA phonons with large linewidths around the *K* symmetry point contribute to the EPC between 260 and 300 cm^{-1}. The LO phonon shows a sharp increase in the linewidth at *K* with minor peaks at several high symmetry points. Weighed by relatively high vibrational frequencies, these modes do not contribute significantly to the EPC parameter.

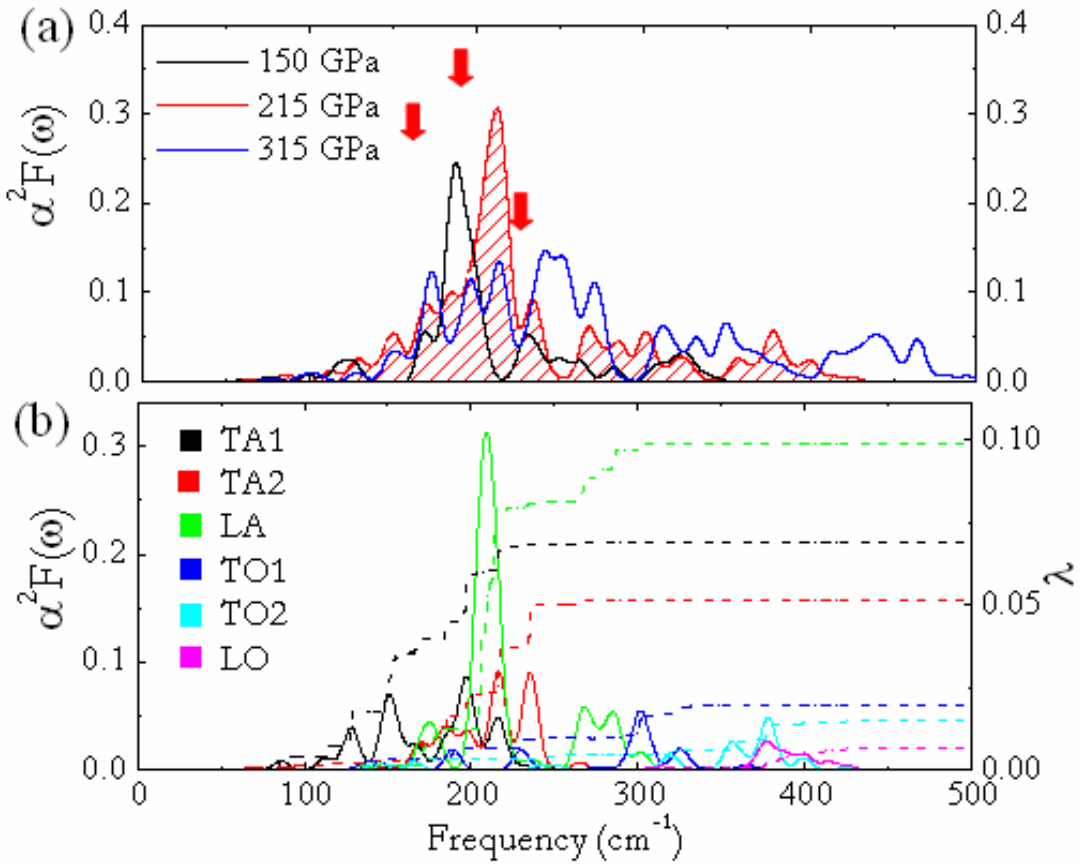

Figure 2.26. The Eliashberg spectral function $\alpha^2F(\omega)$ as a function of vibrational frequency computed at selected pressures. (a) The $\alpha^2F(\omega)$ computed at three pressures. The arrows show the evolution of the most distinct peaks at the three pressures. (b) The projected $\alpha^2F(\omega)$ on different vibrational modes (solid curves) and the integrated λ from each mode (dash-dot curves) as a function of vibrational frequency, obtained at 215 GPa.

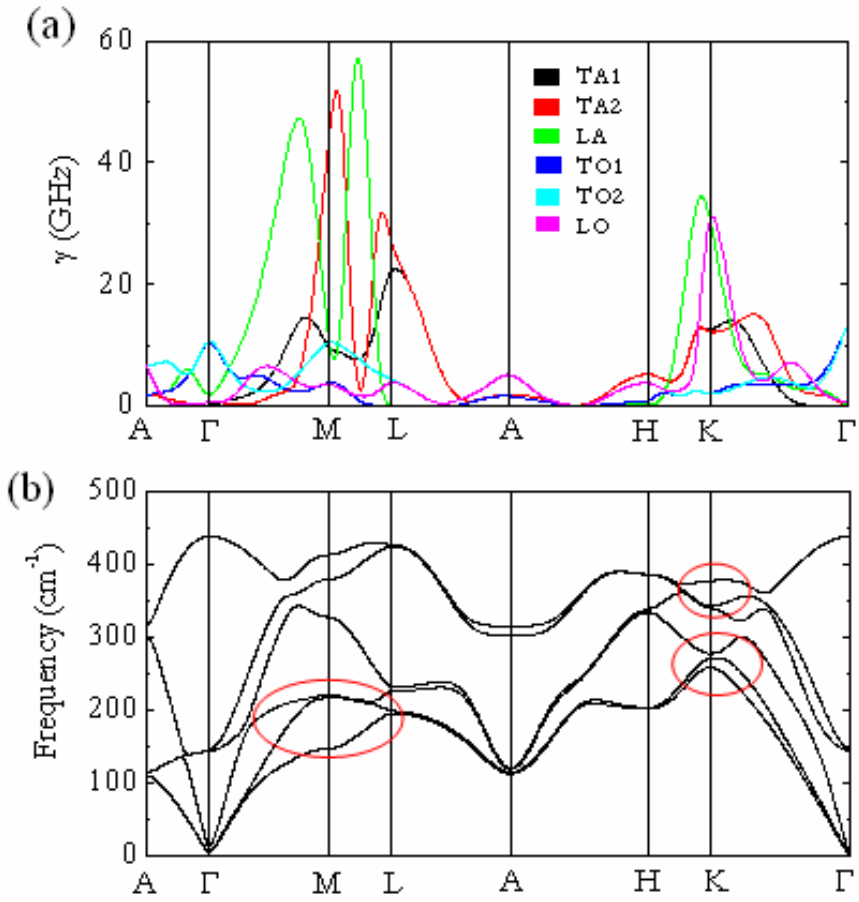

Figure 2.27. (a) The phonon linewidth at 215 GPa along several high-symmetry directions in the first BZ. (b) The phonon band structure computed at 215 GPa.

In summary, the possible superconductivity of HCP Xe has been studied for pressure between 150 and 315 GPa. An ETT is found around 200 GPa. This transition is due to a change in the topology of the FS as a result of the crossing of a conduction band below the Fermi level leading to an anomaly in the ***c*/*a*** ratio. The EPC was found to increase with pressure and to be maximized at 215 GPa. The EPC is facilitated by nestings of the FS. Lattice dynamics and phonon linewidth calculations show that the EPC of HCP Xe is dominated by acoustic vibrations, especially the longitudinal vibrations with frequencies between 200 cm^{-1} and 214 cm^{-1}. The EPC strength was found to be localized around a few high-symmetry points in the first BZ. The logarithmic average of the phonon frequencies ω_{log}, however, was found to be rather small and not

enough to support a superconducting critical temperature T_c higher than 0.04 K (μ^*=0.1) at 215 GPa. The predicted T_c is achievable with current experiment techniques.

2. 7 A perspective

In this chapter, through state-of-the-art numerical computations, the superconducting properties of several high-pressure solids were investigated based on the Migdal-Eliashberg theory [58-61] within the framework of the BCS model [67]. The selected materials, Li, Xe, and Group IV hydrides, each represents a group of chemically distinct system. Alkali metal Li, at ambient conditions behaving like a nearly free-electron gas, has been found to be superconducting with T_c up to 17K under pressure [69-71]. Noble gas Xe is well known for being chemically inert at ambient pressure [72]. However, under pressure, it was predicted that solid Xe could be superconducting albeit with a comparatively low T_c of ~ 0.04 K. Group IV hydrides were predicted as good superconductors under high pressure, where the hydrogen atoms are pre-compressed by heavier Group IV atoms and possess high-frequency vibrations [73-76]. This prediction is supported by the recent experiments on SiH_4, in which the pressure-induced superconducting state was found and T_c up to 17 K was observed [78].

These investigations have revealed several characteristic features in lattice or electronic structures lead to the pressure-induced superconductivity. These features are,

1. High-frequency phonons. High-frequency phonons will increase the logarithmic average of phonon frequencies $\omega_{\log}$, and therefore enhance the EPC. This is the reason that dense pure hydrogen is expected to have very strong EPC and high T_c. The hydrogen atom is the lightest element and possesses the high M-H (M=metal) vibrational frequency in the solid. In the high-pressure phase SnH_4, the high-frequency phonons, are the molecular-like H-H vibrations with frequencies as high as 2800 cm^{-1} [75].

2. Soft phonon modes. All materials studied in this chapter share one common feature, the softening in their phonon band structures. The phonons of the soft modes are strongly coupled and raise the partial EPC to a very high value without causing structural instability. These soft modes are usually localized in a small region of the first BZ. However, their contributions to the total EPC are crucial. For FCC Li, T_c can be as high as 20 K with only the modes near the *K* point strongly coupled [140].

3. FS nestings. Through the study on SnH_4 and Xe, it is observed FS nesting and phonon softening are strongly coupled to each other and contribute significantly to the EPC. Indeed, both FS nesting and phonon softening indicate the structure is close to electronic and structural instability, respectively. Thus, the system is in the proximity of structural phase transition, and this may be stabilized by a transition to superconducting states. In the quantum mechanical description of the EPC in Eq. (2.14), two factors governing EPC and FS nesting, are (i) the possibility of two electrons being paired and (ii) the magnitude of the electron-phonon matrix elements $g^{j}_{\vec{k}n,\vec{k}+\vec{q}m}$ reflecting the strength of the pairing. In all the superconducting materials examined in this thesis, FS nesting is the major driving force for superconductivity. The analysis of FS nesting gave information for a qualitative estimate of the EPC. This analysis is very useful especially when quantitative calculations are not feasible for very large system. For example, Fig. 2.28 shows the 2D and 3D FS of pristine c-C_{60} [115]. FS nestings are expected to exist along the vectors indicated in the figure. Without explicit calculation of EPC, which is not feasible for this complicated system, one can reasonably suggest from the possibility of FS nesting may lead to electronic instability and the enhancement of EPC.

4. Kohn anomalies. Kohn anomaly is a special case of FS nesting with a nesting vector of $2\vec{k}_F$. As shown in the case of SnH_4 (Fig. 2.17), the system underwent a substantial phonon renormalization to lower frequencies at the boundary of the first BZ where the Kohn anomalies happen. This process is accompanied by strong EPC (Fig. 2.20).

5. Parallel electronic bands. The appearance of parallel bands in the electronic band structures is a promising condition for superconductivity. Eq. (2.24) shows that the FS nesting becomes larger when the velocities of two electrons are small and/or collinear. The velocity of an electron is the derivative of its electronic band with respect to momentum. Collinear velocities mean that the two electronic bands are parallel. Small velocity of electrons means that their electronic bands are rather flat and non-dispersive.

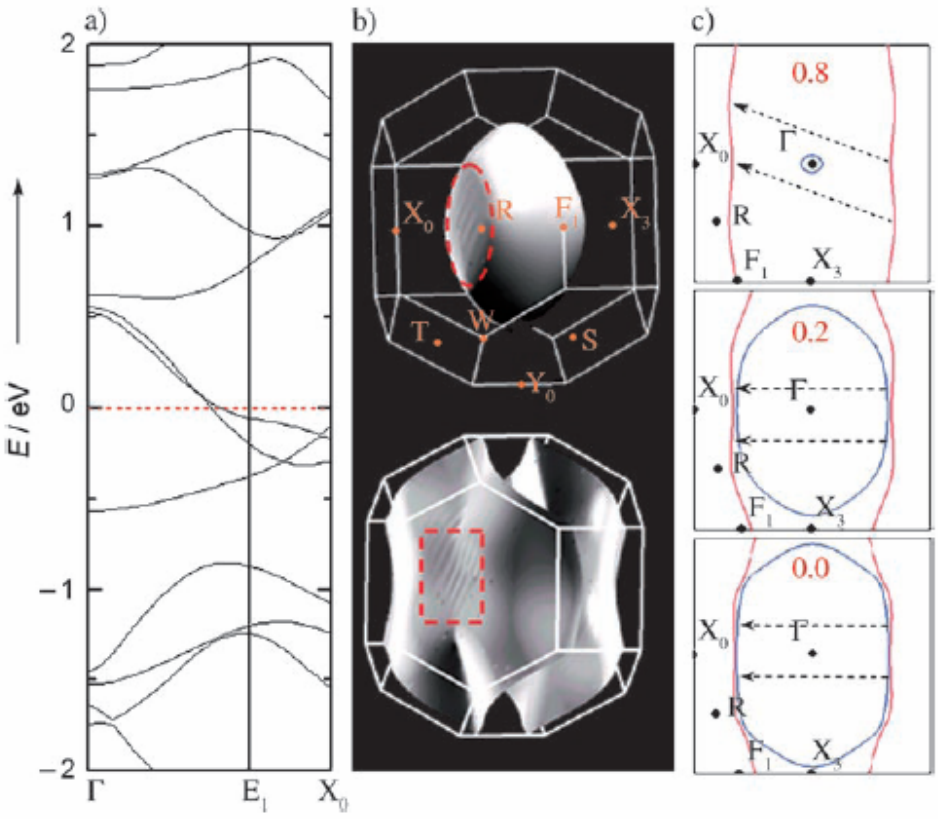

Figure 2.28. (a) The electronic band structure of pristine c-C60 along the G-E_1-X_0 direction. (b) FS for the two bands crossing the Fermi level. (c) 2D cross sections of FS at different k_y values (planes perpendicular to Γ-Y_0 and parallel to the Γ-X_0-X_3 plane) in the first BZ. Arrows indicate possible nesting vectors.

Through detail analysis of electronic and phonon structures, relevant properties

that affect superconductivity in high-pressure solids are generalized above. It is hoped that these understandings can encourage further studies on superconductivity.

CHAPTER 3

Vibrational spectra and electronic structures of high-pressure materials

The IR and Raman absorptions are results of interactions between the lattice vibrations and incident EM field. These are the two widely used spectroscopic techniques to characterize materials. The vibrational spectra probe the potential energy surface of the atoms in the neighborhood of the equilibrium lattice geometry, and thus provide information on structural properties and chemical bonds. IR measures the change in the electric dipole moment and Raman measures the change in the polarizability of the system with lattice vibrations. The EM radiations used in IR and Raman experiments have frequency region between 400 cm^{-1} and 8000 cm^{-1}. The vibrational frequencies of all materials are well within this frequency range. For example, at ambient pressure, the highest reachable vibrational frequency is the H-H stretching in hydrogen molecule, where the frequency is 4200 cm^{-1}. At high pressure, the vibrational frequencies of solids will increase due to enhanced inter-atomic force constants, but are still within the IR range. Only zone center phonons are responsible for the IR and Raman absorptions. Moreover, the IR and Raman absorptions must satisfy specific selection rules.

In this chapter, first-principles calculations of IR and Raman spectra are presented for the high-pressure structures of solid H_2, O_2, and SiH_4. The theoretical results will be compared with available experimental results to assist the characterization of the high-pressure structures. The calculations were performed using the PSPW method within the framework of the DFT [62]. The derivatives of total energy, namely Born effective

charges, polarizability tensors, and Raman tensors were calculated with the DFPT [9]. Details of the theoretical framework will be presented below.

Another subject to be presented in this chapter is the characterization of chemical bonding of a high-pressure solid using the Bader's AIM method [79-81]. The AIM method is based on the analysis of the gradient and Laplacian of the electron density $\rho(\vec{r})$, and offers several advantages over that of the inspection of charge density and/or the ELF technique. First of all, weak features associated with slight variation in the electron density are amplified from the analysis of the derivatives of the charge density. Second, the assignment of a "bond" is based on unambiguous and formal definitions derived from characteristics of the derivatives of the charge density. The AIM method has been employed extensively mostly with great successes for the characterization of chemical bonds in molecular phases. The application of AIM method to solid state structure is new [163-165]. In this chapter, this method was applied to characterize the chemical bonding of the high-pressure ε phase of solid O_2, in which the structure has only been resolved by experiments recently [82, 83].

3. 1 Introduction

3. 1. 1 IR spectrum

When EM radiation interacts with a crystal, the charge distributions will be perturbed by the electric field of the EM waves. This perturbation results in oscillations of the atoms and induces electric dipole transitions within the lattice. In ionic crystals, a long-range macroscopic electric field can also arise from the long wave ($\vec{q}$ ~0) longitudinal optical (LO) vibrations. Since separations between positive and negative ions are changed in the LO vibrations, a macroscopic electric field will be induced and altered the restoring Coulomb forces between ions. These restoring forces will change the frequencies of the LO vibrations and lead to the well known LO-TO splitting phenomenon in ionic crystals [166, 167]. To compute the change of the dipole moment

subject to the lattice vibrations, it is convenient to expand the dipole moment with respect to the normal coordinates of the vibrational modes,

$$\mu_\alpha = \mu_\alpha^0 + \sum_m \left(\frac{\partial \mu_\alpha}{\partial q^m} \right)_0 q^m + O[(q^m)^2]. \tag{3.1}$$

Here α is the Cartesian component x, y, and z. The derivative is evaluated at the equilibrium geometry. The q^m is the normal coordinates associated with the m-th vibrational mode and can be converted to the atomic displacements in Cartesian coordinates by the relation,

$$u_{i,\beta}^m = q^m U_{i,\beta}^m, \tag{3.2}$$

where $u_{i,\beta}^m$ is the atomic displacement of the i-th atom along Cartesian direction β caused by the m-th vibrational mode. The $U_{i,\beta}^m$ is the eigenvector of this mode. The IR intensity of the m-th vibrational mode, essentially proportional to the induced change of the dipole moment, is given by [168]

$$I_{IR}^m \propto \sum_\alpha \left| \frac{d\mu_\alpha}{dq^m} \right|^2. \tag{3.3}$$

Substituting Eq. (3.2) into Eq. (3.3), the IR intensity can be rewritten as

$$I_{IR}^m \propto \sum_\alpha \left| \sum_i \sum_\beta \frac{\partial \mu_\alpha}{\partial u_{i,\beta}} U_{i,\beta}^m \right|^2. \tag{3.4}$$

Using the definition of the Born effective charge, Eq. (3.4) can be represented by [46, 169]

$$I_{IR}^{m} \propto \sum_{\alpha=1} \left| \sum_{i=1} \sum_{\beta=1} Z_{i,\alpha,\beta}^{*} \cdot e_{i,\beta}^{m} \right|^{2}, \tag{3.5}$$

Here $e_{i,\beta}^{m}$ is the atomic displacement eigenvector that is normalized to the atomic displacement by the square root of atomic mass. The evaluation of IR intensity requires the knowledge of the eigenvalues and eigenfunctions of zone center phonons and the associated Born effective charges, both quantities are related to the second derivatives of the total energy and can be calculated using DFPT [9]. The Born effective charge is defined as

$$Z_{i,\alpha,\beta}^{*} = \Omega_0 \frac{\partial P_{mac,\alpha}}{\partial u_{i,\beta}}, \tag{3.6}$$

where $P_{mac,\alpha}$ is the macroscopic polarization in direction α and Ω_0 is the unit cell volume. The Born effective charge describes the change of polarization in direction α caused by the atomic displacement in direction β. In the presence of electric field $\vec{\varepsilon}$, the electric enthalpy of the system is

$$\widetilde{F}(\vec{\varepsilon}) = E_{total}^{0} - \Omega_0 \sum_{\alpha} P_{mac,\alpha} \cdot \varepsilon_{\alpha}, \tag{3.7}$$

where E_{total}^{0} is the total energy of the system in the ground state. Therefore,

$$P_{mac,\alpha} = -\frac{1}{\Omega_0} \frac{\partial \widetilde{F}(\vec{\varepsilon})}{\partial \varepsilon_{\alpha}}. \tag{3.8}$$

Substituting Eq. (3.8) into Eq. (3.6), it is clear that the Born effective charge is a second derivative of the electric enthalpy [169],

$$Z^*_{i,\alpha,\beta} = -\frac{\partial^2 \widetilde{F}(\vec{\varepsilon})}{\partial \varepsilon_\beta \partial u_{i,\beta}}. \tag{3.9}$$

3. 1. 2 Raman spectrum

Raman spectrum is associated with the change of polarizability during the lattice vibrations. Therefore, when the polarizability changes with particular lattice vibrations, these vibrational modes are Raman active. Similar to the analysis of the IR spectrum, the polarizability of the system can be related with the vibrational modes [169],

$$\alpha_{\alpha,\beta} = \alpha^0_{\alpha,\beta} + \sum_m \left(\frac{\partial \alpha_{\alpha,\beta}}{\partial q^m} \right)_0 q^m + O[(q^m)^2]. \tag{3.10}$$

Here the polarizability tensor $\alpha_{\alpha,\beta}$ is the second derivative of the electric enthalpy,

$$\alpha_{\alpha,\beta} = -\frac{\partial^2 \widetilde{F}(\vec{\varepsilon})}{\partial \varepsilon_\alpha \partial \varepsilon_\beta}. \tag{3.11}$$

The polarizability $\vec{\alpha}$ describes the strength of induced dipole moment with external electric field,

$$P_{mac,\alpha} = \alpha_{\alpha,\beta} \varepsilon_\beta. \tag{3.12}$$

The incident EM wave can be represented as

$$\varepsilon_\beta = A_0 \cos(\omega_{in} t), \tag{3.13}$$

where A_0 is the amplitude and ω_{in} is the angular frequency. If the lattice vibrations behave as harmonic oscillations, for each vibrational mode q^m the instantaneous displacement can be written as,

$$q^m = q_0^m \cos(\omega_{vib}^m \cdot t)\,. \tag{3.14}$$

With quantized vibrational energies,

$$E_{vib}^m = \left(n + \frac{1}{2}\right)\hbar\omega_{vib}^m\,,\ n = 0,\ 1,\ 2\ldots \tag{3.15}$$

The interaction between the vibrational modes and incident EM waves can be readily deduced by substituting Eq. (3.14) into Eq. (3.10), and then substituting Eq. (3.10) into Eq. (3.12),

$$P_{mac,\alpha} = \alpha_{\alpha,\beta}^0 A_0 \cos(\omega_{in} t) + \frac{A_0 q_0^m}{2} \sum_m \left(\frac{\partial \alpha_{\alpha,\beta}}{\partial q^m}\right)_0 [\cos(\omega_{in} - \omega_{vib}^m)t + \cos(\omega_{in} + \omega_{vib}^m)t]\,. \tag{3.16}$$

From the above equation, the induced dipole moments will be created at three distinct angular frequencies, namely ω_{in}, $\omega_{in} - \omega_{vib}^m$, and $\omega_{in} + \omega_{vib}^m$. The first term in Eq. (3.16) is corresponding to the elastic scattering in which the frequency ω_{in} of the EM wave and the polarizability $\alpha_{\alpha,\beta}^0$ of the system do not change during the scattering procedure. The other two terms are related to inelastic scattering in which the frequency of the EM wave decreases/increases and the polarizability of the system changes during the scattering procedure. These two scattering procedures are known Raman scattering, with the energy-loss referred to Stokes scattering, and the energy-gain referred to anti-Stokes scattering [170, 171]. The Raman intensity associated with the *m*-th vibrational mode is

$$I_{Raman}^m \propto \left|\hat{e}_S \frac{\partial \alpha}{\partial q^m} \hat{e}_L\right|^2\,, \tag{3.17}$$

where $\hat{e}_S$ and $\hat{e}_L$ are the polarization vectors for the scattered and incident EM waves.

After angular average in the entire space, Eq. (3.17) becomes [168]

$$I_{Raman}^{m} \propto 45\alpha'^{2}_{m} + 7\gamma'^{2}_{m}, \tag{3.18}$$

with

$$\alpha'_{m} = \frac{1}{3}(T_{11}^{m} + T_{22}^{m} + T_{33}^{m}), \tag{3.19}$$

and

$$\gamma'^{2}_{m} = \frac{1}{2}\{(T_{11}^{m} - T_{22}^{m})^2 + (T_{11}^{m} - T_{33}^{m})^2 + (T_{22}^{m} - T_{33}^{m})^2 + 6[(T_{12}^{m})^2 + (T_{13}^{m})^2 + (T_{23}^{m})^2]^2\}. \tag{3.20}$$

In the above equations the tensor $T_{\alpha,\beta}^{m}$ is the Raman tensor, which is the first derivative of the polarizability tensor with respect to the normal-mode coordinates q^m,

$$T_{\alpha,\beta}^{m} = \frac{\partial \alpha_{\alpha,\beta}}{\partial q^{m}}. \tag{3.21}$$

Since the polarizability tensor is the second derivative of the electric enthalpy, to obtain the Raman tensor, third derivatives of the electric enthalpy needed to be calculated. The third derivative can be calculated within the framework of DFPT using the 2*n*+1 theorem (see section 1. 2).

3. 1. 3 AIM analysis

The basic idea of the AIM analysis is to extract bonding information from the electron density $\rho(\vec{r})$ in molecules or solids [79-81]. The analysis of the electron density gradient $\nabla\rho(\vec{r})$ helps to define an atom within a molecule or solid. Since the electron density $\rho(\vec{r})$ is a continuous variable of electron coordinates, it is not well defined how to partition electrons amongst fragments of the system such as atoms. The AIM analysis

is a scheme to divide a molecule into atomic regions based on the electron density gradient $\nabla\rho(\vec{r})$. In a solid or molecule, the atomic regions are defined by the 'zero flux surfaces' (Fig. 3.1), where there is no flux from the electron density gradient $\nabla\rho(\vec{r})$. Therefore,

$$\nabla\rho(\vec{r}_s)\cdot\vec{n}(\vec{r}_s)=0\,. \tag{3.22}$$

Here $\vec{n}(\vec{r}_s)$ is the unit vector normal to the surface at position $\vec{r}_s$.

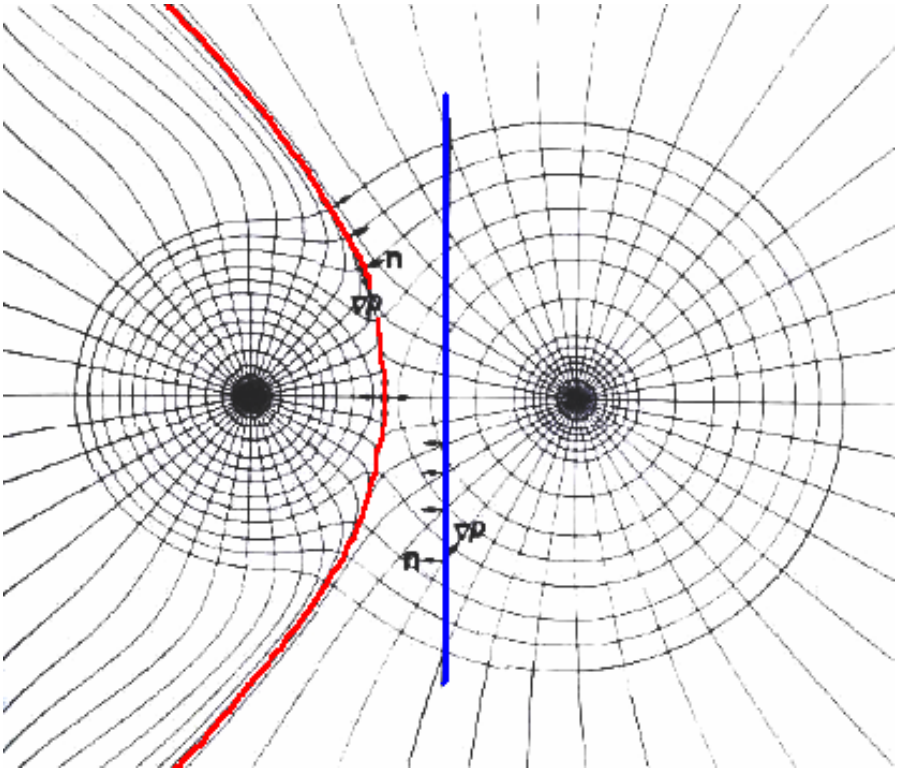

Figure 3.1. The contour map of the electron density $\rho(\vec{r})$ for a diatomic molecule. The curve in red color denotes the 'zero flux surface' that is not crossed by any trajectory of the electron density gradient $\nabla\rho(\vec{r})$. The line in blue color shows an arbitrary surface

that does not satisfy the 'zero flux' boundary conditions. This figure is taken from http://www.chemistry.mcmaster.ca/aim. Similar figure can be found in Ref . 79.

The analysis of the electron density minima and maxima, *i.e.*, at critical points (CP), $\vec{r}_{cp}$ for which $\nabla\rho(\vec{r}_{cp}) = 0$, allows the characterization of the nature of interactions. Once the CP $\vec{r}_{cp}$ points are located and the curvature with respect to the spatial directions calculated, (*i.e.*, the second derivative — Laplacian, $\nabla^2\rho(\vec{r}_{cp})$, or Hessian matrix), different classes of CP's can be distinguished. Each CP is quantified by its principal curvatures, *i. e*\., the eigenvalues of the Hessian matrix. An ordered pair of integers (*n*, *m*) designates its rank (*n* — number of non-zero eigenvalues) and signature (*m* — the difference between the number of positive and negative eigenvalues). For example, in the atomic nuclei, all curvatures in the three mutually perpendicular directions are negative and $\rho(\vec{r})$ is a local maximum at $\vec{r}_{cp}$. These points are classified as (3, -3) CP's. Along the bond direction between two atoms, two curvatures are negative and $\rho(\vec{r})$ is a maximum at $\vec{r}_{cp}$ in the plane defined by their corresponding axes and is a minimum at $\vec{r}_{cp}$ along the third axis that is perpendicular to this plane. This CP is defined as (3, -1). When there is a bond between two atoms, it is observed that two (3, -3) CP's are connected by one and only one gradient line that presents a (3, -1) bond critical point (BCP) in the limit between both basins (Fig. 3.2). This is a signature for the occurrence of a chemical bond. The gradient line connecting both nuclei defines the 'bond path'. The value of $\rho(\vec{r}_{cp})$ at a BCP gives a loose indication of bond strength. In a similar manner, a (3, +1) CP can be assigned where two curvatures are positive and $\rho(\vec{r})$ is a minimum at $\vec{r}_{cp}$ in the plane defined by their corresponding axes. The $\rho(\vec{r})$ is a maximum at $\vec{r}_{cp}$ along the third axis which is perpendicular to this plane. Such CP's are detected somewhere within a ring structure, and therefore, they are also called ring critical points (RCP). Finally a (3, +3) CP, or cage critical point (CCP), is identified

when all curvatures are positive and $\rho(\vec{r})$ is a local minimum at $\vec{r}_{cp}$. These correspond to a cage structure with a (3, +3) point found inside the cage structure.

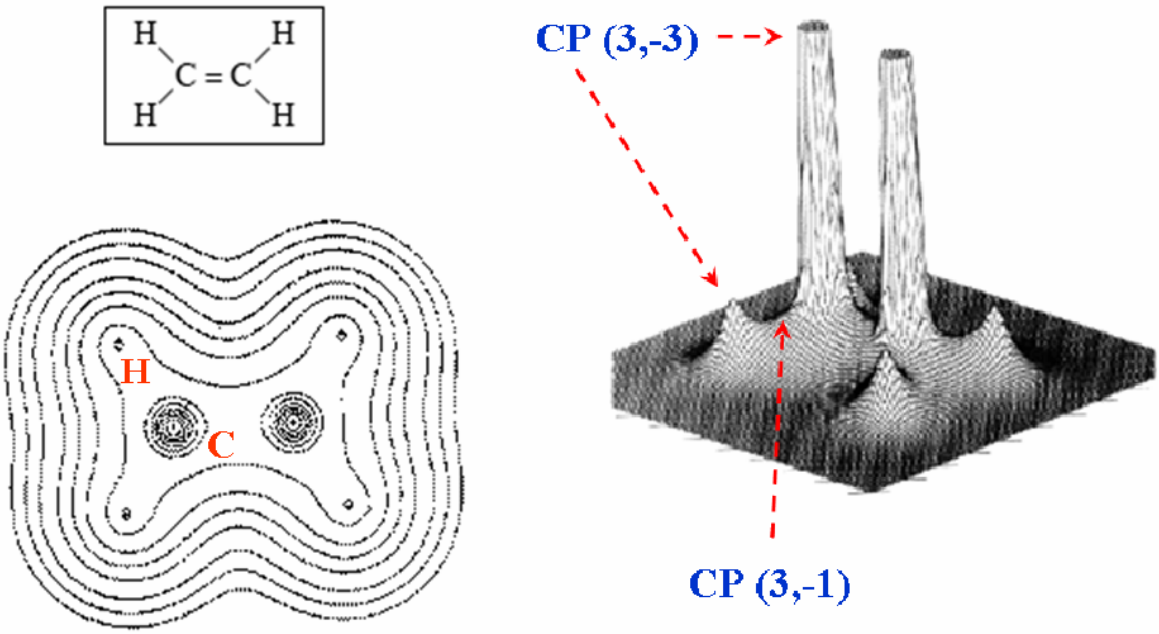

Figure 3.2. A display of the electron density $\rho(\vec{r})$ for an ethene molecule. (Left) The contour map of $\rho(\vec{r})$ projected on the plane that contains two carbon and four hydrogen nuclei. (Right) The three dimension view of $\rho(\vec{r})$. The absolute maxima in $\rho(\vec{r})$ at the carbon nuclei are not shown completely because of their large values. This figure is taken from http://www.chemistry.mcmaster.ca/aim. Similar figure can be found in Ref . 79.

Further information can be obtained once the CP's of a given molecule are defined. The energy at a CP $H(\vec{r}_{cp})$ can be used to distinguish between covalency and ionicity. The $H(\vec{r}_{cp})$ is defined as [172, 173]

$$H(\vec{r}_{cp}) = G(\vec{r}_{cp}) + V(\vec{r}_{cp}), \tag{3.23}$$

where G and V stand for the kinetic and potential energies, respectively. The local virial theorem is written as

$$\frac{1}{4}\nabla^2\rho(\vec{r}) = 2G(\vec{r}) + V(\vec{r}) \ . \tag{3.24}$$

Combining these formulas, the energy at a CP is

$$H(\vec{r}_{cp}) = \frac{1}{4}\nabla^2\rho(\vec{r}_{cp}) - G(\vec{r}_{cp}) \ . \tag{3.25}$$

Since the kinetic energy $G(\vec{r}_{cp})$ is always > 0 and $V(\vec{r}_{cp})$ is always < 0, when $H(\vec{r}_{cp}) < 0$, the potential energy dominates over the kinetic energy in $\vec{r}_{cp}$, the electronic charge stabilizes the system, indicating a covalent bond. On the other hand, when the kinetic energy dominates over the potential energy, the electronic charge at this point destabilizes the system, and $H(\vec{r}_{cp})$ has a positive value and may correspond to closed-shell interactions or an ionic bond. The value of $\rho(\vec{r}_{cp})$, electron density at the BCP, gives a loose indication of bond strength. For a "regular" shared bond, $\rho(\vec{r}_{cp})$ is generally quite high (> 10^{-1} *a.u.*) and so is the Laplacian. In contrast, for a weak "closed-shell" interaction, $\rho(\vec{r}_{cp})$ is substantially smaller (~10^{-2} *a.u.*) and the Laplacian is often positive. It should be emphasized that the topology of the charge density is not a consequence of the geometry. Locations of the critical points are determined by the electron density distribution that is governed by the quantum mechanics of the system.

3. 2 IR and Raman spectra of high-pressure phase III of hydrogen

Solid molecular hydrogen at high pressure has been one of the most challenging research topics for many decades. The strong IR absorption observed at about 150 GPa is a subject that has been investigated often and its understanding is essentially dependent

on the detailed structures of solid hydrogen [112, 174]. Previous studies proposed candidate structures and interpretations [84, 85, 175] for the origin of the sudden increase of IR absorption in the phase III of hydrogen at pressure above 150 GPa. Phase III occupies an unique position in the pressure-induced phase diagram of solid hydrogen. It was found that the IR activity of H_2 vibrons increases dramatically from its precursor phase II. This observation led to the hypothesis on the formation of a charge-transfer complex with an increasing band gap. This suggestion is intriguing since it is suggested that solid hydrogen may not be metallic at high pressure. Recently, based on the theoretically calculated melting curve [176, 177], it was speculated that hydrogen may even become a novel superfluid with superconducting properties [178]. Therefore, the knowledge of the crystal structure for this important phase III is critical. However, the determination of the structures of high-pressure phases of hydrogen is experimentally challenging. Intensity of the X-ray diffraction pattern is expected to be very low and it is difficult to determine the positions of the hydrogen atoms. In principle, it is possible to determine the positions of hydrogen atoms with neutron scattering experiments. However, current technology limits the reachable pressure in neutron experiments under 40 GPa. With these difficulties, the structure of the high-pressure phase III of hydrogen remains unknown. On the other hand, useful structural information can be deduced from the spectroscopic studies, *i.e.*, the IR and Raman experiments. This information might be used as a diagnostic tool to differentiate among proposed structural models. Over the years, many candidate structures have been predicted for phase III of hydrogen through theoretical calculations [84-86]. Among these structures, an orthorhombic *Cmcm* structure was found to be dynamically stable and considered as a promising model [85]. A very recent application of the quasi-random method (A brief description is presented in Chapter 4) to search for stable structures of high-pressure phases of hydrogen, however, obtained a new monoclinic structure with *C*2/*c* space group [44, 86]. To examine this new structure and compare it with the previous *Cmcm* structure, in this section the structures and spectroscopic properties of the *C*2/*c* and *Cmcm* structures are investigated and compared with experimental data. It is found that these two structures have similar structural feature and their spectroscopic properties such as high IR intensity agree with experimental findings near 160 GPa. The Raman and IR spectra as well as the detailed

phonon stabilities of the *C*2/*c* and *Cmcm* structures are examined. The pressure dependence of the IR absorption intensity of the *C*2/*c* structure is shown to be in excellent agreement with experiment.

PSPW first-principles calculations have been performed within the framework of DFPT with the electronic structure package Quantum-ESPRESSO [62] using the PBE GGA. The electronic wavefunction and the charge density were expanded with a kinetic energy cutoff of 80 and 320 Ry, respectively. MP meshes were used for the first BZ integrations in the electronic calculations (*k*-mesh), and the BZ sampling in phonon calculations (*q*-mesh). The electronic band energies were computed with 16×16×16 and 10×20×20 MP *k*-meshes for the *C*2/*c* and *Cmcm* structures, respectively. For the *C*2/*c* structure, individual phonon calculations were performed on a 4×4×4 MP *q*-mesh with a 8×8×8 MP *k*-mesh for the first BZ integrations. For the *Cmcm* structure, individual phonon calculations were performed on a 5×10×10 MP *q*-mesh with a 6×12×12 MP *k*-mesh for the first BZ integrations. Born effective charges, IR and Raman intensities were obtained using DFPT as implemented in the Quantum-ESPRESSO package.

The crystal structures optimized at 160 GPa and the pressure dependence of the enthalpies of the two candidate structures, orthorhombic *Cmcm* and monoclinic *C*2/*c*, are shown in Figs. 3.3 and 3.4. Within this pressure range, the *C*2/*c* structure is lower in enthalpy by ~0.05 eV/atom than the *Cmcm* structure. At 160 GPa, the optimized atomic coordinates and site symmetries for the *C*2/*c* structure are H1: 8*f* 0.1273 0.4460 0.2208; H2: 8*f* 0.2574 0.3314 0.2432; H3: 4*e* 0.00 0.0957 0.250; H4: 4*e* 0.00 0.8521 0.250 with lattice constants a = 5.368, b = 3.063, c = 3.286 Å, and β = 123.19º. At 150 GPa, the optimized coordinates for the *Cmcm* structure are H1: 8*g* 0.8689 0.2919 0.7500; H2 8*g* 0.7525 0.4231 0.7500; H3 4*c* 0.0000 0.6563 0.7500; H4 4*c* 0.0000 0.8997 0.7500 with lattice constant a = 5.319, b = 3.093 and c = 2.798 Å. The *C*2/*c* structure is closely related to the *Cmcm* structure as seen in Fig. 3.3. Both structures are planar but the principal difference is the monoclinic *C*2/*c* structure resulting from a slight compression and shearing of planes. The critical feature of the *C*2/*c* structure is the different molecular H–H bond lengths. At 160 GPa these bond lengths are 0.749 and 0.743 Å and

occur in a 2:1 ratio. This is similar to an earlier structure obtained by first-principles molecular dynamics study, but in that study the shorter bonds were more prominent and the H_2 molecules slightly non-planar.

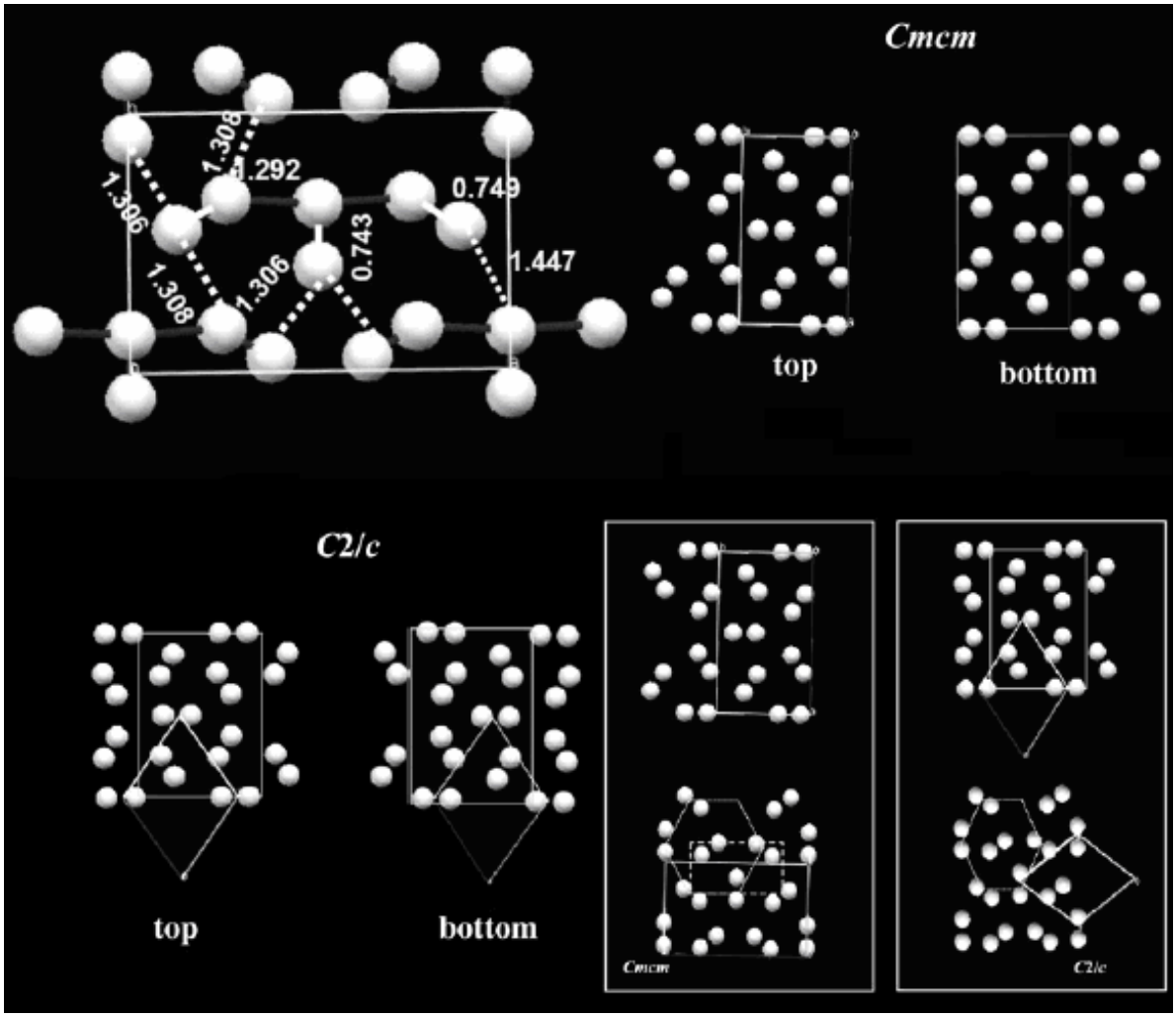

Figure 3.3. Perspective views of two candidate structures of solid hydrogen optimized at 160 GPa. The dotted lines connect adjacent hydrogen atoms.

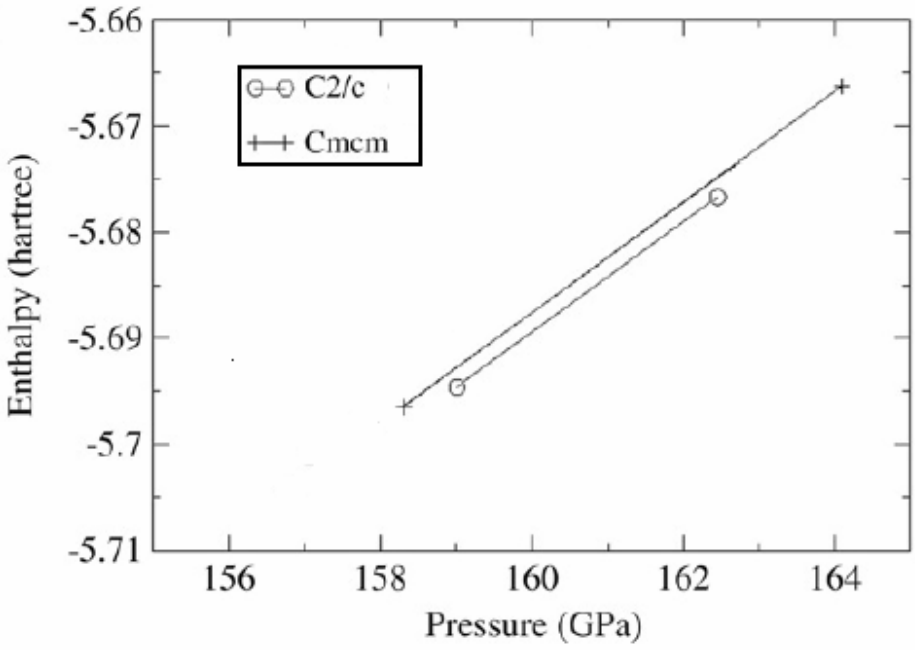

Figure 3.4. Comparison of enthalpies of the *C*2/*c* and *Cmcm* structures near 160 GPa.

The calculated phonon band structures shown in Figs. 3.5 and 3.6 confirm that both the *C*2/*c* and *Cmcm* structures are dynamically stable in the absence of imaginary frequency modes. Additional phonon calculations establish the stability range of these two structures to be between 150 GPa and 200 GPa. The two structures have essentially identical phonon DOS at 150 GPa, with the *C*2/c structure having slightly lower frequencies in the vibron region.

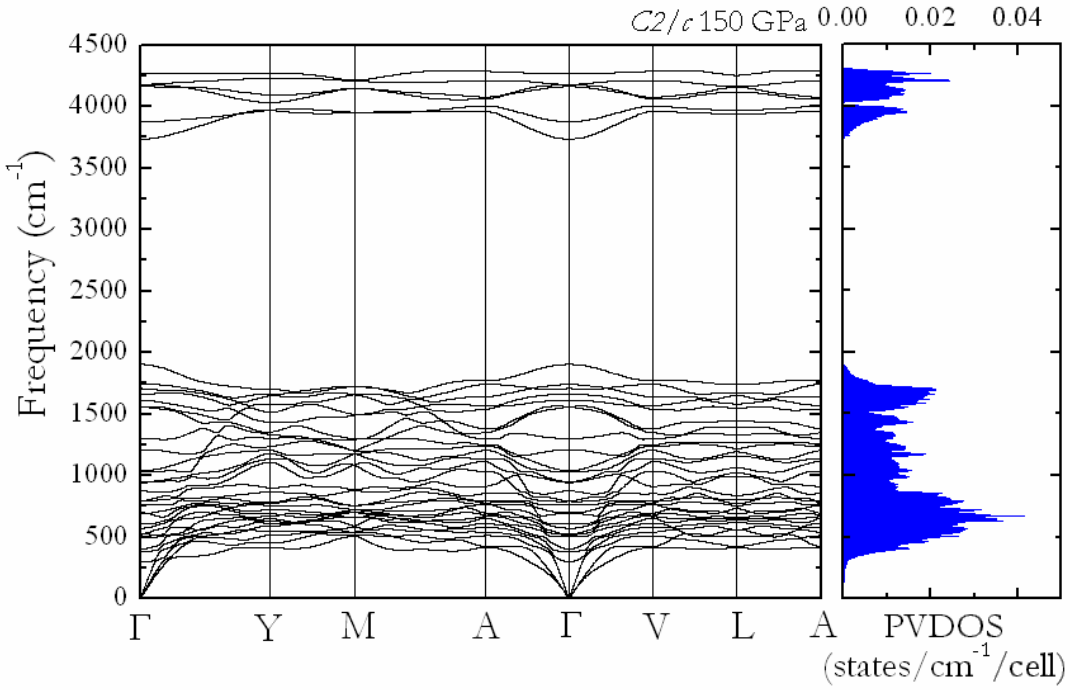

Figure 3.5. Phonon band structure and DOS for the *C*2/*c* structure calculated at 150 GPa.

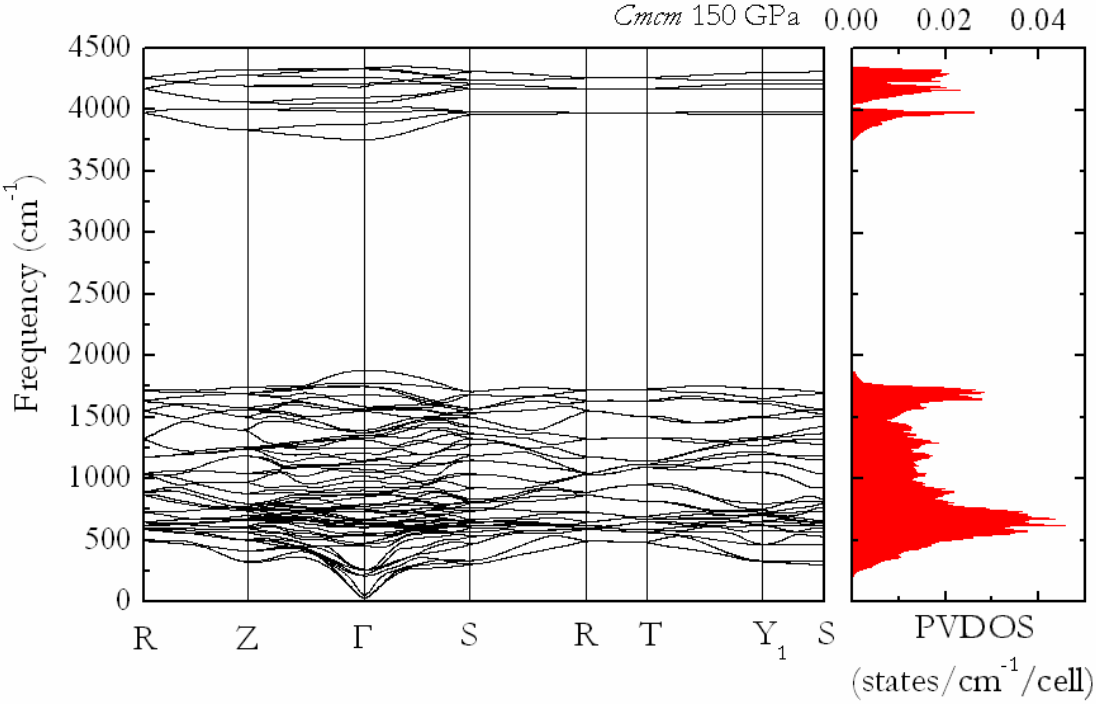

Figure 3.6. Phonon band structure and DOS for the *Cmcm* structure calculated at 150 GPa.

The IR and Raman spectra of the *C*2/*c* and *Cmcm* structures calculated at several pressures are presented in Fig. 3.7. To mimic experiment, a Gaussian width of 50 cm^{-1} was used to broaden the calculated spectra. The calculated and experimental [179] pressure dependences of the infrared active modes are compared in Fig. 3.8. In agreement with the experiment, the calculations show in both the *Cmcm* and *C*2/*c* structures, there are IR activities in both the vibron and lower frequency phonon modes. The calculated pressure dependence for both phonons and vibrons is also in very good agreement with experimental results [179]. In particular, the number of IR and Raman active bands of the *C*2/*c* structure agrees exactly with that observed in the experiment. It should be noted that the present calculation describes the solid at 0 K where there is complete conversion to *para*-hydrogen. All calculations were performed in the spin-restricted formalism. Therefore, non-magnetic structures for both candidate models were assumed implicitly. *Ortho-para*-hydrogen is not described by the methods employed here.

An outstanding question is the understanding the origin of the enhanced IR activity in phase III of hydrogen. The calculated IR intensity of the *C*2/*c* structural model agrees substantially with experiments [179]. A roton mode around 1600 cm^{-1} and its pressure dependence have been studied by Chen *et. al.* at low temperature [180]. This observation is reproduced by an infrared active mode (Fig. 3.8(c)) of the *C*2/*c* structure. The calculated IR and Raman spectra for the *C*2/*c* structure also yield very good agreement in the low frequency region (Fig. 3.8). More significantly, the appearance of a single infrared active band (roton mode) in the 1600 cm^{-1} region is consistent with the *C*2/*c* structure obtained here. The calculated IR spectrum for the *Cmcm* structure, however, gave two H_2 vibron modes separated by 95–107 cm^{-1} between 150 and 200 GPa. Therefore, based on this observation, the *Cmcm* structure can be ruled out. This study illustrates the importance of employing the spectroscopic data for identifying correct structures among competing ones with very similar enthalpies, as is the case for solid hydrogen.

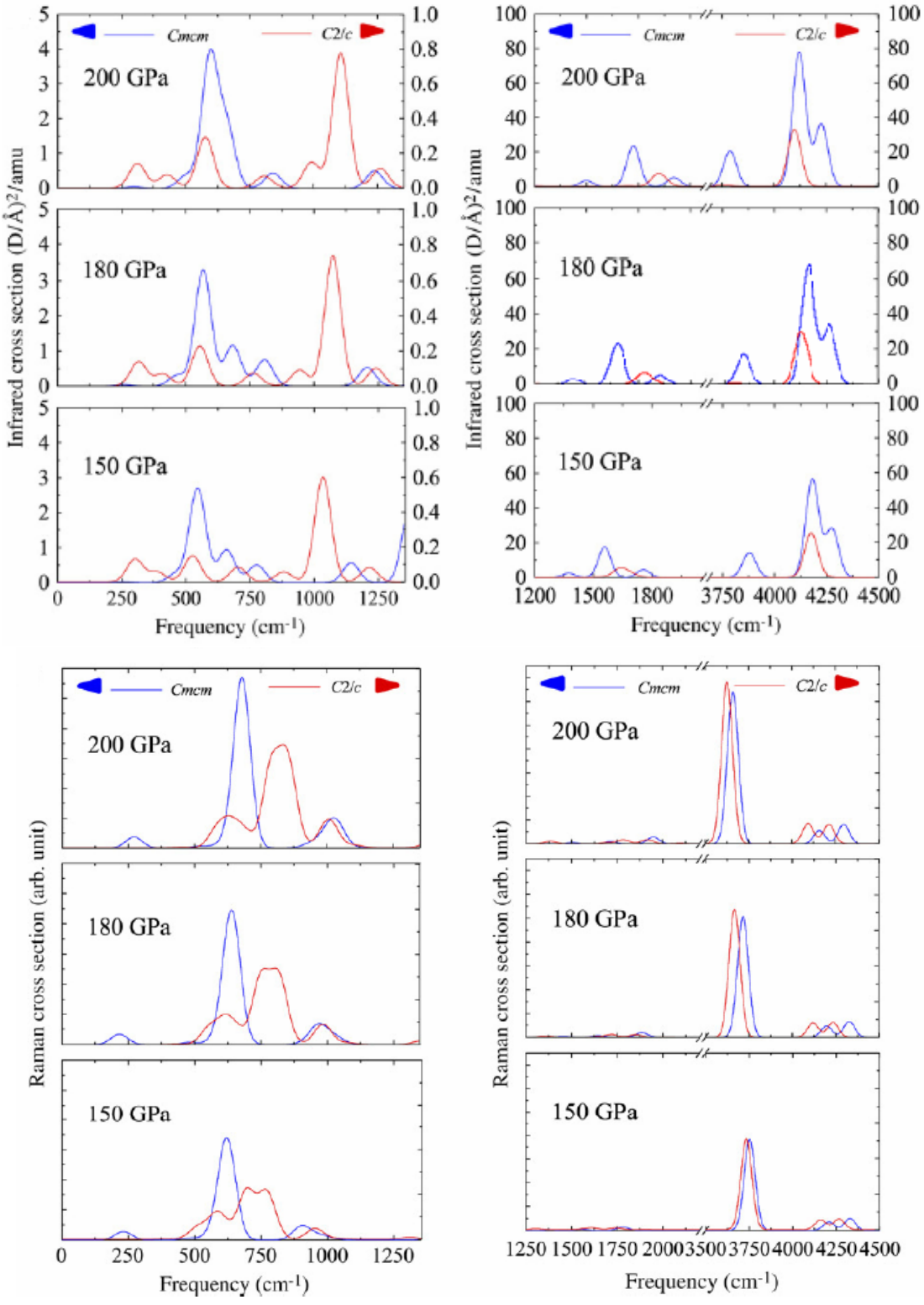

Figure 3.7. Calculated IR and Raman spectra of the *Cmcm* and *C*2/*c* structures at 150, 180, and 200 GPa.

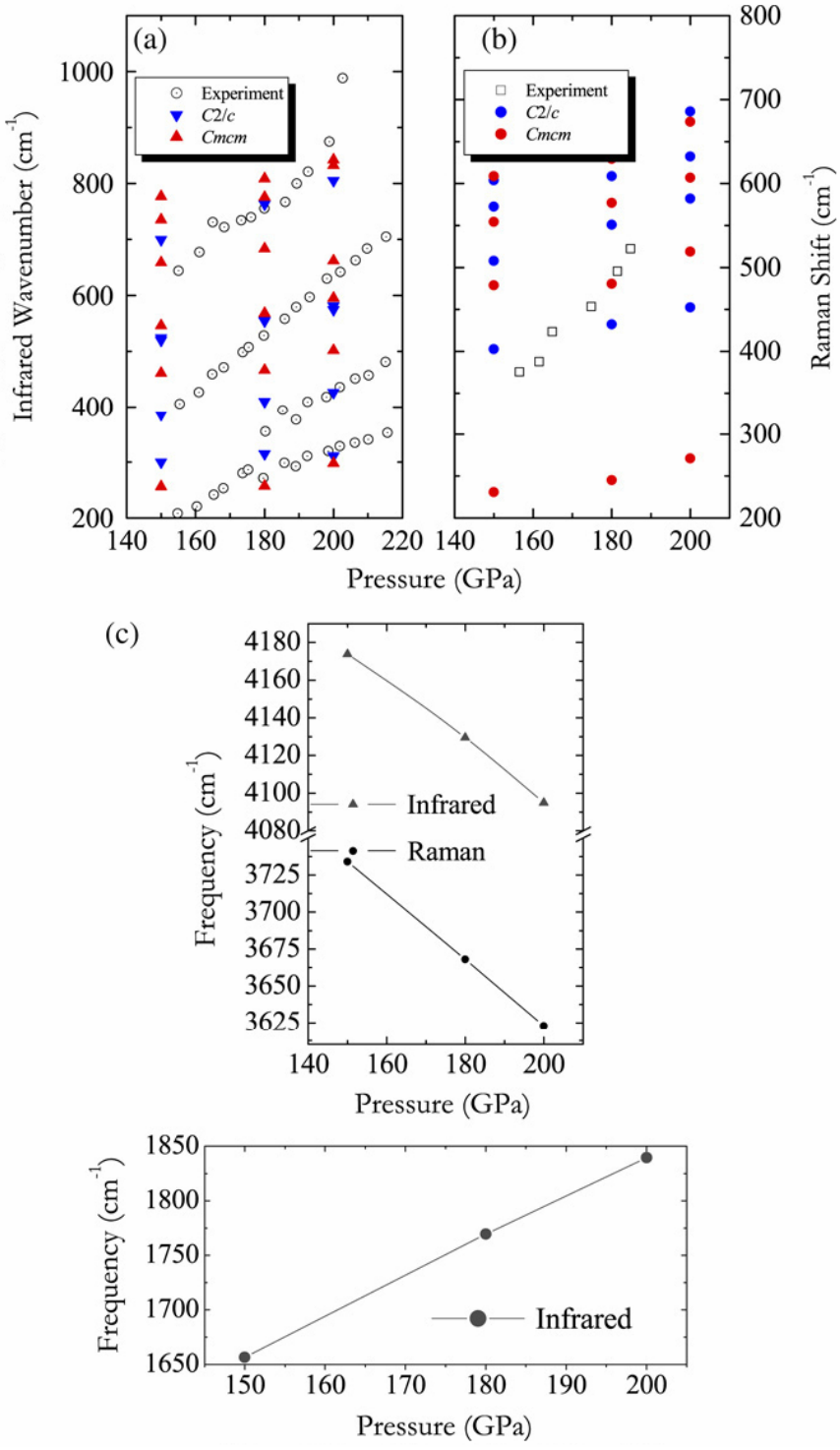

Figure 3.8. Comparison of calculated and experimental pressure dependences of low frequency (a) IR and (b) Raman frequencies for two candidate structures. (c) Calculated high frequency IR and Raman peak frequencies for the *C*2/*c* structure.

An important aspect of the current study is the calculation of the IR intensities and their pressure dependence. A substantial increase in the intensity of the vibron peaks was originally reported on solid hydrogen at 85 K [175]. Several proposals have been suggested to explain this large enhancement of IR intensity and their pressure dependence [84-86]. The suggestions are dependence on the model structure. An objective of the current study is to provide a quantitative comparison of the experimental spectra with different structural models. The pressure dependence of the IR and Raman spectra of the *C*2/*c* and *Cmcm* structures is shown in Figs. 3.7 and 3.8, respectively. The *C*2/*c* structure yields spectra features in the 150–200 GPa region that are in accord with the experimental spectra. At 150 GPa, there is a single broad vibron band composed of two close absorption bands at 4174 and 4180 cm^{-1} (Fig. 3.7). In addition, there is a strong band composed of peaks at 1656 and 1707 cm^{-1} (Fig. 3.7). The calculated intensity of the vibron band is about 4 times more intense than that of the lower frequency phonon band. The lower frequency phonon band is composed of two main translational modes with small contributions from the librations. The pressure dependence of the Born effective charges for the vibron band has also been reported [166]. The pressure dependence of the Born effective charges has been calculated from linear response theory, and the ratio for 200 and 160 GPa is 1.16 for the *C*2/*c* structure compared to the experimental value of 1.19. As shown in Fig. 3.3, the local structure around a hydrogen atom in the *C*2/*c* structure is highly anisotropic. At 160 GPa, there are two distinct H–H bond distances of 0.749 and 0.743 Å indicating that not all the H_2 molecules are equivalent in this structure. The difference of 0.006 Å is consistent with previous predictions for the *Pnma* and *Cmcm* candidate structures [84, 85]. On the other hand, the nearest H–H inter-molecular contacts range from 1.292 to 1.447 Å. A unique feature of the *C*2/*c* structure is the approximate T-shape arrangement of a group of three H_2 molecules. In this configuration, the central hydrogen atom contacts with two hydrogen atoms from the two adjacent H_2 molecules at 1.292 Å. Between the H_2 molecules, there are small but still significant orbital overlaps. In view of the very anisotropic environment and the covalent interactions between H_2 molecules, the enhancement in the observed IR activity can be attributed to dynamical charge transfer in the vibrating H_2 molecules.

The pressure dependence of the low-frequency IR and Raman spectra is compared with the experimental data obtained at 85 K in Fig. 3.8. In the experimental data [179], only the peak positions in the spectra are shown. It should be noted that there are three absorption bands in the calculated Raman spectrum. These bands that are separated by only 50 cm-1 are not resolved in the experiment. The comparison clearly reveals a reasonable agreement between theory and experiment [175].

In summary, the structures, IR and Raman spectra of two competitive candidate structures for high-pressure phase III of solid hydrogen were examined in detail. The results presented here confirm that the *C*2/*c* structure is the most reasonable model at 160 GPa based on a minimum enthalpy. The present results for the IR and Raman spectra demonstrate that the vibrational frequencies are very sensitive to the local structure. This sensitivity can be used as a diagnostic tool to differentiate candidate structural models that have very close calculated enthalpies. The DFPT predicted spectral features for the *C*2/*c* structure are in very good agreement with experiment. Additional phonon calculations substantiate the stability of this structure. The dominant spectroscopic feature of high-pressure phase III of solid hydrogen is the sudden enhancement of the IR intensity of the vibron. This is correctly reproduced by the current calculations. Moreover, the calculated Raman spectra are in very good agreement with low temperature experimental data. The close agreement of the spectral features of the *C*2/*c* structure with experiment indicates that it is a strong candidate for phase III of solid hydrogen.

3. 3 Structure and bonding of the high-pressure phases of oxygen

In the gaseous state, oxygen molecule is paramagnetic since there are two to unpaired electrons occupy the degenerate π^* orbital giving rise to a total spin $\boldsymbol{S} = 1$. Hence, in the condensed state, oxygen exhibits unique properties from competing molecular and magnetic interactions. Over the last twenty years, high-pressure solid

oxygen has been studied using a variety of experimental and computational methods [181]. Unlike other simple molecular solids, such as those formed by N_2 and the halogens, oxygen has a phase diagram consisting of phases exhibiting unusual thermal, magnetic (and non-magnetic), electrical transport, and optical properties. When cooled under ambient pressure, three polymorphic forms (α, β, and γ) of oxygen have been identified. Under compression at room temperature a sequence of structural transformations leads to four distinct phases, namely, β, δ, ε, and ζ. At 300K, the rhombohedral (*R*-3*m*) β phase transforms first to δ phase at 5.4 GPa [181]. The δ phase has a space group of orthorhombic (*Fmmm*) and exhibits long-range anti-ferromagnetic order [182]. At 9.6 GPa, δ-O_2 transforms into the ε phase [183]. The ε phase, is expected to be non-magnetic although the presence of a weak itinerant magnetic moment has not been ruled out [184], is stable up to 97 GPa where it transforms to the metallic ζ phase [185, 186]. The ζ phase is superconducting with a critical temperature of 0.5 K at 105 GPa [187]. The structure of the superconducting ζ phase [186], however, still remains elusive. Despite intense experimental and theoretical efforts, only recently the crystal structure of the ε phase was determined from single crystal [82] and powder X-ray diffraction [83]. The ε phase of oxygen has a remarkable monoclinic *C*2/*m* structure [82, 83]. It is shown to consist of $(O_2)_4$ rhombohedral clusters. At 17.5 GPa, the intermolecular $O_2…O_2$ distance of 2.20 Å is significantly longer than the O_2 intramolecular distance of 1.20 Å, which is incidentally almost identical to that of the free molecule. The very long intermolecular distance however raises an important question on the nature of the bonding between molecules in the $(O_2)_4$ clusters. In particular, the total energy of the observed *C*2/*m* structure computed from first-principles DFT is apparently higher than that of a zigzag *Cmcm* chain structure proposed earlier [54, 188, 189].

In this section, results on the characterization of the nature of bonding in the different models proposed for the ε phase of oxygen through a topological analysis of charge density using the AIM method [79-81] will be presented. As alluded in the introductory remarks, the AIM method is based on the analysis of the gradient and Laplacian of the electron density $\rho(\vec{r})$. The starting point of this investigation is to

reproduce the experimental structure and vibrational spectra (IR and Raman) via first-principles calculations within the gradient corrected (GGA) DFT with several numerical approaches. The nature of the interactions from two competing structures, *viz*., zigzag chain and $(O_2)_4$ clusters, are then analyzed with the AIM method. Conclusions are drawn regarding the nature of the intermolecular bands and the stability of crystalline structures with the application of pressure. Finally, a structure for the metallic and superconducting ζ phase is proposed and discussed.

The main results were obtained from the PSPW package Quantum-ESPRESSO [62]. Additional calculations and verification of the results were carried out using the PSPW packages VASP [63] and ABINIT [190] (Thanks to Dr. Dennis Klug of National Research Council of Canada who performed these calculations). All calculations were performed in the spin-restricted formalism. Therefore, a non-magnetic structure for solid oxygen is assumed implicitly. To support this assumption, spin-unrestricted calculations were performed on the experimentally observed *C*2/*m* structure at 17 GPa with an initial density matrix constructed from oxygen atoms with all spin-up 2*p* electrons. It was found that the self-consistent calculation and geometry optimization converged to the spin-restricted solution. No residual itinerant magnetic moment remained in the structure. For the VASP calculations, the PAW potential was used. For the ABINIT calculations, a Hartwigsen-Goedecker-Hutter potential [191] was used. For the Quantum-ESPRESSO calculations, the GGA pseudopotential was constructed with radius cutoff r_s= 1.2 and r_p= 1.3 *a.u.* and a plane wave energy cutoff E_{cut} of 100 Ry (A description on these parameters is presented in Chapter 1). The generated pseudopotential has been carefully examined by reproducing the equations of states of an isolated O_2 molecule obtained from all-electron calculations. Phonon calculations were performed with Quantum-ESPRESSO and ABINIT using linear response theory. The EPC calculations were carried out using the program Quantum-ESPRESSO. The electron-phonon matrices were computed in a 4×4×2 *q*-point mesh with a 24×24×12 *k*-point mesh for the BZ integration. The AIM analysis was performed with the program *InteGrity* [192]. Total charge density was calculated using the PAW potential with a recent version of VASP where both the atomic core and pseudo-valence charge densities are explicitly included. A very dense mesh

(120×120×120) was used to generate the charge density. A detailed description of the PAW method on how to reconstruct atomic core charge density from the pseudo wavefunctions is presented in Chapter 5.

Adhering to the experimental *C*2/*m* space group for the ε phase [82, 83], high-pressure structures were optimized at selected pressures from 9 to 110 GPa. The *C*2/*m* symmetry was assumed in the structural optimizations using Wentzcovitch's symmetry-conserving algorithm [193]. Results on the predicted structural geometries are compared with the experimental values in Fig. 3.9. Except for the very low pressure region below 20 GPa, the agreement between calculated lattice parameters and experiments is highly satisfactory. The discrepancy at low pressures can be attributed to the fact that the packing of the $(O_2)_4$ clusters arises mainly via dispersive (van der Waals) interactions which are not correctly accounted for by the GGA DFT method. This observation is consistent with the underestimated inter-cluster distances d_3 while the intramolecular O…O bond distances (d_1, see Fig. 3.10) are well described. The perspective view of the optimized *C*2/*m* structure and the notations of atomic distances d_1 to d_5 are depicted in Table 3.1. In separate theoretical studies [54, 189], it was found that the zigzag *Cmcm* structure has a slightly lower energy than the experimentally observed *C*2/*m* structure. In agreement with previous findings, at 25 GPa, the energy of the *C*2/*m* phase is found from our VASP calculations to be higher than that of the *Cmcm* structure by 3.0 mRy/atom. (~1 kcal/mol). The same energy sequence was maintained even with the inclusion of the zero-point vibration energies. The small differences in the calculated energies are beyond the general recognized limit of "chemical accuracy" (< 5 kcal/mol) of current GGA DFT methods and does not affect the ensuing discussion.

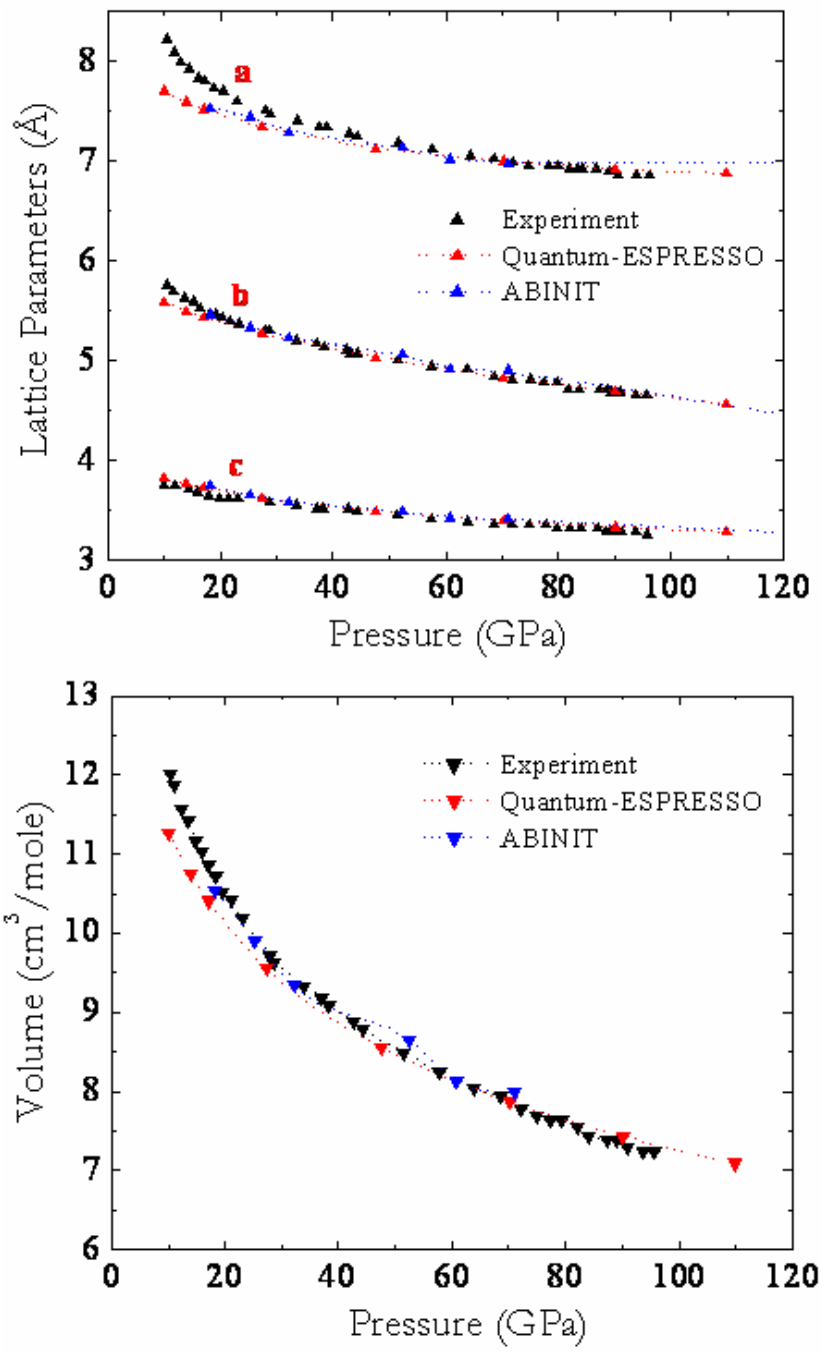

Figure 3.9. Experimental (Ref. 83) and theoretical unit cell parameters (top) and the equation of state (bottom) for the *C*2/*m* structure of ε-O_2.

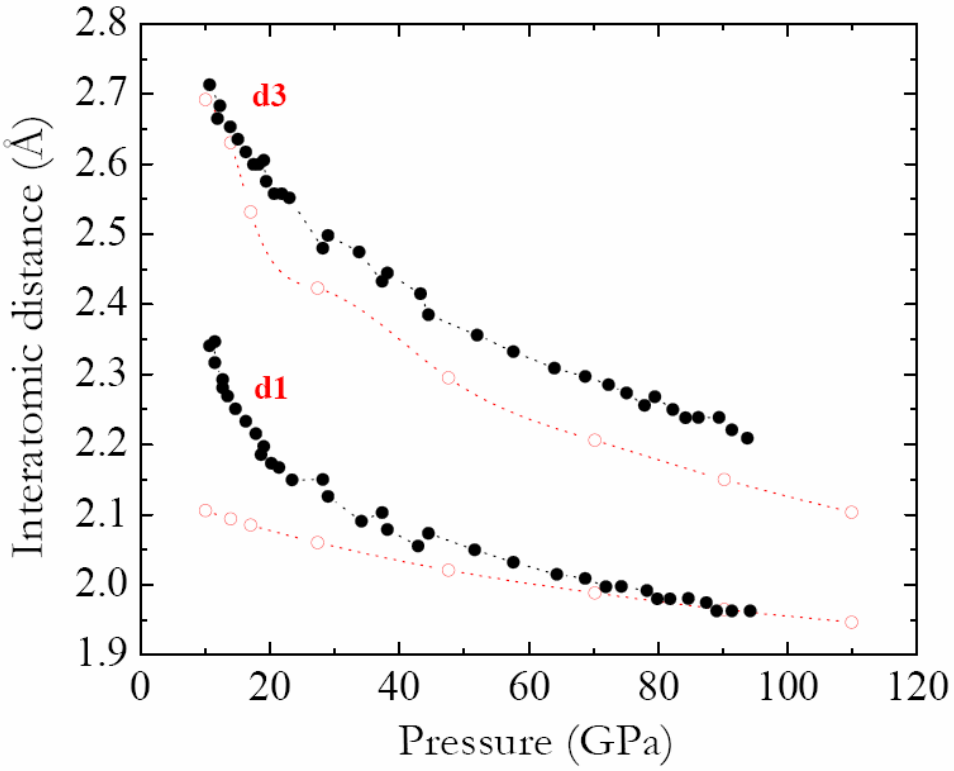

Figure 3.10. Variation of observed and calculated intra- (d_1) and inter- (d_3) cluster molecular distance with pressure (close symbols – experiment (Ref. 83); open symbols – theory).

Three-dimensional total charge densities including the core charge on a fine mesh for the *Cmcm* and *C*2/*m* structures were generated with VASP from the respective structures optimized at 25 GPa. The (3, -1) BCP's obtained from AIM analyses on the *C*2/*m* and *Cmcm* structures are summarized in Tables 3.1 and 3.2, respectively. The AIM analysis successfully identifies all the relevant BCP's anticipated for the $(O_2)_4$ clusters in the *C*2/*m* structure. As expected, the BCP's of the O_2 molecules have the largest value of $\rho(\vec{r}_{cp})$ (~0.55) and $H(\vec{r}_{cp})$ (-1.10 *a.u.*) and indicate genuine O-O covalent bonds. More significantly, intra-cluster BCP's are also found between O_2 molecules forming the $(O_2)_4$ cluster. The charge density at the critical point $\rho(\vec{r}_{cp}) \sim 0.06$ with a positive Laplacian and a negative $H(\vec{r}_{cp})$ (-0.009) are unambiguous signs of covalent interactions between

O_2 molecules although it is much weaker than a 'normal' covalent bond [79, 172, 173]. The positive Laplacian is perhaps surprising since it indicates "closed shell" interactions [79] between the two O atoms of the adjacent O_2 molecules in the $(O_2)_4$ unit. The theoretical analysis is consistent with the observed very long $O_2 \cdots O_2$ separation of about 2.34 Å at 10 GPa and 2.17 Å at 17 GPa [82]. The electron density $\rho(\vec{r})$ at the inter-cluster BCP's (0.028) is much smaller. Moreover, the Laplacian local energy density $H(\vec{r}_{cp})$ is positive which typifies closed shell van der Waals interaction between the clusters [79]. RCP and CCP's were also identified for the $(O_2)_4$ clusters. These CP's are of minor significance and will not be discussed here. A similar charge density topological analysis was also performed on the energetically competing *Cmcm* structure at 25 GPa. The results are presented in Table 3.2. In comparison with the *C*2/*m* structure, the absolute values for the charge density (~0.549), Laplacian and local energy density (~1.104), evaluated at the BCP's for molecular O_2, are smaller. These differences, albeit small, are consistent with a slightly longer O-O distance predicted for O_2 in the *Cmcm* structure (1.205 Å) compared to *C*2/*m* (1.201 Å) as a consequence of a slightly weaker covalent bond. This longer bond is compensated by slightly enhanced intra-chain interactions where in this case the charge density, the Laplacian, and the local energy density are slightly more favorable. A larger difference is observed in the inter-layer BCP's. In comparison with the inter-cluster interactions in the *C*2/*m* structure, the interlayer interactions in the *Cmcm* structure are clearly smaller. The AIM analysis hence provides hints as to how to reconcile the apparent discrepancy that even though the calculated total energy favors the *Cmcm* structure, the slightly more favorable interactions between O_2 in the *C*2/*m* structure may help reduce the activation energy barrier for the transition from the δ phase to the ε phase as observed [82, 83]. When ε oxygen is compressed, the intra-cluster O_2 distance (d_1) and inter-cluster distance (d_3) decrease rapidly. Calculations reproduce the trend but the results are not quantitative (Fig. 3.10). Interestingly, the shape of the $(O_2)_4$ clusters distorts from a square prism to a diamond shape prism with increasing pressure. The O···O···O bond angle decreases gradually from 88° at 20 GPa to 80° near the $\varepsilon \rightarrow \zeta$ transition at 97 GPa (*vide supra*). This distortion leads to changes in the structure and the electron density topology. Table 3.3 reports results of an AIM analysis of a slightly over-pressurized *C*2/*m* structure at 105

GPa. As indicated by $\rho(\vec{r}_{cp})$ and $\nabla^2\rho(\vec{r}_{cp})$ the intra-cluster and inter-cluster interactions of 0.065 and 0.062, respectively, are now almost equivalent. The $(O_2)_4$ clusters in the ***ab*** plane start to connect to each other. At this pressure, the calculated electronic band structure of *C*2/*m* indicates that it is metallic but dynamically unstable. The linking of $(O_2)_4$ clusters may be a precursor for the $\varepsilon \rightarrow \zeta$ phase transition.

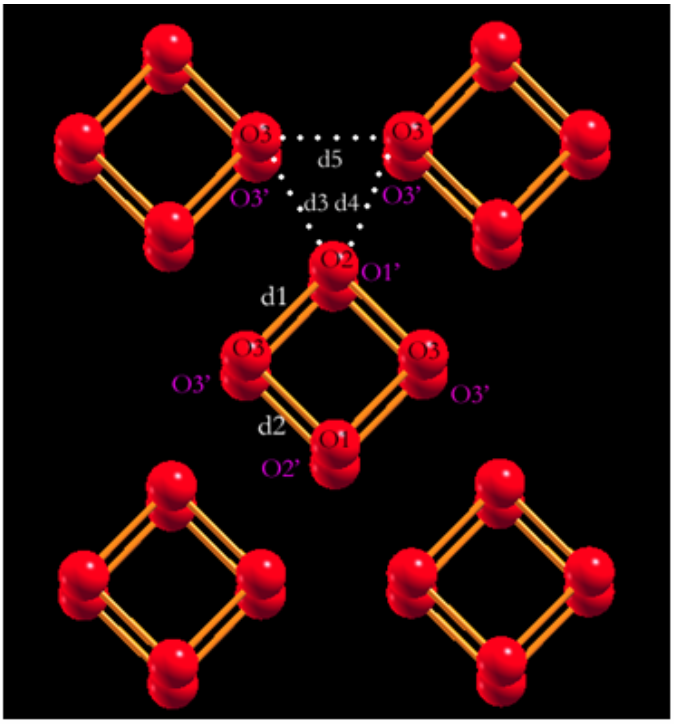

Bond	Type	$\rho(\vec{r}_{cp})$	$\nabla^2\rho(\vec{r}_{cp})$	λ_1	λ_2	λ_3	$H(\vec{r}_{cp})$
O_3-O_3'	Molecular	0.5501	-0.536	-1.555	-1.527	2.546	-1.109
O_1-O_2'	Molecular	0.5468	-0.459	-1.518	-1.510	2.569	-1.087
$O_3\ldots O_2$ (d1)	Intra-cluster	0.0622	0.231	-0.098	-0.091	0.421	-0.009
$O_3\ldots O_1$ (d2)	Intra-cluster	0.0619	0.232	-0.098	-0.091	0.420	-0.009
$O_3\ldots O_2$ (d3)	Inter-cluster	0.0276	0.099	-0.025	-0.024	0.148	0.003
$O_3\ldots O_2$ (d4)	Inter-cluster	0.0194	0.089	-0.020	-0.019	0.128	0.003
$O_3\ldots O_3$ (d5)	Inter-cluster	0.0163	0.080	-0.017	-0.017	0.122	0.004

Table 3.1. Bond critical points for *C*2/*m* ε-O_2 at 25 GPa.

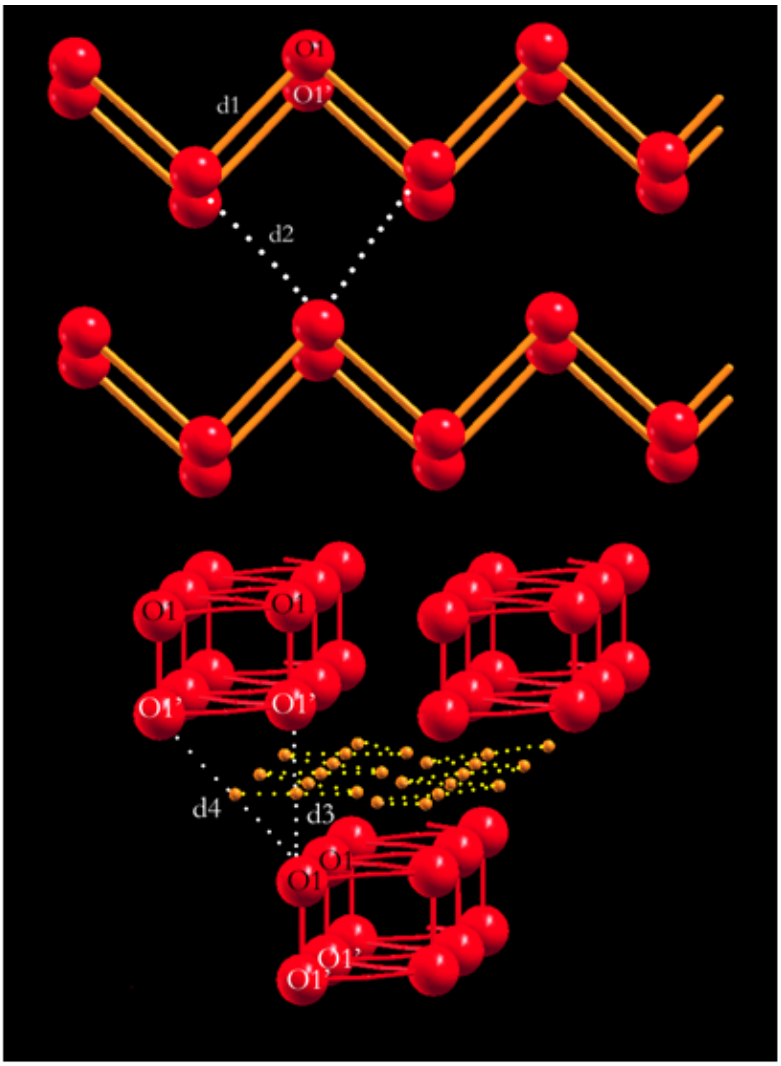

Bond	Type	$\rho(\vec{r}_{cp})$	$\nabla^2\rho(\vec{r}_{cp})$	λ_1	λ_2	λ_3	$H(\vec{r}_{cp})$
$O_1 - O_1'$	Molecular	0.5489	-0.600	-1.540	-1.535	2.474	-1.104
$O_1 \ldots O_1$ (d1)	Intra-chain	0.0663	0.254	-0.108	-0.091	0.461	-0.010
$O_1 \ldots O_1$ (d2)	Inter-chain	0.0207	0.093	-0.023	-0.021	0.137	0.003
$O_1' \ldots O_1$ (d3)	Inter-layer	0.0165	0.090	-0.018	-0.015	0.123	0.005
$O_1' \ldots O_1$ (d4)	Inter-laver	0.0143	0.068	-0.007	-0.005	0.080	0.004

Table 3.2. Bond critical points for the *Cmcm* chain structure at 25 GPa.

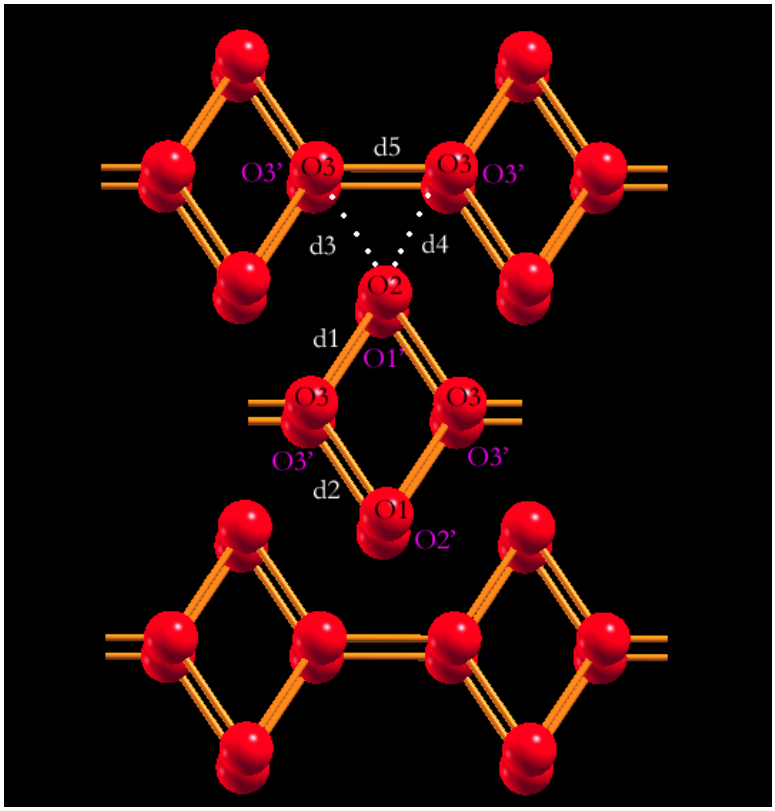

Bond	Type	$\rho(\vec{r}_{cp})$	$\nabla^2\rho(\vec{r}_{cp})$	λ_1	λ_2	λ_3	$H(\vec{r}_{cp})$
$O_3 - O_3$'	Molecular	0.5882	-0.737	-1.702	-1.657	2.622	-1.253
$O_1 - O_2$'	Molecular	0.5866	-0.663	-1.659	-1.642	2.638	-1.238
$O_3 \ldots O_3$ (d5)	Inter-cluster	0.0652	0.291	-0.100	-0.093	0.484	-0.006
$O_3 \ldots O_2$ (d1)	Intra-cluster	0.0619	0.280	-0.094	-0.086	0.456	-0.005
$O_3 \ldots O_1$ (d2)	Intra-cluster	0.0619	0.282	-0.093	-0.084	0.459	-0.004
$O_3 \ldots O_2$ (d3)	Inter-cluster	0.0484	0.219	-0.066	-0.057	0.341	-0.001
$O_3 \ldots O_2$ (d4)	Inter-cluster	0.0449	0.204	-0.058	-0.051	0.312	0.001

Table 3.3. Bond critical points for an over-pressurized *C*2/*m* ε-O_2 at 105 GPa.

The IR and Raman spectra for the ε phase has been recorded up to the transition to the ζ phase, *i.e.*, from 27 GPa to 100 GPa. A comparison of experimental and calculated IR and Raman vibrational frequencies over the entire stability range of the ε phase are shown in Fig. 3.11 (Thanks to Dr. Serge Desgreniers of the University of Ottawa for providing the experimental Raman data). The overall agreement with the experiment is excellent. For example, at 30 GPa, the experimental spectrum [82] shows three Raman active bands at 1610, 1430, and 450 cm^{-1}, which are to be compared with the calculated Raman absorptions at 1613, 1372, and 648 cm^{-1}. The calculated relative intensities are also in reasonable accord with the experiment [82]. The highest energy Raman band is assigned to O-O intra-molecular vibration. The weak Raman peak calculated at 1372 cm^{-1} can be assigned to an anti-symmetric vibration of coupled O_2-O_2 in the $(O_2)_4$ unit; this is a signature of the *C2/m* structure. This assignment is in full agreement with that deduced from the experiment and preliminary calculations for an isolated $(O_2)_4$ unit. The calculated Raman band at 648 cm^{-1} is identified to be an inter-cluster vibration mode. This should correspond to the observed band at 450 cm^{-1}. The overestimated vibrational wavenumber is almost certainly due to the deficiency of DFT to provide a correct description of weak dispersive interactions. This shortcoming is also reflected in a shorter calculated O···O distance (see Fig. 3.10) between the $(O_2)_4$ clusters at 30 GPa and that observed experimentally. The calculated and observed IR spectra of the ε phase are also in good agreement (Fig. 3.11a). Two mid-IR active bands were observed. At 16 GPa, the observed bands at 391 and 1507 cm^{-1} correspond well to the calculated vibrations at 419 cm^{-1} (consisting of two overlapping vibrational modes) and 1432 cm^{-1}, respectively. The calculated pressure coefficients between 25 and 70 GPa for the low/high frequency bands of 2.65/1.67 cm^{-1}/GPa are in good agreement with the experimentally measured values of 1.24/3.80 cm^{-1}/GPa, respectively [82].

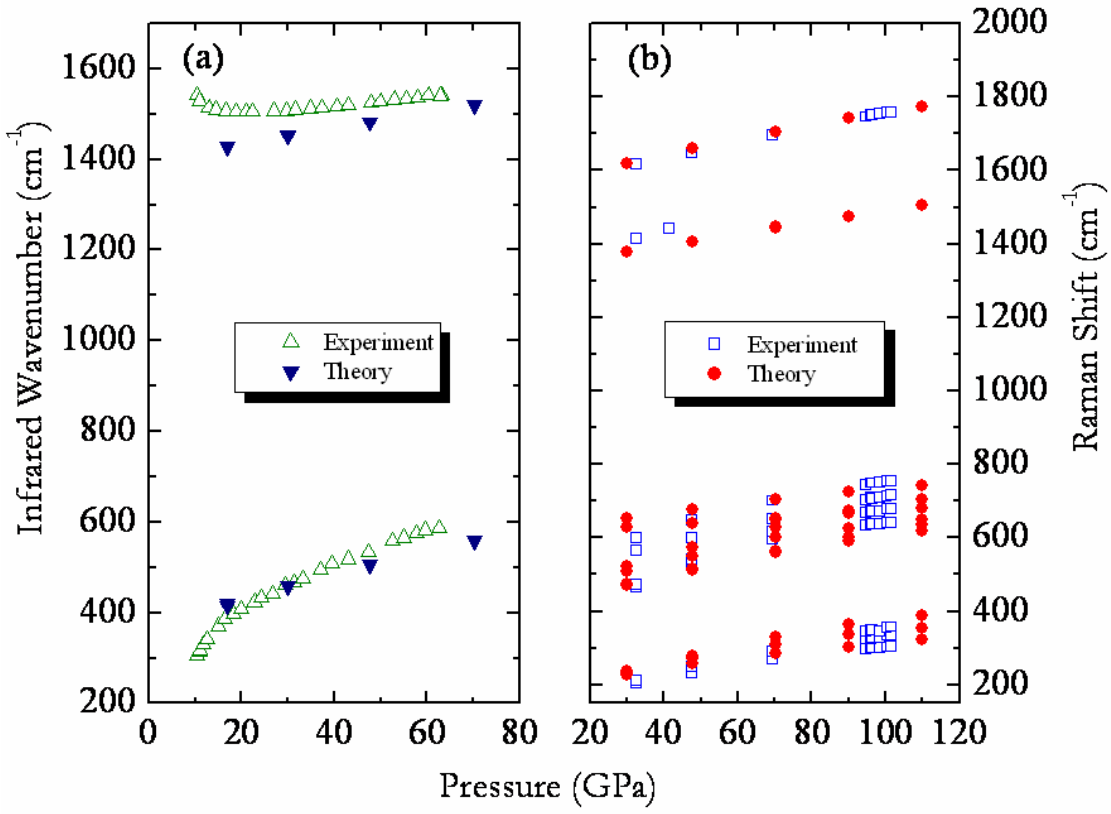

Figure 3.11. Comparison between high-pressure experimental and theoretical infrared (a) and (b) Raman spectra for the ε phase of oxygen.

When the ε phase of solid oxygen was compressed, a phase transition to a new metallic phase (ζ phase) was found at 97 GPa [185, 186]. This metallic phase was shown to be superconducting with a critical temperature T_c of 0.5 K at 110 GPa [187]. The detailed structure of the ζ phase has not been determined from experiment. However, inspection of the powder X-ray diffraction pattern [185] and the more recent but somewhat limited single crystal diffraction data for the ζ phase [194] shows that the number of observed Bragg peaks has been reduced across the ε-ζ phase transition. This observation may suggest the transformation to a structure of higher symmetry space group. There have already been several theoretical predictions on the possible structures of the ζ phase [195]. In the present work, it is found from phonon band structure calculations that ε-O_2 with the $C2/m$ structure is dynamically unstable (appearance of

imaginary frequencies) at pressures exceeding ~100 GPa. To determine possible structural models for the high-pressure phase, a series of simulated annealing MD calculations [196] employing the variable cell Parrinello-Rahman procedure [197] with the program SIESTA [64] were performed. Starting from the precursor ε structure, a supercell consisting of 216 oxygen atoms was generated. A localized basis set pseudopotential program was used for the MD calculations. Structures selected from the MD trajectory were quenched and then fully optimized using the PW codes listed.

Two energetically competitive structures with space group *R*-3*m* and *C*2/*c* were found through simulated annealing calculations. In view of the higher symmetry, the electronic and dynamical stability of the *R*-3*m* structure were first examined (*a*=*b*=2.088, *c*=8.990 Å. O 6*c* 0, 0, 0.935). It is found that this structure is metallic, but is not dynamically stable at 110 GPa with an imaginary frequency at the *L* symmetry point, and therefore, this structure cannot be a viable candidate for the ζ phase. The *C*2/*c* structure consists of 4 O_2 molecules per unit cell with cell parameters *a*=6.149, *b*=2.105, *c*=7.803 Å and $\beta=153^{o}$, O 8*f* -0.633, 0.032, -0.784 at 113 GPa. This phase is found to be metallic and energetically slightly more favorable (lower enthalpy) than the *R*-3*m* structure. Furthermore, it is dynamically stable up to at least 125 GPa, the highest pressure studied here. Further examination of the structure shows that it can be derived from the *R*-3*m* structure with very small distortions and their X-ray diffraction patterns could hardly be distinguishable experimentally. The experimental X-ray diffraction pattern of the ζ phase is much simpler than that of the ε phase, *i.e.*, with fewer Bragg reflections [185]. The calculated X-ray diffraction pattern of the predicted *C*2/c structure is in substantial agreement with the experiment [185] as shown in Fig. 3.12. All the X-ray diffraction peaks observed in the experiment are correctly reproduced. The relative intensities of the Bragg peaks are also well reproduced. It is significant that the weak X-ray diffraction peak observed at about 14^{o} is correctly predicted by the *C*2/*c* structure. A previous theoretically suggested structure did not reproduce this small but significant feature [195]. The transformation pathway from the *C*2/*m* ε-structure to the *C*2/*c* ζ structure is depicted in Fig. 3.13. At low pressure, the $(O_2)_4$ clusters in the ε-O_2 structure resemble square-based prisms. Near the phase transition, the $(O_2)_4$ clusters distorted into diamond shape

prisms and the linking of these prisms in the ***ab*** plane eventually led to the *C*2/*c* structure. The breaking of the $(O_2)_4$ clusters in favor of linking at high pressure is reflected in the gradual increase of the inter-cluster BCP's. For example, $\rho(\vec{r}_{cp})$ and $\nabla^2\rho(\vec{r}_{cp})$ increase from ~0.02 and 0.09, respectively at 24 GPa to 0.045 and 0.21, respectively at 105 GPa (see Tables 3.1 and 3.3). The transition pressure calculated from the equation of state of the *C*2/*m* and *C*2/*c* structure using the common tangent method is 92 GPa, which is very close to the observed transition pressure of 96 GPa at room temperature.

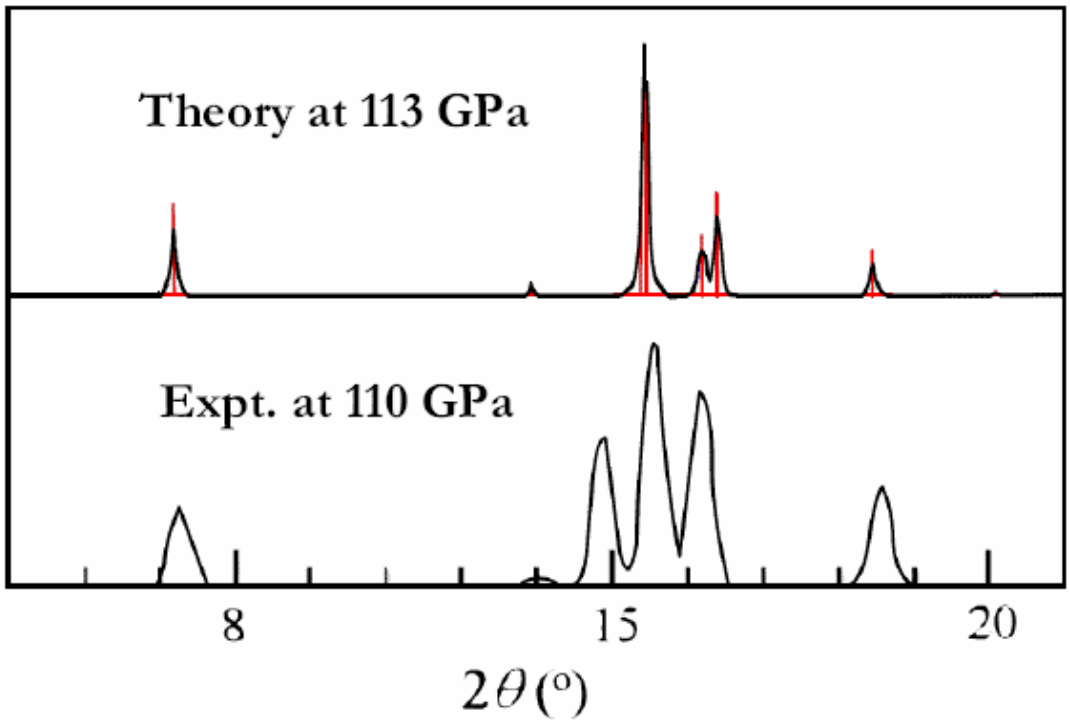

Figure 3.12. Comparison between calculated (*C*2/*c)* and experimental (ζ phase) powder X-ray diffraction patterns (λ=0.4817Å) near 110 GPa.

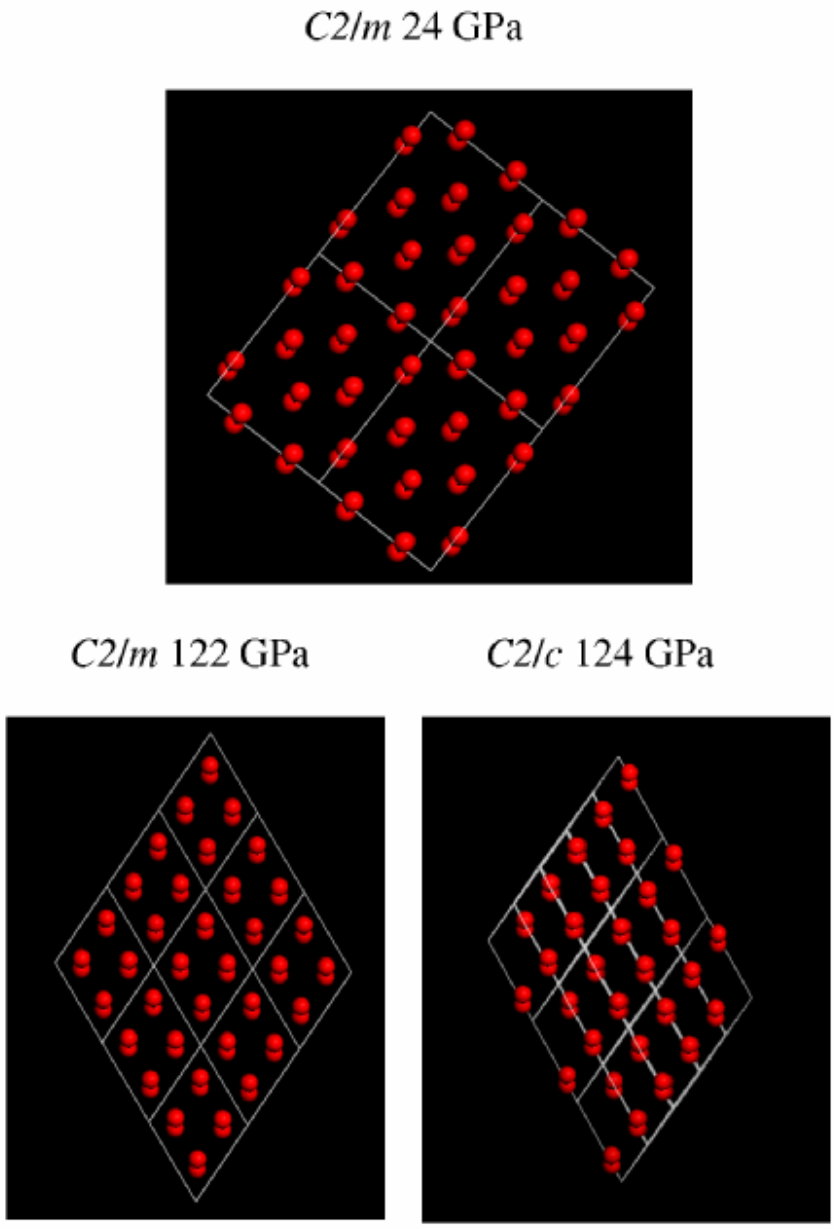

Figure 3.13. A comparison of the *C*2/*m* and *C*2/*c* structures showing the gradual change in the crystal structure as pressure increases.

Calculations show that the *C*2/*c* structure is superconducting with a calculated EPC parameter λ=0.71 at 125 GPa. It is noteworthy that the EPC is localized around a small number of soft phonon modes in the BZ, which makes an accurate evaluation of λ

difficult. It may require a much larger q-mesh beyond our current capability. The T_c can be estimated from the semi-empirical Allen-Dynes modified McMillan equation (Eq. (2-18)). The logarithmic average of the vibration frequency $\omega_{\log}$ can be evaluated from the Eliashberg spectral function. Although μ^* can be computed from first principles, the computation is rather complicated for a low symmetry structure as the one proposed here. To match the experimental T_c of 0.5 K at 105 GPa, a $\mu^* \sim 0.3$ is needed. Nevertheless, the calculations confirmed that superconductivity exists in the $C2/c$ model for the ζ phase, consistent with the experiment.

In summary, the nature of the interactions between O_2 molecules and the preference of the formation of $(O_2)_4$ clusters in the $C2/m$ structure of the high-pressure ε phase have been rationalized from the analysis of the electron charge density using Bader's atoms-in-molecules theory. It was shown that overall interactions, in particular, weak non-bonding interactions between $(O_2)_4$ clusters help to stabilize the experimentally observed structure over an energetically competitive zigzag chain structure predicted from theoretical calculations. Changes in the geometry of the $(O_2)_4$ cluster and the vibrational spectra with pressure have been examined; the overall agreement with the experiments is excellent. It is shown that the lower pressure square prism cluster of ε phase deforms into a diamond-shaped prism at pressure close to the observed insulator-metal transition. It is shown that the enhanced interactions between the clusters lead to a structural phase transition at a calculated pressure of 92 GPa. The predicted structure for the higher-pressure ζ phase has a $C2/c$ space group. The calculated diffraction pattern is in agreement with that observed for the ζ phase of oxygen to-date. More significantly this structure is also found to be metallic and superconducting. Therefore, the $C2/c$ structure is proposed as a strong candidate for the still unresolved ζ phase.

3. 4 IR and Raman spectra for high-pressure phase of SiH_4.

The superconducting properties of the high-pressure phases of SiH_4 have been investigated in Chapter 2. From first-principles calculations, a series of pressure-induced phase transitions were predicted for SiH_4 [76]. At low pressure, SiH_4 adopts a tetragonal $P4_2/nmc$ structure with two molecules per unit cell. The calculated electronic density of states shows that this molecular phase is insulating [76]. The width of the band gap in the $P4_2/nmc$ structure decreases with increasing pressure. At 60 GPa, the band gap completely closes and the material becomes metallic. With increasing pressure, the tetragonal $P4_2/nmc$ structure transforms to an intermediate orthorhombic *Ccca* structure, which is a subgroup of its precursor. At 90 GPa SiH_4 transforms to a monoclinic $C2/c$ superconducting phase. The predicted trend of phase transitions is supported by the experiments carried out afterwards [78]. A detailed discussion of these phase transitions and corresponding crystal structures is presented in Chapter 2.

The high-pressure structures of SiH_4 above 20 GPa are not known. The objective of this study is to compute the IR and Raman spectra of the proposed structures in the hope that the results will be useful for future comparison with experiments. Raman studies on SiH_4 have identified multiple transformations into insulating phases before the threshold of pressure-induced metallization [78, 198, 199]. Starting from a few GPa, the Raman spectra show the characteristic bands corresponding to internal vibrations of molecular SiH_4, in accordance with known data at ambient pressure. Discontinuities in the pressure dependence of Raman frequencies at 5 to 7 GPa and near 25 GPa indicate possible phase transitions. Between 50 and 65 GPa, the sample suddenly darkened and Raman signals could no longer be detected. This measured metallization pressure is in a good agreement with the theoretically proposed value of 60 GPa, at which pressure the band gap closes in the predicted $P4_2/nmc$ structure. The calculated Raman spectrum of the $P4_2/nmc$ structure and the experimental Raman spectra (provided by Dr. Mikhail Eremets of Max Planck Institute für Chemie) are presented in Fig. 3.14 (b) and (c),

respectively. The calculated frequencies of Raman shifts for the $P4_2/nmc$ structure are in very good agreement with the experiments [78]. In particular, the number of Raman active modes agrees with that of the experiments in the low frequency range. The Raman bands around 1000 cm^{-1} are characteristic of vibrations associated with Si-H bending modes. The higher frequency bands around 2250 cm^{-1} are assigned to Si-H stretching modes. The calculated IR spectrum for the $P4_2/nmc$ structure is presented in Fig. 3.14 (a). So far, without refined structural information from X-ray diffraction patterns, there are no conclusive structures for the low-pressure insulating phases of SiH_4. On the other hand, the good agreements of the Raman spectrum and metallization pressure of the $P42/nmc$ structure with the experiments indicate that it may be a good candidate structural model.

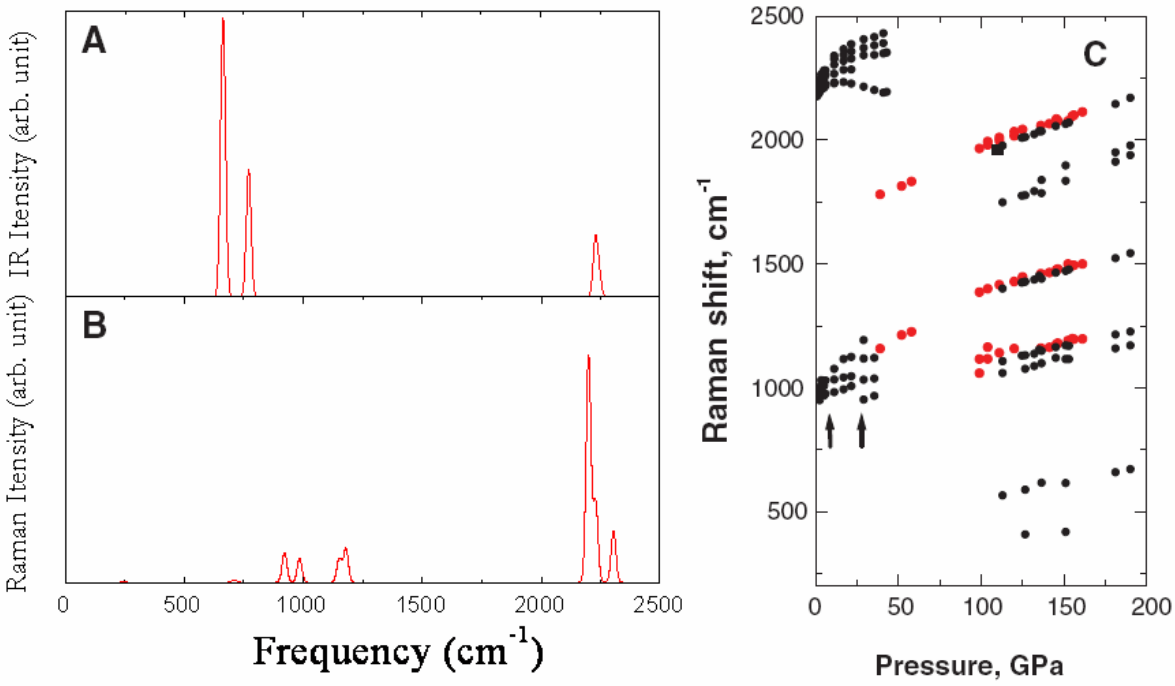

Figure 3.14. The calculated (a) IR and (b) Raman spectra for the $P4_2/nmc$ structure of SiH_4 at 35 GPa. (c) The measured pressure dependence of Raman frequencies of SiH_4 (Ref. 78). No Raman signal could be detected in the 50 to 110 GPa range by increasing pressure. The Raman signal persists to higher pressures by releasing pressure (red dots).

3. 5 Summary

In this chapter, the IR and Raman spectra for three selected high-pressure materials, solid H_2, O_2, and SiH_4 were investigated using first-principles PSPW calculations within the framework of density functional perturbation theory. The Bader's atoms in molecules method was used to characterize electron topology and bonding of $(O_2)_4$ clusters in the newly discovered *C*2/*m* structure of the high-pressure ε phase of solid O_2. For solid H_2 the objective was to examine two candidate structures for high-pressure phase III, the *Cmcm* structure and the *C*2/*c* structure proposed recently. The local H_2 environments of these two structures are similar but there are subtle structural differences. Thus, although intensities of the calculated IR spectra share many similarities and both agree with the experimental spectrum recorded at 160 GPa. Detailed Raman and IR features of the low-frequency vibrations reveal that *C*2/*c* is the more appropriate structure for phase III of hydrogen. The calculated pressure dependence of the IR and Raman absorption intensities of the *C*2/*c* structure were shown to be in excellent agreement with experiment. For solid O_2 the experimental structure and vibrational spectra (IR and Raman) of the recently resolved *C*2/*m* structure of the high-pressure ε phase were well reproduced via density functional theory using generalized gradient approximation. The nature of the interactions from two competing structures, the theoretically proposed *Cmcm* chain structure and observed cluster *C*2/*m* structure were analyzed with the atoms in molecules method. The nature of intermolecular interactions and the stability of the structure with increasing pressure were related to the changes in charge density. A possible structure for the metallic and superconducting ζ phase was proposed and discussed. For SiH_4, the Raman spectrum of the theoretically predicted $P4_2/nmc$ structure of the high-pressure insulating phase was calculated and compared with experimental data. The good agreement between the calculated spectrum and experiments indicates that the *P*42/*nmc* structure is a candidate structural model for the high-pressure insulating phase of SiH_4.

CHAPTER 4

High-pressure crystal structure prediction via genetic algorithm

A feature of crystallography at high pressure is the existence of a rich diversity of crystal structures. With recent advancements in structural refinement techniques and synchrotron instrumentation, many new crystal structures of solid materials at high pressure have been discovered. These structures are often novel and not seen in any solids under ambient conditions. While it is now possible to determine crystal structures from experimental powder X-ray diffraction patterns, there are plenty of cases that the experimental data are not complete or not even available, especially under very high pressure, where high quality spectra are often difficult to obtain. Therefore, it is important to develop a reliable theoretical structure prediction method to assist the solution of unknown structures. The design of reliable method for crystal structure prediction will also provide a practical way for finding new materials.

Conventional theoretical methods for predicting unknown crystal structures usually involve dynamical simulations. Among those, the method of stimulated annealing employing molecular dynamics is widely used [200-204]. In molecular dynamics, each atom in the system interacts with all other atoms and the net force drives the atom toward a new configuration to minimize the total energy of the system. The outcome of this method depends heavily on the initial configurations. Molecular dynamics simulation is not a very efficient method since it only relaxes a set of chosen initial configurations to nearby minima in the free energy surface. There is no guarantee

that the lowest-energy structure corresponds to the most stable structure. One must choose the initial configurations sufficiently close to the optimum structure otherwise the configurations would be trapped in higher-energy local minima. This is a severe problem because the number of local minima increases exponentially with the number of freedom of the system. On the other hand, under high pressure the experimentally observed structure may not necessary be the lowest-energy one. More problematically, most often the observed structure may be controlled by kinetic and it may be a meta-stable state with slightly higher energy than the thermodynamically most stable one. The deficiency of the dynamics method is the lack of the ability to broadly explore the free energy surface due to the limited searching pathways confined mainly in neighboring regions of the initial configuration. In this chapter, an approach for crystal structure perdition based on genetic algorithm (GA) [205-210] is employed. The algorithm is comprised of several strategies proposed recently by several research groups [53-56], with additional improvements made by us that were found to be more efficient [52]. The GA has been found to be able to predict energetically most stable or meta-stable structures requiring no prior knowledge of structural information except for the numbers of the constituent elements in the unit cell. The search starts with a population of randomly generated structures. The population is improved through genetic operations by producing energetically favorable offspring structures from mating of selected parents. In successive generations, new low-energy structures evolve and replace the high-energy structures in the preceding generation. In this way, the search is self-improving and locates the optimal structures by zooming in promising regions of the free energy surface. Therefore, the GA method is expected to have a higher searching efficiency compared with the molecular dynamics method.

4. 1 Method

In this section the GA for predicting energetically favorable crystal structures, including both the lattice types and the internal atomic coordinates, is presented. The method employed in the present study combines the algorithms proposed recently with additional features developed by us.

```
initialize X, cont      # generate a group of random structures X with constraints cont.
 initialize igen = 1    # set the index igen for the first generation as 1.
100 optimize X          # perform structural optimizations on X.
 accept (X, p, fit_X)   # accept p percentages of X as candidate parents,
                          according to the fitting function fit_X.
 update cont            # update constraints cont.
 while not done; do     # produce offspring configurations Y.
   do i=1, NH                      # produce NH new structures from heredity
     Y(i) = OPH (X, cont)            operation OPH.
   done
   do i=NH+1,NH+NM                 # produce NM new structures from mutation
     Y(i) = OPM (X, cont)            operation OPM.
   done
   do i=NH+NM+1, NH+NM+NK
     Y(i) = OPK (X, cont)          # keep NK best structures of previous
   done                              generation.
 done
 X=Y                               # update X
 if (igen=gens) then               # if the evolution reaches user-defined
   stop                              number of steps gens, stop.
 else
   igen ++; goto 100
 end if
```

Figure 4.1. The GA used for crystal structure prediction.

The structure searching method adopted here uses a GA that simultaneously explores several parts of the free energy surface. A population of crystal structures, each representing a possible realization of lattice configuration is defined. These populations start from structures with the cell angles and cell vector lengths generated randomly. The positions of the constituent atoms are chosen and distributed randomly within the unit cell. Hard constraints are applied to inter-atomic distances, cell angles and the lengths of cell vectors, to ensure these randomly generated structures chemically reasonable. First-principles electronic structure methods are then used to fully optimize the atomic volume, unit cell shape, and atomic positions of each structure at a given external pressure until a minimum energy structure is reached. For the optimized population, a fitness score using the total energy/enthalpy is assigned to each structure. Structures in the population are

chosen according to the fitness scores to generate new structures by genetic operations of heredity and mutation. Once the new structures are produced, the structure optimization step is repeated. New populations are produced by replacing the structures with highest energies from the current population with the new generated structures. Replacing the highest energy structures with new lower-energy structures is a way to sample new regions of the free energy surface with local minima whose energy may be lower than that of the local minima found in the previous generations. New generations of the population are created iteratively in this way until no new low-energy structures are generated in several successive generations. A pseudo code demonstrating this algorithm is presented in Fig. 4.1. GA often invokes the heredity and mutation operations. Details of these two procedures are described in the following section.

4. 1. 1 Heredity operation

Heredity operation produces an offspring structure through the mating of two parent structures. A good heredity operation should pass on preferable properties of the parent structures to the offspring. An often-used heredity operation [209, 210] is encoding structural information with binary strings and using string recombination to produce the offspring. This approach has gained considerable successes, but it was found not to be very efficient for complicated systems mainly because it does not preserve the characteristics of the parent structures. In the present study the 'cutting-shifting-splicing' procedure originally proposed for determining the carbon fullerene structure and recently adapted to periodic systems is used [52-56]. This operation is achieved by taking a spatially coherent fractional slab from each parent and assembling them together to produce the offspring (Fig. 4.2). In this procedure, before cutting a slab from each parent structure, it is convenient to map both parent structures onto a metric cell. This step is achieved by transforming the atomic positions in the unit cell from Cartesian coordinates into fractional coordinates,

$$\vec{r}_i^{\,f} = A^{-1}\vec{r}_i^{\,c}, \tag{4.1}$$

where $\vec{r}_i^{\,f}$ and $\vec{r}_i^{\,c}$ are the fractional and Cartesian coordinates of the *i*-th atom in the unit cell, respectively. Here *A* is a 3x3 lattice matrix defined in terms of lattice vectors $\vec{a}_i$,

$$A = [\vec{a}_1, \vec{a}_2, \vec{a}_3]\,. \tag{4.2}$$

This transformation maps the original unit cells onto a metric cell with unitary cell vectors. The fractional atomic coordinates are between 0 and 1. The representation of the crystal structures in terms of fractional coordinates makes it easier to formulate a procedure for mating two parent structures with different cell shapes. The cutting plane is chosen randomly passing through the center of mass of each parent structure. The two parent structures are cut in this plane, and the offspring structure is assembled from the atoms that lie above the plane in one parent and the atoms that lie below the plane in the other. The offspring generated in this way may not contain the correct number of atoms. If this is the case, the parent structures are translated by an equal distance in the opposite direction normal to the cut plane to change the number of atoms in the offspring (Fig. 4.2). If the translation of a complete lattice period still does not yield the correct number of atoms, the redundant atoms are removed randomly from the offspring. After the atomic coordinates are generated, the unit cell of the offspring structure is produced by a linearly weighted combination of the lattice vectors of the parent structures,

$$A_{offspring} = w_1 A_1 + w_2 A_2\,, \qquad w_1 + w_2 = 1\,. \tag{4.3}$$

The weighting factors w_1 and w_2 of the parent cell A_1 and A_2 can be chosen randomly or decided by the fitness scores of the parent structures.

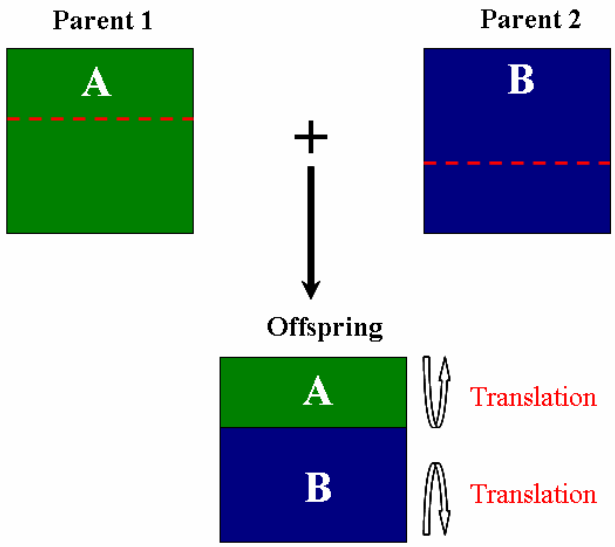

Figure 4.2. An offspring structure generated through heredity operation by mating two parent structures. Slab A from parent 1 and slab B from parent 2 are assembled together. The dotted line denotes the cutting plane of each parent structure.

4. 1. 2 Mutation operation

Mutation operation introduces distortions on a parent structure to generate the offspring structure. This operation serves the purpose of 'neighboring span' in the free energy surface, by distorting the structure from one local minimum to another in the neighboring region. It is achieved by subjecting the unit cell shape and atomic positions in the parent structure to small changes where the directions and size of the distortions are chosen randomly [52-56]. In this study, the new unit cell *A'* is produced by applying a symmetric strain matrix on the matrix *A* representing the unit cell of the parent structure:

$$A'(i,j) = \begin{vmatrix} 1+ep(1,1) & ep(1,2)/2 & ep(1,3)/2 \\ ep(1,2)/2 & 1+ep(2,2) & ep(2,3)/2 \\ ep(1,3)/2 & ep(2,3)/2 & 1+ep(3,3) \end{vmatrix} \cdot A(i,j)\,. \qquad (4.4)$$

Here the matrix elements $ep(i, j)$ are zero-mean Gaussian random numbers defined by

$$f(x) = \frac{1}{\sigma\sqrt{2\pi}} \exp[-\frac{x^2}{2\sigma^2}], \tag{4.5}$$

where σ is the standard deviation and represents the width of Gaussian distribution. The offspring cell is generated from a slight distortion of the unit cell of the parent structure (Fig. 4.3). The resulting cell vectors are then re-scaled to produce the desired volume.

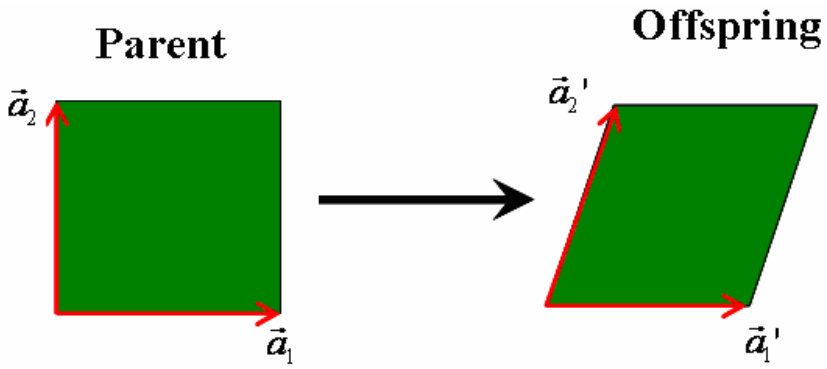

Figure 4.3. The unit cell of an offspring structure generated through mutation operation by distorting the unit cell of the parent structure.

4. 1. 3 Retaining operation

A retaining operation [52] is applied to the population after structural optimizations. This procedure keeps a small subset of lowest-energy structures in the population to pass their genomes onto successive generations. It is noteworthy that the GA tends to produce a large number of identical low-energy structures. An ideal scenario is that during the evolution, the lowest-energy (fittest) structure evolves, reproduces itself, and eventually dominates the entire population. The considerable redundancy constitutes a statistically strong indication that the redundant structures are energetically favored [211, 212]. However, under high pressure, it is not uncommon that meta-stable structures with slightly higher energies exist. In this aspect, to avoid

eliminating meta-stable structures, it is helpful to remove redundancy of lowest-energy structures and retain only a single copy from the set of identical low-energy structures in the population. The preference for the fittest structure is then decided by the fitness rank, *i.e.*, lower-energy structure has higher priority for being selected as a parent structure. The evolution cycle is repeated until no new low-enthalpy structures are generated in several successive generations. By using the retaining operation, best-fit structures in each generation are carried over to the next generation. A criterion for convergence of the evolution is that the subset of lowest-enthalpy structures and their relative energy order are maintained within several new generations.

4. 1. 4 Structure separating and evolutionary tracking

A structure analysis package [213] has been implemented to examine structural similarity based on comparison of the radial distribution functions (RDF) and space group symmetries of the fully relaxed structures (Fig. 4.4). Distinguishing structurally distinct structures, besides using them in the 'retaining' operation, is useful in the heredity operations to avoid mating between *identical* structures. A monitoring routine [52] has been developed to trace the evolutionary history and analyze the production efficiency (Fig. 4.5). Specifically, for each generation, a record of (i) the number of offspring structures having lower energy than their parents, (ii) the number of offspring structures different from their parents and (iii) the structural information and space groups of newly generated and disappeared structures is kept. These records are needed for analysis of the evolutionary track of new structures from the closest kin.

Index	U/H	GPa	Volume	bin1	bin2	bin3	#1	#2	#3	SG
CONTCAR0001	-35.3813	58.79	44.1900	1.36	2.24	2.36	24	48	24	I2_13
CONTCAR0002	-35.3244	58.96	44.1700	1.36	2.24	2.36	24	48	24	I2_13
CONTCAR0027	-35.1311	59.56	44.0800	1.36	2.24	2.36	24	48	24	I2_13
CONTCAR0041	-34.1061	60.14	43.4200	1.36	1.50	2.18	16	8	16	I2_13
CONTCAR0003	-34.1202	59.98	43.3800	1.36	1.50	2.18	16	8	16	Cmca
CONTCAR0043	-34.1025	60.10	43.4000	1.36	1.50	2.18	16	8	16	Cmca
CONTCAR0039	-33.4806	60.12	44.3100	1.36	1.48	1.50	16	4	4	P2/m
CONTCAR0016	-33.4718	60.19	44.3300	1.36	1.48	1.50	16	4	4	P2/m
CONTCAR0033	-33.4456	60.28	44.3300	1.36	1.48	1.50	16	4	4	P2/m

Figure 4.4. A sample output of the structure analysis package developed by us. A group of fully relaxed structures was analyzed with each output line showing the results for one structure. The structures are sorted in order of increasing energy, and thus the first structure is the lowest-energy structure. For each structure, the calculated total energy, external pressure, atomic volume, sizes of concentric cells defined in the RDF analysis, the numbers of atoms in each concentric cell, and the space group symmetry are printed out. The current version of GA code was implemented for VASP package.

```
Total =  80 structures
         29 U/H lower than parents,   0.36%
         29 different from parents,   0.36%
          2 new structures        ,   0.03%
          2 structures diappeared ,   0.03%

The new structures:
                            I2_13
                            Pm

The disapeared structures:
                            P2_12_12_1
                            Fdd2
```

Figure 4.5. A sample output of the evolutionary monitoring routine developed in this work.

4. 2 Tests and results

This section presents results of structure prediction of three high-pressure solids, single-boded phase of nitrogen, phases IV and V of calcium, and phase II of simple hydride AlH_3.

4. 2. 1 High-pressure single-bonded phases of nitrogen—a prediction prior to experiment.

At ambient pressure, two nitrogen atoms form a diatomic molecule with a triple covalent bond. Under high pressure, the molecular structure undergoes several phase transitions into non-molecular structures. Since the dissociation energy of a triple bond is extremely high, the decomposition of a non-molecular structure back into the molecular form, if could be realized, would release a large amount of energy. Therefore, non-molecular nitrogen compounds might serve as potential high-energy storage materials and this possibility has been investigated for decades.

Many theoretical predictions of non-molecular nitrogen started from distortion of the simple cubic (SC) structure [214]. For example, the earlier proposed A7 and black phosphorus (BP) structures were obtained from rhombohedral and orthorhombic distortions of SC, respectively [214]. Recently a systematic search method spanning all possible distortions of SC was developed and several new SB structures were proposed [215]. The other group of non-molecular nitrogen has a chain-like structure in which nitrogen atoms are connected by alternating single- and double-bonds, *e.g.*, the *Cmcm* [216] and *Imma* [217] chain structures. A breakthrough in investigating non-molecular nitrogen is the theoretical prediction [214] of the 'cubic gauche' (CG) structure that has been successfully synthesized in laboratory after intensive efforts [218]. In the present work, the GA is used to search for high-pressure single-bonded (SB) structures of nitrogen. We not only recover the lowest-energy structures (CG, *C*2/*c*, BP and *Cmcm* chain) [54, 219, 220], but also reveal a novel metastable SB structure.

The search for high-pressure structures of nitrogen at 80 GPa has been performed with a population of 80 eight-atom unit cells. An 8-atom model comprises of possible structures with 1, 2, 4 and 8 atoms per primitive cell. In each generation, the top 20% highest enthalpy structures are rejected. In the generation of new offspring structures, the parents are chosen according to the enthalpies (fitness score). The 10% of the structures in the new generation are retained from the pervious generation. The 70% of the structures are produced from heredity operations and the remaining 20% from mutation operations. The atomic volume, unit cell shape, and atomic positions of each candidate structure are fully optimized at constant pressure. Electronic calculations are performed with the VASP [63] package employing a PAW pseudopotential [147] and a PW energy cutoff of 910 eV. The GGA (PBE) exchange-correlation functional is employed. No symmetry is assumed in the calculations. The MP meshes were used for the first BZ sampling. The MP *k*-point meshes are generated by scaling according to the length of the reciprocal lattice vectors of the structure with a basic division of 4 and rounded to the nearest higher even integers. Lowest-enthalpy structures evolved from each generation are re-optimized with more stringent convergence criteria and doubling the size of the *k*-point grid.

The evolution is performed for 20 generations. Fig. 4.6 (a) shows results of the first 8 generations. Candidate structures are sorted in order of increasing enthalpy, and thus the first structure in each generation is the lowest-enthalpy structure. The efficiency of the evolution is analyzed and summarized in Fig. 4.6 (d). Structures of the first 10 generations are compared with their parents from previous generations. The percentage of offsprings having lower enthalpies than their parents is indicated by open circles. The percentage was initially fairly high, but decreased dramatically and then stabilized around 30%. This observation reveals the evolutionary trend of 'chaos'→ 'local minima'→ 'neighborhood spanning' on the free-energy surface. As shown in Fig. 4.6 (a) the first known non-molecular structure appears is the *Cmcm* chain structure that has the lowest enthalpy in the second generation. The CG structure appears in the third generation. The evolution of the CG structure is presented in Fig. 4.6 (b). The structure is the heredity offspring of the *Cmcm* chain structure and a higher-enthalpy SB *C*2 structure. The *Cmcm*

chain and *C2* structures are both offsprings of distinct *P*1 structures. The discovery of the CG structure from the GA is not trivial. The CG structure exhibits all-*gauche* helicity in which all dihedral angles in single bonds have the *gauche* conformation to minimize the internal energy. This unique structural topology makes it isolated in energy space by high activation barriers.

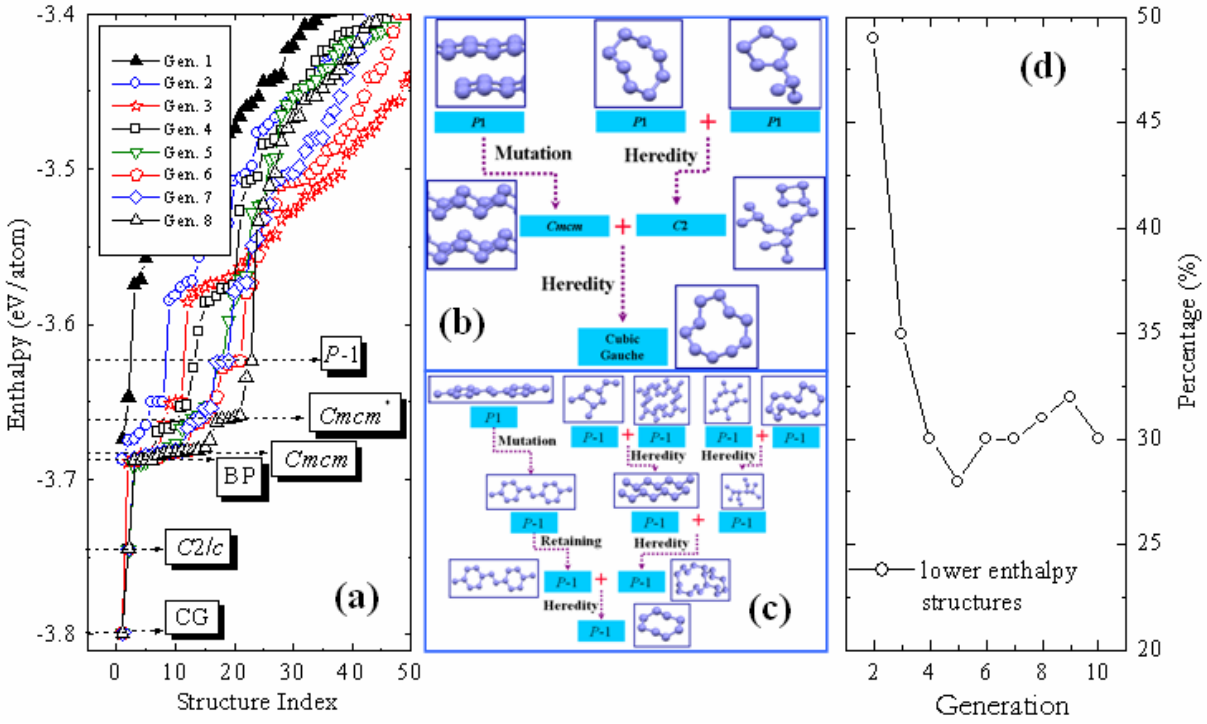

Figure 4.6. (a) The evolutionary procedure showing the first 8 generations by different symbol curves. The *Cmcm* structure marked with the asterisk is a distorted form of the known *Cmcm* chain structure. (b) The detailed evolution of the CG structure recovered in the third generation. (c) The detailed evolution of the new *P*-1 structure found in the fourth generation. (d) The searching efficiency analysis for the first ten generations; the percentage of offspring structures having lower enthalpies than their parents as a function of generation.

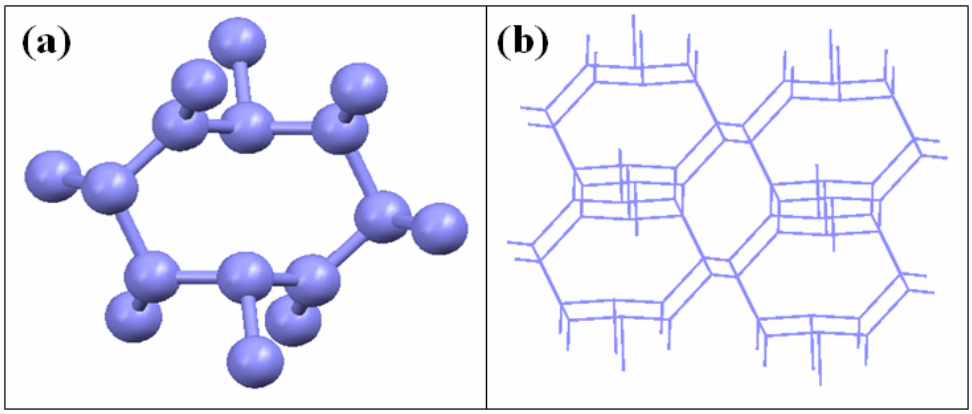

Pressure (GPa)	Space group	Lattice parameters (Å, °)	Atomic coordinates (fractional)
80	*P*-1	a = 3.13 b = 3.48 c = 4.51	2i 0.8226 0.1801 0.5103
		α = 71.22 β = 83.18 γ = 74.41	2i 0.8528 0.4956 0.2508
			2i 0.4838 0.3398 0.9432
			2i 0.8892 0.2526 0.7701

Table 4.1. Details of the new *P*-1 structure at 80 GPa. Inset (a) The primitive cell shows a puckered eight-member ring. (b) Connections between the eight-member rings in the crystal structure.

A new SB structure with *P*-1 symmetry appears in the fourth generation. Fig. 4.6 (c) shows its evolutionary pathway. This structure has eight atoms in the primitive cell and the structural details at 80 GPa are given in the Table 4.1. Inset (a) of Table 4.1 shows that the eight nitrogen atoms are arranged in a puckered eight-member ring with inversion symmetry. Each ring is connected to six neighboring rings with alternating *gauche*- and *trans*-dihedral angles. This topology is energetically favorable since the *gauche*- and *trans*-dihedral angles are two minimum-energy conformers in SB nitrogen [214, 221]. The equation of states of the new *P*-1 structure and several earlier proposed structures are compared in Fig. 4.7. At 80 GPa, the new *P*-1 structure is the fifth lowest-

enthalpy phase *c.a.* 0.17 eV/atom higher than the CG phase. The enthalpy of the *P*-1 structure approaches that of the *Cmcm* chain structure with increasing pressure and becomes lower at *c.a.* 110 GPa. Besides the CG and *Cmcm* chain structures, two lowest-enthalpy structures proposed earlier, the *C2/c* [54] and BP [214] structures, are recovered in the fourth and sixth generation, respectively (Fig. 4.6 (a)). However, the A7 [214], #8 [210], #11 [210], and *Imma* chain [217] (not shown) structures were not observed. These structures have higher enthalpies than that of the new *P*-1 structure, with the enthalpy differences vary from 0.08 to 0.45 eV/atom at 80 GPa. Since the GA is based on "survival of the fittest", only a subset of the lowest-enthalpy structures survives. Besides the structures discussed above, there are two other proposed SB nitrogen structures, LB [219] and CW [220]. The LB structure has proven to be unstable *via* phonon calculation. The CW structure has six atoms per primitive cell and therefore is not obtained in the present eight-atom simulation. However, using the reported structure, the enthalpy is found to be 0.03 eV/ atom higher than that of the new *P*-1 structure at 80 GPa.

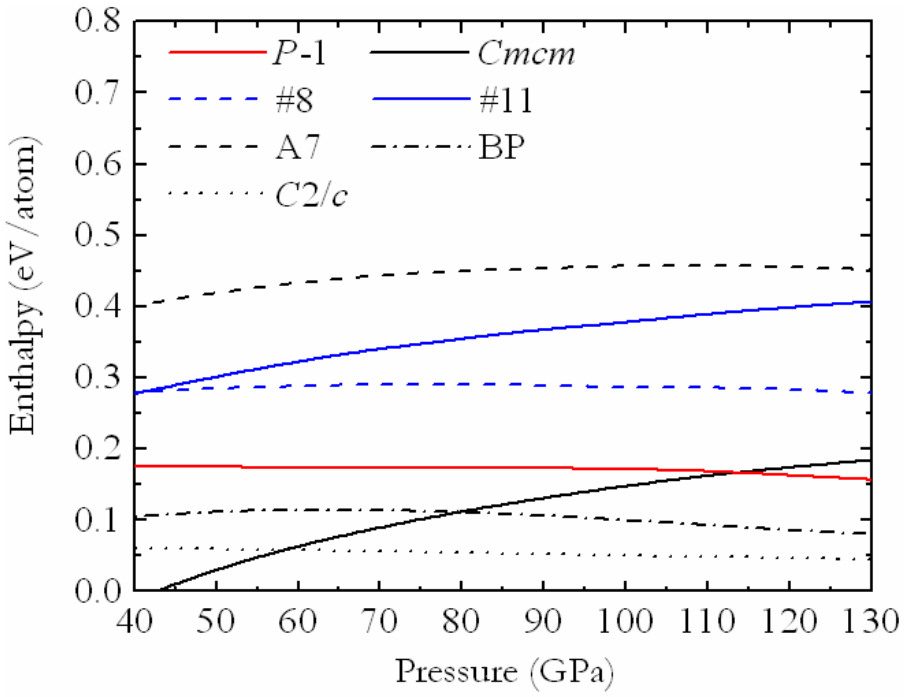

Figure 4.7. Enthalpies per nitrogen atom of the new *P*-1 structure and selected earlier proposed non-molecular structures as a function of pressure. The enthalpy of the CG structure is taken as reference.

The energetic order of the lowest-energy SB structures shown in Fig. 4.7 can be understood from the analysis of the long-pair interaction between adjacent nitrogen atoms. Theoretical investigations [221-223] on X_2N-NX_2 (X=F, H, etc.) isomers have shown that the interaction is characterized by the dihedral angle. The most unstable structure is the *cis* conformation with the zero dihedral angle. As the dihedral angle increases, the bond energy decreases and reaches a minimum at the *gauche* conformation. For example, in the CG structure the *gauche* angle is 107° [214]. The second energy minimum is found at the *trans* conformation with the dihedral angle of 180°. In the CG structure, nitrogen atoms are arranged entirely in the *gauche* conformation and therefore have the lowest enthalpy. The BP structure, having both *gauche* and *trans* dihedral angles, is the second lowest energy structure and has only 0.11 eV/atom higher energy than that of the CG structure at 80 GPa. In the new *P*-1 structure, four out of the eight dihedral angles (±125°, ±106°) in the eight-member ring are close to the global minimum identified by the *gauche* arrangement. The remaining four dihedral angles of ±48°and ±27°, especially the latter, are close to the *cis* conformation, and therefore the energy is expected to be higher than that of both the CG and BP structures.

To examine the stability of the new *P*-1 structure the phonon dispersion has been calculated at 80 GPa. The results are presented in Fig. 4.8 (a). The absence of imaginary frequency mode confirms that the new *P*-1 structure is stable. The electronic band structure at 80 GPa (Fig. 4.8 (b)) shows that this structure is an insulator with an indirect band gap of 2.8 eV between the *U* and *V* points.

In summary, the GA for crystal structure prediction with first-principles structural optimizations has been applied to investigate SB structures of nitrogen at 80 GPa. The four observed or predicted lowest-energy structures, CG, *C*2/*c*, BP and *Cmcm* chain, have been identified successfully. A novel SB nitrogen structure with three-dimensionally connected eight-member rings has been discovered. This new structure is stable and has only 0.17 eV/atom higher enthalpy than that of the CG phase at 80 GPa. It is noteworthy that a previously proposed search procedure [215] based on rearrangements and distortions of SC cell failed to predict this new structure.

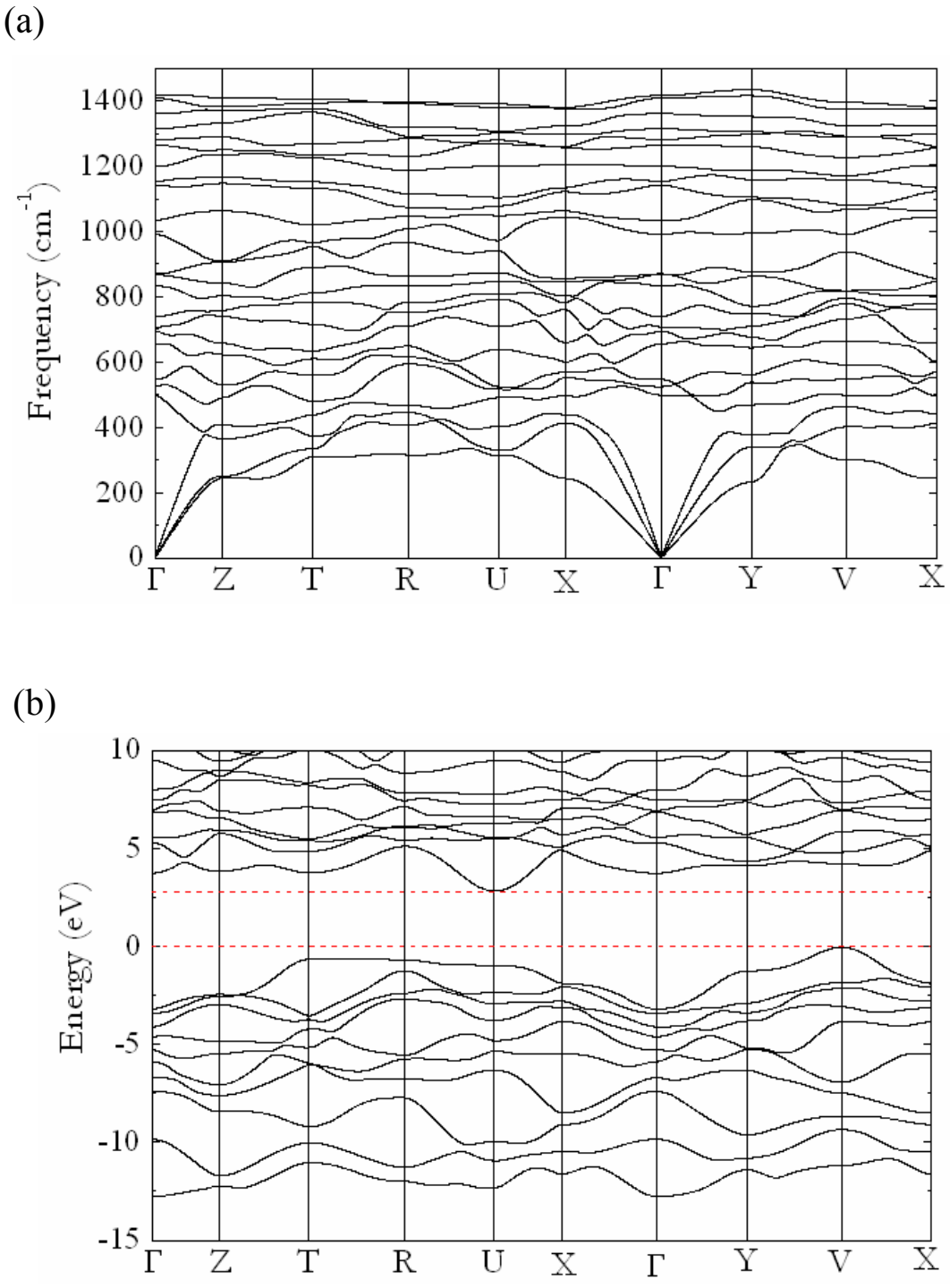

Figure 4.8. The phonon dispersion (a) and electronic band structure (b) of the new *P*-1 structure calculated at 80 GPa.

4. 2. 2 Structures of the high-pressure Ca IV and V phases—an explanation to the elusive experimental data

Recent experiments have revealed surprisingly high superconducting critical temperatures, T_c, of Ca under high pressure [98]. The T_c increases with pressure and reaches 25 K at 161 GPa, which is the *highest* observed T_c for all pressure-induced superconductors up to date. At ambient pressure Ca has a FCC structure. Under high pressure, it undergoes successive phase transitions into a BCC phase at 20 GPa then to a SC phase at 32 GPa [224]. At higher pressures, two new phases have been identified [99-101]: Ca-IV near 100-110 GPa and Ca-V at about 139 GPa. The SC, Ca-IV, and Ca-V phases were all found to be superconducting. The knowledge of the lattice dynamics of these superconducting phases is crucial for understanding their electron-phonon mechanisms. Unfortunately, the structures of Ca-IV and Ca-V could not be determined from experimental diffraction patterns [99] due to overlapping Bragg peaks from different phases and from the gasket material used in the diamond anvil apparatus (see Fig. 4.9).

In the present study, an extensive search for possible structures for Ca-IV and Ca-V was made using GA [52-56]. It was found that the lowest enthalpy structure for Ca-IV has a *Pnma* symmetry, while the high-pressure Ca-V has *Cmca* symmetry [89]. The calculated diffraction patterns for both phases are in good accord with the experimental patterns. The strategy for structure searching, parameters used in the algorithm are similar to those described in section 4. 2. 1. GA calculations were performed at 120 GPa and 165 GPa with a population of 80 candidate structures with supercells containing 8 Ca atoms. The genetic evolution cycle was repeated until the results achieve convergence, *i.e.*, with no new low-enthalpy structures appear in successive generations. In the present study, it is found that for each pressure, 20 generations were more than enough to locate the most stable structure. Structural optimizations were performed with the program VASP [63] employing the PAW pseudopotential [147]. The Ca pseudopotentials employ 3s3*p*4*s* as valence states. No crystal symmetry was assumed in the search. The MP

meshes were scaled according to the length of the reciprocal lattice vectors of the candidate structure with a basic division of 4, *i.e.*, 4×4×4 is the smallest mesh.

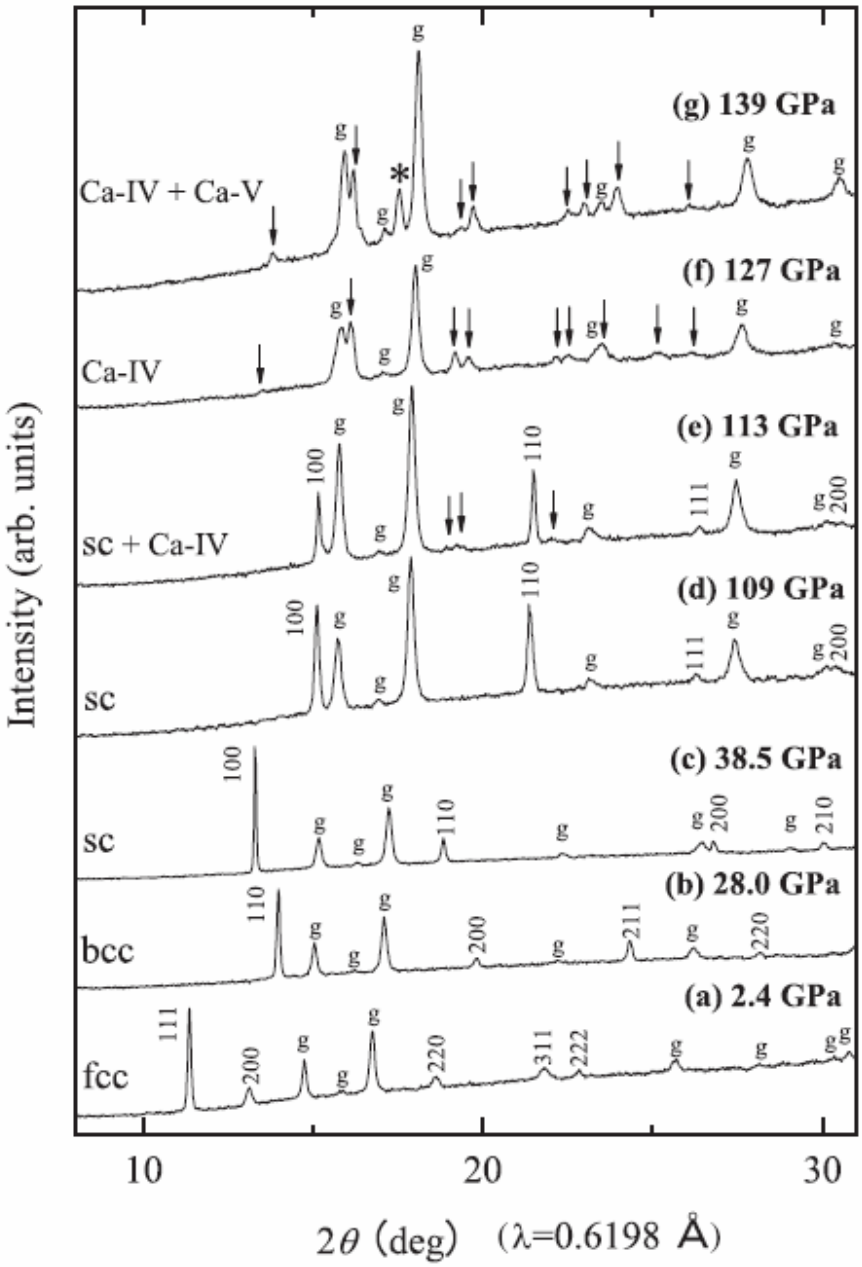

Figure 4.9. X-ray diffraction patterns of Ca at several pressures. The diffraction pattern of the SC phase continuously shifted at pressures from 32 to 109 GPa. The peaks with arrows show the new phase, Ca-IV. The peak with the star indicates another new phase, Ca-V. The ‘‘g’’ mark denotes the peak from the Re gasket.

The lowest enthalpy structures found for Ca-IV and Ca-V have space groups of *Pnma* and *Cmca*, respectively (Fig. 4.10). Details of the predicted structures are presented in Table 4.2. The SC to Ca-IV transition pressure is predicted to *c.a.* 90 GPa (Fig. 4.10). The theoretical value corresponds well to the observed abrupt drop in electrical resistance from 100-110 GPa. The calculated enthalpy differences between the *Pnma* and *Cmca* structures are very small. For example, at 160 GPa the enthalpy of the *Cmca* structure is only *c.a.* 0.02 eV/atom lower than the *Pnma* structure. A very small enthalpy difference indicates that these two phases may co-exist over a pressure range of 90 – 140 GPa and the precise location of the Ca IV $\rightarrow$ V transition pressure will be difficult to identify.

Phase	Pressure (GPa)	SG	Lattice parameters (Å)		Atomic coordinates (fractional)		
Ca-IV	120	*Pnma*	***a***=4.420 ***b***=3.386 ***c***=2.959	4*c*	0.326	0.250	0.614
Ca-V	140	*Cmca*	***a***=4.414 ***b***=4.373 ***c***=4.381	8*f*	0.000	0.169	0.685

Table 4.2. Structural parameters for the predicted structures of Ca-IV and Ca-V.

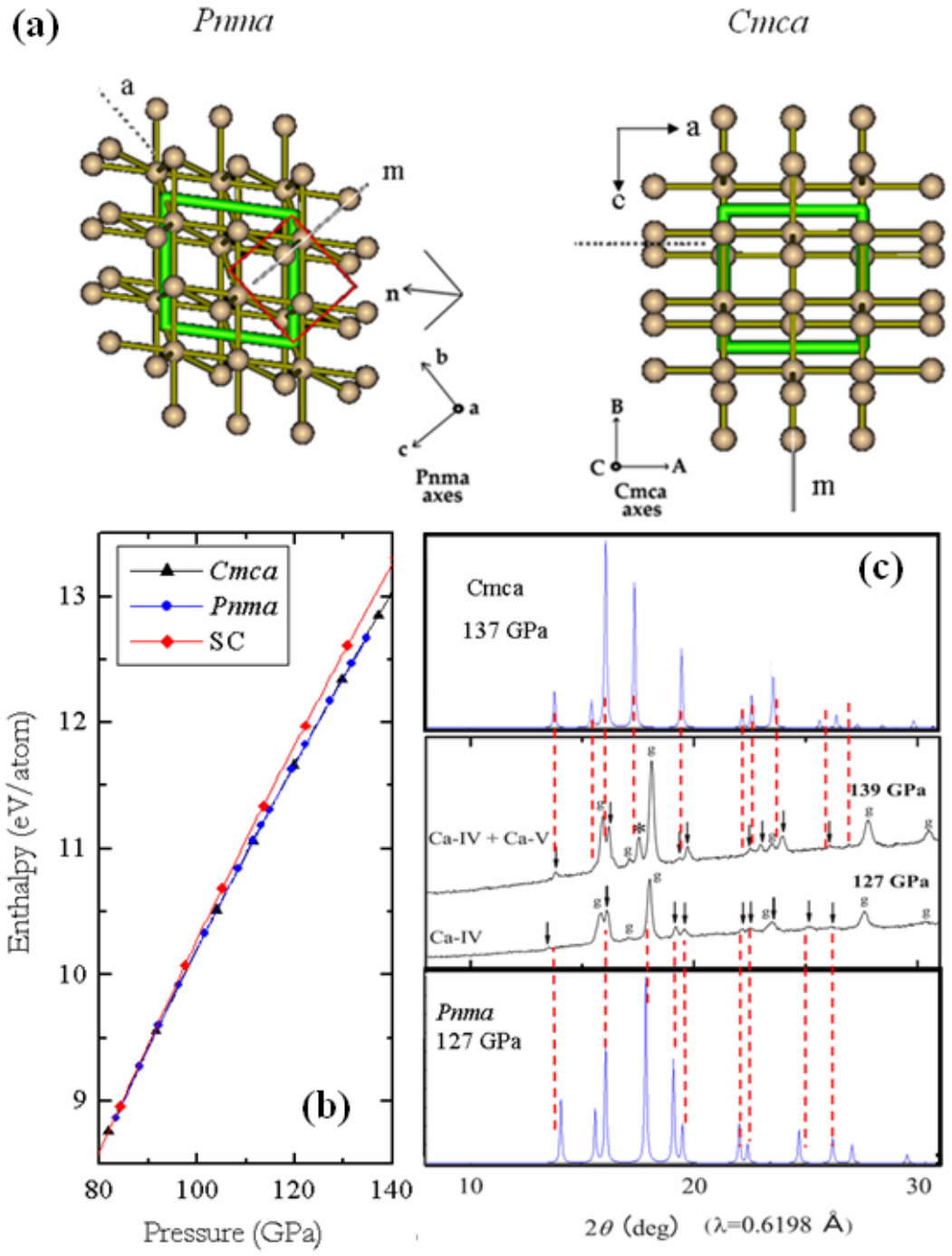

Figure 4.10. (a) Perspective view of the predicted structures for Ca-IV (*Pnma*) and Ca-V (*Cmca*). (b) Calculated enthalpy versus pressure and (c) comparison of calculated and observed (middle, black) diffraction patterns for Ca-IV (*Pnma*) and Ca-V (*Cmca*). The

experimental diffraction patterns are taken from Ref. 99. The red lines are intended as a guide to the eye for matching the theoretical and observed positions of the Bragg peaks.

The experimental diffraction patterns for Ca-IV and V has been indexed successfully with the predicted structures. A comparison between calculated diffraction patterns of the *Pnma* and *Cmca* structures to the experimental data of Ca-IV and Ca-V is given in Fig. 4.10. As shown in Table 4.3, except for two spurious peaks that can be attributed to Ca-IV, all the experimental diffraction peaks can be indexed with the proposed *Cmca* structure of Ca-V. In particular, the "new" diffraction peak observed at 17.86^{o} in the experiment (shown in Fig. 4.10 with an asterisk), which was attributed in Ref. 99 to the presence of phase V, is correctly reproduced and is assigned to the strong 021 reflection. The unit cell parameters derived from fitting the experimental pattern are very close to the theoretical predictions (Table 4.2 and 4.3). The indexing for Ca-IV was not immediately obvious. Indices for calculated low-angle reflections of the proposed *Pnma* structure can be assigned unambiguously to the low-angle Bragg peaks (Table 4.3). The recalculated cell parameters then index all the peaks with valid *Pnma* reflections. A strong reflection belonging to Ca-IV coincidentally overlaps with the gasket (marked *g*) at *c.a.* 18^{o}.

Fig. 4.11 (a) and (b) show the electronic band structures of the *Pnma* and *Cmca* phases calculated at 120 and 140 GPa, respectively. A distinct feature observed in both band structures is the simultaneous occurrence of 'flat band and steep band' near the Fermi level, *e.g.* at the *X* point of the *Pnma* band structure, and in the midway of the $T_2 \rightarrow Z$, $Z \rightarrow \Gamma$ and $\Gamma \rightarrow Y_2$ lines of the *Cmca* band structure. These are common features in pressure-induced superconductors, and this scenario has been suggested as favorable conditions for enhancing electron pairing essential to superconductivity [156]. The phonon band structure of the *Pnma* and *Cmca* phases calculated at 120 GPa and 140 GPa are depicted in Fig. 4.11 (c) and (d). The absence of imaginary vibration modes shows that the *Pnma* and *Cmca* phases are stable.

Phase	Pressure (GPa)	SG	Lattice parameters (Å) (derived from experiment)	2θ(exp)	Indices	2θ(cal)
Ca-IV	127	*Pnma*	$\boldsymbol{a}$ = 4.560 $\boldsymbol{b}$ = 3.227 $\boldsymbol{c}$= 3.040	13.45	1 0 1	14.08
				16.12	0 1 1	16.11
				19.17	2 1 0	19.17
				19.54	2 0 1	19.57
				22.15	0 2 0	22.15
				22.50	2 1 2	22.52
				23.53	0 0 2	23.54
				25.13	1 0 2	24.83
				26.14	1 2 1	26.35
Ca-V	139	*Cmca*	$\boldsymbol{a}$=4.508 $\boldsymbol{b}$=4.481 $\boldsymbol{c}$= 4.407	13.77	1 1 1	13.81
				16.15	0 0 2	16.18
				17.50	0 2 1	17.86
				19.32	spurious (Ca-IV)	
				19.70	1 1 2	19.71
				22.50	2 2 0	22.50
				22.97	2 0 2	22.69
				23.94	2 2 1	23.94
				26.04	spurious (Ca-IV)	
				26.92	1 1 3	26.89
				29.03	0 2 3	29.23

Table 4.3. A comparison of predicted and observed diffraction pattern of Ca-IV and V

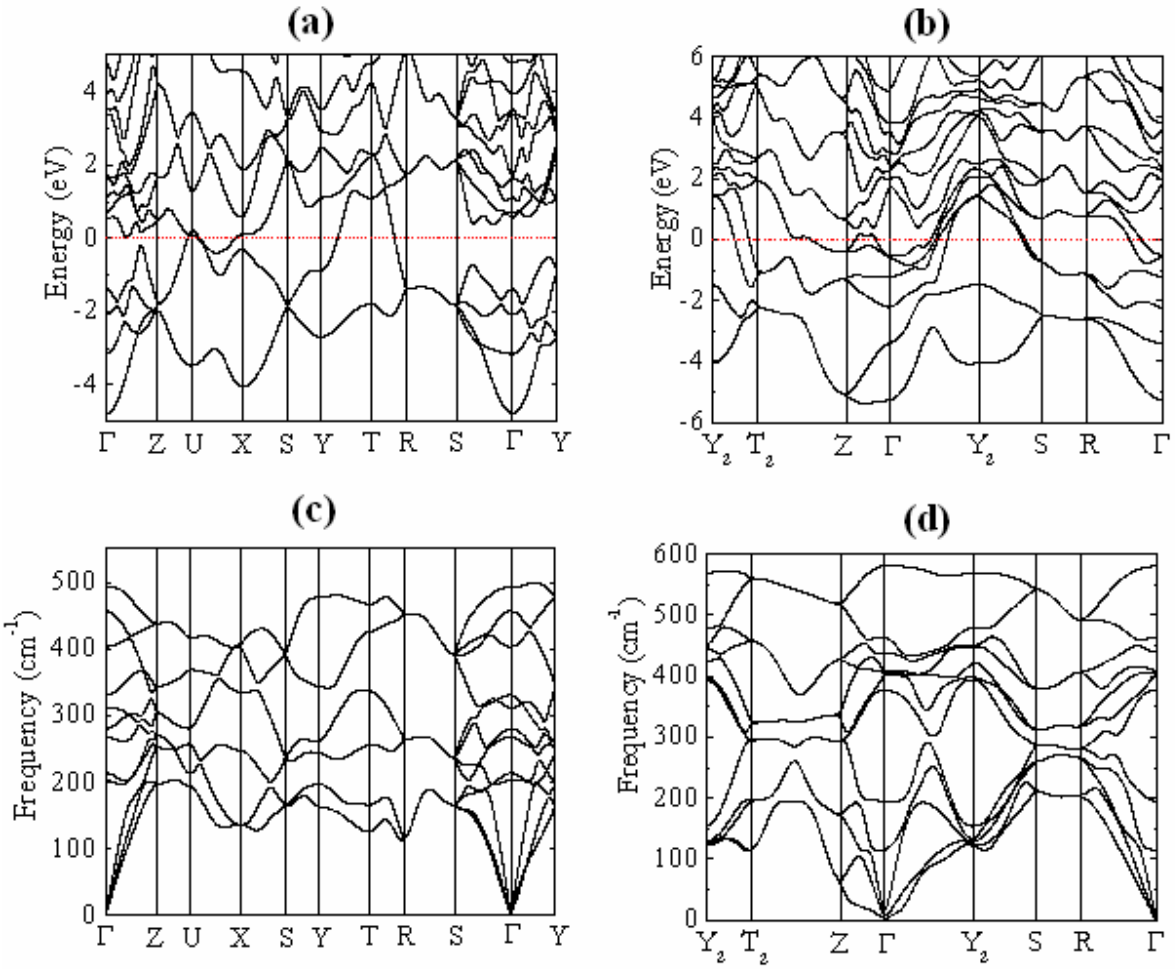

Figure 4.11. Calculated electronic band structure and phonon dispersion for the *Pnma* (a) and (c) at 120 GPa; *Cmca* (b) and (d) at 140 GPa.

In summary, using the GA, two lowest enthalpy structures corresponding to the high-pressure Ca-IV and V phases were found. From comparisons with experimental diffraction patterns, a *Pnma* structure is suggested for Ca-IV and a *Cmca* structure for Ca-V.

4. 2. 3 The structures of the high pressure Phases II and III of AlH_3 – a case beyond single type of atom

Dense hydrogen is expected to possess unusual properties, such as metallic conductivity and high-T_c superconductivity [177, 225-227]. However, despite enormous experimental efforts up to pressure of 320–340 GPa, the elusive goal of producing metallic hydrogen in the solid phase has not been achieved [112-114]. On the other hand, it was suggested that dense, metallic hydrogen-rich compounds might show similar properties to those of metallic hydrogen [73, 74, 228]. Specifically a ‘‘hydrogen-dominant’’ metallic state might be found under pressure in covalent hydrides, which are insulators at ambient pressure. Heavy compression is expected to result in the overlap of electronic bands and the hydrides become metallic. Assuming that in the high-pressure metallic phases hydrogen atoms form a three-dimensional network, one would expect to obtain a hydrogen-dominant state having properties similar to metallic hydrogen. As presented in Chapter 2, this suggestion has been proved by the investigation on dense SiH_4, in which the metallic and superconducting state has been observed at high pressure with the maximum T_c of 17 K.

The first experimental proof of a pressure-induced hydrogen-dense metallic state in a covalent hydride, prior to the breakthrough discovery of SiH_4, was achieved in compressed AlH_3 [90]. At ambient pressure, the most stable structure of AlH_3 is known to have a trigonal cell with space group *R*-3*c* (phase I) [229-234]. This structure has been found to be stable up to at least 35 GPa [235, 236]. New X-ray diffraction experiments have been performed up to 110 GPa, and two new high-pressure structures (denoted as phase II and phase III) have been discovered [90]. The pressure-induced metallization has been observed at around 100 GPa accompanying the phase transition from phase II to phase III. The low-pressure X-ray results are in agreement with earlier reports that indicate a *R*-3*c* structure. With increasing pressure, drastic changes in the diffraction pattern were observed at 63 GPa (Fig. 4.12). The new phase (phase II) was tentatively described by a distorted unit cell of the initial *R*-3*c* structure. The large broadening of diffraction peaks suggests that the symmetry of this structure is very low, perhaps

triclinic cell. It was difficult to make a definitive index of the experimental X-ray diffraction patterns. Phase-II is stable between 63-100 GPa. A second phase transition (phase III) was observed at around 100 GPa. The X-ray diffraction pattern of phase III is remarkably simple and can be indexed as two aluminum atoms forming a simple BCC lattice. However, in both cases, the positions of the hydrogen atoms cannot be determined from the X-ray data due to their negligible contribution to the diffraction peaks.

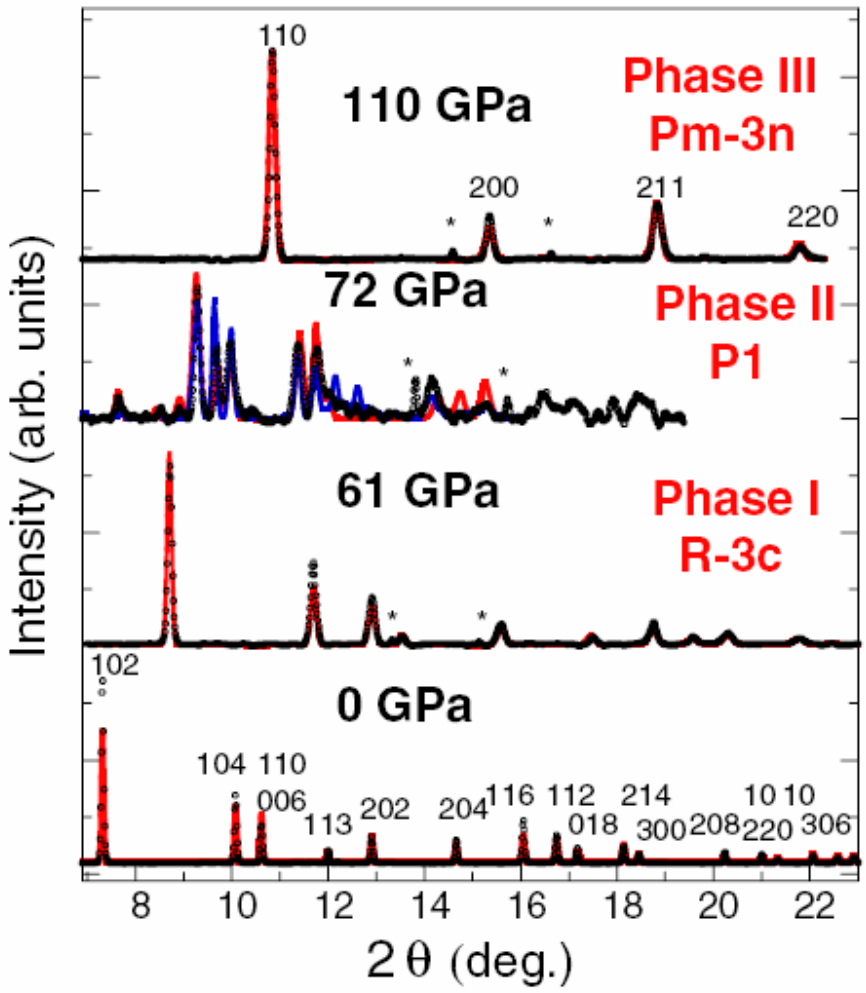

Figure 4.12. X-ray diffraction patterns of the phases I, II and III of AlH_3 at pressures of 61, 72 and 110 GPa, respectively. The incident wavelength is 0.412 Å. Solid curves are calculated diffraction patterns. Asterisks mark diffraction peaks from the gasket. Phase I

has a hexagonal cell with a = 4.44 and c = 11.8 Å. The Al atoms occupy atomic positions 6*b* 0.00 0.00 0.00, and the H atoms are in positions 18*e* 0.63 0.00 0.25. Phase II at 72 GPa was described in a monoclinic unit cell (space group *P*2) with lattice parameters a = 3.21 Å, b = 6.18 Å, c = 2.95 Å, and α = 119.7º containing 3 AlH_3 units (solid red line), or in a trigonal unit cell (space group *P*1) with a = 3.83 Å, b = 5.12 Å, c = 6.72 Å, α = 112.6 º, β = 111.9 º, and γ = 56.6 º containing 6 AlH_3 units suggested by the theory (solid blue line). Phase III has a cubic unit cell with a = 3.08 Å at 110 GPa. The Al atoms are in positions (0, 0, 0) and (0.25, 0.25, 0.25).

The identification of the structure of phase III is quite straightforward since the positions of Al atoms are known from the X-ray diffraction pattern (Fig. 4.12). In a cubic unit cell consisting of two AlH_3 units, there are only two possibilities to locate 6 H atoms. The H atoms either occupy the centers of the faces and centers of the edges of the cell, or are grouped in pairs and located on the faces, forming linear chains along the cubic axes. The resulting structures have space groups of *Im*-3*m* and *Pm*-3*n* in the two cases, respectively (Fig. 4.13, left). The *Im*-3*m* structure is the well-known ReO_3 type structure but the *Pm*-3*n* structure has never been observed in any other compounds before. Both *Im*-3*m* and *Pm*-3*n* structures are characterized by the same H-H distances (1.54 Å at 110 GPa). This H-H distance at 110 GPa are the shortest ever reported except for the H_2 molecule. From the extrapolation of the low-pressure data, H_2-H_2 distances of the same value are expected in molecular hydrogen at 400 GPa [237]. The Al-H distances are 1.54 and 1.72 Å in the *Im*-3*m* and *Pn*-3*m* structures, respectively. The calculated energy of the *Pm*-3*n* structure is lower than that of the *Im*-3*m* structure, suggesting that it is more energetically favorable (Fig. 4.13, right). The difference in energy is very large (2 eV at 100 GPa) and far exceeds any anticipated error in the DFT calculations. It is therefore concluded that the *Pm*-3*n* structure is likely to be the structure for phase III. In addition to the analysis of the equation of states (EOS), a structure search for candidate structures of phase III was made using GA. The search has been performed at 110 GPa with a population of unit cells containing 12 AlH_3 units. The choice of a 12 AlH_3 units is commensurate with both trigonal and cubic unit cells. At 110 GPa, the lowest-energy structure revealed from GA is the same as described above, *viz.* the *Pm*-3*n* structure. As

expected, the calculated diffraction pattern of this predicted structure is almost identical to the experimental data (Fig. 4.14).

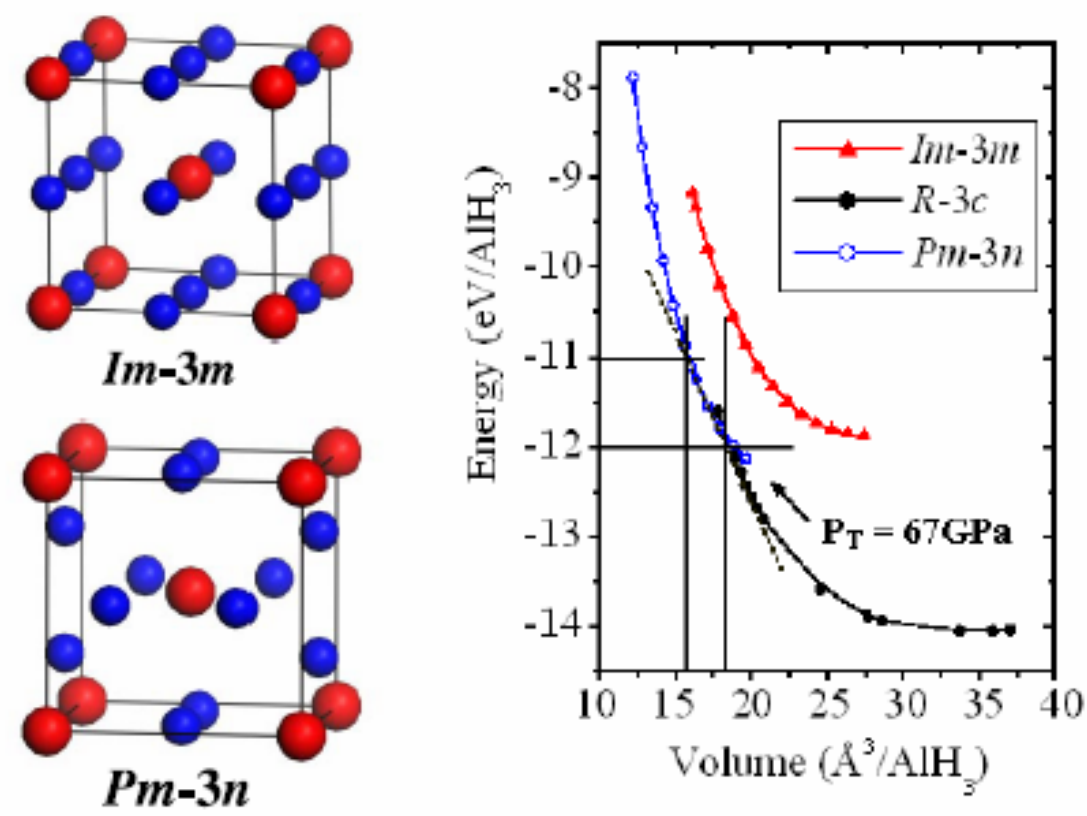

Figure 4.13. Left: the *Im*-3*m* (up) and *Pm*-3*n* (down) structures suggested for phase III. Al atoms are shown in red and H atoms are shown in blue. Each cell contains 2 AlH_3 units and Al atoms form a BCC frame. In the *Pm*-3*n* structure, hydrogen atoms occupy positions (1/2, 1/4, 0), (1/2, 3/4, 0), (1/4, 0, 1/2), (3/4, 0, 1/2), (0, 1/2, 1/4), (0, 1/2, 3/4). Right: calculated EOS for the *R*-3*c*, *Im*-3*m*, and *Pm*-3*n* structures. The *Pm*-3*n* structure is substantially lower in energy than the *Im*-3*m* structure.

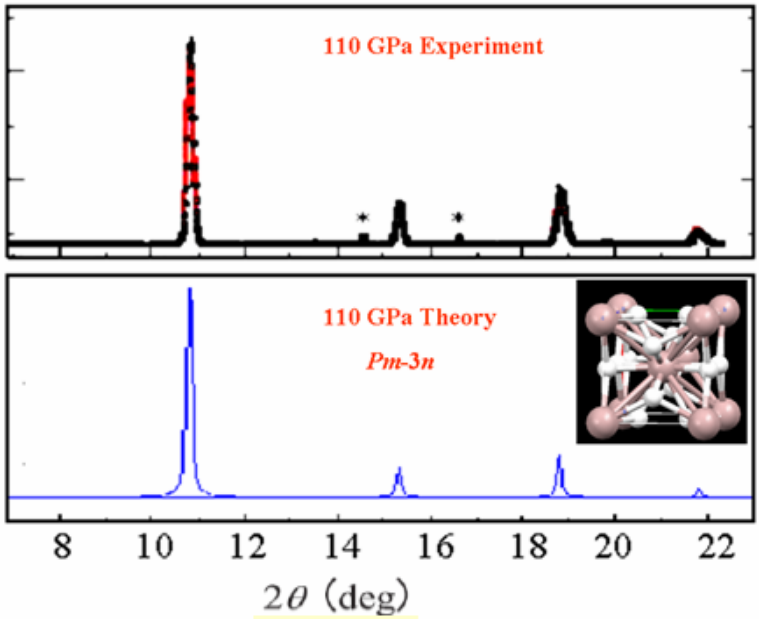

Figure 4.14. Comparison between calculated diffraction pattern of the predicted *Pm*-3*n* structure and experimental data. Asterisks mark diffraction peaks from the gasket.

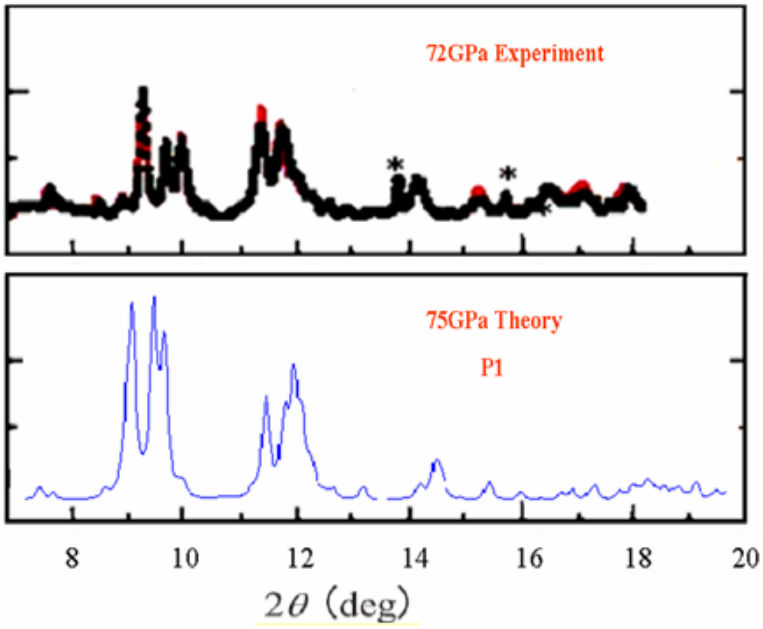

Figure 4.15. Comparison between calculated diffraction pattern of the predicted *P*1 structure and experimental data.

To search for possible structures of phase II of AlH_3 stable between 70 to 110 GPa, genetic evolution calculations were performed at 70 GPa. A structure that reproduces the observed X-ray diffraction pattern has a triclinic unit cell (space group *P*1) formed by distorted and shifted triangular Al planes. The calculated lattice parameters of the triclinic structure at 72 GPa are, a = 4.13 Å, b = 5.25 Å, c = 6.7 Å, α = 114.8º, β = 114.4º, and γ = 53.7º, which agrees well with the experimental data (Fig. 4.15). The EOS of the *P*1 structure is calculated from 60 GPa to 100 GPa. As shown in Fig. 4.16, the calculated EOS of the *P*1 structure is in very good agreement with experiment.

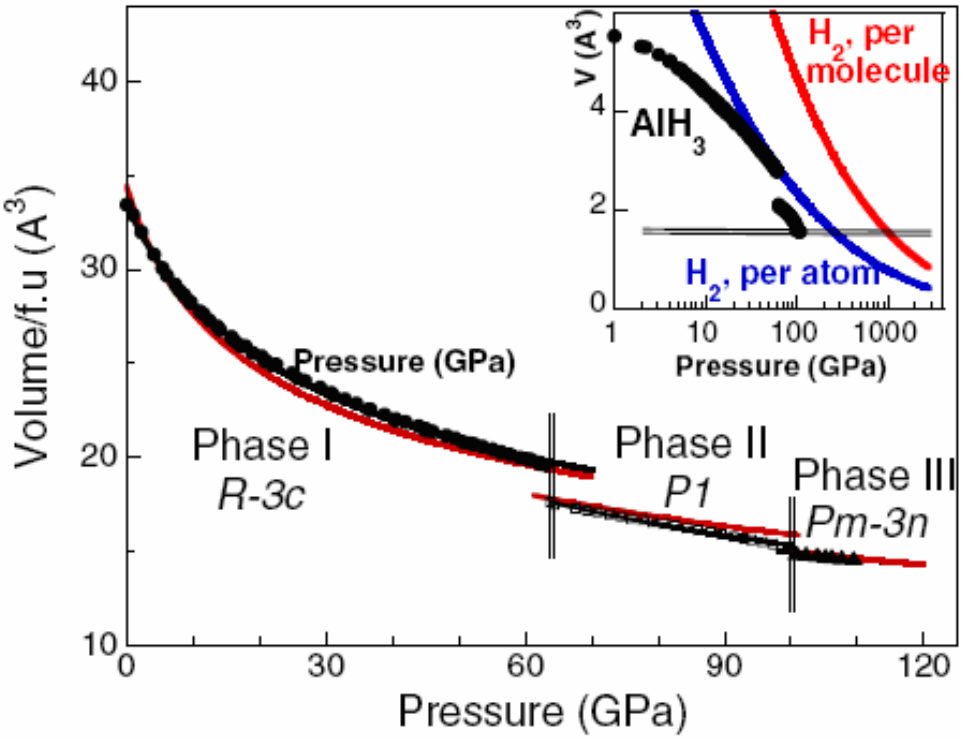

Figure 4.16. Volume per AlH_3 unit as a function of pressure. Black curves are fits of the experimental data by the Murnaghan-Birch equation. Red curves are results from *ab initio* calculations. In the inset, partial hydrogen volume per H atom in AlH_3 (circles) are compared with the volume per H atom (blue curve) and per H_2 molecule (red curve) expected in molecular hydrogen. Double lines are a guide to the eye.

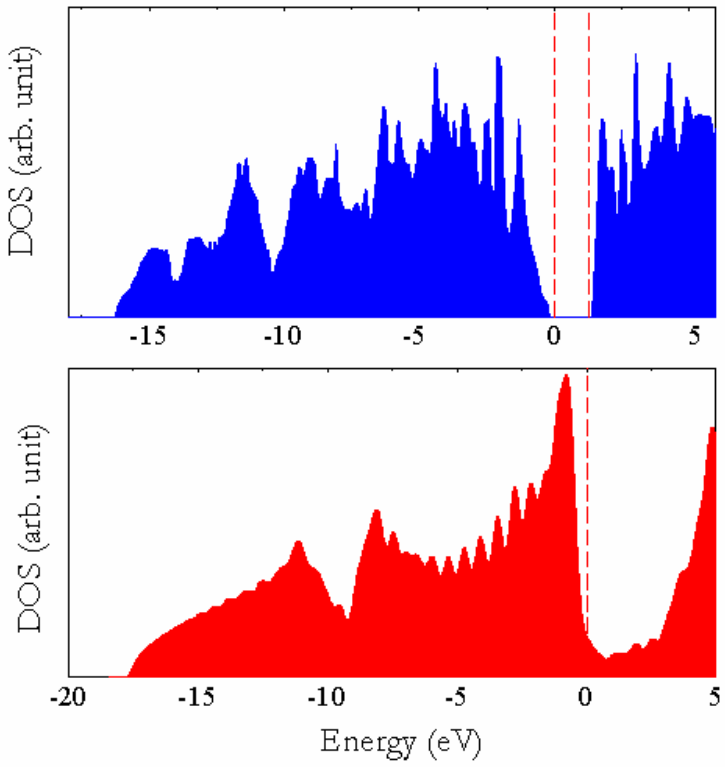

Figure 4.17. Pressure-induced metallization of AlH_3. (Top) Calculated DOS of the *P*1 structure at 75 GPa. (Bottom) Calculated DOS of the *Pm*-3*n* structure at 110 GPa.

In was found in experiment [90] that the structural transitions of AlH_3 are accompanied by drastic changes in electronic properties. At 60 GPa the sample starts to darken, indicating a gradual transformation to a semiconducting state. At 100 GPa, at the onset of the phase II—phase III structural transformation, the sample becomes black and electrical resistance shows a remarkably sharp insulator-metal transition. Variation of electrical resistance in the temperature range 4–300 K shows a typical metallic behavior for phase III. To examine the electronic properties of the predicted *P*1 and *Pm*-3*n* structures, the electronic DOS have been computed. The calculated DOS for candidate structures of phase II (*P*1 structure) and phase III (*Pm*-3*n* structure) support the experimentally observed pressure-induced metallization (Fig. 4.17). An energy gap in the DOS suggests that the *P*1 structure is an insulator. On the other hand, the absence of an energy gap in the DOS suggests that the *Pm*-3*n* structure is metallic. Metallization is

expected to occur accompanying the phase transition from phase II to phase III, as suggested by the experiments [90]. The good agreement of the calculated and observed diffraction patterns, EOS, and electronic structure strongly indicate that the predicted structures are correct.

In summary, GA has been used to search for candidate structures for high-pressure phase II and phase III of AlH_3, which have been observed by experiments recently. The proposed structure of phase III has a cubic cell with the Al atoms forming a BCC framework. The H atoms are grouped in pairs and located on faces and form linear chains along the cubic axes. This arrangement of the H atoms results in a *Pm*-3*n* space group. The arrangement of hydrogen atoms is consistent with that derived from structural analysis. The predicted structure for phase II has a triclinic cell. The predicted lattice parameters, unit cell volumes, and diffraction patterns agree reasonably well with the experimental data. The calculated electronic density of states also supports the pressure-induced metallization observed in the experiments.

4. 3 Summary and discussion

A reliable method for the prediction of the crystal structure of a solid is a central problem in high-pressure crystallography. Traditional theoretical methods for predicting unknown crystal structures usually involve dynamical processes that strongly depend on the initial configurations. An unreasonable initial guess may result in configurations being trapped in higher-energy local minima. GA presents an attractive alternative to these methods, since it does not need any assumption of the topology of the energy landscape and initial structures, and is efficient in investigating the free energy surface. The recently proposed GA for crystal structure prediction with our own new features has been implemented and applied to the investigation of multiple high-pressure phases of three solids, N, Ca, and AlH_3. The procedure successfully recovered the known structures established by experiments, that is, the '*cubic gauche*' structure in solid N and *Pm*-3*n* structure of phase III of AlH_3. Moreover, the GA method also revealed several energetically highly competitive meta-stable structures of solid N. For unknown

structures lacking comprehensive experimental data, such as the Ca-IV, Ca-V, and phase II of AlH_3, genetic evolution calculations have predicted possible structures for each case where the calculated diffraction patterns were in close agreement with the experimental patterns.

A random-search strategy [149] for the search of crystal structures was proposed recently. In the random-search method, a large population of trial structures are generated randomly and fully optimized to local minima. One then search for lowest enthalpy structures. In this method, the trial structures are independent of each other, and the energetically favorable structures do not further evolve to produce new offspring structures. This procedure is essentially equivalent to the generation of the initial candidate structures in GA, but with a much larger pool in the population. The random-search method has been found to be quite successful in several cases. Examples are the high-pressure $I4_1/a$ structure of SiH_4 [149], the high-pressure phase III of solid H_2 [86], and the high-pressure cubic phase III of AlH_3 [238]. The search strategies employed in GA and random-search method are different. The GA is 'self-improving' while the random-search method requires an 'exhaustive' search. Therefore, the GA can employ a small population of trial structures but the "quality" of population is improved through genetic operations to produce lower-energy offspring structure and locates the optimal structure by zooming in promising regions of the free-energy surface. The quasi-random method requires a much larger population of trial structures. As both methods have been shown to be successful to locate correct structures, the only difference between them is the efficiency. However, the efficiency is dependent on the complexity of the crystal structures. For simple crystals, such as mono-atomic structures, an exhaustive search of the free-energy surface is often good enough. In this case, the random-search method is very efficient. Fig. 4.18 shows the results of the random-search method on Si performed at ambient pressure. A population of 1250 trial structures with 8 atoms per unit cell was generated. After structural optimization, 225 trial structures belong to the correct Si-I (diamond) structure. The search efficiency for this particular case is very high, 225/1250 ~ 18%. We have tested the random-search method carefully by searching high-pressure Si structures from 0 to 70 GPa. All previously observed structures within this pressure

range, including the 7 stable structures and 2 meta-stable structures, were successfully recovered with a population of 500 trial structures (Fig. 4.19). For complicated structures, the exhaustive search of the free-energy surface is very difficult to achieve, because the diversity of possible configurations goes up with the structural complexity. In these cases GA is more efficient, since it is self-improving and tends to direct the search to the most promising region of the free-energy surface. As shown in this chapter, the lowest-enthalpy phase of solid nitrogen at high pressure, *cubic gauche* structure, has been recovered using GA in the third generation, with each generation comprising 80 candidate structures. Therefore, GA was able to locate the *cubic gauche* structure with only 240 candidate structures. On the other hand, using the random-search method we failed to predict the correct *cubic gauche* structure from over 500 trial structures. Therefore, at least for this particular case, the efficiency of GA seems to be superior over the random-search method.

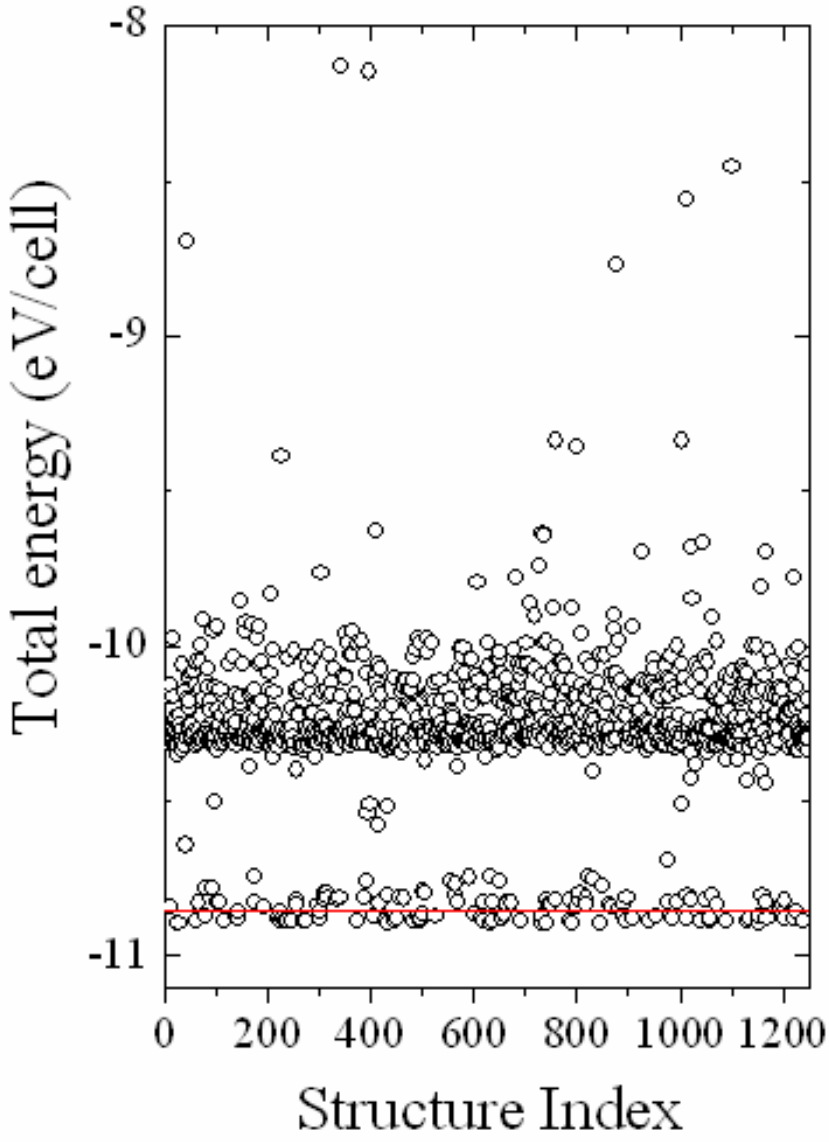

Figure 4.18. The total energies of an optimized population of trial structures for Si calculated at ambient pressure. The trial structures have 8 Si atoms in the unit cell. This population contains 1250 trial structures and 225 of them are trapped in the low energy region (near the red line) after structural optimization.

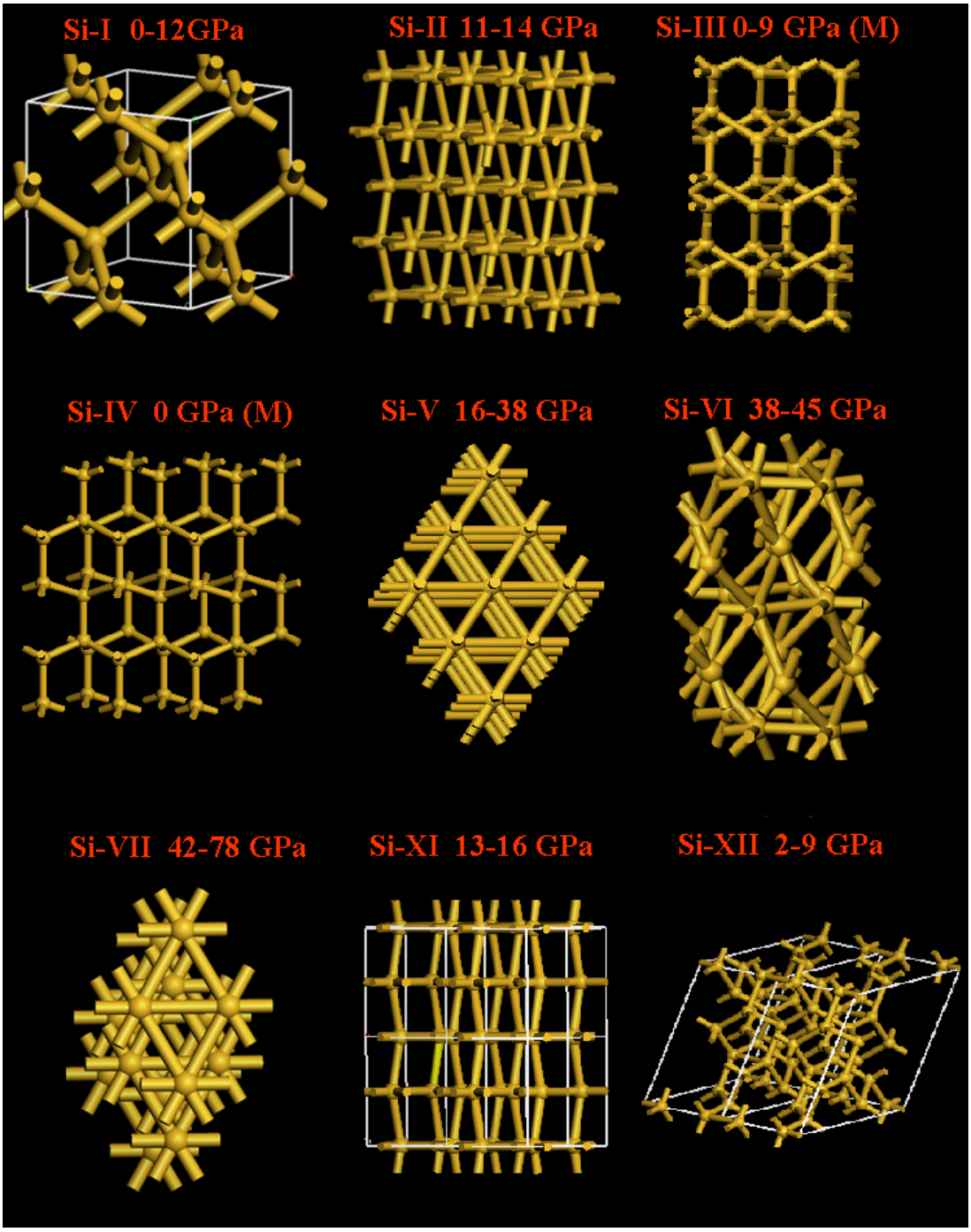

Figure 4.19. The Si structures found by random-search method at different pressures. The meta-stable structures are marked by M. The structure search calculations were performed between 0 and 70 GPa with a population of 500 trial structures. The trial structures have 8 Si atoms in the unit cells.

CHAPTER 5

First-principles X-ray absorption spectroscopy

XAS is a widely used spectroscopic technique to probe unoccupied electronic states of a material by creating electronic excitations from an occupied core state to unoccupied valence states [239-241]. The excited electron is normally originated from a deep core 1s or 2p state. To the first approximation, the resulting spectrum directly images the energy distribution of the electronic states satisfying dipole excitation rules [242]. The creation of electronic excitations from core states requires high-energy X-ray and thus XAS is often performed with synchrotron radiations. According to the excitation energy, excitations are broadly classified into three regions as shown in Fig. 5.1. The first type is 'Low-Energy Near-Edge X-ray Absorption Fine Structure (LENEXAFS)', the excited electron does not have enough energy to leave the absorbing atom, and promoted from a core state to a bounded unoccupied valence state. This type of transition gives rise to discrete edge peaks at the absorption bands. The second type of excitation is 'Near-Edge X-ray Absorption Fine Structure (NEXAFS)'. The excited electron has enough energy to escape the atom into the continuum. However, the kinetic energy of the excited electron is still low, and the electron will strongly interact with neighboring atoms and undergoes multiple scattering processes that contribute to fine structure near the absorption edge. The last type of excitation is the 'Extended X-ray Absorption Fine Structure (EXAFS)', in which case the excited electron has high enough kinetic energy that it only experience weak backscattering the immediate neighbor atoms. An absorption edge is the energy of the incident photon is sufficient to excite an electron of the absorbing atom from a core state into the continuum. By convention, the absorption edges are labeled as, *K*, *L*,…, corresponding to the excitation of an electron

from the 1*s*, 2*p*,…, orbitals, respectively. Energies of the absorption edge are dependent on the nature of the element and have higher energies with higher atomic numbers.

In this chapter, a numerical method for first-principles calculations of X-ray XAS within the framework of the DFT employing the PAW method is described. This method is implemented in the widely used electronic structure package Quantum-ESPRESSO [63] and takes advantage of reconstructed all-electron wavefunctions. In the following, the method and implementation will be presented in detail. To demonstrate the versatility of the code, validation tests were applied to three different solids and a molecule, namely, diamond, fullerene C_{60}, α-quartz and water molecule. The results will be compared with the literature and experiments.

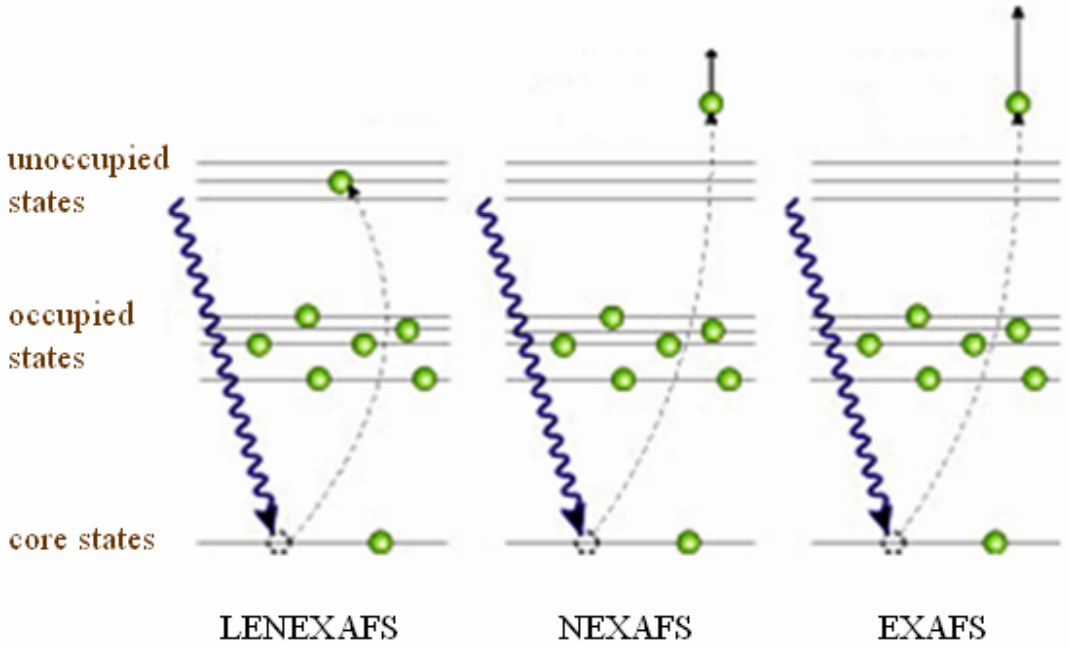

Figure 5.1. Three types of electronic excitations distinguished by the kinetic energy of excited electron. The figure is taken from L-A. Näslund's Licentiate thesis (Uppsala University, 2003).

5. 1 Theoretical calculation of XAS

In this section, the theoretical background for first-principles calculations of XAS is presented. The aim of this chapter is to numerically model electronic excitations, in particular, transitions from core states into lower unoccupied states. The absorption cross section of XAS is given by the Fermi golden rule [243] as a sum of probabilities (per unit of time) for transition from an initial core state to an unoccupied final state through an interaction Hamiltonian,

$$\sigma(\omega) = 4\pi^2 \alpha_0 \hbar\omega \sum_f |< \psi_f \mid \hat{O} \mid \psi_{core} >|^2 \delta(E_f - E_{core} - \hbar\omega), \qquad (5.1)$$

where α_0 is the fine structure constant. $\hbar\omega$ is the energy of the incident photon, which should match the energy difference E_f -E_{core} between the initial and final electronic states $|\Psi_{core}>$ and $|\Psi_f>$. $<\Psi_f \mid \hat{O} \mid \Psi_{core}>$ is the transition moment matrix element. It is evaluated in the present work within the electric-dipole approximation as

$$< \psi_f \mid \hat{O} \mid \psi_{core} > \sim < \psi_f \mid \hat{\varepsilon} \cdot \bar{r} \mid \psi_{core} >, \qquad (5.2)$$

where $\hat{\varepsilon}$ is the polarization direction of the incident EM field, and $\bar{r}$ is the single electron position operator. The initial core state $|\Psi_{core}>$ is the localized ground core state of the absorbing atom. The final state $|\Psi_f>$ is the unoccupied valence state where the electron is excited into. $|\Psi_f>$ is obtained from the solution of the Schrödinger equation with an effective potential to mimic screenings by other electrons after the core excitation.

5. 1. 1 PAW formalism

Since the eigenvalue of a core state is much lower than those of the valence states, it can be treated as a localized wavefunctions around the absorbing nucleus. In order to maintain the orthogonality with the core wavefunctions, the valence wavefunctions have

to oscillate rapidly in the core region. Emulation of the oscillations of the valence wavefunction in the core region will require a very large plane wave basis sets and therefore makes electronic calculations very expensive [10]. As described in Chapter 1, the pseudopotential approximation [21, 244] is widely used in numerical calculations of solids to overcome these problems. This approximation replaces the core electrons and strong nuclear potential by a weaker pseudopotential that acts on a set of pseudo wavefunctions. The pseudopotential is constructed in such a way that there are no radial nodes in the pseudo wavefunctions in the core region and can thus speed up the calculation substantially. The pseudo wavefunctions and pseudopotential are identical to the all-electron wavefunction and potential outside a cutoff radius r_c (Fig. 1-2).

The pseudo wavefunctions have exactly the same eigenvalues and functional forms outside a prescribed cutoff distance from the core as the corresponding all-electron wavefunctions. It is a good approximation for the calculation of the total energy and electronic properties for which matrix elements are dominated by the valence regions outside the core. However in the calculation of XAS, detailed description of the all-electron wavefunctions in the core region is crucial. In this case, the deficiency of the pseudopotential approximation is evident. It explicitly neglects components of the wavefunctions near the nucleus and therefore cannot be used to simulate neither the initial state $|\psi_{core}>$ nor the final state $|\psi_f>$, which are needed in evaluation of the transition matrix elements $<\psi_f|\hat{O}|\psi_{core}>$. To resolve this problem and avoid using expensive all-electron calculations, Van de Walle and Blöchl proposed a solution based on Blöchl's PAW electronic structure method [50-51]. This method offers a general approach to calculation of all-electron properties from pseudopotential-based schemes by reconstructing all-electron wavefunctions from the pseudo wavefunctions [245-246]. This approach has been used for the calculation of hyperfine parameters [245]. In the present study, the same approach has been used to develop formalism for the calculation of XAS from first-principles.

In the pseudopotential approximation, the pseudo wavefunctions are exact outside the core region and artificially chosen to be as smooth as possible inside. Thus the

wavefunctions need to be corrected within the cutoff radius r_c. Near the atomic nucleus, the core potential is much stronger than the potentials from neighboring nuclei. Therefore, the wavefunction should be approximately 'atomic-like' in the core region and can be expanded in terms of the all-electron partial waves [92]. This expansion is then used as corrections to the core wavefunctions in the PAW formalism. When the all-electron partial waves are added to the total wavefunction, the corresponding pseudo partial waves must be subtracted (Fig. 5.2) from the total wavefunction. The reconstructed all-electron wavefunction is therefore a combination of the pseudo wavefunction outside the core region and the all-electron wavefunction inside the core region [92].

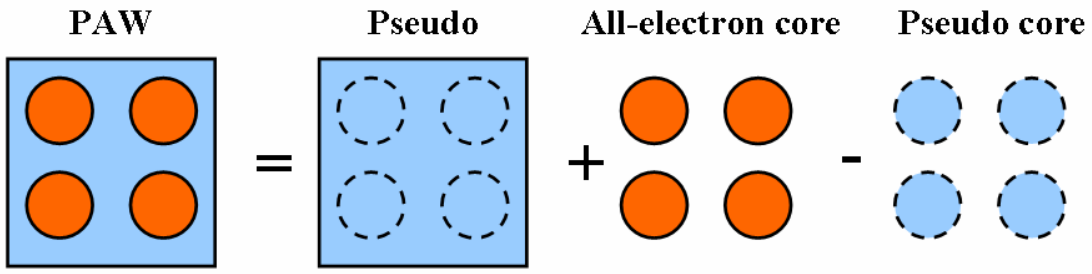

Figure 5.2. A simplified depiction of reconstructed PAW wavefunction that contains on-site and out-of-site contributions from all-electron and pseudo wavefunctions.

The remainder of this section presents the quantum mechanical description of the PAW formalism. The all-electron wavefunction of the final state $|\Psi_f>$ can be related to the corresponding pseudo wavefunction $|\tilde{\psi}_f>$ through a linear operator $\hat{T}$ [93, 247],

$$|\psi_f>=\hat{T}\,|\tilde{\psi}_f>. \tag{5.3}$$

These two wavefunctions can be expanded in terms of the all-electron and pseudo partial waves for different orbital basis sets:

$$\psi_f = \sum_{\vec{R},n} C_{\vec{R},n} \phi_{\vec{R},n} \quad , \tag{5.4}$$

$$\tilde{\psi}_f = \sum_{\vec{R},n} C_{\vec{R},n} \tilde{\phi}_{\vec{R},n} \quad , \tag{5.5}$$

where $\phi_{R,n}$ and $\tilde{\phi}_{R,n}$ are the all-electron and pseudo partial waves at atomic site $\vec{R}$. The index *n* here refers to the angular momentum quantum numbers and to an additional number, which is used if there is more than one projector per angular momentum channel [248]. The $C_{\vec{R},n}$ is the expanding coefficient that can be obtained self-consistently. In the pseudopotential approximation, the pseudo wavefunction is identical to the all-electron wavefunction outside the core region so that

$$\phi_{\vec{R},n} = \tilde{\phi}_{\vec{R},n} \quad r > r_c \, . \tag{5.6}$$

Defining $C_{\vec{R},n} = < \tilde{P}_{\vec{R},n} | \tilde{\psi}_f >$ in which the vector $< \tilde{P}_{\vec{R},n} |$ is the projector function, Eq. (5.3) can be written as

$$\psi_f = \tilde{\psi}_f + \sum_{\vec{R},n} (\phi_{\vec{R},n} - \tilde{\phi}_{\vec{R},n}) < \tilde{P}_{\vec{R},n} | \tilde{\psi}_f > . \tag{5.7}$$

This equation is the quantum mechanical description of Fig. 5.2. The PAW wavefunction is the summation of the pseudo wavefunction outside and the all-electron wavefunction inside the core region. It is clear that the projector function $< \tilde{P}_{\vec{R},n} |$ should be zero outside the core region.

The projector function $< \tilde{P}_{\vec{R},n} |$ satisfies the orthogonal condition with the pseudo partial waves. One can rewrite the pseudo-wavefunction of the final state $| \tilde{\psi}_f >$ in Eq. (5.5) as

$$|\tilde{\psi}_f>=\sum_{\vec{R},n}<\tilde{P}_{\vec{R},n}|\tilde{\psi}_f>|\tilde{\phi}_{\vec{R},n}>=\sum_{\vec{R},n}\sum_{\vec{R}',n'}|\tilde{P}_{\vec{R}',n'}><\tilde{P}_{\vec{R}',n'}|\tilde{\phi}_{\vec{R},n}><\tilde{P}_{\vec{R},n}|\tilde{\psi}_f>, \quad (5.8)$$

and considering

$$|\tilde{\psi}_f>=\sum_{\vec{R},n}|\tilde{P}_{\vec{R},n}><\tilde{P}_{\vec{R},n}|\tilde{\psi}_f>, \quad (5.9)$$

the orthogonal rule is reduced to

$$<\tilde{P}_{\vec{R},n}|\tilde{\phi}_{\vec{R}',n'}>=\delta_{n,n'}\delta_{\vec{R},\vec{R}'}. \quad (5.10)$$

Within the PAW approach, one can reformulate the XAS matrix elements in Eq. (5.2) by replacing the all-electron wavefunction of final state $|\Psi_f>$ with the expansion in Eq. (5.7). The transition matrix then becomes

$$\begin{aligned}&|<\psi_f|\hat{O}|\psi_{core}>|^2\\&=\sum_n\sum_{n'}<\tilde{\psi}_f|\tilde{P}_{\vec{R}_0,n}><\tilde{P}_{\vec{R}_0,n'}|\tilde{\psi}_f><\phi_{\vec{R}_0,n}|\hat{O}|\psi_{core}><\psi_{core}|\hat{O}|\phi_{\vec{R}_0,n'}>,\end{aligned} \quad (5.11)$$

where the summation over all atomic site $\vec{R}$ reduces to a single term at the absorbing site $\vec{R}_0$, since at a given time only one electron can be excited. In the present study, the pseudo final state $|\tilde{\psi}_f>$ is computed using the Quantum-ESPRESSO package [63] within the framework of DFT. The projector function $<\tilde{P}_{\vec{R},n}|$ was computed using the GIPAW (Gauge-Including Projector Augmented Waves) [249] module in the Quantum-ESPRESSO package. The calculation of the interaction matrix element $<\phi_{\vec{R}_0,n}|\hat{O}|\psi_{core}>$ is described in the following section.

5. 1. 2 The XAS matrix elements

To compute the transition matrix element $< \phi_{\vec{R}_0,n} | \hat{O} | \psi_{core} >$, the electric dipole approximation is used for the incident EM field,

$$\exp(i\vec{k} \cdot \vec{r}) \approx 1 + i\vec{k} \cdot \vec{r} + O(\vec{r}^{\,2}) . \tag{5.12}$$

The transition matrix element $< \phi_{\vec{R}_0,n} | \hat{O} | \psi_{core} >$ then reduces to,

$$< \phi_{\vec{R}_0,n} | \hat{O} | \psi_{core} > \approx < \phi_{\vec{R}_0,n} | \hat{\varepsilon} \cdot \vec{p} | \psi_{core} > , \tag{5.13}$$

where $\hat{\varepsilon}$ is the polarization direction of the incident EM field, and $\vec{p}$ is the single-electron momentum operator. Since the system Hamiltonian $\hat{H}$ commutes with the single-electron position operator $\vec{r}$, the single-electron momentum operator $\vec{p}$ can be written as

$$\vec{p} = i[\hat{H}, \vec{r}] . \tag{5.14}$$

Substitute Eq. (5.14) into Eq. (5.13), one has the relation

$$< \phi_{\vec{R}_0,n} | \hat{\varepsilon} \cdot \vec{p} | \psi_{core} > = i\hat{\varepsilon} \cdot < \phi_{\vec{R}_0,n} | [\hat{H}, \vec{r}] | \psi_{core} >$$

$$= i(E_{\vec{R},n} - E_{core}) < \phi_{\vec{R}_0,n} | \hat{\varepsilon} \cdot \vec{r} | \psi_{core} > , \tag{5.15}$$

where $E_{\vec{R},n}$ and E_{core} are the eigenvalues of $| \phi_{\vec{R}_0,n} >$ and $| \psi_{core} >$, respectively. If one defines $\hat{\varepsilon}$ and $\vec{r}$ as

$$\hat{\varepsilon} = \varepsilon_i \vec{i} + \varepsilon_j \vec{j} + \varepsilon_k \vec{k}\,, \tag{5.16}$$

$$\vec{r} = x\vec{i} + y\vec{j} + z\vec{k}\,, \tag{5.17}$$

the interaction matrix element $< \phi_{\vec{R}_0,n} \mid \hat{\varepsilon} \cdot \vec{r} \mid \psi_{core} >$ reduces to three matrices that couple initial and final states by position operators *x*, *y*, *z* for three orthogonal directions, $< \phi_{\vec{R}_0,n} \mid x \mid \psi_{core} >$, $< \phi_{\vec{R}_0,n} \mid y \mid \psi_{core} >$, and $< \phi_{\vec{R}_0,n} \mid z \mid \psi_{core} >$.

To calculate the reduced matrices, it is convenient to use spherical coordinates and separate the wavefunction into its radial and angular part,

$$\mid \psi_{\vec{R}_0,n} >= \mid R_{\vec{R}_0,n} > \mid Y_{lm} >, \tag{5. 18}$$

$$\mid \psi_{core} >= \mid R'_{\vec{R}_0,1s} > \mid Y_{00} >. \tag{5. 19}$$

Here for the core state, the 1s orbital is taken as an example (*K*-edge). The three components of the reduced matrix become

$$< \phi_{\vec{R}_0,n} \mid x \mid \psi_{core} >=< R_{\vec{R}_0,n} \mid r \mid R'_{\vec{R}_0,1s} >< Y_{lm} \mid \sin\theta\cos\phi \mid Y_{00} >, \tag{5. 20}$$

$$< \phi_{\vec{R}_0,n} \mid y \mid \psi_{core} >=< R_{\vec{R}_0,n} \mid r \mid R'_{\vec{R}_0,1s} >< Y_{lm} \mid \sin\theta\sin\phi \mid Y_{00} >, \tag{5. 21}$$

$$< \phi_{\vec{R}_0,n} \mid z \mid \psi_{core} >=< R_{\vec{R}_0,n} \mid r \mid R'_{\vec{R}_0,1s} >< Y_{lm} \mid \cos\theta \mid Y_{00} >. \tag{5. 22}$$

The first terms on the right hand side of Eqs. (5.20) to (5.22) depend only on the radial part of the wavefunctions. The radial function $\mid R'_{\vec{R}_0,1s} >$ is the 1s core wavefunction, obtained from the solution of the Schrödinger equation for an isolated absorbing atom (ground state). The partial waves $\mid R_{\vec{R}_0,n} >$ are valence wavefunctions with angular

momentum quantum numbers *n* reconstructed by the PAW formalism from the pseudo wavefunctions, which are obtained by solving the Schrödinger equation for a potential with only one 1s electron in the absorbing atom (excited states).

The second terms on the right hand side of Eqs. (5.20) to (5.22) are integrations of a product of multiple spherical harmonics. However, the spherical harmonics $|Y_{lm}>$ are complex functions, whose integrations are not straightforward. To avoid dealing with imaginary numbers, the complex function $|Y_{lm}>$ is represented by a linear combination of cubic harmonics $|\widetilde{Y}_{lm}>$ [250, 251]. The cubic harmonics $|\widetilde{Y}_{lm}>$ are real functions and form a complete basis set that is equivalent to $|Y_{lm}>$. Sometimes the cubic harmonics $|\widetilde{Y}_{lm}>$ is also referred to as real spherical harmonics. The relation between $|Y_{lm}>$ and $|\widetilde{Y}_{lm}>$ is [251]

$$\widetilde{Y}_{lm} = \frac{1}{\sqrt{2}}[(-1)^m Y_{lm} + Y_{l-m}] \quad m > 0, \tag{5.23}$$

$$\widetilde{Y}_{lm} = \frac{1}{i\sqrt{2}}[(-1)^m Y_{lm} - Y_{l-m}] \quad m < 0, \tag{5.24}$$

$$\widetilde{Y}_{lm} = Y_{lm} \quad m = 0. \tag{5.25}$$

In the $|\widetilde{Y}_{lm}>$ representation, the position operators *x*, *y*, *z* can be written as

$$\begin{pmatrix} x \\ y \\ z \end{pmatrix} = \sqrt{\frac{4\pi}{3}} r \begin{pmatrix} \widetilde{Y}_{11} \\ \widetilde{Y}_{1-1} \\ \widetilde{Y}_{10} \end{pmatrix}, \tag{5.26}$$

by using the relations,

$$Y_{1,\pm 1}(\theta,\phi) = \mp\sqrt{\frac{3}{8\pi}} \sin\theta \cdot e^{\pm i\phi}, \tag{5.27}$$

$$Y_{1,0}(\theta,\phi) = \sqrt{\frac{3}{4\pi}}\cos\theta\,. \tag{5.28}$$

By means of Eq. (5.26), the complex integrals in Eqs. (5.20) to (5.22) are reduced to the following real integrals

$$< Y_{lm} \mid \hat{x} \mid Y_{00} >= \int_0^{2\pi} d\phi \int_0^{\pi} \sin\theta d\theta \cdot \widetilde{Y}_{lm} \cdot \widetilde{Y}_{11} \cdot Y_0^0\,, \tag{5. 29}$$

$$< Y_{lm} \mid \hat{y} \mid Y_{00} >= \int_0^{2\pi} d\phi \int_0^{\pi} \sin\theta d\theta \cdot \widetilde{Y}_{lm} \cdot \widetilde{Y}_{1-1} \cdot Y_0^0\,, \tag{5. 30}$$

$$< Y_{lm} \mid \hat{z} \mid Y_{00} >= \int_0^{2\pi} d\phi \int_0^{\pi} \sin\theta d\theta \cdot \widetilde{Y}_{lm} \cdot \widetilde{Y}_{10} \cdot Y_0^0\,. \tag{5. 31}$$

These integrals can be calculated analytically and it is reduced essentially to the evaluation of the Clebsch-Gordan (C-G) coefficients [253]. Moreover, if there is a need to extend the XAS calculation to higher angular momentum absorption edges, it can be done by changing the cubic harmonics $\mid \widetilde{Y}_{lm} >$ to those corresponding to the core state.

To obtain the value of real spherical harmonics $\mid \widetilde{Y}_{lm} >$, one can use the associated Legendre functions $Q(\theta,\varphi,l,m)$ [254],

$$\widetilde{Y}_{lm}(\theta,\varphi,l,m) = \sqrt{\frac{2l+1}{2\pi}} \cdot Q(\theta,\varphi,l,m) \cdot \cos(m\varphi) \qquad m > 0\,, \tag{5. 32}$$

$$\widetilde{Y}_{lm}(\theta,\varphi,l,m) = \sqrt{\frac{2l+1}{2\pi}} \cdot Q(\theta,\varphi,l,m) \cdot \sin(m\varphi) \qquad m < 0\,, \tag{5. 33}$$

$$\widetilde{Y}_{lm}(\theta,\varphi,l,m) = \sqrt{\frac{2l+1}{2\pi}} \cdot Q(\theta,\varphi,l,m) \qquad m = 0\,. \tag{5. 34}$$

The higher-order Legendre functions can be derived from their lower-order counterpart using the recursion rule [254]:

$$Q(\theta,\varphi,l,m) = \frac{2l-1}{\sqrt{l^2-m^2}}\cdot\cos(\theta)\cdot Q(\theta,\varphi,l-1,m) - \sqrt{\frac{(l-1)^2-m^2}{l^2-m^2}}\cdot Q(\theta,\varphi,l-2,m), \quad (5.35)$$

$$Q(\theta,\varphi,l,l-1) = \sqrt{2l-1}\cdot\cos(\theta)\cdot Q(\theta,\varphi,l,l-1), \quad (5.36)$$

$$Q(\theta,\varphi,l,l) = -\sqrt{\frac{2l-1}{2l}}\cdot\sin(\theta)\cdot Q(\theta,\varphi,l,l-1). \quad (5.37)$$

Since the total angular momentum must be conserved during the electronic excitation, the angular momentum ($|\widetilde{Y}_{lm}>$) for the final state $|\Psi_f>$ cannot be arbitrary. Instead, it is governed by the selection rules of the C-G coefficients,

$$M = m_f + m_{core}, \quad (5.38)$$

$$\left|l_f - l_{core}\right| \le L \le l_f + l_{core}. \quad (5.39)$$

Here (L, M) is the angular momentum quantum number for position operators x, y, and z. The (m_{core}, l_{core}) and (m_f, l_f) are the angular momentum quantum numbers for the initial core and final valence state, respectively. For K-edge XAS the initial core state is 1s. Applying the selection rules of Eqs. (5.38) and (5.39), the summations over angular momentum quantum numbers in Eq. (5.11) reduce to

$$\sum_{lm} <\widetilde{Y}_{lm}\,|\,x\,|\,\widetilde{Y}_{00}> = <\widetilde{Y}_{11}\,|\,x\,|\,\widetilde{Y}_{00}>, \quad (5.40)$$

$$\sum_{lm} < \widetilde{Y}_{lm} \mid y \mid \widetilde{Y}_{00} > = < \widetilde{Y}_{1-1} \mid y \mid \widetilde{Y}_{00} >, \quad (5.41)$$

$$\sum_{lm} < \widetilde{Y}_{lm} \mid z \mid \widetilde{Y}_{00} > = < \widetilde{Y}_{10} \mid z \mid \widetilde{Y}_{00} >. \quad (5.42)$$

5. 2 The excitation process

An electronic excitation occurs when the energy of the incident photon is sufficient to promote an electron from a core state to an unoccupied state. Once the electron is ejected, it will leave a deep potential well in the core state (core hole) of the absorbing atom. The electrons within the system will respond to the new potential and migrate toward the core hole. This effect is called as electron screening [255]. The nuclei might also be displaced according to the core hole potential, and this often result in structural change [92]. It is important to determine whether the structural change should be treated before attempting any calculation of XAS. This can be decided qualitatively by comparing the timescale of the electronic excitation and that of respective electronic and ionic relaxations. The timescale of an electronic excitation can be estimated from knowledge of the approximate bandwidth of the final state and the corresponding velocity of the excited electron. The timescale of electron screening is related to the plasmon energy, and is much shorter than that of electronic excitations, approximately 1% of the latter. The lattice relaxation takes much longer, the timescale of which is about 10 times that of electronic excitations. The well-separated timescales indicate that for an electronic excitation to take place the electronic system has time to respond but the lattice is essentially fixed in its ground state configuration [92]. In the present study, the electronic system is relaxed self-consistently to the ground state in the presence of the core hole [63]. This calculation is consisted of two separate steps:

1. Generation of an excited pseudopotential for the absorbing atom by removing a single electron or a fractional part of one electron to simulate the core hole effects, from the core state from which the electron is excited [256]. An example of the excited

pseudopotential is shown in Fig. 5.3.

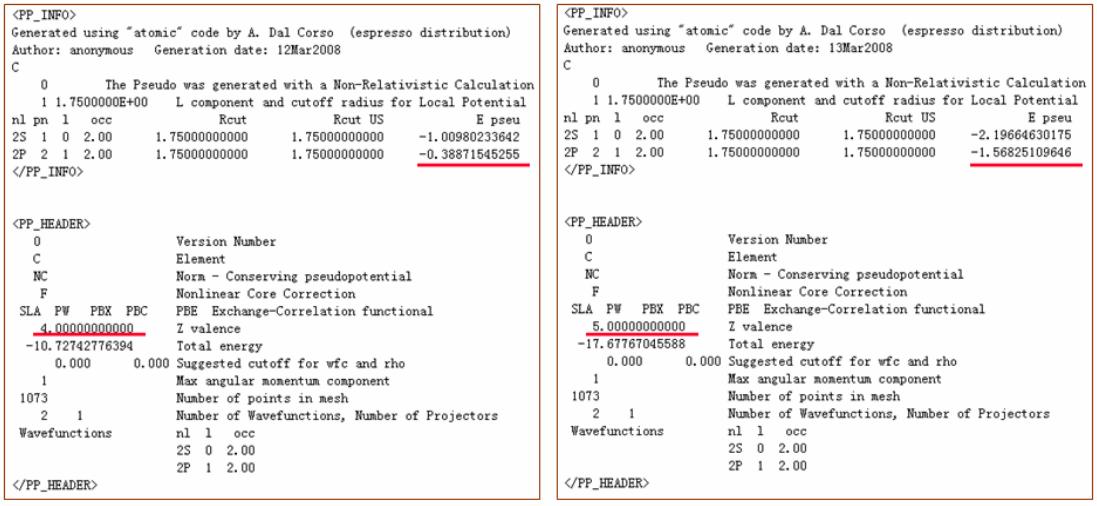

Figure 5.3. The headers for the two Quantum-ESPRESSO pseudopotentials of carbon, with a full core hole (left) and without any core hole (right). Red lines indicate the eigenvalues for the valence orbital 2s and 2p and the number of valence electrons.

2. Relax the total electronic wavefunction to the hole state with the new ionic potential. No structural relaxation is needed since the ground-state geometry has no time to respond. During the self-consistent calculation, the core hole will then be screened by electrons. The electronic calculations have been performed with PW approach within the DFPT using Quantum-ESPRESSO package [63].

It is important to know that at a given time only one core electron at a certain absorbing atom is excited. The absorbing atom needs to be treated separately from other atoms that stay in the neutral state. As a result, the lattice symmetry of the system is broken when the excitation occurs. Since the PW approach employs periodic boundary conditions, the supercell approximation [257] must be used in the calculation of core hole effects. The supercell is constructed by replicating the unit cells of the bulk material. One of the atoms in the supercell is chosen to be excited. In the core-excited state of the

system, the absorbing atom is represented by a core hole pseudopotential and the screening by the valence electrons is simulated by performing a self-consistent calculation. This is then followed by a band structure calculation for unoccupied KS eigenstates (Eq. (1-12)) up to the energy for which the absorption spectrum is required. It should be noted that in the supercell approximation unphysical interactions between the core holes from neighboring supercells must be minimized. To avoid such interactions one should extend the distance between neighboring excited atoms by increasing the size of supercell. Strictly speaking, the size of the supercell should be increased until the calculated XAS spectrum converges [8].

5. 3 Tests and results

A computer program for the calculations of XAS using the method described above in this chapter has been developed and implemented in the Quantum-ESPRESSO package [63]. At present, the electronic spectrum is simulated by using the dipole approximation, but higher-order multipoles can easily be included in the calculation. In this section, simple tests of *K*-edge XAS were applied on three solids and one molecule, diamond, fullerene C_{60}, α-quartz and water molecule. The calculated spectra will be compared with the literature and experiments.

5. 3. 1 *K*-edge XAS of diamond

The first test case is the carbon *K*-edge spectrum of diamond excluding core hole effects in the calculations. This is a 'pseudo process' that describes a nonphysical excitation from a neutral ground state to itself. In a non-excitonic interpretation, the final states evolve according to the ground state charge density, and therefore the XAS should resemble the *p*-electronic density of the unoccupied states. Due to its simplicity, this approach has been used to provide a rough approximation of XAS. However, it explicitly excludes the complexity of introducing the core hole in the calculations, and therefore

serves as a good test for debugging purposes. For these reasons, this test has been widely applied and the results are available in the literature [92, 255].

In order to reconstruct the all-electron response in a pseudopotential calculation using the PAW approach, the projectors are constructed with the all-electron and pseudo wavefunctions corresponding to each pseudopotential. These wavefunctions are produced during the generation of the pseudopotentials. For each type of atom, and selected orbital angular momentum (l), it is necessary to have two projectors to describe the bounded and unbounded states. Therefore for each orbital momentum two all-electron and pseudo wavefunctions are needed. For this purpose, the valence and the first excited wavefunction of each orbital momentum were used. For example, the electron atomic configuration $1s^2 2s^2 2p^2 3s^0 3p^0$ was to generate the carbon pseudopotential. The valence $2s^2 2p^2$ and excited $3s^0 3p^0$ describe the bounded and unbounded states, respectively. For all calculations in the present study, the pseudopotentials are generated employing the GGA (PBE) exchange-correlation functional [18].

The calculated carbon *K*-edge spectrum of diamond excluding core hole effects is presented in Fig. 5.4 (a) and compared with those available in the literature [92, 255] in Fig. 5.4 (b). The present calculated XAS successfully reproduces all the spectral features reported previously. Considering the fact that the previous calculation has used a different exchange correlation functional (LDA) [11] and computer programs (CASTEP [258, 259]), the agreements is highly satisfactory. This test validates the present implementation of the PAW approach.

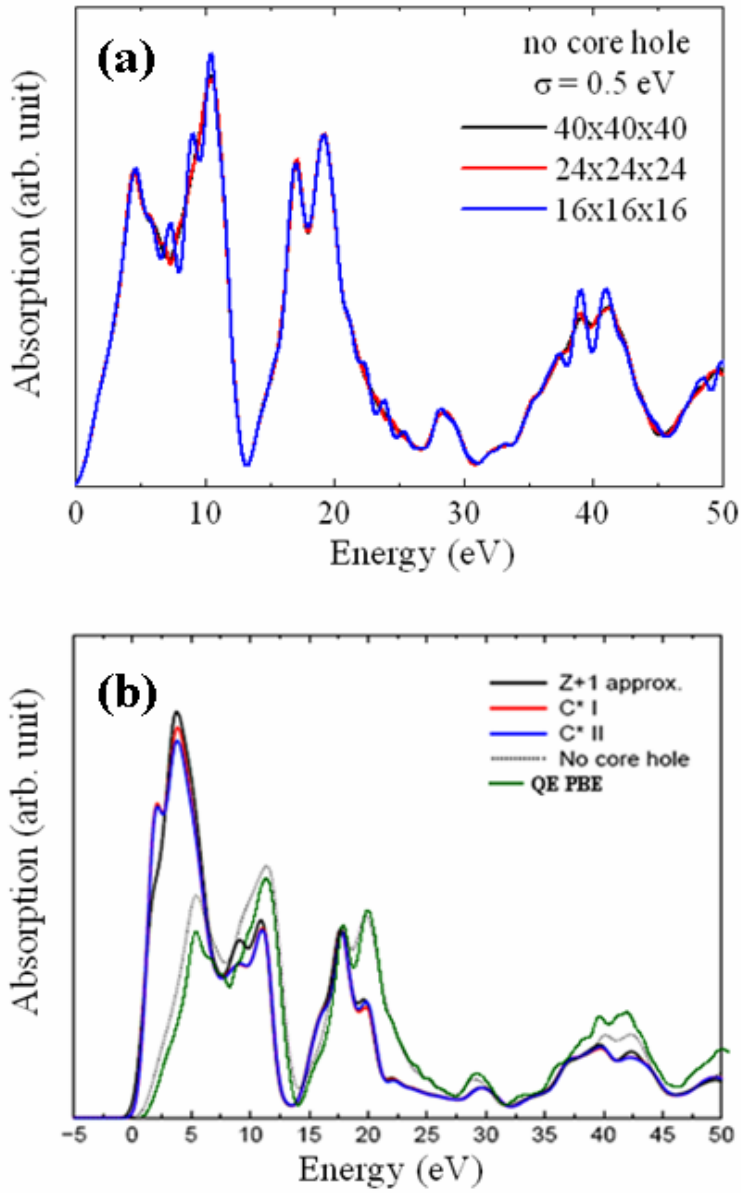

Figure 5.4. (a) The XAS calculated for the carbon *K*-edge of diamond excluding core hole effects. The calculation has been repeated with multiple *k*-point meshes for the first BZ sampling and the convergence has been achieved with a 24x24x24 *k*-point mesh. A 0.5 eV Gaussian smearing has been applied to all spectra. (b) The calculated spectrum is compared with the previously reported spectrum. The grey curve indicates the data represented in Ref. 92 and the green curve is the new calculated spectrum. The curves denoted by C*I and C*II are the XAS calculated for carbon *K*-edge of diamond including

the core-hole effects using two different excited pseudopotentials [92]. The C*I pseudopotential was generated using the atomic configuration $1s^2 2s^2 2p^2$ with the one core electron being fully removed from the system, while the C*II pseudopotential was generated using the same atomic configuration but one core electron is excited to the 2p orbital [92].

5. 3. 2 Core hole effects on diamond

After successful validation of the computer code, the next step is to include the core hole effects in diamond and examine the improvements on the spectrum. In the present study, the core hole effects are simulated by a core hole pseudopotential and electron screening in the self-consistent calculation. As described above, since the timescale for electron screening in molecules and solid are very different, it is a common observation that for a solid the inclusion of a full core hole in the absorbing atom potential produces XAS spectra in better agreement with experiments [260]. On the other hand for molecules, removing partial electron (usually half) from the core state seems to perform better [261, 262]. For this reason the test on diamond started with the full core hole approximation. Two different electron configurations, $1s^1 2s^2 2p^2 3s^0 3p^0$ and the other is $1s^1 2s^2 2p^3 3s^0 3p^0$, were used in the generation of the full core hole carbon potential. For both configurations one electron is removed from the 1s orbital. The difference is in the 2p orbital. In the first configuration, the excited electron is assumed to be fully removed from the atom so that the valence states are identical to their reference configurations. In the second pseudopotential, the excited electron is considered to be promoted to the valence state 2p, so the configuration of the 2p orbital is changed from $2p^2$ to $2p^3$. However, it is found that these two configurations produce almost identical carbon *K*-edge spectra. For the rest of this study the type I configuration $1s^1 2s^2 2p^3 3s^0 3p^0$ is used.

In passing it is worthy to comment that for a realistic description of the electronic excitation, the excited core electron does not vanish completely from the system as was done here. It is promoted to an unoccupied state and in a time-dependent way, also contributes to the screening of the nuclear charge [92]. An accurate modeling of this

process can in principle be achieved by investigating excitons using the time-dependent DFT [263, 264]. Therefore, within the present time-independent approach, several approximations were made to include average electron screening effects. There are two simplest approximations that may be thought of as two extreme cases, no screening and complete screening. In the no screening case the excited electron is removed entirely from the system, and results in a charged supercell. In this case there is no electron screening from the excited electron. In the complete screening case the excited electron is included as an extra valence electron, and results in a neutral supercell. In this case the excited electron is able to participate fully in the screening of the core hole. In the self-consistent calculation, this extra electron is attracted by the deeper potential well in the absorbing atom and it is expected to relax close to its valence orbital. The carbon *K*-edge XAS of diamond was re-calculated using both approximations and the results are presented in Fig. 5.5. The general shapes of two spectra are very similar to each other and the positions of the peaks are almost identical. However, in detail intensities of several peaks were observed to change - especially at the low-energy region where electron screening is expected to be more important. In the neutral cell calculation, an extra electron is introduced to screen the core hole, thus the strength of the core hole potential is reduced and the valence states are less confined and resulted in reduced peak intensities at the energy threshold. In the higher energy region, the two calculated spectra are essentially identical to each other. The result with correct electron screening is expected to lie somewhere between the two curves in Fig. 5.5 represented by the two extreme approximations. However, it is needed to note that for molecules, the charged cell and neutral cell calculations produce quite different results, and neutral cell calculations tend to give better agreement with experiment [265].

In Fig. 5.6 the carbon *K*-edge XAS for diamond calculated with a full core hole and a charged cell is compared with the previously calculated and experimental spectra reported in Ref. 247. It is clear that our calculated spectrum is in a substantially good agreement with the previous calculation. The overall agreement between the calculated spectrum and the experiment is fairly good. All characteristic features in the experimental spectrum are recognizable in the calculated spectrum except for the first

low energy peak. This peak has been attributed to carbon 1s core excitons that are not included in the present method. The features from *d* to *i* are correctly reproduced in both positions and relative intensities. In the low-energy region, the agreement between the experiment and calculations is not as good. In Ref. 247, it was demonstrated that the low-energy spectrum is affected strongly by the interaction between core-holes from neighboring supercells. This is an artifact of the supercell model and thus the quality of spectrum can be improved by increasing the size of supercell. Comparing the carbon *K*-edge XAS of diamond calculated with a full core hole in Fig. 5.6 with the same spectrum calculated without core hole in Fig. 5.4, a significant improvement is observed. This observation suggests that the inclusion of the core hole effects is crucial for the calculations of XAS.

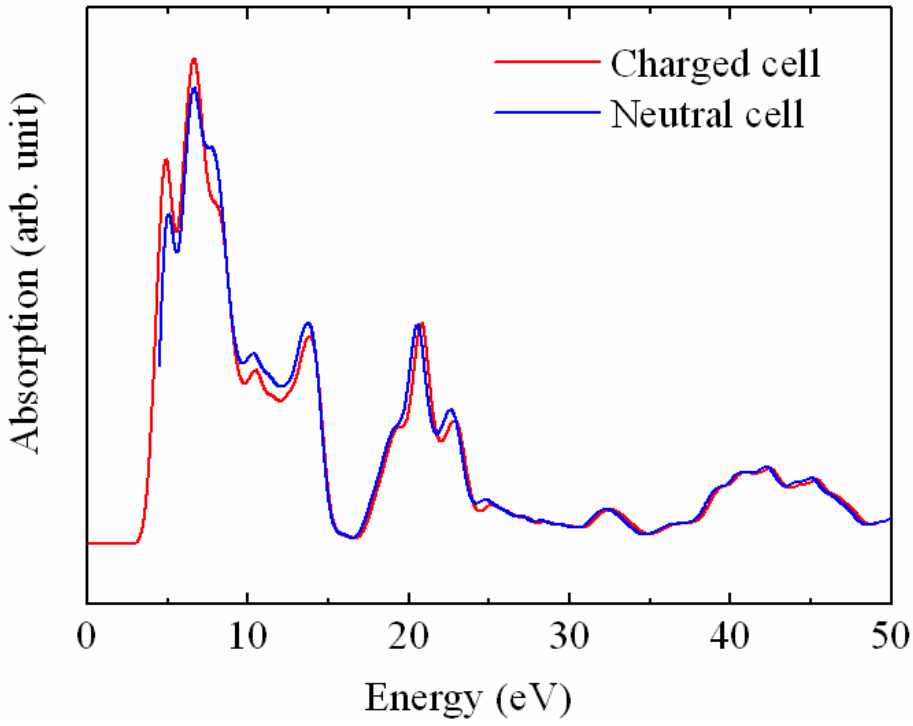

Figure 5.5. A comparison between calculated carbon *K*-edge XAS of diamond with charged cell and neutral cell. A full core hole is included in both calculations. A supercell of 16 atoms (2x2x2 primitive cell) and a 12x12x12 *k*-point mesh have been used. A 0.5 eV Gaussian smearing has been applied to both spectra.

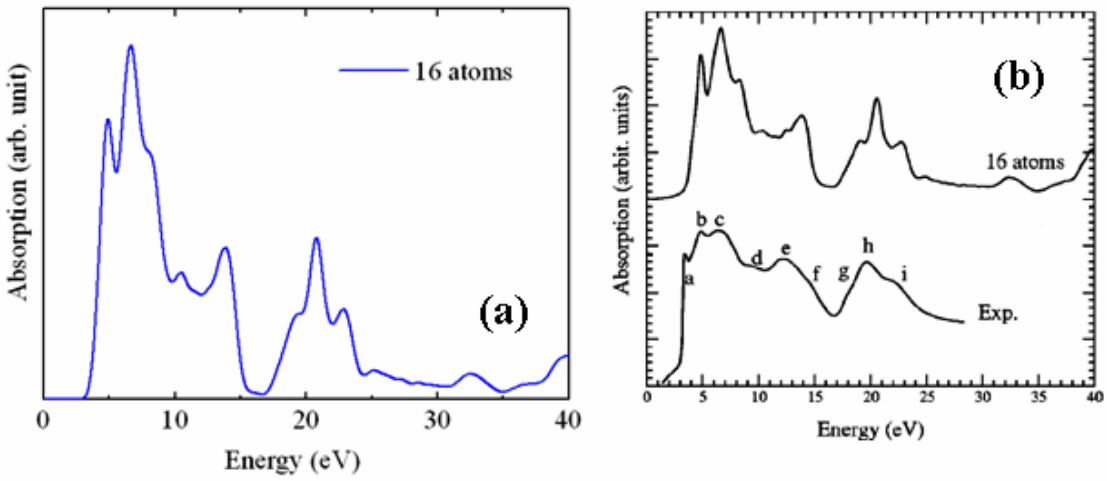

Figure 5.6. (a) The calculated carbon *K*-edge XAS of diamond with a full core hole and a charged cell. A supercell of 16 atoms and a 12x12x12 *k*-point mesh have been used. (b) The calculated and experimental carbon *K*-edge XAS of diamond reported in Ref. 247

5. 3. 3 *Z*+1 approach

An alternative approach to include the core hole effects in the XAS calculations is the so-called *Z*+1 method [92]. The core hole effects can be approximated either by removing one electron from the core state as in the core hole approach, or by increasing the nuclear charge of the absorbing atom by one. The latter case is the *Z*+1 approach. For example, one can use the nitrogen pseudopotential to model the excited-core carbon atom in XAS calculations. Fig. 5.7 shows the carbon *K*-edge XAS of diamond calculated by both the *Z*+1 and core hole approach. The results are broadly similar and the peak positions produced by the two methods agree. On the second threshold, the agreement is very good on both positions and relative intensities of the peaks. However, once again, near the threshold of the absorption spectrum where core hole effects are more important, the difference between the calculated observed intensity is quite large and the *Z*+1 spectrum is less accurate. This observation indicates the deficiency of the *Z*+1 approach. The Z+1 approach attempts to mimic the excited core by placing an additional charge at the nucleus. This procedure can simulate the charge compensation in a general way, but clearly the spatial variation of the resulting potential is incorrect. For example there is no

distinction between the core hole in 1s and 2p orbital, so it is impossible to separate *K*-edge and *L*-edge spectra. As described in previous section, the core hole approach can be achieved in a straightforward way. Therefore, there is no advantage to use the less accurate Z+1 approximation.

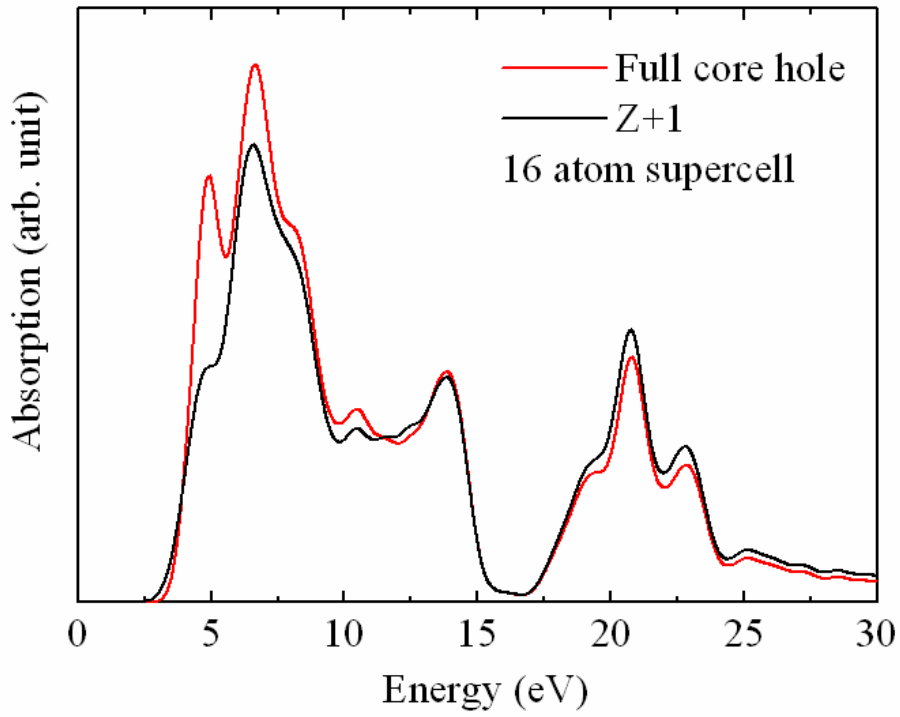

Figure 5.7. A comparison between the carbon *K*-edge XAS of diamond calculated using the core hole and *Z*+1 approach. A supercell of 16 atoms and a 12x12x12 *k*-point mesh have been used. Nitrogen pseudopotential is used to simulate the excited carbon atom.

5. 3. 4 C_{60} fullerene –experiments and theory

Since the discovery of C_{60} [266], the buckyball, fullerenes and related materials have been the subject of great interest [267-268]. Among different experimental techniques, XAS measurements have been used to study electronic and changes in geometric conformations [269, 270]. In this section the carbon *K*-edge XAS for C_{60}

fullerene is calculated and compared with the experimental spectrum. The experimental spectrum was measured at the National Laboratory of Italian CNR-INFM ELETTRA Light Source [271]. The optimized structure of C_{60} fullerene is shown in Fig. 5.8. There are three non-equivalent carbon atoms marked as C1, C2 and C3. The structure resembles a soccer ball made of twenty hexagons and twelve pentagons with a carbon atom at the vertices of each polygon. The hexagons are constructed by alternative single- and double-bonds with the lengths of 1.45 Å and 1.37 Å. The carbon *K*-edge XAS for C_{60} fullerene has been calculated for an isolated molecule with a full core hole in a charged supercell. Only one *k*-point (gamma point) was used in the calculation. The calculated spectra were found to be very similar for the three types of carbon atoms and the C1 type XAS is selected for presentation. Fig. 5.9 compares the calculated and experimental spectra. The calculated spectrum is observed to be in very good agreement with the experiment [271]. All the observed peaks are correctly reproduced by the calculations.

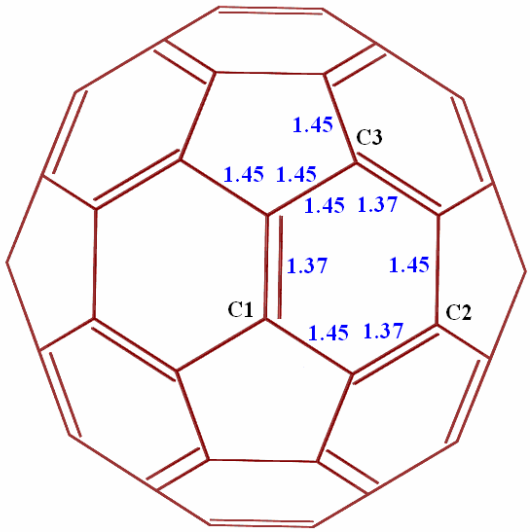

Figure 5.8. Optimized C_{60} structure. The three non-equivalent carbon atoms are labeled as C1–C3. The two different bonds are marked with their bond lengths 1.37 Å and 1.45 Å.

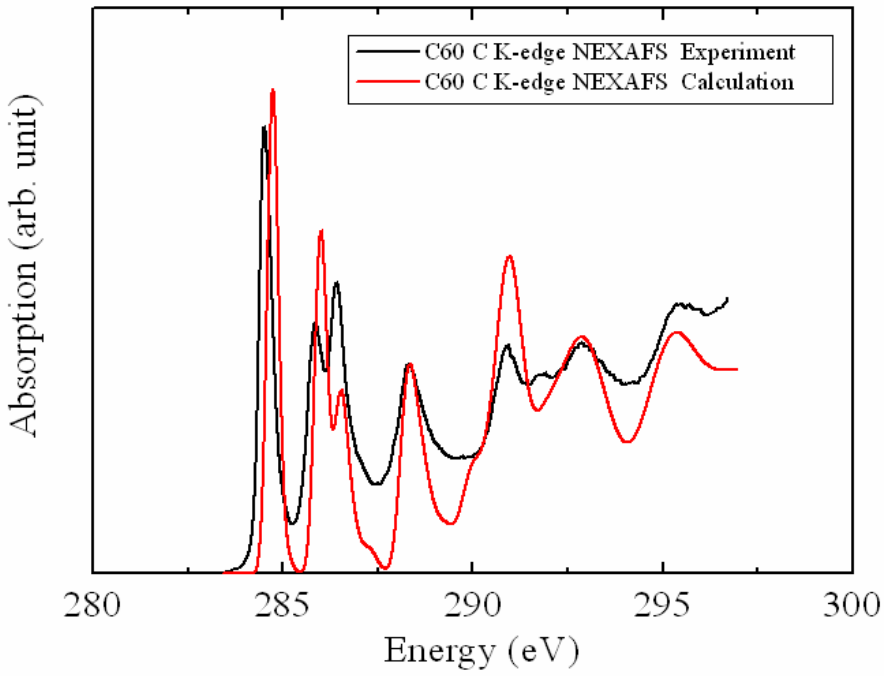

Figure 5.9. A comparison between the calculated and measured carbon *K*-edge XAS of C_{60} fullerene.

5. 3. 5 *α*–quartz : an angular dependent case

Besides the isotropic XAS spectra presented in previous sections, angular dependent XAS is also implemented in the calculations of XAS. In this section, an example of calculated angular dependent absorption spectrum will be shown for the silicon *K*-edge XAS of *α*-quartz. *α*-quartz has a trigonal space group $P3_221$ with a hexagonal unit cell. Since the point group is *D*3, *α*-quartz is a dichroic compound [243]. There are two distinct angular dependent absorption spectra $\sigma_{//}$ and $\sigma_{\perp}$ for *α*-quartz, corresponding to the polarization direction $\hat{\varepsilon}$ of incident EM field parallel and perpendicular to the ternary axis [001] of the hexagonal cell, respectively [272-275]. Any absorption spectrum in *α*-quartz can be expressed as a linear combination of these two distinct spectra. For example, the isotropic absorption spectrum can be approximated by the special average $(\sigma_{//} + 2\sigma_{\perp})/3$, which has been found well reproduce measured XAS of *α*-quartz using powder sample [247].

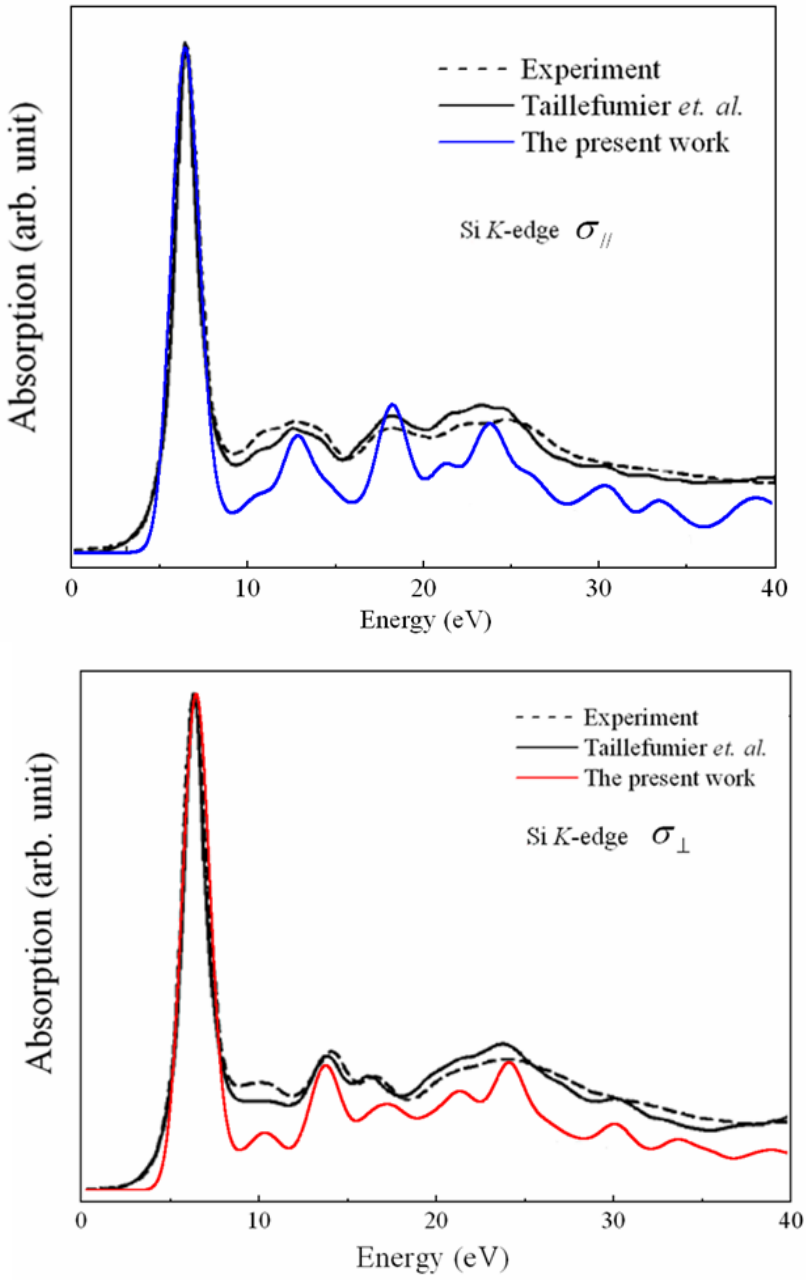

Figure 5.10. The calculated silicon *K*-edge polarized XAS of α-quartz compared with previously reported calculations and experiments. (Top) The XAS for polarization direction $\hat{\varepsilon}$ parallel to the ternary axis [001]. (Bottom) The XAS for polarization direction $\hat{\varepsilon}$ perpendicular to the ternary axis [001]. The previous calculations and experimental data are reported in Ref. 247.

In the present study, the absorption spectra $\sigma_{//}$ and $\sigma_{\perp}$ of silicon *K*-edge of *α*-quartz were calculated. The coordinates and site symmetries for *α*-quartz used in the present calculations are Si : 3*a* 0.0000 0.4699 0.3333; H : 6*c* 0.4141 0.2681 0.7854 with lattice constants *a*=4.913, and *c*= 5.405 Å. The full core hole approach is used with a charged supercell. Construction of the pseudopotential for the absorbing silicon atom employed the electron configuration $1s^1 2s^2 2p^2 3d^6 3s^0 3p^0 3d^0$ with one electron removed from the 1s orbital. A 72 atom supercell (2x2x2 primitive cell) has been used. Charge density has been calculated with only one *k*-point in the BZ. In order to mimic experiments, a Gaussian smearing of 1.0 eV was used to broaden the calculated spectra. The calculated spectra $\sigma_{//}$ and $\sigma_{\perp}$ are presented in Fig. 5.10 and compared with previous reported calculations and experiments [247]. It is observed that our calculated spectra agree very well with those from the previous theoretical calculation and the experiment. The positions and relative intensities of all the features are correctly reproduced.

5. 3. 6 Water molecule in gas phase

For molecules, it was found that the choice of core hole potential, *e.g.*, half or full core hole, plays an important role in the calculated XAS. Usually the half core hole potential produces XAS that agree better with experiments [261, 262]. The quality of XAS of molecules also depends on the treatment of electron screening. As shown in section 5. 3. 2, the two extreme cases of electron screening, no screening (charged cell) and complete screening (neutral cell), produce similar and reasonable carbon *K*-edge XAS for diamond. For molecular phases the situation is very different. Molecules experience substantial excitonic modifications in electronic excitations, and XAS calculated with the two extreme limits of electron screening are very different [276, 277]. In this section, the XAS calculation of molecules is explored by calculating the oxygen *K*-edge XAS of water molecule in the gas phase. The calculations are performed with both half and full core hole potential, and with both charged and neutral cell. The results are compared with experiments [278] and previously reported theoretical calculated spectra [260].

The oxygen *K*-edge XAS of water molecule calculated with different core hole potentials representing different electron screening are compared with the experimental spectrum [278] in Fig. 5.11. The experimental XAS spectrum is characterized by three main features at 535.7, 537.6, and 538.8 eV. The positions of the first two peaks with a gap of about 2 eV, and their relative intensities (the first about half the height of the second) are well reproduced in all the calculated spectra. For the third peak and higher-energy but weaker peaks, the calculated and observed results are very different. It is interesting that only the no core hole potential correctly reproduces both the position and relative intensity of the third peak. The full core hole potential with neutral cell, and the half core hole potential with charged cell, reproduce the third peak correctly in relative positions, but with a much lower intensity. As shown in the experimental spectrum [278], intensities of the higher-energy peaks are much lower when compared with the three main peaks. This spectral feature is reproduced by all the calculated spectra except the one calculated with the no-core hole potential. In general, the XAS spectrum calculated using the half core hole potential with a charged cell is the closest to the experimental spectrum. However, it is clear that the agreement with the experiment, even in the best case, is not as good as the agreement achieved for solid materials. As shown in Fig. 5.11, the full core hole potential produces similar spectrum as the half core hole potential, but tends to overestimate the energy gap between the second and third main peaks. This observation indicates that the full core hole potential exaggerates the contraction of the low energy empty valence orbitals. The contraction enhances the transition intensities of the two low-energy peaks and pushes other peaks to higher energies. This behavior of the full core hole spectrum has also been observed in Ref. 260. It was reported in Ref. 260 that the combination of the half core hole potential and charged cell produce the best agreement of XAS for water molecule with experiment. Fig. 5.12 shows the comparison between the oxygen *K*-edge XAS of water molecule calculated in the present study and that presented in Ref. 260. Both spectra were calculated with the half core hole potential with a charged cell. In the present study, the PAW approach and a PW basis set were used. In previous calculations [260], the all-electron approach and localized basis set aug-cc-PV5Z were used. In Fig. 5.12, the first two main peaks are clearly reproduced by both calculations. For the third and fourth peaks, the all-electron calculation reproduces

the correct relative intensities but the predicted excitation energies are shifted to higher energies. In conclusion, it is unfortunate that none of the above calculations reproduces the oxygen *K*-edge XAS of water molecule that agrees well with the experiment. However, improvements were achieved by modifying the core hole potential and electron screening. The calculations presented provided information on the modeling of the effects of proper screening is difficult even in simple molecules as water. Some of the discrepancies may be attributed to the neglect of vibrational and lifetime effects.

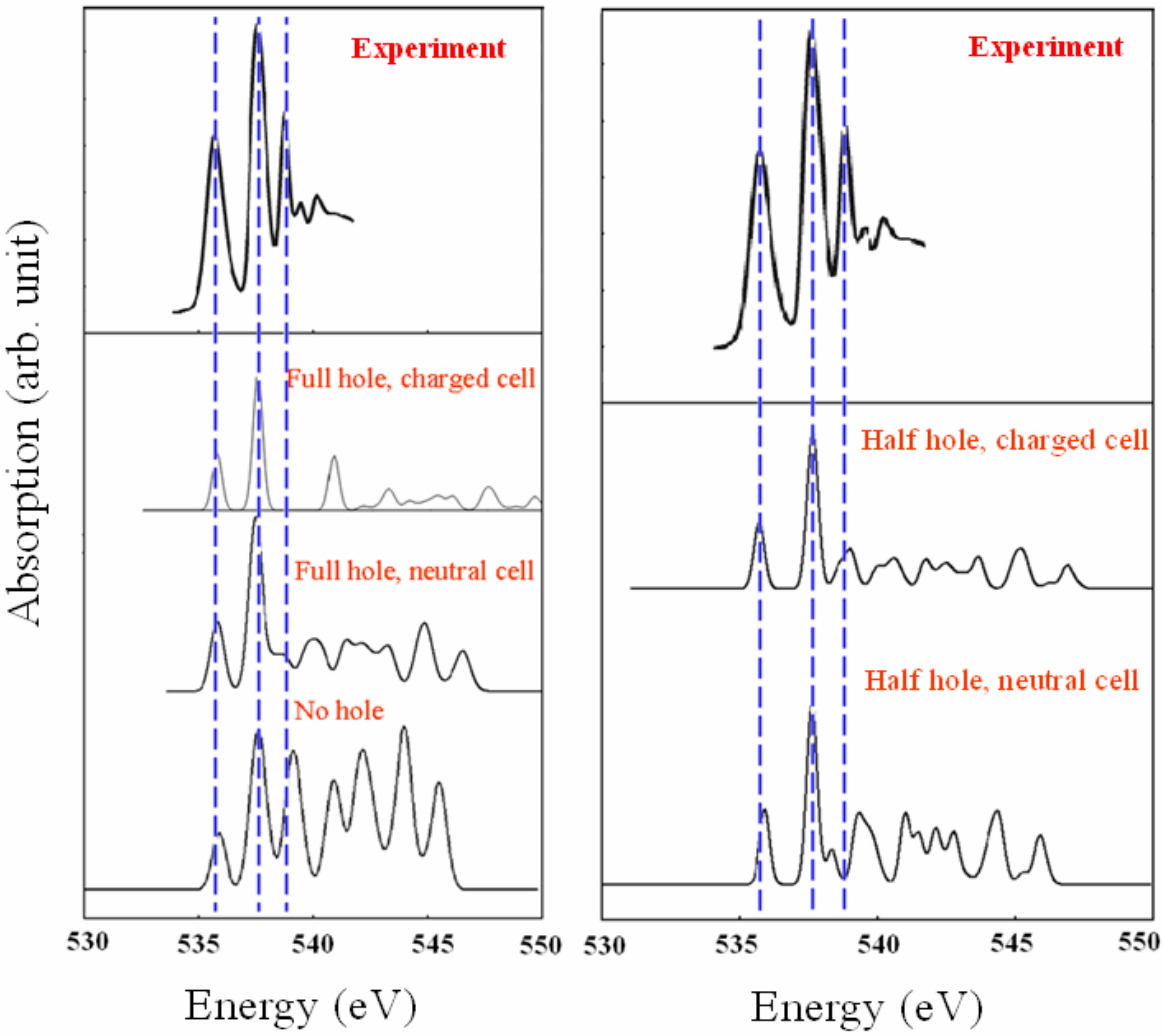

Figure 5.11. The oxygen *K*-edge XAS of water molecule calculated with different core hole potential and electron screening. A Gaussian smearing of 0.5 eV is used to smooth all spectra. The experimental spectrum is reported in Ref. 278.

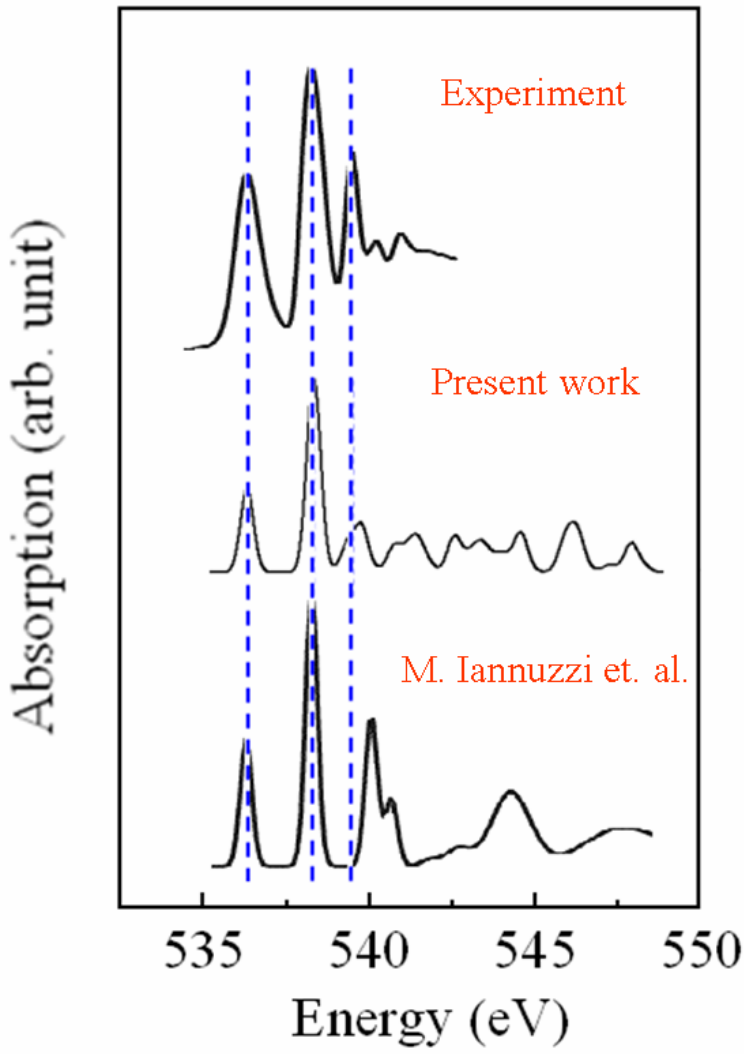

Figure 5.12. A comparison between the calculated oxygen *K*-edge XAS of water molecule and previously reported data [260].

5. 4 Summary

A numerical method employing the projector augmented wave method has been developed for the calculation of X-ray absorption spectrum within the framework of density functional theory. This method has been coded and implemented into the electronic structure package Quantum-ESPRESSO. To test the implementation, the carbon, silicon, and oxygen *K*-edge XAS were calculated for diamond, fullerene C_{60}, α-

quartz and water molecules. It is observed that for solid materials, the agreement between calculated XAS and experiments are very good. For molecules, the quality of the calculated XAS sensitively depends on details of the theoretical treatment of core hole potential and electron screening.

Chapter 6

Summary and Perspectives

An interesting property of solids under high pressure is the ubiquitous presence of superconducting states. Most often, crystal structures at ambient pressure become unstable at high pressure and transform into new phases. Under suitable conditions, many of these new structures are superconductive. One of the objectives of this research is to identify the favorable conditions in the formation of a superconducting state. To this end, the possibility of pressure-induced superconductivity was investigated for selected materials, including dense Li, Xe, and Group IV (Si, Sn) hydrides using the Migdal-Eliashberg theory within the framework of the BCS superconducting theory. Alkali metal Li, generally regarded as a free-electron metal at ambient condition, was found to transform into two superconducting phases (FCC and *cI*16) at high pressure with a maximum superconducting critical temperature T_c up of 17K. In Chapter 2, the phase transitions and superconductivity in these two phases were investigated. The calculated pressure for the FCC $\rightarrow$*cI*16 transformation is in good agreement with experiment. Strong electron-phonon coupling was found in both phases. For the FCC phase, experimental T_c was reproduced with the theoretically calculated EPC parameter only if an unusually large Coulomb pseudopotential μ^*~0.22 is used. In contrast, the calculated T_c of the *cI*16 phase are also in good agreement with experiments but with a more nominal μ^* of 0.14. This observation may indicate that strong *s*/*p* hybridization increases the strength of the Coulomb repulsion in the FCC phase but the *cI*16 phase behaves more like a 'normal' superconductor. More importantly, the calculations also successfully reproduced the observed maximum in T_c immediately preceding the FCC $\rightarrow$ *cI*16 transition. A surprising superconducting property is found in solid Xe. Noble gas is

known as being chemically inert at ambient pressure. Under high pressure, however, Xe undergoes a displacive phase transition to the HCP structure above 70 GPa and becomes metallic at 140 GPa. The possibility of superconductivity of the metallic HCP phase was investigated from 150 to 315 GPa. The results reveal that the EPC of Xe is spatially localized in separated regions in the first BZ. The EPC is found to be largest at 215 GPa with a T_c of 0.04 K was predicted. Recently Group IV hydrides have been suggested as good superconductors under high pressure because the H atoms are pre-compressed by heavier Group IV atoms and possess high-frequency vibrations. The validity of this suggestion was confirmed by detailed analysis of the high-pressure phases of SiH_4 and SnH_4. Very high T_c was predicted in SiH_4 and SnH_4 compounds at a pressure higher than 100 GPa. This prediction is confirmed by a recent experiment on SiH_4, in which a pressure-induced superconducting state was found with a T_c up to 17 K.

The results obtained here offer a glimpse on the properties that determine superconductivity at high pressure. It is shown that superconductivity is likely to occur in low-dimensional structures, most favorable in two-dimensional planar structures [75, 279]. It is shown that the simultaneous occurrence of dynamical and electronic instabilities of the materials help to enhance the EPC. A remarkable feature found in these pressure-induced superconductors is the ubiquitous presence of soft phonon modes as a result of FS nestings and/or Kohn anomalies [75]. The good agreement found between theory and experiment demonstrated that first-principles methods can be used reliably to estimate T_c. In the future, we expect to extend the investigation of pressure-induced superconductivity to other materials at high pressure. For example, as an extension of the superconductivity on Group IV hydrides, the Li-Be alloys have been suggested as a candidate material for pressure-induced superconductors [280]. As the density increases with pressure, the core orbitals of Li atoms start to overlap and expel valence electrons into two-dimensional layers characterized by delocalized nearly free electron states near Be ions. This phenomenon is very similar to the procedure that the H atoms experience in the high pressure SnH_4 [75]. Moreover, since both Li and Be are superconductors, the Li-Be alloys may well merit assessment for superconductivity. Another group of peculiar materials under pressure is the intercalated graphite. In recent

experiment, $CaLi_2$ was found that the hexagonal polymorph of Laves-phase $CaLi_2$ is superconducting at high pressure with a maximum T_c of 13K at 81 GPa [281, 282]. Moreover, the superconducting state of Ca-intercalated graphite CaC_6 has also been found with a T_c up to 11.4K [283-285]. The experiments on graphite also leads to an interesting question that, can doped-grapheme, which is structurally similar to graphite, be superconducting as well? The answer to these questions and the theoretical investigation on the high-pressure materials mentioned above will further extend the understanding on pressure-induced superconductivity. On the other hand, further developments in the theoretical method are also desirable. Instead of the empirical McMillan equation, or its' extension by Dynes and Allen, the complete Eliashberg gap equations should be solved to obtain more accurate estimate of T_c [58-61]. Moreover, a better scheme for BZ sampling for the treatment of spatially localized EPC is needed. For many pressure-induced superconductors, the EPC is localized in small regions in the BZ, which makes an accurate evaluation of EPC parameter difficult. Using the current MP sampling scheme, the accurate calculations of T_c for these systems may require impractically larger q-mesh beyond the current computational capability. A possible solution to this problem is proposed through the study of boron-doped diamond by Giustino *et. al.* [286, 287], who designed a scheme to improve sampling of the first BZ with millions points using spatially localized Wannier orbitals [288]. Very accurate electron-phonon matrix elements at arbitrary phonon wavevector can then be easily evaluated. Another factor affecting the reliability of the estimated T_c is the repulsive electron-screened Coulomb interactions or the Coulomb pseudopotential μ^*. μ^* is very complicated to compute from first-principles [129, 289]. Thus in practice, empirical values of μ^* between 0.10-0.13 are often used. However, the choice of an empirical value of μ^* sometimes can be problematic. For example, μ^* is found as high as 0.22 in the FCC phase of Li [141]. To solve this problem, Lüders *et.al.* proposed a new method [200-292] to calculate the T_c directly from the DFPT. The Coulomb repulsion enters the perturbative treatment on the same footing as EPC and is explicitly calculated from DFPT. In this way, a truly *ab initio* calculation of T_c can be achieved which does not need any empirical parameters. An efficient implementation of this scheme to handle larger system is urgently needed.

A feature of the crystallography at high pressure is the existence of a rich diversity of morphologies. At high pressure, it is possible that many candidate structural models have very similar enthalpy. X-ray diffraction patterns are often used to differentiate the structural models. However, it is sometimes very difficult to obtain reliable experimental data at high pressure. It was demonstrated in Chapter 3 that through the calculation of Bader's AIM analysis, IR and Raman spectroscopes can be used as sensitive diagnostic tools to differentiate among candidate structural models. These methods were applied to solid H_2, O_2, and SiH_4. In solid H_2, IR and Raman spectra are used to examine two recently proposed competing structures of the high-pressure phase III; the *Cmcm* and *C*2/*c* structures. These two structures have very similar local structural motifs and therefore, the profile and the intensity of the IR active vibrons of both structures are also similar and apparently both agree with experiment. Instead, it is found that Raman and IR spectra of low-frequency vibrations are very sensitive to the local structure. The calculated Raman spectrum of the *C*2/c structure gives much better agreement with experiment than the *Cmcm* structure. Moreover, the calculated pressure dependence of the IR absorption intensity of the *C*2/*c* structure is also shown to be in excellent agreement with experiment. For solid O_2, the experiment observed structure, IR and Raman spectra of the recently solved *C*2/*m* structure of the high-pressure ε phase were well produced using the DFPT method. Although, it was found that the observed *C*2/*m* structure has a slightly higher enthalpy than the theoretically proposed *Cmcm* chain structure. Using Bader's AIM method and from the analysis of the electron charge density, the preference on the formation of $(O_2)_4$ clusters in the *C*2/*m* structure and the nature of the interactions between O_2 molecules is explained. It was shown that weak non-bonded interactions between $(O_2)_4$ clusters help to stabilize the structure. Changes in the geometry of the $(O_2)_4$ cluster and the Raman vibrations with pressure have been examined and the overall agreement with experiments is excellent. A new structure for the metallic and superconducting ζ phase is proposed and discussed. For SiH_4, IR and Raman spectra were calculated for our predicted $P4_2/nmc$ structure and the agreement with available experiment results is very good. More significantly, the predicted metallization pressure is also in a good accord with experiment. The good agreement of the calculated and observed spectral features indicates that the $P4_2/nmc$ structure is a

reasonable candidate for the high-pressure insulating phase of SiH_4.

As commented by John Maddox [293], 'One of the continuing scandals in the physical sciences is that it remains in general impossible to predict the structure of even the simplest crystalline solids from knowledge of their chemical composition.' Indeed, predicting the diverse crystal structures of a solid is one of the central problems in (high-pressure) crystallography. Traditional theoretical methods for predicting unknown crystal structures usually involve dynamical processes and have obvious shortcomings. The dynamical methods have limited ability to overcome energy barriers in the free energy surface, and therefore the accuracy is strongly dependent on the initial guess of structural configurations. An unreasonable initial guess may result in the subsequent configurations being trapped in higher energy local minima. On the other hand, GA presents an attractive solution to these problems, since it does not need any prior information on the topology of the energy landscape and initial structures, and is efficient in investigating the free energy surface. The only information needed is the knowledge of chemical composition of the solids. A recently proposed GA for crystal structure prediction with new developments have been implemented and applied to investigate high-pressure structures of solid N, Ca and AlH_3. For solid N, the GA method not only recovered the four lowest-energy non-molecular structures, CG, *C*2/*c*, BP, and *Cmcm* chain predicted theoretically or known experimentally, but also revealed a meta-stable single-bonded three-dimensional structure. The stability of this structure at high pressure was established by phonon calculations. For Ca, recently two new high-pressure phases, Ca IV and V, have been found and shown to possess surprisingly high T_c. However, the crystal structures of these two phases cannot be identified due to the lack of reliable structural information. The GA method was used to search for lowest enthalpy candidate structures, and unambiguously identified stable structures for Ca IV and V. The calculated diffraction patterns of predicted structures of both phases are in substantial agreement with experiments. For AlH_3, the GA method was used to search for candidate structures for high-pressure phase II and phase III of AlH_3 identified by experiments recently. It is found that the structure for phase III has a space group of *Pm*-3*n* with Al atoms forming a BCC framework and H atoms locating on faces and forming linear

chains along the cubic axes. The predicted structure for phase II has a triclinic cell with space group $P1$. The predicted lattice parameters, unit cell volumes, diffraction patterns of the $P1$ structure fit reasonably well the experimental data. The calculated electronic density of states also support the pressure-induced metallization observed in experiments.

We demonstrated in this thesis that the current implementation of GA method for the search of crystal structure is successful. Other than the materials presented in this thesis, there are still plenty of unknown high-pressure crystal structures need to be determined/predicted. For example, there are evidences found in recent ac susceptibility and Raman spectroscopic studies that Li might transform into an intermediate phase around 50 GPa and stabilizes into another stable phase above 62 GPa [134]. The structures of these two possible phases remain unknown. In the future, it is also expected to extend this method to more complex structures. In the present study, we have employed the GA method to crystal structures containing up to 12 atoms (AlH_3). It would be interesting to apply this method on more complicated systems. In a recent proposal, it was claimed that in principle, a well-tuned GA is reliable for searching crystal structures containing several tens of atoms [294]. A very challenging project will be resolving the structure of high-pressure ξ phase of solid N. X-ray diffraction experiment has identified a phase transition from the molecular rhombohedral ($R3/c$) ε phase to another molecular phase, ξ phase at 60 GPa [295-297]. The structure of the ξ phase is unknown. However, the X-ray diffraction experiment suggests that the primitive unit cell of the ξ phase can contain up to 24 N atoms [295]. Moreover, the N atoms form three types of bonds at high pressure, single-, double-, and triple-bonds. As discussed in Chapter 4, at high pressure, solid N prefers to crystallize in chain-like structures in which N atoms are connected by alternating single- and double-bonds, *e.g.*, the *Cmcm* and *Imma* chain structures. Thus, to search for the molecular N structures that are solely constructed by triple-bonds, an efficient screening scheme needs to be developed to separate the offspring structures containing double and triple bonds. On the aspect of further developing the algorithm, a new genetic operation, permutation, could be added to the current implementation. A possible realization of permutation operation is to randomly exchange the positions of different types of atoms in the parent structure. The

purpose of the permutation operation is to accelerate the location of correct atomic ordering. The current GA code is implemented for the electronic band structure package VASP. It is also possible to implement it to other first-principle codes, for example, Quantum-ESPRESSO and SIESTA.

In Chapter 5, a first-principles approach was developed for the calculation of XAS within the framework of the DFT. The PAW method was used to reconstruct the core orbitals. These orbitals are essential for the calculation of the transition matrix elements. This approach provides a straightforward framework for the investigation of single particle core hole and electron screening effects, which have been demonstrated to be significant for all investigated materials. To test the implementation, the C, Si, and O *K*-edge XAS were calculated for diamond, fullerene C_{60}, α-quartz and water molecule. In all cases, the calculated XAS agree very well with experiments. For water molecule, the quality of the calculated XAS sensitively depends on the delicate theoretical treatment of core hole potential and electron screening. The overall agreement between the calculated XAS and experiment is reasonable.

The reliability demonstrated by the reported cases indicates the current implementation of the first-principles calculations of XAS is successful. A good project in the future is to extend the XAS calculations to disordered solids. A few improvements can be added to the current method. For example, the current code can only calculate the XAS for spin-restricted systems. It is possible to extend the implementation to spin-polarized systems in near future. At present the interaction matrix is restricted to dipole approximation, we plan to extend it to higher-order multipoles. Current XAS spectra are broadened by Gaussian smearing with constant linewidth. In the future, a more realistic energy-convoluted broadening scheme needs to be developed. Moreover, a reliable code for generating core hole PAW pseudopotential needs to be implemented. Within the DFT framework first-principles simulations of several other spectroscopes, such as EELS and the XES, can also be developed.

In this thesis, electronic properties of materials under high pressure were studied through state-of-the-art computational methods. The calculations were based on the first-principles PW pseudopotential method within the framework of DFPT. The work summarized in this thesis is comprised of four themes. Separate chapter was devoted to each research topic. The electronic structure, FS, IR and Raman spectrum, Bader's AIM analysis, animation of atomic vibrations, lattice dynamics, and EPC all require tremendously large amount of computing time. For example, EPC calculations of the high-pressure $C2/c$ phase of SiH_4 at 125 GPa took 19200 computational hours on a fast-interconnected (full-bidirectional InfiniBand) Opteron cluster with 64 processors. I have developed several major computer programs. These include the genetic algorithm package used in Chapter 4 and the XAS code described in Chapter 5. The genetic algorithm package was developed such that the evolutionary procedures are automatic and no users' interference is needed. An introduction of the genetic algorithm package and a user manual is given in Appendix B. The XAS code was developed in collaboration with DEMOCRITOS National Simulation Center of the Italian CNR-INFM in Trieste, Italy. This code was implemented into the Quantum-ESPRESSO package and will be released to the scientific community in near future. Other programs developed in the thesis include a code for calculating the partial phonon DOS projected into atomic contribution (Appendix A) and the analysis of nesting of FS.

APPENDIX A

Calculation of atom projected phonon DOS

At a given phonon frequency ω, the total phonon DOS is defined as:

$$\rho_{tot}(\omega) = \frac{1}{A}\sum_{j}\sum_{\vec{q}}\delta(\omega - \omega_{\vec{q}j}), \tag{A.1}$$

where $\omega_{\vec{q}j}$ is the phonon frequency of mode ($\vec{q}j$). $\omega_{\vec{q}j}$ can be obtained as the square root of the eigenvalue of the dynamical matrix. The index *j* runs over all phonon branches. The *q*-point forms a complete MP mesh [22]. A is a normalization factor can be computed from a simple rule: the integrated sum of the total phonon DOS should be equal to 3 times the number of atoms in the primitive cell.

If the primitive cell contains more than one atom, the partial phonon DOS projected on the *a*-th atom is calculated as follows. At a given phonon wavevector $\vec{q}$, the *a*-th atom's contribution to the *j*-th branch phonon frequency $\omega_{\vec{q}j}$ is [298]

$$factor(j,\vec{q},a) = \frac{\sum_{i} C_{ai}^{2}(j,\vec{q})}{\sum_{s}\sum_{i} C_{si}^{2}(j,\vec{q})}. \tag{A.2}$$

Here $C_{ai}(j,\vec{q})$ and $C_{si}(j,\vec{q})$ are coefficients of the eigenvectors corresponding to phonon frequency $\omega_{\vec{q}j}$. The index *i* indicates three Cartesian directions. The index *s* sums over

all atoms in the primitive cell. Thus it is straightforward to write the partial phonon DOS projected to the α-th atom as

$$\rho_a(\omega) = \frac{1}{A}\sum_j \sum_{\vec{q}} factor(j,\vec{q},a)\delta(\omega - \omega_{\vec{q}j}) . \quad (A.3)$$

This double summation in Eq. (A.3) is calculated using the tetrahedron integration scheme. The complete q-point mesh forms N tetrahedra. The vertices of the n-th tetrahedron are defined as $\vec{q}_k^{\,n}$ with k=1, 4 [298]. Eq. (A.3) is calculated by summing over all tetrahedra inside the BZ,

$$q_a(\omega) = \frac{1}{A}\sum_n \sum_j V_T^n g^n \sum_k [I_k^n \times factor(j, q_k^n, a)] . \quad (A.4)$$

Here g^n is the weight of the n-th tetrahedron. I_k^n is the weight of the k-th vertex of the n-th tetrahedron. The normalization of the weights requires that $\sum_n g^n = 1$ and $\sum_k I_k^n = 1$ for each tetrahedron n. The V_T^n is the volume of the n-th tetrahedron. This method has been implemented in the first-principles electronic structure code Quantum-ESPRESSO [62]. An example is shown in Fig. A.1 on the calculated partial phonon DOS for AlAs projected on Al and As atom.

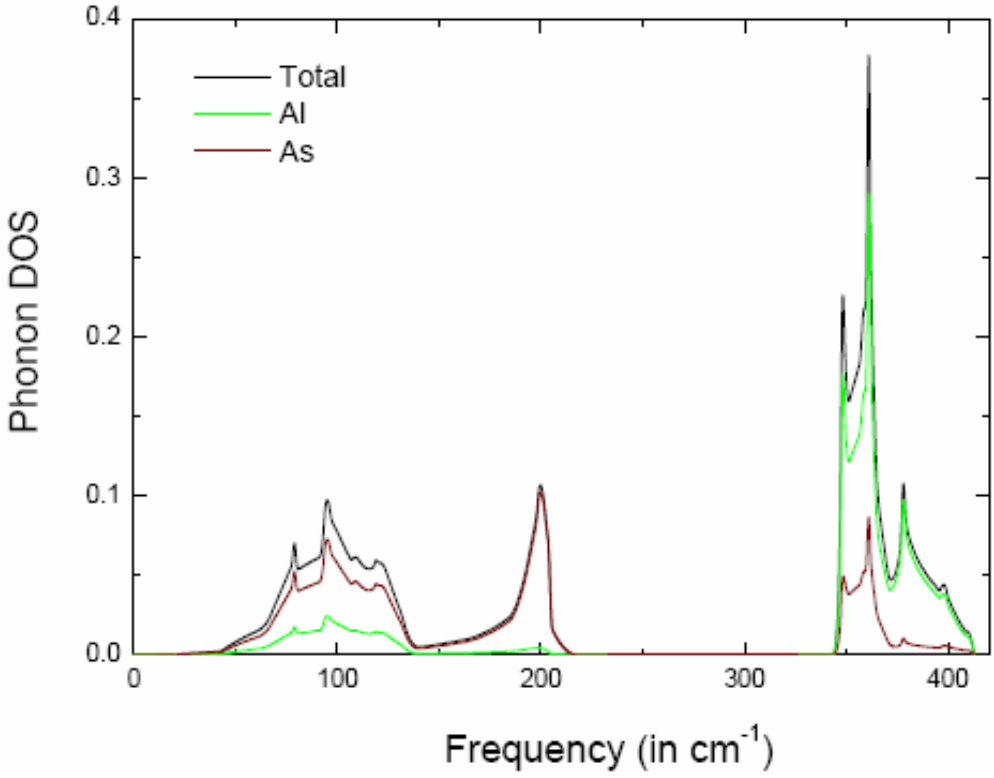

Figure A.1. Calculated total phonon DOS and partial phonon DOS projected on Al and As atom for AlAs.

APPENDIX B

User 's guide for ASAP

B. 1 Introduction

This guide covers the installation and usage of ASAP (Advanced Structure seArching Package). ASAP is a suite of code and shell-script to perform structure prediction calculations based on the recently proposed genetic algorithms [52-56]. The goal is to predict the most stable crystal structure and/or energetically favorable meta-stable crystal structures from the knowledge of only constituent elements at any given pressure or volume condition. The search starts with a population of randomly generated structures. The population is improved through genetic operations by producing energetically favorable structures. In successive generations, new low-energy structures evolve and replace the highest-energy structures in the preceding generation.

For each generation, there are essentially two computational steps,

I. Generate the candidate structures by applying the genetic operations, namely heredity, mutation, and maintain operations on structures selected from current generation. This step is performed by ASAP.

II. Perform structural optimization on the generated structures of step I. This step needs to be done with first-principles code. The current version of ASAP code is implemented for VASP [63] only.

As seen from step I, ASAP code is used to analyze a population of candidate structures (optimized by VASP). This step does not contain any first-principles calculations, and therefore it serves as a post-processing code. Thus, the ASAP code works only in *serial* mode.

B. 2 Installation

The ASAP code contains four executables: **analy, asap, pos2cif,** and **writeSYM.** The function and usage of these executables will be explained later. To install the ASAP code, one should use the Makefile. A sample Makefile is provided with the code designed for Inter Fortran Compiler (ifort). The ASAP code does not use any external math libraries and the optimization level is not important. To "make" the code, execute the command,

make

To uninstall the code, one uses the command,

make clean

An external executable **findsym** [213] that calculates the space group of a crystal structure is used in the ASAP code. The code can be downloaded from **http://stokes.byu.edu/isolinux.html.** It is a pre-compiled package so does not need to be installed. However, one has to set environment variable in order to run the program. Please follow the instructions provided on the website.

B. 3 Usages

1. asap

This is the main executable for the ASAP code. It performs the genetic operations as described above. The input file looks like this:

```
100                     # control flag
110.0                   # defined volume, in a^3
0.00 0.00 0.00 0.00 0.00 0.00       # user-defined cell
2                       # of different elements
2   8                   # of Si atoms, # of H atoms
0.00 0.00 0.00 0.00             # user-defined constraints
11                      # of offsprings
4                       # kscale
11                      # of parents, for ical =1 and 100 only.
ENERGY.gen1
RDF.gen1
SYM.gen1
GENE_INFO.gen2              # Structure information, for ical=1 only.
```

Explanation:

Line 1. This is the type of calculations. There are three choices.

0 : generate a population of random structures. For each structure, the POSCAR and KPOINTS files will be generated. The naming of POSCAR and KPOINTS following this rule,

POSCAR0001 …POSCAR0010 … POSCAR 0100… POSCAR 1000

KPOINTS0001…KPOINTS0010…KPOINTS0100…KPOINTS1000

1 : generate a new population of structures by applying genetic operations on selected structure from the current population . For each structure, the POSCAR and KPOINTS files will be generated.

100 : analyze a population of optimized structures. For each structure, the OUTCAR and CONTCAR are needed for the analysis. The naming of OUTCAR and CONTCAR following the same rule as POSCAR and KPOINTS,

OUTCAR0001 …OUTCAR0010 …OUTCAR0100…OUTCAR1000
CONTCAR0001…CONTCAR0010…CONTCAR0100…CONTCAR1000

The calculated energies, structural information of each structure will be printed out into an ENERGY file (Line 10). The radial distribution function will be printed out into the RDF file (Line 11).

Line 2. This is the user-defined volume of unit cell (in $Å^3$) for the structures to be generated. For calculation type = 0 the program generates an initial population of random structures with the volumes scaled to the preset value. For calculation type =1 the program generates a new population of structures based on genetic operations and the input volume is not used. Instead, a weighted average of this volume and the optimal volume extracted from the current population is used to scale the generated structures. Detail information on the weighted average is presented in the header file 'parameters.inc'.

Line 3. User-defined unit cell. Input *a, b, c, α, β, γ* of the unit cell you would like to use. Otherwise the code will generate the unit cells either randomly (if Line 1 = 0) or from the parent structures (if Line 1 = 1). In these two cases, hard constraints on lattice vectors and cell angles will be applied on the generated unit cells. These hard constrains can be adjusted in the file 'parameters.inc'. The units here are Å and degree. These parameters are optional, and if used the line 2 will be blocked. Input all '0' if this line is not needed.

Line 4. Number of different types of elements in the unit cell.

Line 5. Number of atoms for each type of elements in the unit cell. The order of elements input here will be used to generate the POSCAR file. Make sure the atom pseuopotentials in the POTCAR file are arranged in the same order.

Line 6. User-defined hard constraints on the shortest distances permitted between atoms. This key is optional. The current implementation can treat only two types of atoms. Input the desired shortest distances, A-A, B-B, A-B. Input all '0' if this line is not needed, then the hard constraints will be automatically generated by scale the volume of unit cell. Detail information on automatically generated constraints is presented in the header file 'parameters.inc'.

Line 7. Number of offspring structures to be generated.

Line 8. The basic division of *k*-point used in KPOINTS files. Depends on the hard constraints used, the generated structure could have arbitrary cell shapes. Thus it is not reasonable to use an unitary *k*-point mesh to optimize them. The ASAP code therefore generate a KPOINTS file for each structure. A uniform *k*-point mesh is generated by scaling according to the length of the reciprocal lattice vectors of the structure with a basic division and rounded to the nearest higher even integers. For example, if the basic division is 4 and the ratio between three lattice vectors is 1:2:3, the generated *k*-point mesh will be 12 x 8 x 4.

Line 9. Number of parent structures in the population.

Line 10. Filename for the ENERGY file. This file stores the structural information and calculated energy for each optimized structure in the population. Here, if the structure optimization is constant-volume, the total energy of each structure will be printed out. However, if the structure optimization is done at constant-pressure, the enthalpy of each structure will be printed out. The structures are sorted in order of increasing energy/enthalpy, and thus the first structure in each generation is the lowest-energy/enthalpy structure. For some structures that the structural optimizations fail to

converge, they will be sorted to the end regardless the energies/ enthalpies. For calculation type = 100 that analyze the optimized structure, this file is written. For calculation type = 1 that generates structures based on genetic operations, this file is read.

Line 11. Filename for the RDF file. This file is similar to the ENERGY file except the radial distribution function for each structure is added in.

Line 12. Filename for the SYM file. This file is similar to the RDF file except the space group for each structure is added in. This file is generated by another subroutine **writeSYM** that will be explained below. For calculation type = 1 that generates structures based on genetic operations, this file is read.

Line 13. Filename for the GENE_INFO file. This file is written when calculation type = 1. This file keeps a record of each new generated structure on the info of their parent structures and type of genetic operation used.

2. pos2cif

This subroutine produces the .cif files (to be used with Material Studio and Mercury) for a population of optimized structures. The ENERGY file is needed in this step to read structural information from. The input file is like this,

```
1               # of different elements
8               # of Ca atoms
Ca              Element names
66              # of structures
ENERGY.gen1         # ENERGY file
```

Explanation :

Line 1. Same as Line 4 of the input file for **asap**.

Line 2. Same as Line 5 of the input file for **asap**.

Line 3. Element names. Please make sure the order of elements here is consistent with the ENERGY file.

Line 4. Number of structures in this population.

Line 5. The filename of the ENERGY file.

3. writeSYM

This subroutine analyzes the structural information of a population of optimized structures (structural information stored in the ENERGY files), and produce the SYM file. The space group of each structure is calculated using the program **findsym** [6]. The **writeSYM** subroutine produces input files and collect output files for **findsym.** The input file for **wirteSYM** is as follow,

```
 0                # calculation type, 0: write input files  1: analyze results
1                 # of different elements
8                 # of Si atoms, # of H atoms
66                # of parents
ENERGY.gen1       # ENERGY file
RDF.gen1          # RDF file
SYM.gen1          #  SYM file
 0.08                       # tolenrance
```

Explanation :

Line 1. Type of calculation. There are two choices,

0 : produces input files for **findsym**

1 : analyze the output files from **findsym** and produce the SYM file.

Line 2. Same as line 4 of the input file for **asap**

Line 3. Same as line 5 of the input file for **asap**

Line 4. Same as line 9 of the input file for **asap**

Line 5. Same as line 10 of the input file for **asap**

Line 6. Same as line 11 of the input file for **asap**

Line 7. Same as line 12 of the input file for **asap**

Line 8. User defined value of tolerance in the calculation of symmetry (in fractional coordinates).

4. analy

This subroutine analyzes the genetic track of the parent population and offspring population. Specifically, it reports the record on (i) the number of offspring structures having lower energy than their parents, (ii) the number of offspring structures different from their parents and (iii) structural information and space groups on newly generated and disappeared structures is kept. The input file of **analy** is as follow,

SYM.gen2
SYM.gen1
GENE_INFO.gen2
ANALY.gen2

Explanation :

Line 1. The SYM file for the offspring population.

Line 2. The SYM file for the parent population.

Line 3. The GENE_INFO file for offspring generation.

Line 4. The filename for the ANALY file. The analyzed results are stored in this new file.

5. parameters.inc

This header saved the adjustable parameters used by the various programs. If it is necessary to adjust some parameters, please first uninstall the code by '**make clean**' and reinstall the code afterwards. The explanation on these parameters are given in the file.

REFERENCES

[1] J. S. Tse, Z. Kristallogr. **220**, 521 (2005).

[2] M. Born and J. R. Oppenheimer, Ann. Phys. **84**, 457 (1927).

[3] P. Hohenberg and W. Kohn, Phys. Rev. **136**, B864 (1964).

[4] T. L. Gilbert, Phys. Rev. B **12**, 2111 (1975).

[5] W. Kohn and L. J. Sham, Phys. Rev. **140**, A1133 (1965).

[6] J. C. Phillips, Phys. Rev. **112**, 685 (1958).

[7] J. C. Phillips and L. Kleinman, Phys. Rev. **116**, 287 (1959).

[8] M. L. Cohen and V. Heine, Solid State Physics **24**, 37 (1970).

[9] S. Baroni, S. de Gironcoli, A. Dal Corso, and P. Giannozzi, Rev. Mod. Phys. **73**, 515 (2001).

[10] M. C. Payne, M. P. Teter, D. C. Allan, T. A. Arias, and J. D. Joannopoulos, Rev. Mod. Phys. **64**, 1045 (1992).

[11] J. P. Perdew and A. Zunger, Phys. Rev. B **23**, 5048 (1981).

[12] D. M. Ceperley and B. J. Alder, Phys. Rev. Lett., **45**, 566 (1980).

[13] J. P. Perdew, Phys. Rev. Lett. **55**, 1665 (1985).

[14] J. P. Perdew, J. A. Chevary, S. H. Vosko, K. A. Jackson, M. Pederson, D. J. Singh, and C. Fiolhais, Phys. Rev. B **46**, 6671 (1992).

[15] A. D. Becke, J. Chem. Phys. **38**, 3098 (1988).

[16] M. Levy and J. P. Perdew, Phys. Rev. A **32**, 2010 (1985).

[17] J. P. Perdew and Y. Wang, Phys. Rev. B **45**, 13244 (1992).

[18] J. P. Perdew, K. Burke, and M. Ernzerhof, Phys. Rev. Lett. **77**, 3865 (1996).

[19] C. S. Wang, B. M. Klein, and H. Krakauer, Phys. Rev. Lett. **54**, 1852 (1985).

[20] P. Bagno, O. Jepsen, and O. Gunnarsson, Phys. Rev. B **40**, 1997 (1989).

[21] D. R. Hamann, Phys. Rev. Lett. **76**, 660 (1996).

[22] H. J.Monkhorst and J. D. Pack, Phys. Rev. B **135**, 188 (1976).

[23] R. Orlando, R. Dovesi, C. Roetti, and V. R. Saunders, J. Phys. Condens. Matter **2**, 7769 (1990).

[24] V. R. Saunders, R. Dovesi, C. Roetti, M. Causà, N. M. Harrison, R. Orlando, and C. M. Zicovich-Wilson, CRYSTAL'98 User's Manual (University of Torino, Torino) (2003).

[25] J. M. Soler, E. Artacho, J. D. Gale, A. Garcia, J. Junquera, P. Ordejon, and D. Sanchez-Portal, J. Phys. Cond. Matt. **14**, 2745 (2002).

[26] J. S. Lin, A. Qteish, M. C. Payne, and V. Heine. Phys. Rev. B **47**, 4174 (1993).

[27] R. P. Feynman, Phys. Rev. **56**, 340 (1939).

[28] H. Hellmann, Einfu¨hrung in die Quantenchemie (Deuticke, Leipzig) (1939).

[29] S. Baroni, P. Giannozzi and A. Testa, Phys. Rev. Lett. **58**, 1861 (1987).

[30] X. Gonze, Phys. Rev. A **52**, 1086 (1995).

[31] X. Gonze, Phys. Rev. A **52**, 1096 (1995).

[32] E. A. Hylleras, Z. Phys. **65**, 209 (1930).

[33] A. Dalgarno and A. L. Stewart, Proc. R. Soc. London Ser. A **238**, 269 (1956).

[34] F. Dupont-Bourdelet, J. Tillieu and J. Guy, J. Phys. Radium **21**, 776 (1960).

[35] O. Sinanoglu, J. Chem. Phys. **34**, 1237 (1961).

[36] H. Olijnyk, S. K. Sikka, and W. B. Holzapfel, Phys. Lett. A **103A**, 137 (1984).

[37] J. Z. Hu and I. L. Spain, Solid State Commun. **51**, 263 (1984).

[38] M. Hanfland, U. Schwarz, K. Syassen, and K. Takemura, Phys. Rev. Lett. **82**, 1197 (1999).

[39] P. D. De Cicco and F. A. Johnson, Proc. R. Soc. London Ser. A **310**, 111 (1969).

[40] R. Pick, M. H. Cohen, and R. M. Martin, Phys. Rev. B **1**, 910 (1970).

[41] P. Giannozzi, S. de Gironcoli, P. Pavone, and S. Baroni, Phys. Rev. B **43**, 7231 (1991).

[42] S. Baroni, P. Giannozzi, and E. Molinari, Phys. Rev. B **41**, 3870 (1991).

[43] S. J. Gardiner, Harmonic Approximations (Cambridge press, UK), (1995).

[44] J. S. Tse, D. D. Klug, Y. Yao, Y. Le Page and J. R. Rodgers, Solid State Comm. **145**, 5 (2007).

[45] L. Landau and E. Lifschits, Electrodynamics of Continuous Media (Pergamon Press), (1960).

[46] M. Veithen, X. Gonze, and Ph. Ghosez, Phys. Rev. B **71**, 125107 (2005).

[47] J. J. Rehr and R. C. Albers, Rev. Mod. Phys. **72**, 621 (2000).

[48] F. de Groot, Chem. Rev. **101**, 1779 (2001).

[49] D. E. Sayers, E. A. Stern, and Farrel W. Lytle, Phys. Rev. Lett. **27**, 1204 (1971).

[50] C. G. Van de Walle and P. E. Blöchl, Phys. Rev. B **47**, 4244 (1993).

[51] P. E. Blöchl, Phys. Rev. B **50**, 17953 (1994).

[52] Y. Yao, J. S. Tse and K. Tanaka, Phys. Rev. **B 77**, 052103 (2008).

[53] D. M. Deaven and K. M. Ho, Phys. Rev. Lett. **75**, 288 (1995).

[54] A. R. Oganov and C. W. Glass, J. Chem. Phys. **124**, 244704 (2006).

[55] G. Trimarchi and A. Zunger, Phys. Rev. B **75**, 104113 (2007).

[56] N. L. Abraham and M. I. Probert, Phys. Rev. B **73**, 224104 (2006).

[57] Y. Yao, S. Fabris, J. S. Tse, S. de Gironcoli and S. Scandolo, (in preparation).

[58] G. M. Eliashberg, Sov. Phys. JETP **11**, 696 (1960).

[59] G. M. Eliashberg, Zh. Eksp. Teor. Fiz. **38**, 966 (1960).

[60] A. B. Migdal, Sov. Phys. JETP **34**, 996 (1958).

[61] A. B. Migdal, Zh. Eksp. Teor. Fiz. **34**, 1438 (1958).

[62] Quantum-ESPRESSO is a community project for high-quality quantum-simulation software, based on density functional theory, and coordinated by Paolo Giannozzi. See http://www.quantum-espresso.org and http://www.pwscf.org.

[63] G. Kresse and J. Furthmüller, Comput. Mater. Sci. **6**, 15 (1996).

[64] J. M. Soler, E. Artacho, J. D. Gale, A. García, J. Junquera, P. Ordejón and D. Sánchez-Portal, J. Phys.: Condens. Matter **14**, 2745 (2002); http://www.uam.es/departamentos/ciencias/fismateriac/siesta/

[65] L. Kleinman and D. M. Bylander, Phys. Rev. Lett. **4**, 1425 (1982).

[66] D. Vanderbilt, Phys. Rev. B. **41**, 8412 (1990).

[67] J. Bardeen, L. N. Cooper, and J. R. Schrieffer, Phys. Rev. **108**, 1175 (1957).

[68] M. Hanfland, K. Syassen, N. E. Christensen and D. L. Novikov, Nature **408**, 174 (2000).

[69] K. Shimizu, H. Ishikawa, D. Takao, T. Yagi, and K. Amaya, Nature (London) **419**, 597 (2002).

[70] V.V. Struzhkin, M. I. Eremets, W. Gan, H.-K. Mao, and R. J. Hemley, Science **298**, 1213 (2002).

[71] S. Deemyad and J. S. Schilling, Phys. Rev. Lett. **91**, 167001 (2003).

[72] Y. Yao and J. S. Tse, Phys. Rev. **B 75**, 134104 (2007).

[73] N. W. Ashcroft, Phys. Rev. Lett. **92**, 187002 (2004).

[74] N. W. Ashcroft, J. Phys. Condens. Matter. **16,** S945 (2004).

[75] J. S. Tse, Y. Yao and K. Tanaka, Phys. Rev. Lett. **98**, 117004 (2007).

[76] Y. Yao, J. S. Tse, Y. Ma and K. Tanaka, Europhys. Lett. **78**, 37003 (2007).

[77] J. S. Tse, Y. Yao and Y. Ma, J. Phys.: Condens. Matter **19,** 425208 (2007).

[78] M. I. Eremets, I. A. Trojan, S. A. Medvedev, J. S. Tse and Y. Yao Science **319** 1506 (2008).

[79] R.F.W. Bader, Atoms in Molecules – A Quantum Theory, Oxford University Press, Oxford (1990).

[80] R.F.W. Bader, Acc. Chem. Res. **18**, 9 (1985).

[81] R.G.A. Bone and R.F.W. Bader, J. Phys. Chem. **100**, 10892 (1996)

[82] L.F. Lundegaard, G. Weck, M.I. McMahon, S. Desgreniers, and P. Loubeyre, Nature **443**, 201 (2006).

[83] H. Fujihisa, Y. Akahama, H. Kawamura, Y. Ohishi, O. Shimomura, H. Yamawaki, M. Sakashita, Y. Gotoh, S. Takeya, and K. Honda, Phys. Rev. Lett. **97**, 085503 (2006).

[84] J. S. Tse and D. D. Klug, Nature **378**, 595 (1995).

[85] J. Kohanoff, S. Scandolo, S. de Gironcoli, and E. Tosatti, Phys. Rev. Lett. **83**, 4097 (1999).

[86] C.J. Pickard, R.J. Needs, Nat. Phys. **3**, 473 (2007).

[87] J. S. Tse, Y. Yao, D. D. Klug, and S. Desgreniers, J. Phys. Conf. Series **121**, 012006 (2008).

[88] J. S. Tse, Y. Yao, D. D. Klug, and S. Desgreniers, (in preparation).

[89] Y. Yao, J. S. Tse, Z. Song, D. D. Klug, J. Sun and Y. Le Page, Phys. Rev. B **78**, 054506 (2008).

[90] I. N. Goncharenko, M. I. Eremets, M. Hanfland, J. S. Tse, M. Amboage, Y. Yao and I. A. Trojan, Phys. Rev. Lett. **100**, 045504 (2008).

[91] M. Taillefumier, D. Cabaret, A. M. Flank, and F. Mauri, Phys. Rev. B **66**, 195107 (2002).

[92] C. J. Pickard, Ph.D. Thesis, (1997)

[93] D. Cabaret, E. Gaudry, M. Taillefumier, P. Sainctavit, and F. Mauri, Physica Scripta. **T115**, 131 (2005).

[94] Edward Teller, Jour. Supercond. **14**, 299 (2004).

[95] N. W. Ashcroft, Nature **419**, 569 (2002).

[96] M. M. Dacorogna, K. J. Chang, and M. L. Cohen, Phys. Rev. B **32** 1853 (1985).

[97] K. J. Chang, M. M. Dacorogna, M. L. Cohen, J. M. Mignot, G. Chouteau, and G. Martinez, Phys. Rev. Lett. **54**, 2375 (1985).

[98] T. Yabuuchi, T. Matsuoka, Y. Nakamoto, and K. Shimizu, J. Phys. Soc. Jpn. **75**, 083703 (2006).

[99] T. Yabuuchi, Y. Nakamoto, K. Shimizu, and T. Kikegawa, J. Phys. Soc. Jpn. **74,** 2391 (2005).

[100] Y. Nakamoto, T. Yabuuchi, T. Matsuoka, K. Shimizu, and K. Takemura, J. Phys. Soc. Jpn. **76,** 25 (2007).

[101] S. Okada, K. Shimizu, T. C. Kobayashi, K. Amaya, and S. Endo, J. Phys. Soc. Jpn. **65,** 1924 (1996).

[102] M. I. Eremets, K. Shimizu, T. C. Kobayashi, and K. Amaya, Science **281**, 1333 (1998).

[103] W. L. McMillan, Phys. Rev. **167**, 331 (1968).

[104] J. Tuoriniemi, K. Juntunen-Nurmilaukas, J. Uusvuori, E. Pentti, A. Salmela and A. Sebedash, Nature **447**, 187 (2007).

[105] C. F. Richardson and N. W. Ashcroft, Phys. Rev. B **55**, 15130 (1997).

[106] A. P. Jephcoat, H.-K. Mao, L. W. Finger, D. E. Cox, R. J. Hemley and C.-S. Zha, Phys. Rev. Lett. **59**, 2670 (1987).

[107] W. A. Caldwell, J. H. Nguyen, B. G. Pfrommer, F. Mauri, S. G. Louie and R. Jeanloz, Science **277**, 930 (1997).

[108] H. Cynn, C. S. Yoo, B. Baer, V. Iota-Herbei, A. K. McMahan, M. Nicol and S. Carlson, Phys. Rev. Lett. **86**, 4552 (2001).

[109] K. A. Goettel, J. H. Eggert, I. F. Silvera, and W. C. Moss, Phys. Rev. Lett. **62**, 665 (1989).

[110] R. Reichlin, K.E. Brister, A.K. MaMahan, M. Ross, S. Martin, Y.K. Vohra and A.L. Ruoff, Phys. Rev. Lett. **62**, 669 (1989).

[111] E. G. Maksimov and D. Y. Savrasov, Solid State Commun. **119**, 569 (2001).

[112] H. K. Mao and R. J. Hemley, Rev. Mod. Phys. **66**, 671 (1994).

[113] P. Loubeyre, F. Occelli, and R. LeToulec, Nature (London) **416**, 613 (2002).

[114] Ch. Narayana, H. Luo, J. Orloff, and A. L. Ruoff, Nature (London) **393**, 46 (1998).

[115] J. Yang, J. S. Tse, Y. Yao and T. Iitaka, Angew. Chem. Int. Ed. **46**, 2675 (2007).

[116] J. R. Schrieffer, Theory of Superconductivity, Benjamin, New York (1964).

[117] J. G. Bednortz and K. A. Muller, Z. Phys. B **64**, 189 (1986).

[118] T. Timusk and B. Statt, Rep. Prog. Phys. **62**, 61 (1999).

[119] J. P. Carbotte, Rev. Mod. Phys. **62**, 1027 (1990).

[120] A. Y. Liu and A. A. Quong, Phys. Rev. B **53**, 7575 (1996).

[121] S. Y. Savrasov, Phys. Rev. B **54**, 16470 (1996).

[122] S. Y. Savrasov and D. Y. Savrasov, Phys. Rev. B **54**, 16487 (1996).

[123] R. Bauer, A. Schmid, P. Pavone, and D. Strauch, Phys. Rev. B **57**, 11276 (1998).

[124] D. J. Scalapino, in Superconductivity, Marcel Dekker, New York, (1969).

[125] W. L. McMillan and J. M. Rowell, Phys. Rev. Lett. **14**, 108 (1965).

[126] P. B. Allen and R. C. Dynes, J. Phys. C **8**, L158 (1975).

[127]P. B. Allen and R. C. Dynes, Phys. Rev. B **12**, 905 (1975)

[128] P. Morel and P. W. Anderson, Phys. Rev. **125**, 1263 (1962).

[129] Y. G. Jin and K. J. Chang, Phys. Rev. B **57**, 14684 (1998)

[130] J. K. Freericks, S. P. Rudin, and A. Y. Liu, Physica B **425**, 284 (2000).

[131] N. E. Christensen and D. L. Novikov, Phys. Rev. B **73**, 224508 (2001).

[132] M. Hanfland, I. Loa, K. Syassen, U. Schwarz and K. Takemura, Solid State Comm. **112**, 123 (1999).

[133] V. V. Struzhkin, R. J. Hemley and H. K. Mao, Bull. Am. Phys. Soc. **44**, 1489 (1999).

[134] A. F. Goncharov, V. V. Struzhkin, H. K. Mao and R. J. Hemley, Phys. Rev. B **71**, 184114 (2005).

[135] R. Rousseau, K. Uehara, D. D. Klug, and J. S. Tse, Chem-PhysChem **6**, 1703 (2005).

[136] N. E. Christensen and D. L. Novikov, Phys. Rev. Lett. **86**, 1861 (2001).

[137] R. E. Alonso, S. Sharma, C. Ambrosch-Draxl, C. O. Rodriguez, and N. E. Christensen, Phys. Rev. B **73**, 064101 (2006).

[138] J. S. Tse, Y. Ma, and H. M. Tutuncu, J. Phys.: Condens. Matter **17**, S911 (2005).

[139] S. U. Maheswari, H. Nagara, K. Kusakabe, and N. Suzuki, J. Phys. Soc. Jpn. **74**, 3227 (2005).

[140] D. Kasinathan, J. Kunes, A. Lazicki, H. Rosner, C. S. Yoo, R. T. Scalettar, and W. E. Pickett, Phys. Rev. Lett. **96**, 047004 (2006).

[141] G. Profeta, C. Franchini, N. N. Lathiotakis, A. Floris, A. Sanna, M. A. L. Marques, M. Lüders, S. Massidda, E. K. U. Gross, and A. Continenza, Phys. Rev. Lett. **96**, 047003 (2006).

[142] K. Iyakutti and C. Nirmala Louis, Phys. Rev. B **70**, 132504 (2006).

[143] L. Shi and D. A. Papaconstantopoulos, Phys. Rev. B **73**, 184516 (2006).

[144] Y. Xie, J. S. Tse, T. Cui, A. R. Oganov, Z. He, Y. Ma and G. Zou, Phys. Rev. B **75**, 064102 (2007).

[145] R. A. Jishi, M. Benkraouda, J. Bragin, J. Low Temp. Phys. **147** 549 (2007).

[146] A. Rodriguez-Prieto, A. Bergara, V. M. Silkin, and P. M. Echenique, Phys. Rev. B **74**, 172104 (2006).

[147] G. Kresse and D. Joubert, Phys. Rev. B **59**, 1758 (1999).

[148] J. Feng, W. Grochala, T. Jaron, R. Hoffmann, A. Bergara, and N.W. Ashcroft, Phys. Rev. Lett. **96**, 017006 (2006).

[149] Pickard C. J. and Needs R. J., Phys. Rev. Lett. **97**, 045504 (2006).

[150] L. Sun, J. Phys.: Condens. Matter **18**, 8573 (2006).

[151] X. J. Chen, APS March meeting bulletin **23**, 00013 (2007).

[152] Y. Yao, J. S. Tse, Y. Ma and K. Tanaka, Europhys. Lett. **78**, 37003 (2007).

[153] N. Troullier and J. L. Martins, Phys. Rev. B **43**, 1993 (1991).

[154] X. Xu and W. A. Goddard III, J. Chem. Phys. **121**, 4068 (2003).

[155] A. D. Becke and K. E. Edgecombe, J. Chem. Phys. **92**, 5397 (1990).

[156] A. Simon, Angew. Chem., Int. Ed. Engl. **36**, 1788 (1997)

[157] M. Wierzbowska, S. de Gironcoli and P. Giannozzi, condmat/0504077.

[158] J. M. An et al., Phys. Rev. B **66**, 220502(R) (2002).

[159] P. B. Allen, Phys. Rev. B **6**, 2577 (1972).

[160] R. W. Lynch and H. G. Drickamer, J. Phys. Chem. Solids **26**, 63 (1965).

[161] Z. Q. Li and J. S. Tse, Phys. Rev. Lett. **85**, 5130 (2000).

[162] R. Micnas, J. Ranninger, and S. Robaszkiewicz, Rev. Mod. Phys. **62**, 113 (1990).

[163] C. Gatti, Z. Kristallogr. **220**, 399 (2005).

[164] X. Xu and W.A. Goddard, J. Chem. Phys. **121**, 4068 (2004).

[165] C. Katan, P. Rabiller, C. Lecomte, M. Guezo, V. Oison, M. Souhassou, J. Appl. Cryst. **36**, 65 (2003)

[166] X. Gonze and C. Lee, Phys. Rev. B **55**, 10355 (1997).

[167] G. K. Horton and A. A. Maradudin Dynamical Properties of Solids Volume **1**, North-Holland Publishing Company, Amsterdam (1974).

[168] D. Porezag and M. R. Pederson, Phys. Rev. B **54**, 7830 (1996).

[169] P. Giannozzi and S. Baroni, J. Chem. Phys. **100**, 8537 (1994).

[170] M. Cardona, in Light Scattering in Solids, edited by M. Cardona and G. Guntherodt (Springer-Verlag, Berlin), 1982, Vol. **50**.

[171] W. F. Murphy, W. Holzer, and H. J. Bernstein, Appl. Spectrosc. **23**, 211 (1969).

[172] D. Cremer and E. Kraka, Croat. Chem. Acta. **57**, 1259 (1984).

[173] D. Cremer and E. Kraka, Agnew. Chem. **23,** 627 (1984).

[174] A. F. Goncharov, E. Gregoryanz, R. J. Hemley, and H. K. Mao, Proc. Natl. Acad. Sci. USA **98**, 14234 (2001).

[175] R. J. Hemley, Z. G. Soos, M. Hanfland, and H. K. Mao, Nature **369**, 384 (1994).

[176] S. Scandolo, Proc. Natl. Acad. Sci. **100**, 3051 (2003).

[177] S. Bonev, E. Schwegler, T. Ogitsu, and G. Galli, Nature **431**, 669 (2004).

[178] E. Babaev, A. Sudba, and N.W. Ashcroft, Nature **431**, 666 (2004).

[179] I. I. Mazin, R. J. Hemley, A. F. Goncharov, M. Hanfland, H.K. Mao, Phys. Rev. Lett. **78**, 1066 (1997).

[180] N. H. Chen, E. Sterer, and I. F. Silvera, Phys. Rev. Lett. **76**, 1663 (1996).

[181] Y. A. Freiman and H. J. Jodl. Phys. Rep. **401**, 1 (2004).

[182] D. Schiferl, et.al. Acta Cryst. **B39**, 153 (1983).

[183] M. Nicol, K.R. Hirsch and H.B. Holzapfel, Chem. Phys. Lett., **68**, 49 (1979)

[184] I.N. Goncharenko, Phys. Rev. Lett. **94**, 205701 (2005)

[185] S. Desgreniers, Y.K. Vohra and A.L. Ruoff, J. Phys. Chem., **94**, 1118 (1990)

[186] Y. Akahama, H, Kawamura, D. Häusermann and M. Hanfland, Phys. Rev. Lett., **74**, 4690 (1995).

[187] K. Shimizu, K. Suhara, M. Ikumo, M.I. Eremets and K. Amaya, Nature **393**, 767 (1998).

[188] J.B. Neaton and N.W. Ashcroft, Phys. Rev. Lett. **88**, 205503 (2002).

[189] B. Militzer and R.J. Hemley, Nature, **443**, 150 (2006).

[190] X. Gonze, et.al., Comput. Materials Science, **25**, 478 (2002). http://www.abinit.org/

[191] C. Hartwigsen, S. Goedecker, and J. Hutter, Phys. Rev. B, **58**, 3641 (1998).

[192] I.D. Brown. Struct. Chem., **13**, 339 (2002).

[193] R. M. Wentzcovitch, J. L. Martins, and G. D. Price, Phys. Rev. Lett. **70**, 3947 (1993).

[194] G. Weck, P. Loubeyre and R. LeToullec, *Phys. Rev. Lett*., **88**, 035504 (2002).

[195] S. Serra, G. Chiarotti, S. Scandolo and E. Tosatti, *Phys. Rev. Lett*., **80**, 5160 (1998).

[196] V. Buch, R. Martonak and M. Parrinello*, J. Chem. Phys*., **123,** 051108 (2005).

[197] M. Parrinello and A. Rahman, *J. Appl. Phys*., **52**, 71 (1981).

[198] O. Degtyareva, M. M. Canales, A. Bergara, X. J. Chen, Y. Song, V. V. Struzhkin, H. K. Mao, and R. J. Hemley*, Phys. Rev. B.* **76**, 064123 (2007).

[199] X. J. Chen, V. V. Struzhkin, Y. Song, A. F. Goncharov, M. Ahart, Z. Liu, H. K. Mao, and R. J. Hemley, *Proc. Nat. Acad. Sci.* **105**, 20-23 (2008).

[200] S. Kirkpatrick, C. D. Gelatt, and M. P. Vecchi, Science **220**, 671 (1983).

[201] V. Cerny, J. Opt. Theo. App. **45**, 41 (1985).

[202] N. Metropolis, A.W. Rosenbluth, M.N. Rosenbluth, A.H. Teller, and E. Teller, J. Chem. Phys. **21**, 1087 (1953).

[203] A. Das and B. K. Chakrabarti, Quantum Annealing and Related Optimization Methods, Lecture Note in Physics, Vol. **679**, Springer, Heidelberg (2005).

[204] J. De Vicente, J. Lanchares, and R. Hermida, Phys. Lett. A **317**, 415 (2003).

[205] Z. Michalewicz and D. B. Fogel, *How to solve it : Modern Heuristics* (Springer, Berlin, 2000).

[206] A. E. Eiben and J. E. Smith, *Introduction to Evolutionary Computing* (Springer, Berlin, 2003).

[207] D. M. Deaven and K. M. Ho, Phys. Rev. Lett. **75**, 288 (1995).

[208] T. S. Bush, C. R. A. Catlow, and P. D. Battle, J. Mater. Chem. **5**, 1269 (1995)

[209] S. M. Woodley, P. D. Battle, J. D. Gale, and C. R. A. Catlow, Phys. Chem. Chem. Phys. **1**, 2535 (1999).

[210] S. M. Woodley, Struct. Bonding (Berlin) **110**, 95 (2004).

[211] S. V. Barabash, V. Blum, S. Müller, and A. Zunger, *Phys. Rev. B* **74**, 035108 (2006).

[212] G. L. W. Hart, V. Blum, M. J. Walorski, and A. Zunger, Nat. Mater. **4**, 391 (2005).

[213] H. T. Stokes, D. M. Hatch, and B. J. Campbell, (2007). ISOTROPY, http://stokes.byu.edu/isotropy.html

[214] C. Mailhiot, L. H. Yang, and A. K. McMahan, Phys. Rev. B **46**, 14 419 (1992).

[215] F. Zahariev, S. V. Dudiy, J. Hooper, F. Zhang, and T. K. Woo, Phys. Rev. Lett. **97**, 155503 (2006).

[216] W. D. Mattson, D. Sanchez-Portal, S. Chiesa, and R. M. Martin, Phys. Rev. Lett. **93**, 125501 (2004).

[217] M. M. G. Alemany and J. L. Martins, Phys. Rev. B **68**, 024110 (2003).

[218] M. I. Eremets, A. G. Gavriliuk, I. A. Trojan, D. A. Dzivenko, and R. Boehler, Nat. Mater. **3**, 558 (2004).

[219] F. Zahariev, A. Hu, J. Hooper, F. Zhang, and T. K. Woo, Phys. Rev. B **72**, 214108 (2005).

[220] F. Zahariev, J. Hooper, S. Alavi, F. Zhang, and T. K. Woo, Phys. Rev. B **75**, 140101(R) (2007).

[221] L. Radom, J. Baker, P. M. W. Gill, R. H. Nobes, and N. V. Riggs, J. Mol. Struct. Theochem. **126**, 271 (1985).

[222] A. H. Cowley, D. J. Mitchell, M. H. Whangbo, and S. Wolfe, J. Am. Chem. Soc. **101**, 5224 (1979).

[223] J. O. Williams, J. N. Scarsdale, L. Schäfer, and H. J. Geise, J. Mol. Struct. Theochem. **76**, 11 (1981).

[224] H. Olijnyk and W. B. Holzapfel, Phys. Lett. A **100**, 191 (1984).

[225] N.W. Ashcroft, Phys. Rev. Lett. **21**, 1748 (1968).

[226] E. G. Browan, Yu. Kagan, and A. Kholas, Sov. Phys. JETP **35**, 783 (1972).

[227] J. E. Jaffe and N.W. Aschroft, Phys. Rev. B **23**, 6176 (1981).

[228] A. R. Ubbelohde, Proc. R. Soc. A **159**, 295 (1937).

[229] F. M. Brower, N. E. Matzek, P. F. Reigler, H.W. Rinn, C. B. Roberts, D. L. Schmidt, J. A. Snover, and K. Terada, J. Am. Chem. Soc. **98**, 2450 (1976).

[230] J.W. Turley and H.W. Rinn, Inorg. Chem. **8**, 18 (1969).

[231] H.W. Brinks, A. Istad-Lem, and B. C. Hauback, J. Alloys Compd. **433**, 180 (2007).

[232] H.W. Brinks, A. I. Lem, and B. C. Hauback, J. Phys. Chem. B **110**, 25833 (2006).

[233] V. A. Yartus, R.V. Denys, J. P. Maehlen, C. Frommen, M. Fichtner, B.M. Bulychev, and H. Emerich, Inorg. Chem. **46**, 1051 (2007).

[234] H.W. Brinks, C. Brown, C. M. Jensen, J. Graetz, J. J. Reilly, and B. C. Hauback, J. Alloys Compd. **441**, 364 (2007).

[235] B. Baranowski, H. D. Hochheimer, K. Strossner, and W. Honle, J. Less-Common Met. **113**, 341 (1985).

[236] J. Graetz, S. Chaudhuri, Y. Lee, and T. Vogt, Phys. Rev. B **74**, 214114 (2006).

[237] P. Loubeyre, R. LeToullec, D. Hausermann, M. Hanfland, R. J. Hemley, H.K. Mao, and L.W. Finger, Nature (London) **383**, 702 (1996).

[238] C. J. Pickard and R. J. Needs, Phys. Rev. B **76**, 144114 (2007).

[239] C. Wagner, W. Riggs, L. Davis, and J. Moulder, in *Handbook of x-ray photoelectron spectroscopy*, edited by G.E. Muilenberg (Perkin Elmer Corporation, Eden Prairie, Minnesota, 1979).

[240] C. Wöll and M. Wühn, *Spektroskopie von elektronischer Struktur und molekularer Orientierung mittels NEXAFS* (Lehrstuhl für Physikalische Chemie I, Ruhr-Universität Bochum, Bochum, 1999).

[241] J. Stoehr, *NEXAFS Spectroscopy*, Vol. **25** of *Springer Series in Surface Science* (Springer Verlag, Berlin, 1996).

[242] R. D. Cowan, *The Theory of Atomic Structure and Spectra*, (University of California Press, Berkeley,1981).

[243] Ch. Brouder, J. Phys.: Condens. Matter **2**, 701 (1990).

[244] D. R. Hamann, Phys. Rev. B **40**, 2980 (1989).

[245] M. Profeta, F. Mauri, and C. J. Pickard, J. Am. Chem. Soc. **125**, 541 (2003).

[246] J. R. Yates, C. J. Pickard, and F. Mauri, Phys. Rev. B **76**, 024401 (2007).

[247] M. Taillefumier, D. Cabaret, A. M. Flank, and F. Mauri, Phys. Rev. B **66**, 195107

(2002).

[248] R. K. Harris, P. Hodgkinson, C. J. Pickard, V. Zorin, and J. R. Yates Magn. Reson. Chem. **45**, S174 (2007).

[249] Chris J. Pickard and Francesco Mauri, Phys. Rev. B **63**, 245101 (2001).

[250] Sidney Golden and Thomas R. Tuttle, Jr. Phys. Rev. B **42**, 6916 (1990).

[251] J. Muggli, Zeit. Angew. Math. Phys. **23**, 311 (1972).

[253] M. E. Rose, Elementary Theory of Angular Momentum. New York, Dover, 1995.

[254] G. Arfken, Mathematical Methods for Physicists, Academic Press, Orlando, 1985.

[255] C. J. Pickard and M. C. Payne, Elec. Micro. Analy **153**, 179 (1997).

[256] We used the pseudopotential generation code from the http://www.quantum-espresso.org distribution.

[257] G. K. Wannier. *Rev. Mod. Phys.* **64**, 1045 (1992).

[258] M. D. Segall, P. L. D. Lindan, M. J. Probert, C. J. Pickard, P. J. Hasnip, S. J. Clark, and M. C. Payne J. Phys.: Cond. Matt. **14**, 2717 (2002).

[259] S. J. Clark, M. D. Segall, C. J. Pickard, P. J. Hasnip, M. J. Probert, K. Refson, and M. C. Payne, Z. Kristal **220**, 567 (2005).

[260] M. Iannuzzi and J. Hutter, Phys. Chem. Chem. Phys. **9**, 1599 (2007).

[261] D. Prendergast and G. Galli, Phys. Rev. Lett. **96,** 215502 (2006).

[262] J. S. Tse, D. M. Shaw, D. D. Klug, S. Patchkovskii, G. Vanko, G. Monaco, and M. Krisch, Phys. Rev. Lett. **100,** 095502 (2008).

[263] E. Runge and E. K. U. Gross, Phys. Rev. Lett. **52**, 997 (1984).

[264] E. K. U. Gross and W. Kohn, Phys. Rev. Lett. **55**, 2850 (1985).

[265]Y. Ma, N. Wassdahl, P. Skytt, J. Guo, J. Nordgren, P. D. Johnson, J. E. Rubensson, T. Boske,W. Eberhardt, and S. D. Kevan, Phys. Rev. Lett. **69**, 2598 (1992).

[266] H. W. Kroto, J. R. Heath, S. C. O'Brien, R. F. Curl, and R. E. Smalley, Nature **318**, 162 (1985).

[267] C. T. Chen, L. H. Tjeng, P. Rudof, G. Meigs, J. E. Rowe, J. Chen, Jr., J. P. McCauley, A. B. Smith III, A. R. McGhie, W. J. Romanow, and E. W. Plummer, Nature **352**, 603 (1991).

[268] R. Mitsumoto, H. Oji, I. Mori, Y. Yamamoto, H. Shinohara, K. Seki, K. Umishita, S. Hino, S. Nagase, K. Kikichi, and Y. Achiba, J. Phys. IV **7**, 525 (1997).

[269] Amos B. Smith, III, Fullerene Chemistry, Pergamon, Oxford (1996).

[270] M. Nyberg, Y. Luo, L. Triguero, and L. G. M. Pettersson, Phys. Rev. B **60**, 7956 (1999).

[271] S. Fabris *et.al.*, (in preparation).

[272] F. Jollet and C. Noguera, Phys. Status Solidi B **179**, 473 (1993).

[273] J. Chaboy, M. Benfatto, and I. Davoli, Phys. Rev. B **52**, 10 014 (1995).

[274] I. Tanaka, J. Kawai, and H. Adachi, Phys. Rev. B **52**, 11 733 (1995).

[275] Z.Wu, F. Jollet, and F. Seifert, J. Phys.: Condens. Matter **10**, 8083 (1998).

[276] J. Slater and K. Johnson, Phys. Rev. B **5**, 844 (1972).

[277] D. Jayawardane, C. Pickard, L. Brown and M. Payne, Phys. Rev. B **64**, 115107 (2001).

[278] S. Myneni, Y. Luo, L. Naslund, M. Cavalleri, L. Ojamae, H. Ogasawara, A. Palmenschikov, P. Wernet, P. Vaterlaein, C. Heske, Z. Hussain, L. Pettersson and A. Nilsson, J. Phys.: Condens. Matter **14**, 213 (2002).

[279] W. E. Pickett, Physica C **468**, 126 (2008).

[280] J. Feng, R. G. Hennig, N. W. Ashcroft & R. Hoffmann, Nature **451**, 445 (2008).

[281] T. Matsuoka, M. Debessai, J.J. Hamlin, K. Suzuki, and J.S. Schilling, Phys. Rev. Lett. **100**, 197003 (2008).

[282] J. Feng, N. W. Ashcroft, and R. Hoffmann, Phys. Rev. Lett. **98**, 247002 (2007).

[283] J. S. Kim, L. Boeri, J. R. O'Brien, F. S. Razavi, and R. K. Kremer, Phys. Rev. Lett. **99**, 027001 (2007).

[284] A. Sanna, G. Profeta, A. Floris, A. Marini, E. K. U. Gross, and S. Massidda, Phys. Rev. B **75**, 020511(R) (2007).

[285] M. Calandra and F. Mauri, Phys. Rev. Lett. **95**, 237002 (2005).

[286] F. Giustino, J. R. Yates, I. Souza, M. L. Cohen and S. G. Louie, Phys. Rev. Lett. **98** 047005 (2007).

[287] F. Giustino, M. L. Cohen and S. G. Louie, Phys. Rev. B **76** 165108 (2007).

[288] G. H. Wannier, Phys. Rev. **52**, 191 (1937).

[289] J. W. Garland, Jr., Phys. Rev. Lett. **11**, 114 (1963).

[290] M. Lüders, M. A. L. Marques, N. N. Lathiotakis, A. Floris, G. Profeta, L. Fast, A. Continenza, S. Massidda, and E. K. U. Gross, Phys. Rev. B **72**, 024545 (2005).

[291] M. A. L. Marques, M. Lüders, N. N. Lathiotakis, G. Profeta, A. Floris, L. Fast, A. Continenza, E. K. U. Gross, and S. Massidda, Phys. Rev. B **72**, 024546 (2005).

[292] A. Floris, G. Profeta, N. N. Lathiotakis, M. Lüders, M. A. L. Marques, C. Franchini, E. K. U. Gross, A. Continenza, and S. Massidda, Phys. Rev. Lett. **94**, 037004 (2005).

[293] J. Maddox, Nature **335**, 201 (1988).

[294] A. R. Oganov and C. W. Glass *J. Phys.: Condens. Matter* **20**, 064210 (2008).

[295] E. Gregoryanz, A. F. Goncharov, C. Sanloup, M. Somayazulu, H. K. Mao, and R. J. Hemley. J Chem. Phys. **126**, 184505 (2007).

[296] E. Gregoryanz, C. Sanloup, R. Bini, J. Kreutz, H. J. Jodl, M. Somayazulu, H. K. Mao, and R. J. Hemley, J. Chem. Phys. **124**, 116102 (2006)

[297] M. I. Eremets, A. G. Gavriliuk, N. R. Serebryanaya, I. A. Trojan, D. A. Dzivenko, R. Boehler, H. K. Mao, and R. J. Hemley, J. Chem. Phys. **121**, 11296 (2004).

[298] A. H. MacDonald, S. H. Vosko, P. T. Coleridge, J. Phys. C: Solid State Phys. **12**, 2991 (1979).